GEM TN-93-288

The RDT-RPC Technology Option for GEM

Boston University, Brown University, C.S. Draper Laboratories, Indiana University, Institute for Theoretical and Experimental Physics - (ITEP) Moscow, Joint Institute for Nuclear Research, Lawrence Livermore National Laboratory, LeCroy Corporation, Louisiana State University, Massachusetts Institute of Technology, Michigan State University, Moscow State University, Superconducting Super Collider Laboratory, University of Rome & Instituto Nazionale di Fisica Nucleare, University of Tennessee

January 29, 1993

Abstract:

A muon system for the GEM SSCL detector based on Round Drift Tubes (RDT) has many attractive features. The Pt-trigger and beam crossing tag for the RDT tracking system can be accomplished by either a PWC system, similar but less costly in design than Cathode Strip Chambers, or by a promising new type of RPC chamber. Given the economic construction of these chamber technologies a system can be envisioned with both good momentum reconstruction performance and pattern recognition capabilities. Full-scale chamber prototypes based on the RDT and RPC technologies have been constructed and tested successfully at the Texas Test Rig. Spatial resolutions have been measured in two designs of RDT chambers which meet or exceed the baseline resolution requirement of 100μm per chamber layer.

The RDT-RPC Technology Option for GEM

Boston University, Brown University, Draper Laboratories, Indiana University,
ITEP-Moscow, JINR-Dubna, Lawrence Livermore National Laboratory,
LeCroy Corporation, Louisianna State University,
Massachusetts Institute of Technology, Michigan State University,
Moscow State University, Superconducting Super Collider Laboratory,
University of Rome & Instituto Nazionale di Fisica Nucleare,
University of Tennessee

January 29, 1993

Abstract:

A muon system for the GEM SSCL detector based on Round Drift Tubes (RDT) has many attractive features. The Pt-trigger and beam crossing tag for the RDT tracking system can be accomplished by either a PWC system, similar but less costly in design than Cathode Strip Chambers, or by a promising new type of RPC chamber. Given the economic construction of these chamber technologies a system can be envisioned with both good momentum reconstruction performance and pattern recognition capabilities. Full-scale chamber prototypes based on the RDT and RPC technologies have been constructed and tested successfully at the Texas Test Rig. Spatial resolutions have been measured in two designs of RDT chambers which meet or exceed the baseline resolution requirement of 100 μm per chamber layer.

Table of Contents

(1) Introduction 3

(2) Chamber Layout 6

(3) System Parameters 17

(4.0) Design of the Round Drift Tube Chambers 23

(4.1) RDT Stereo 40

(5) RPC Design 43

(6.0) RDT R&D Results 61

(6.1) Factors Affecting Precision 99

(6.2) RPC R&D Results 116

(7) Trigger 122

(8) System Performance 145

(8.1) Trigger Performance 145

(8.2) Momentum Reconstruction 149

Appendix A: RPC Construction and Costs 159

Appendix B: Details of Accidental Calculation 206

Appendix C: Costs 214

Appendix D: RDT System with a PWC T_0Trigger 216

Appendix E: RDT Stand-alone Trigger 221

(1.0) Introduction:

The muon system described in this report is based on RDTs for precision tracking and RPCs (or PWCs) for triggering. Drift tubes, 2.54 cm in diameter, are configured in each of three superlayers with a multiplicity of 8:10:8. Pairs of anode wires of the even (odd) tubes of a given layer in a superlayer are tied together through a delay line. The time difference yields a correlated X-Y measurement. The Y resolution (along the wire) by this method is about 10 cm RMS. In each superlayer there will be 2U and 2Y chamber planes oriented in small angle (4mr) stereo. The other layers in a superlayer will have either 4 or 6 axial tubes [parallel (perpendicular) to the axis of the solenoid for barrel (endcaps)]. The small-angle stereo layers in a superlayer will contribute almost equally to the momentum resolution as the axial layers, while also providing redundant non-bend plane coordinate measurements. It is proposed that both the barrel and endcaps have this 8:10:8 small-angle stereo configuration.

The trigger of the RDT system would be either Resistive Plate Counters (RPCs) or Proportional Wire Chambers (PWCs). The RPC solution was adapted at the onset of the GEM R&D Program because of its many attractive features. At this time the RPC technology has not demonstrated the rate performance needed for application in the endcaps at $L=10^{33}/cm^2sec$ given the uncertainties of the neutron fluence there. However the RDT technology has sufficient strong points not to discard it completely as a concept, and to propose a substitute for the RPCs. In fact one can envision a conservative muon system based on RDT tracking with a PWCs acting as a trigger. Preliminary estimates indicate that such a system would be both inexpensive, straightforward, and have the appropriate performance characteristics.

To maintain a simplicity of design, all the RDT and RPC (PWC) chambers in the proposed detector will be rectangular. Perhaps surprisingly, rectangular chambers, which are a natural deployment for the barrel region, also offer several attractive features for the endcaps and none of putative drawbacks there. First, we find that the momentum and trigger resolutions meet the baseline specification in the endcaps with this rectangular chamber design. Second, roughly 1/3 of the chamber area is overlapped and hence a muon penetrating this region will traverse twice the usual number of tubes where the resolution at high momentum and pattern recognition will be improved and the low momentum resolution not significantly degraded. Third, the alignment paths in both the barrel and endcaps are located through small cracks between chamber planes allowing chambers within a sector as well as chambers of different sectors to be tied together while maintaining almost full solid angle coverage.

The trigger function will be performed with three layers of RPCs mounted in each of the superlayers. (PWCs could also be deployed for this purpose.) In a trigger system based on RPCs each chamber in a superlayer will furnish a bend plane (X) and non-bend plane (Y) signal for the Level 1 trigger. There would be three chambers per superlayer. A 2/3 coincidence requirement of the RPC layers in each superlayer will

be imposed to yield an efficient trigger. All three superlayers of RPCs are in turn placed in coincidence. A similar system could be envisioned based on PWCs.

The following is a list of advantages of the technologies proposed:

RDT Features for Momentum Reconstruction:

- Proven technology - used by several groups at SLAC, CDF, E706-FNAL, AMY-TRISTAN, and several groups at CERN.
- Can be operated in either the proportional or limited streamer mode.
- Can be pressurized to improve resolution: 50 μm has been obtained at 4.5 atm.
- Full-scale prototypes have been constructed by the GEM Muon group which have demonstrated the baseline resolution.
- RDTs can be used to trigger the muon system - adding redundancy to the system in a stand-alone mode or with an external T0 signal.
- A RDT chamber forms a laminated tube structure which is both rigid and light weight. Hence the chamber need be supported only at its ends, making the support structure and alignment path layout practical.
- Layer resolution independent of the angle of incidence.
- Inherent cylindrical symmetry makes Lorentz angle correction straightforward.

Trigger:

Based on RPC

- Intrinsically fast device - measured jitter at low rates < 2 ns.
- Easy to construct - light weight laminated structure with both X and Y readout possible for each chamber gap.
- Large pulses - typically 0.5 V in 50 Ω.
- X-Y readout for each chamber gap.

Based on PWC

- Principle of operation can be modeled so that characteristics can be designed.

- A narrow gap chamber (2.5 mm wire spacing) will be intrinsically fast.

- Can be instrumented to give T0 from the anode wires, and a bend plane measurement for a Pt-dependent signal. (CSC design without precision.)

The muon chambers of the GEM detector will have to operate in a hostile environment. Not only must the system discriminate against low momentum charged particles, but also operate gracefully in a large fluence of neutrons. For these reasons the pattern recognition and rate capabilities of the system are as important as the single track momentum resolution. A priori, the muon system must be redundant - having as many space points and cross check as is economically feasible.

The following table lists the information provided by this system.

Table 1.1
Information per Incident Muon Track

	Bend plane		Non-bend plane		
	Trigger	Tracking	Trigger	Tracking time	stereo
Sl1	3	8	3	4	4
Sl2	3	10	3	6	4
Sl3	3	8	3	4	4

We note that there are a total of 35 measurement points in each of the bend and non-bend planes for a muon track. Such a high redundancy will be quite useful in making the proposed system operational at the expected high background to signal environment.

(2.0) Chamber Layout

A sectional view of the RDT chambers in a quadrant of the GEM detector is shown in Fig. 2.1. Both the barrel and endcap regions are divided into 16 equal segments in the ϕ dimension. These segments are subdivided into projective towers consisting of 3 superlayers of 8+10+8 planes. Each superlayer has 4 layers of small angle stereo tubes (2U+2V) in addition to the 4+6+4 axial tubes.

In the barrel region, 3 chambers are required to cover the half-length in the middle and outer superlayers, while two chambers are sufficient in the inner superlayer. The cracks associated with these divisions are arranged to accommodate the projective alignment scheme and to maximize the acceptance high quality tracks. An axial view of a barrel quadrant is shown in Fig. 2.2. To allow penetration for support structure and alignment paths, the middle superlayer in the barrel consist of 6 chambers that are alternately long-narrow or short-wide as shown in Fig. 2.3. The details of the ϕ and θ sections are shown in Figs. 2.4 and 2.5, respectively. The barrel layers overlap in the ϕ dimension due to the beveled chamber edges, as shown in the drawing labeled Section A. Section D shows the crack in θ due to the chamber end plate and plugs (5 cm), plus a gap of 5 cm for cables, connectors, support structure, etc. Sections B and C show the larger gaps that exist only at the chamber corners for the alignment paths. The number, channel count, location, size and weight of the chambers in the barrel regions are specified in Table 2.1.

In principle there can be an alignment path at each corner of each of the chambers in the barrel, a total of 24 paths per segment. However, we believe that it should be possible to design a fixture which would tie together the corners of adjacent chambers within a segment. This would allow these corners to be referenced by a single alignment path and reduce the number of paths to 12 per segment.

In the endcap regions, there are two projective sections in the θ dimension. Since there is a larger radial separation in this region, the chambers are allowed to overlap in both θ and ϕ. This permits the use of rectangular chambers, identical in design to the barrel chambers, as shown in Fig. 2.6. Rectangular chambers in the endcap segments have two other advantages. Alignment paths along the 16° projection can be easily accommodated in triangular shaped cracks that exist where four chambers meet. The chambers also have a substantial overlap area that will help with local and global alignment. There are a total of 9 alignment paths per endcap segment. Table 2.2 specifies the number, channel count, location, size and weight of the chambers in the endcaps.

The RPC (or PWC) layout exactly matches the RDT chambers. Since the RPC's are expected to be light and flexible, they could be attached to the surface of the RDT's. The estimated acceptance of the RDT/RPC system is listed in Table 2.3. The chamber ends and alignment paths add up to a 6% loss of solid angle which is equal to .09

units of η (excluding the region which is adjacent to the inaccessible forward direction).

RDT QUADRANT LAYOUT
ELEVATION VIEW

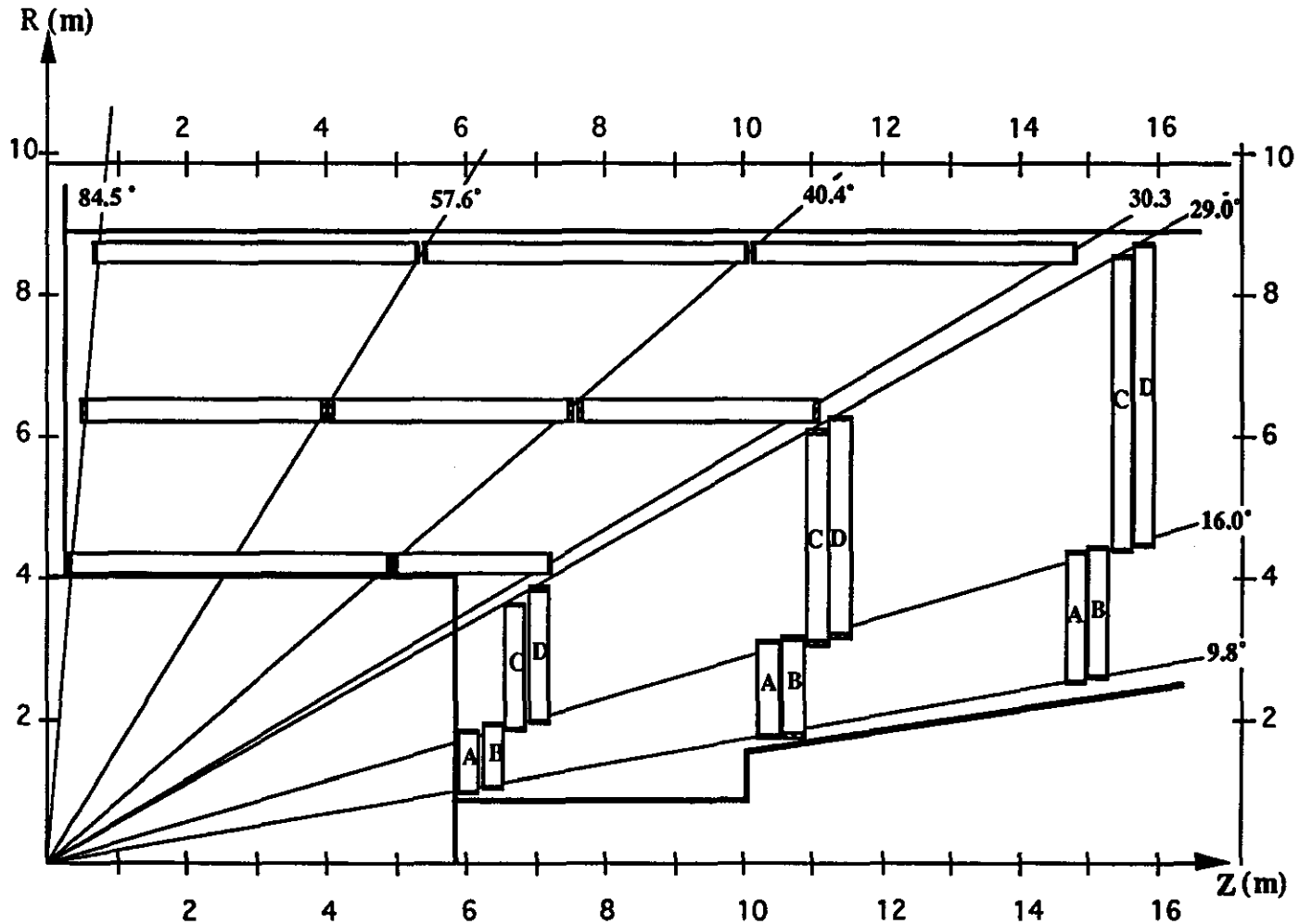

Fig. 2.1

RDT BARREL QUADRANT
AXIAL VIEW

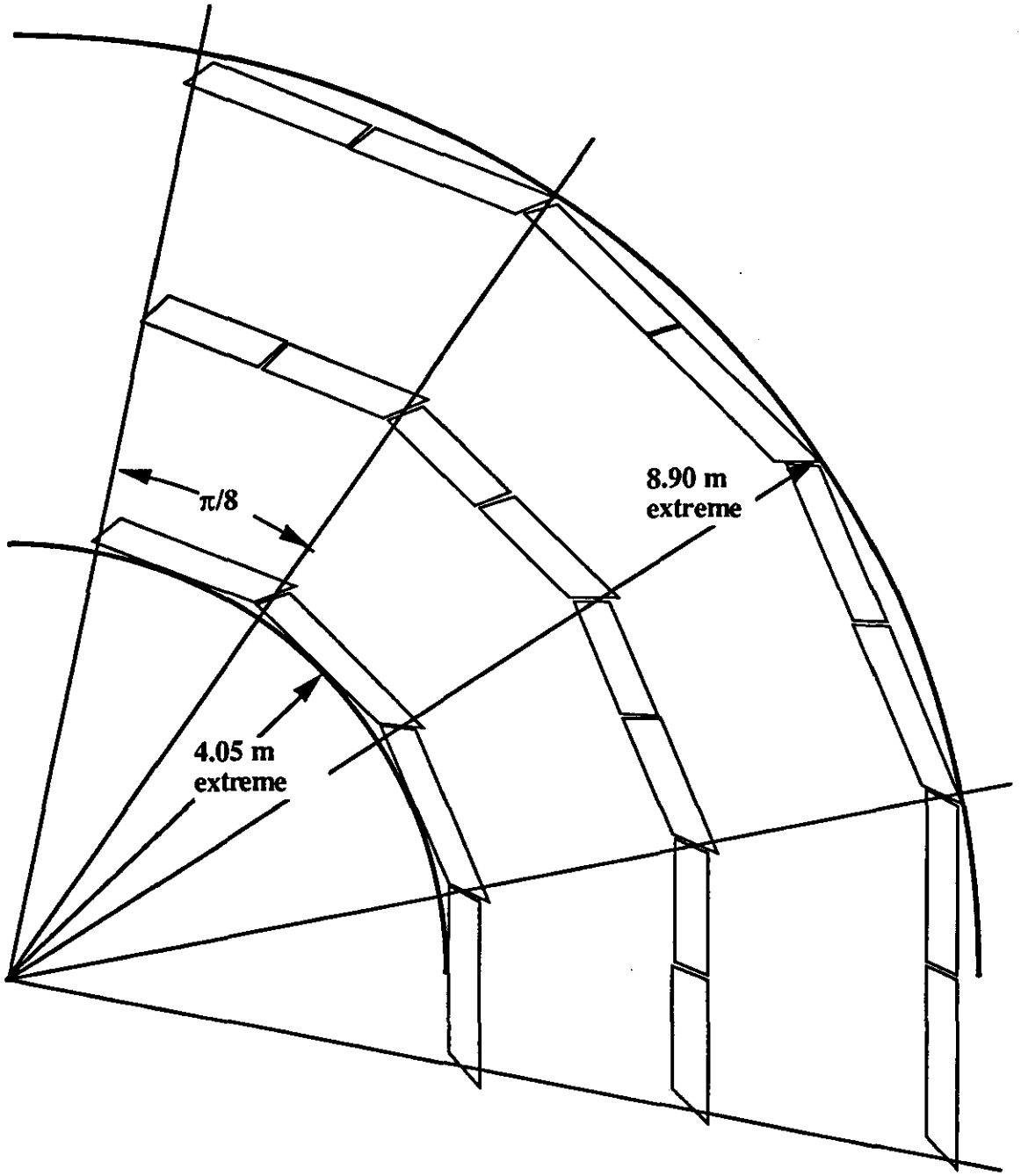

Fig. 2.2

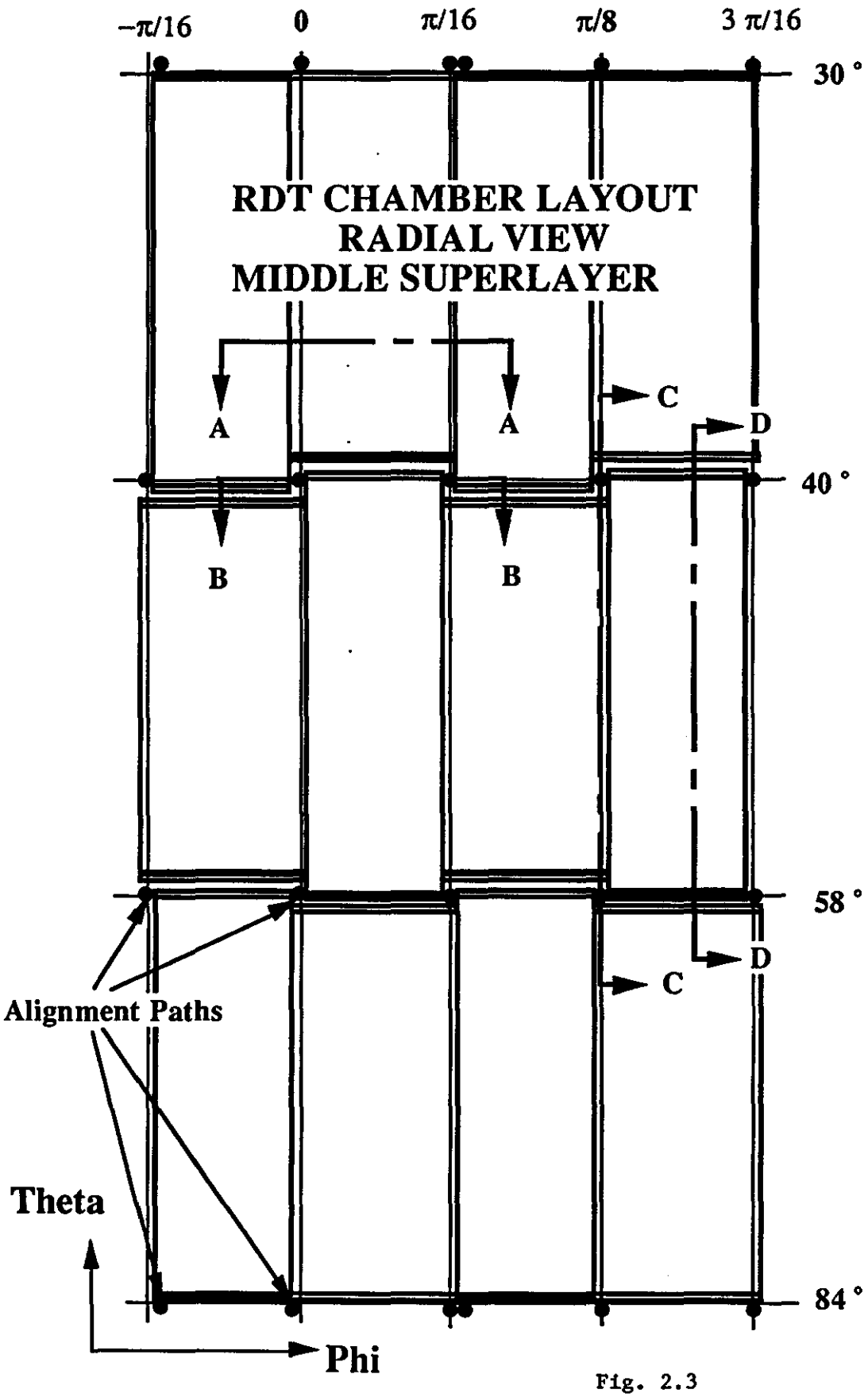
−π/16
0
π/16
π/8
3 π/16
30 °
RDT CHAMBER LAYOUT
RADIAL VIEW
MIDDLE SUPERLAYER
A
A
C
D
40 °
B
B
58 °
D
C
Alignment Paths
Theta
84 °
Phi

Fig. 2.3

RDT BARREL, MIDDLE SUPERLAYER
PHI OVERLAP DETAIL

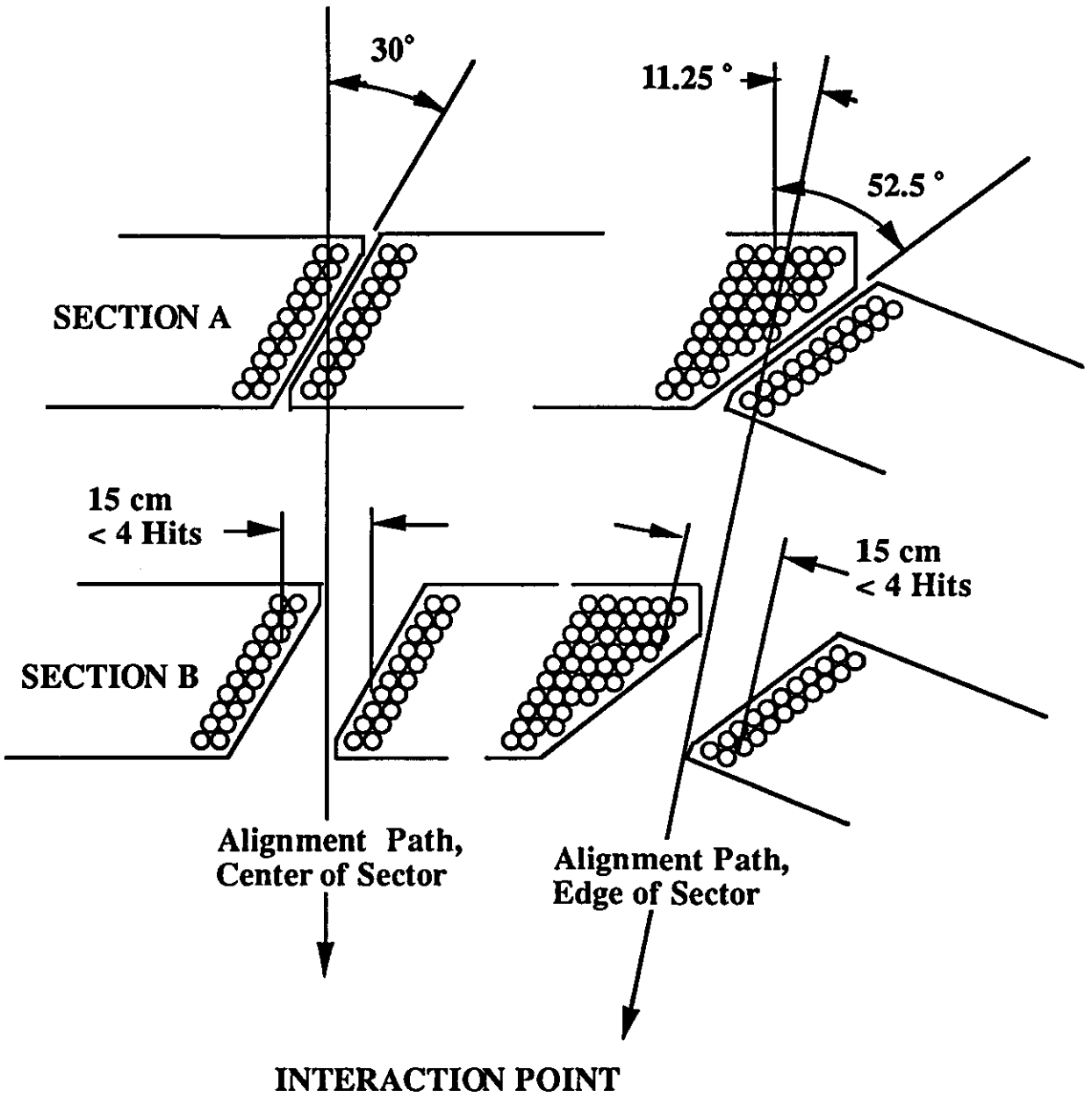

Fig. 2.4

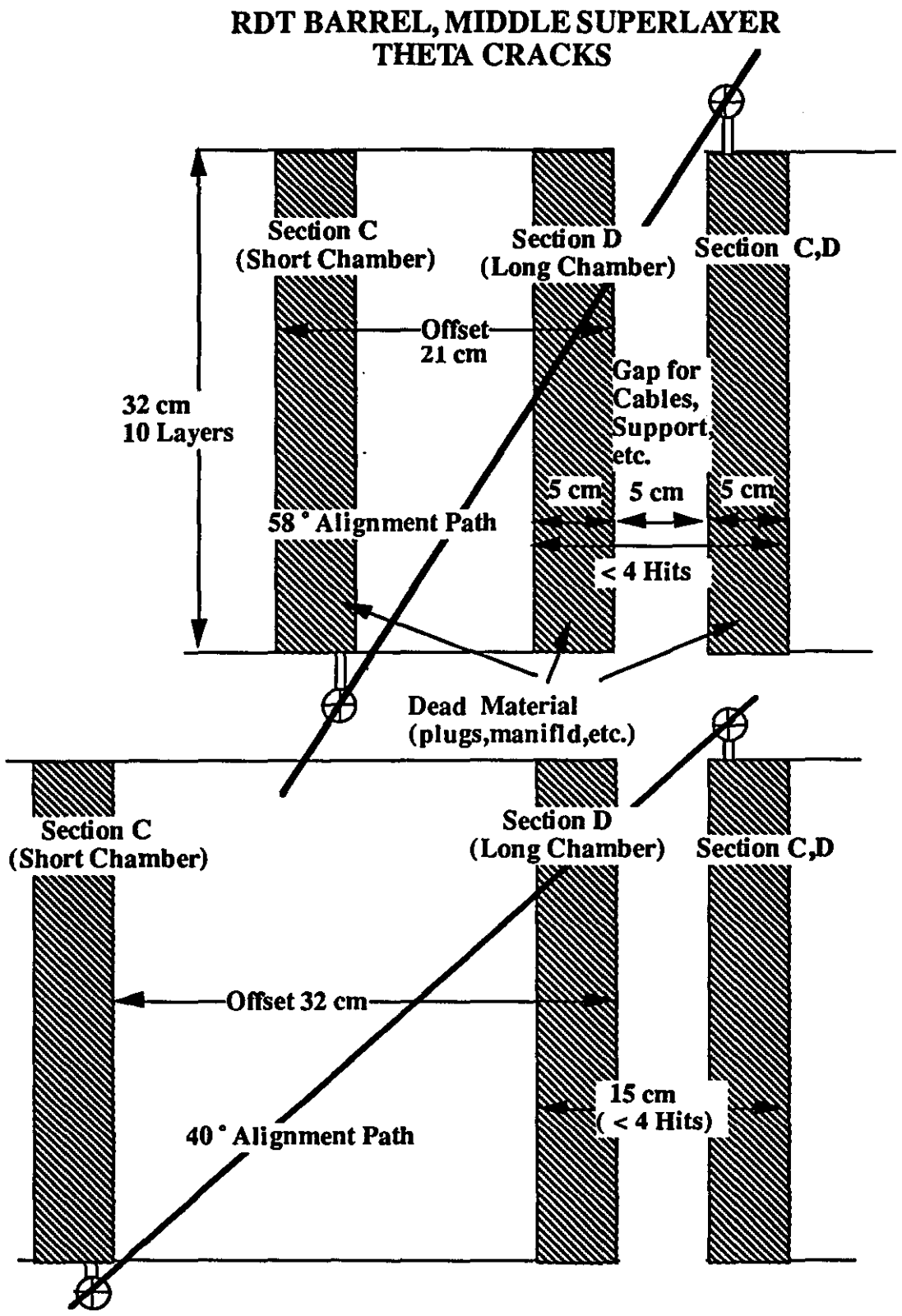
RDT BARREL, MIDDLE SUPERLAYER
THETA CRACKS
Section C
(Short Chamber)
Section D
(Long Chamber)
Section C,D
Offset
21 cm
32 cm
10 Layers
Gap for
Cables,
Support,
etc.
5 cm
5 cm
5 cm
58 ° Alignment Path
< 4 Hits
Dead Material
(plugs,manifld,etc.)
Section C
(Short Chamber)
Section D
(Long Chamber)
Section C,D
Offset 32 cm
15 cm
(< 4 Hits)
40 ° Alignment Path

Fig. 2.5

GEM BARREL RDT CHAMBER SPECS
16 SECTORS; 8+10+8; 25 mm Dia.

INPUT PARAMETERS:				
Theta angular coverage :		84.5	30.3	
Tube Material, density:		Alum.	2.7	
Tube Wall: (mm)		0.30		
Plate Thickness (mm), density:		19.05	2.7	
Case Thickness (mm), density:		6.40	0.25	
# of Segments:		16		
VARIABLES:				
Radius (m):	**4.2**	**6.4**	**8.6**	**TOTAL**
Chambers/Theta	2	3	3	
Chambers/segmnt	1	2	2	
# of Layers:	8	10	8	26
Tube Dia: (mm)	25.4	25.4	25.4	
RESULTS:				
Tube Length: (m)	3.4	3.4	4.6	**909 km**
Tubes/Chamber:	512	496	528	
Avg. width: (m)	1.67	1.26	1.69	
Chamb. thick.: (m)	0.28	0.32	0.28	
Chambers/Half:	32	96	96	224
Chambers Total	64	192	192	**448**
Tubes/Half:	16384	47616	50688	114688
Tubes Total	32768	95232	101376	**229376**
Weight/chamber (lb)				
Tubes:	247	243	348	
Manifold plates:	105	92	106	
Plugs:	57	55	59	
Case:	50	41	68	
Electronics,cable:	256	248	264	
Total/Chamber:	715	679	844	
Weight/Segment:	1429	4075	5066	
Weight/Half:	22867	65208	81051	85 ton
Weight Total	45733	130415	162102	**169 ton**

Table 2.1

RDT ENDCAP LAYOUT
PROJECTIVE VIEW

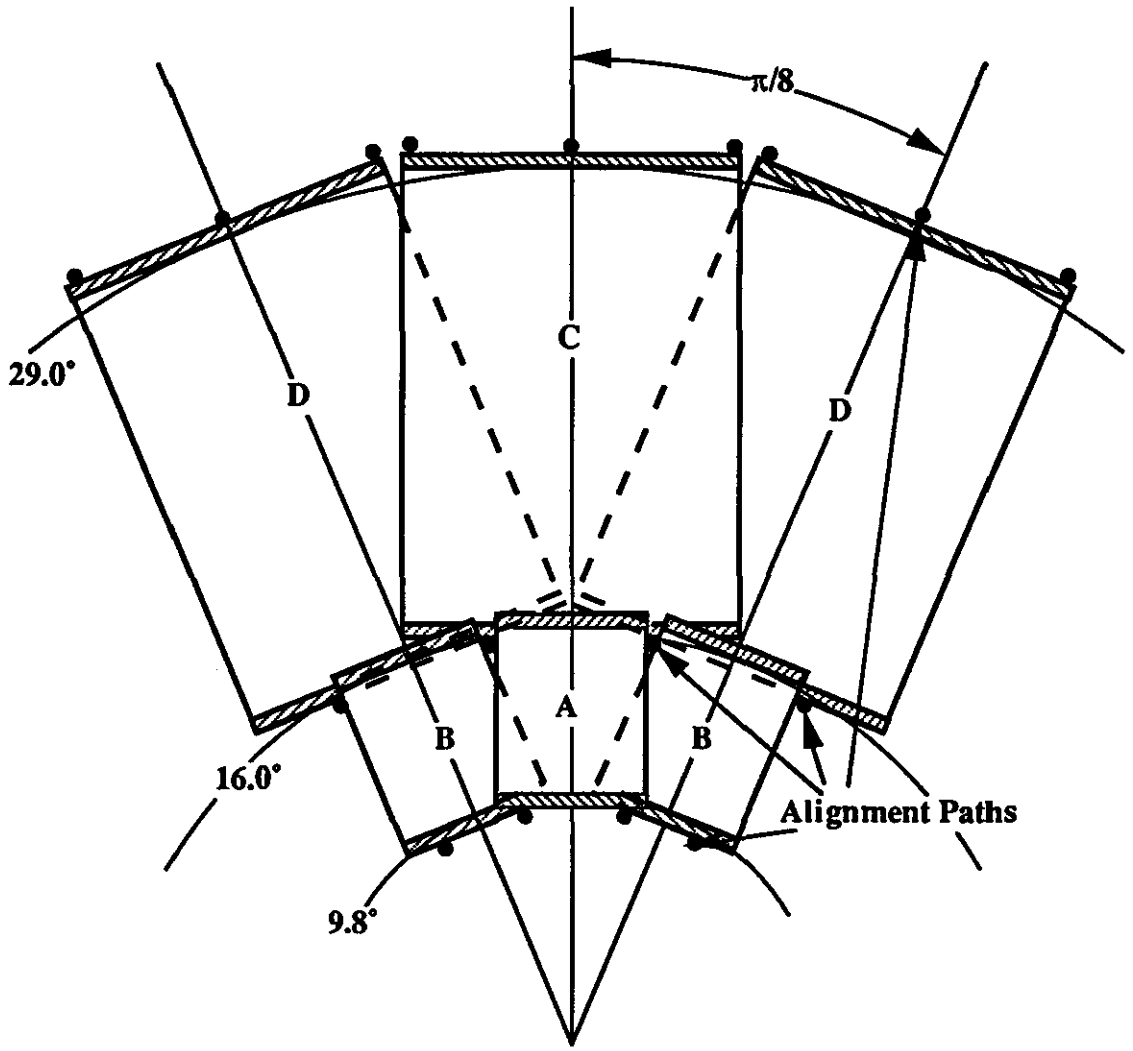

Fig. 2.6

GEM END CAP RDT CHAMBERS
16 SECTORS; 8-10-8; 25 mm Dia.

INPUT PARAMETERS:

Tube Material, density:	Alum.	2.7
Tube Wall: (mm)	0.30	
M. Plate Thickness (mm), de	19.05	2.7
Case Thickness (mm), densit	6.40	0.25
# of Sectors:	16	

VARIABLES:

Avg. Z (m):	6.25	6.85	11.20	10.60	15.60	15.00	Total
Inner Theta	9.8	16.0	16.0	9.8	16.0	9.8	
Outer Theta	16.0	29.0	29.0	16.0	29.0	16.0	
Chambers/segmnt:	1	1	1	1	1	1	
# of Layers:	8	8	10	10	8	8	26
Tube Dia: (mm)	25.4	25.4	25.4	25.4	25.4	25.4	

RESULTS:

Tube Length: (m)	0.7	1.8	3.0	1.2	4.2	1.7	314 km
Tubes/Chamber:	224	464	960	464	1072	528	
Chamb. width: (m)	0.71	1.51	2.47	1.21	3.44	1.71	
Chamb. thick.: (m)	0.28	0.28	0.32	0.32	0.28	0.28	
Chambers/Half:	16	16	16	16	16	16	96
Chambers Total	32	32	32	32	32	32	192
Tubes/Half:	3584	7424	15360	7424	17152	8448	59392
Tubes Total	7168	14848	30720	14848	34304	16896	118784
Weight/chamber (lb)							
Tubes:	23	121	409	80	636	128	
Manifold plates:	45	95	179	88	215	107	
Plugs:	25	52	107	52	120	59	
Case:	6	26	64	16	116	27	
Electronics,cable:	112	232	480	232	536	264	
Total/Chamber:	211	525	1240	467	1624	586	
Weight/Half:	3372	8407	19844	7475	25976	9374	37 ton
Weight Total	6744	16814	39689	14951	51953	18748	74 ton

Table 2.2

RDT MUON ACCEPTANCE LOSSES

SOURCE	Crack Size (mm)	R, Z (mm)	Θ (degree)	Δ(Θ) (radian)	η	Φ/2π	LOSS (% 4π)
Central Membrane	250	4000	86.4	.0623	.063	1.00	6.2%
Barrel-Endcap			30.0	.0262	1.317	1.00	1.3%
Forward Region			8.7	.1518	2.576	1.00	2.3%
					Base Loss		**9.8%**
Chamber End	100	4000	84.5	.0248	.096	1.00	2.5%
Chamber Ends	150	6000	57.6	.0178	.598	1.00	1.5%
Alignment Path	360	6400	57.6	.0401	.598	0.13	0.4%
Chamber Ends	150	4000	40.4	.0158	1.000	1.00	1.0%
Alignment Path	470	6400	40.4	.0308	1.000	0.13	0.3%
Alignment Path	125	6000	16.0	.0193	1.962	0.04	0.0%
Chamber End	100	6000	9.8	.0162	2.457	1.00	0.3%
					Additional Loss		**6.0%**

Table 2.3

(3.0) Summary of System Parameters

The GEM Muon System is based on a large and open solenoidal magnet with an air flux return. Three superlayers of muon tracking chambers will be deployed between the calorimeter and magnet cryostat to reconstruct the sagitta in the magnetic field. Iron flux concentrators will be placed along the central axis of the magnet to create a radial component of the B-field, thereby increasing the bend power at small angles. Muon trajectories will be reconstructed using Round Drift Tubes (RDTs) from $|\eta| = 0$ to 2.5, over most of the azimuth. The design goals for the momentum resolution of the system are for Pt = 500 GeV/c, $\delta Pt/Pt = 5\%$ at $|\eta| = 0$ and = 13% for $|\eta| = 2.5$.

The magnet will furnish a field at the IP of 0.8T. It will consist of a superconducting coil of 9.5 m. radius constructed in two segments, each with a coil length of approximately 14.25 m. The coil segments will be separated by 1.5 m. The inner cryostat radius is 9.0 m. and constrains the outer radius of the barrel muon chambers. The steel of the flux concentrator will be located in a cone of half-angle 9.4^0, (non-projective angle) extending from 10 m. to 18 m. from the IP.

The resolution of the reconstructed muon momentum will be limited by the chamber resolution, the alignment precision within a superlayer and between superlayers, the bending power of the magnet (BL^2), and "unreconstructable" fluctuations of the energy loss in the calorimeter. For the barrel region the lever arm, L, at 90° will be 4.4 m., and in the endcaps equal to, or larger than, 8.6 m. (plus angle factors). Multiple layers of chambers will be required with exacting spatial resolutions (of order 100 μm/detector element) and systematic alignment (of order 25 μm) between superlayers to reach the desired momentum resolution.

(3.1) Physics Goals:

(1) Provide muon identification - track penetrating 12 to 14 λ of calorimeter
(2) Charge assignment of muons
(3) Pt trigger
(4) Beam crossing time marker
(5) Muon momentum determination from a few GeV/c to a few TeV/c.
Design goal: $\delta P_t/P_t = 5\%$ (13%) at $|\eta| = 0$ (2.5), for $P_t = 500$ GeV/c.

(3.2) System Parameters:

(3.2.1) Barrel Region:

Geometry:

Rmagnet (inner radius of cryostat)	9.0 m
B-field at the IP	0.8 T
Rcalorimeter (outer radius of calorimeter)	3.70 m
Calorimeter thickness at $\|\eta\| = 0$	11 λ
Assumed calorimeter material	Pb/Cu/Sc/Kr
Number of sectors in ϕ	16
Location of neutron shield (20 cm B-Poly)	3.70 m < R <3.90 m
Chamber stay-clear (neutron shield or magnet cryostat) 10 cm	

RDT Chamber Parameters:

(a) Tracking - bend plane:

Spatial resolutions (baseline assumption):	
Chamber single-layer resolution	< 100 μm (RMS)
Internal chamber alignment	< 50 μm
Superlayer-to-superlayer alignment	< 25 μm
Tube wall thickness	300 μm
Radiation length/tracking chamber layer	1.14 % (Al-tubes)
Tube diameter	2.54 cm
Chamber layers/SuperLayer (SL1:SL2:Sl3)	8:10:8
Stereo configuration:	
SL1	4 axial-2 U-2V
SL2	6 axial-2 U-2V
SL3	4 axial-2 U-2V
Angle of stereo (α)	4 mr
Radii of barrel superlayer midplanes:	
	SL 1 = 4.2 m
	SL 2 = 6.4 m
	SL 3 = 8.6 m
Barrel lever arm	4.4 to 4.5 m

Half-lengths of superlayers along (Z) (approx.)	
	SL 1 = 7.0 m
	SL 2 = 10.8 m
	SL 3 = 14.4 m
ϕ Widths of sectors (approx.)	
	SL 1 = 1.67 m
	SL 2 = 2.55 m
	SL 3 = 3.42 m
Coverage:	
Polar angle: (gaps not included)	$29.6^{\circ} < \theta < 85.8^{\circ}$
Pseudo-rapidity:	$0.074 < \lvert\eta\rvert < 1.33$
Azimuthal angle: (goal)	94 %
Number of alignment paths	768
Number of drift tubes in barrel:	229,376
(b) Tracking - nonbend plane: (RPC)	
Number of RPC gaps/superlayer	3
Information/RPC gap	X and Y
Radial locations of RPCs (chamber midplanes) (approx.)	
	SL 1 = 4.35 m
	SL 2 = 6.55 m
	SL 3 = 8.45 m
RPC Radiation length/superlayer (2 gaps)	1.66 %
Chamber thickness for 2 gap package	3.3 cm
Nonbend plane RPC segment widths:	
	SL1 = 3.9 cm
	SL2 = 6.5 cm
	SL3 = 8.9 cm
Nonbend plane electronic channel count:	15,936
(c) Tracking-nonbend plane: (RDT)	
Number of RDT stereo layers/superlayer	SL1: 4 axial - 2U-2V
	SL2: 6 axial - 2U-2V
	SL3: 4 axial - 2U-2V
Angle of stereo	4 mr
Information per superlayer from stereo	2 Y
Resolution/Y measurement	1.8 cm RMS
(d) Triggering: Resistive Plate Chambers (RPC)	
Measurements - Bend plane:	
Segment width	1.3 cm
Number of electronic trigger channels:	25,056
Time jitter of chamber	< 1.5 ns
Time jitter of T0 determination	< 8.3 ns

(e) Triggering: Round Drift Tubes (RDT)

Bend plane segment size	1.25 cm
Non-bend plane segment (by timing)	10 cm RMS

(3.2.2) Endcap region:

Geometry:

B-field at IP	0.8 T
Length of magnet cryostat	15 m
Z-separation of coils	1.5 m
Flux concentrator (FC):	
Zfront	10.0 m
Zrear	18.0 m
OD-half angle of steel	9.4º non-projective
ID	1.2 m
Zcalorimeter (half-length of calorimeter along Z)	5.70 m
Calorimeter thickness at $\lvert\eta\rvert = 2.5$	$< 17\lambda$
Zmax	16.5 m
Number of sectors in ϕ	16
Location of neutron shield	5.70 m < Z < 5.90 m
Chamber stayclear	10 cm

Chamber Parameters (RDT):

Spatial resolutions (baseline assumption):	
Chamber single-layer resolution	< 100μm (RMS)
Internal chamber alignment	< 50 mm
Superlayer-to-superlayer alignment	< 25 μm
Tube wall thickness	300 μm
Radiation length/tracking chamber layer	1.14 % (Al-tubes)
Tube diameter	2.54 cm
Chamber layers/SuperLayer (SL1:SL2:Sl3)	8:10:8
Stereo configuration:	
SL1	4 axial-2 U-2V
SL2	6 axial-2 U-2V
SL3	4 axial-2 U-2V
Angle of stereo	4 mr
Polar angle regions:	
	$9.75º < \theta < 16º$
	$16º < \theta < 29º$

Channel count:

Number of RDT channels	118,784
Nonbend plane: Small angle stereo	

Coverage:

Polar angle:	$9.75º < \theta < 29º$
Pseudo-rapidity:	$1.35 < \lvert\eta\rvert < 2.46$

Azimuthal angle:	94 %
Number of alignment paths	288

(a) Forward angle region: $9.75^\circ < \theta < 16^\circ$ $(1.96 < |\eta| < 2.46)$

Chamber configuration: segmented in ϕ:

<u>Segment A:</u>
Z location of chambers:

SL 1 = 6.05 m
SL 2 = 10.6 m
SL 3 = 15.4 m

<u>Segment B:</u>
Z location of chambers:

SL 1 = 6.45 m
SL 2 = 11.0 m
SL 3 = 15.8 m

(b) Outer angle region: $16^\circ < \theta < 30^\circ$ $(1.32 < |\eta| < 1.96)$

<u>Segment C:</u>
Average Z location of chambers:

SL 1 = 6.65 m
SL 2 = 11.2m
SL 3 = 15.85m

<u>Segment D:</u>
Average Z location of chambers:

SL 1 = 7.05 m
SL 2 = 11.6 m
SL 3 = 16.25 m

<u>Triggering:</u> Resistive Plate Chambers (RPC)

Bend plane:	
Segment width $9.75^\circ < \theta < 16^\circ$ $(1.96 < \|\eta\| < 2.46)$	0.44 cm
Segment width $16^\circ < \theta < 29^\circ$ $(1.32 < \|\eta\| < 1.96)$	0.60 cm
Number of trigger channels:	71,104
Nonbend plane:	
Segment width $9.75^\circ < \theta < 16^\circ$ $(1.96 < \|\eta\| < 2.46)$	
SL1	3.8 cm
SL2	6.5 cm
SL3	9.3 cm
Segment width $16^\circ < \theta < 30^\circ$ $(1.32 < \|\eta\| < 1.96)$	
SL1	3.8 cm
SL2	6.5 cm
SL3	9.3 cm
Number of nonbend plane trigger channels:	6,336
Time jitter of chamber	< 1.5 ns

Time jitter of T0 determination	< 8.3 ns

Note that a backup trigger based on RDTs is envisioned.

(3.2.3) Grand Totals:

Number of RDT tubes(Channels)	348,160
Number of RPC channels	118,432
Number of alignment paths	1056
Coverage (within Muon System)	94 %

(4.0) Design of Round Drift Tube Chambers

I. RDT Design Goals and Characteristics

The RDT design goals are to provide:

- Precise placement of wires.
- Reliable, gas tight seals for possible pressurization.
- Epoxy-bonded tubes creating a strong mechanical unit.
- Simple assembly procedures requiring a minimum of technical skill.
- A high-level of safety features for gas-flexiblity.

The Drift-tube technology and the RDT concept in particular emphasize the following characteristics:

- A high-level of redundancy is possible with a reasonable number of electronics channels at a practical cost.
- The wires are physically and electronically isolated from each other, wire breakage will cause the loss of only that tube.
- The symmetry of the round tubes will result in a drift time which can be simply and accurately corrected for the Lorentz angle effects.
- The laminated tube structure leads to a very strong and yet light package allowing large chamber structures and a minimum of alignment components.
- Projective alignment paths can be incorporated in a natural way with a minimum of acceptance loss.
- Resolution below 100 μm in both the LS and Proportional modes and a demonstrated resolution improvement path through pressurization.

Two prototypes were delivered to the Texas Test Rig at the SSCL, one constructed by the Dubna group and another by the MSU group. The two detectors have been tested jointly and have achieved similar results. The mechanical construction of the MSU prototype is recognized as having several very desirable features and has been adopted by both groups. The components for a second chamber of this design have been sent to Dubna. The electronics for the MSU prototype are standard, off-the-shelf, amplifier/discriminator cards. The Dubna prototype emphasized low-noise amplifiers and has been shown to have superior performance. Elements of the Dubna design will be used to optimize the electronics for the GEM detector.

II. Drift Tube Design and Construction Details

A Drift-Tube Design Considerations

The end plugs and gas manifolds are the most critical components in the design of the MSU RDT. The plugs must seal the end of the tube at up to 4 atmospheres of pressure while providing a passage for the flow of gas through the tube; they must insulate the high voltage on the anode wire from the tube and provide for electrical contact between the conductive surface of the tube and the grounded gas manifold; they must center the tube on the wire with moderate precision (to within 250 μm) and allow for the highly accurate relative positioning of the wires (to within 25 μm). The design uses standard parts, such as O-rings, wherever possible and takes advantage of modern mass production techniques, such as injection molding or automatic screw machines and our own magnetic crimping device. One important feature of the precision manifold plate design is that there are **no other contributions to the systematic error in the wire placement.**

B. Precision Gas Manifolds

Drawings of the gas manifold are shown in Figs. 4.0.1-4.0.2. One should note that the specification in Fig. 4.0.2 for the hole placement is a "true position" specification. The tolerance of 0.005 cm means that the true position of the hole centers in the manifold must lie within a circle 0.005 cm in diameter. We found that a local machine shop was able to hold only .01 cm tolerances in producing our prototype plates which results in a 20 μm RMS on the systematic hole placement. While **these plates are already within the GEM systematic error limits,** we believe that alternative procedures exist for production of the manifold plates that will be more accurate and less expensive than these plates.

C. Tube End-Plug

A section drawing of the region of the chamber near the tube ends is shown in Fig. 4.0.3. The aluminum tube is terminated by a two part plug whose details are shown in Figs. 4.0.4-4.0.6 and machined from glass filled (15%) Delrin. We have determined that production of an injection-molded part is feasible and, based upon a firm quotation, will be much less costly but may require the use of a different material. The large plug part (Fig. 4.0.4) has a O-ring which insures a good gas seal on the inner surface of the aluminum tube. This plug part is crimped into the tube end by a magnetic crimping machine which was constructed at MSU specifically for this purpose. The compressive force on the tube walls needed for the crimp is produced by the interaction of a rapidly changing magnetic field (created by discharging a capacitor through a copper coil wrapped around the tube) with the induced current. The tube can be crimped in a highly repeatable fashion with this device. The plug has been shaped so that the tube, once crimped, holds the plug firmly and the tube is wrapped neatly over the plug. This allows easy electrical contact from the tube wall to the manifold plate through a phosphor-bronze spring.

The second part of the plug, Figs. 4.0.5 and 4.0.6, looks like a hollow bolt. Three small O-rings make up the gas seal. The threads on the bolt need not be precise as the first O-ring (the one closest to the threads) seals the bolt into the plug. The remaining two O-rings on the bolt seal above and below the gas channels in the manifold plate. Gas flows through a hole in the bolt into the tube and is removed by an identical plug at the opposite end of the tube. The assembly procedure for the chamber is greatly simplified by this two part plug: the manifold plates can be rigidly mounted on the assembly table at the correct separation, the pre-plugged tubes placed between the manifold plates and the bolt then inserted through the manifold plate into the plug.

D. Wire Location:

The wire is located in the manifold plate by a precisely drilled jewel (accurate in diameter to a few microns) which itself is positioned accurately on the centerline of the bolt near its head. At this location on the shaft of the bolt is a spherical surface designed so that the bolt fits precisely in the center of a manifold plate hole but can still change its angle somewhat to adjust to small imperfections in the bolt and plug manufacture (particularly in the threads) while not disturbing the precise centering of the jewel. The parts of the wire location system are shown in Fig. 4.0.7.

To wire a tube, the 50 μm tungsten wire is attached to thin stiff rod which is then passed through the hollow of the bolts in both ends. The tungsten wire is removed from the rod and threaded through the jewel hole in both pins and the pins are then pressed into the bolt heads. The wire is tensioned, held firmly by a high tensile strength silver alloy solder and then epoxy is injected into a small hole which gas-seals the pin and provides a second mechanical hold on the wire. The solder we use (Sn62) has also been recommended for its lower gold amalgamation properties.

We have made some measurements on the accuracy of the jewel hole placement in the center of the manifold plate holes. This was done by a inserting a plug in a spare manifold plate and focusing a microscope on the center of the 50 μm hole in the jewel. The plug was then slowly rotated in the hole. The center of the hole in the jewel moved in a circle whose diameter was recorded. Without moving the microscope a series of other plug and jewel combinations were inserted in the same hole and similar measurements made on them. The data are shown in Fig. 4.0.8, where we have chosen a random rotation for each jewel while the error in the concentricity is taken from the measurements. The RMS displacement of the jewel hole center along the manifold plate (x-direction) from the nominal hole center is 12 μm. This will be a random position error and will add (in quadrature) a negligible amount to the 100μm resolution expected for the drift distance measurements.

E. Costs:

The costs are summarized in Tables 4.0.2, 4.0.3, 4.0.4. The major labor cost is in inserting the wire in the tubes, and the major material costs are in the tubes.

Table 4.0.1

GEM RDT Design Parameters:

No. of Chambers	
Barrel	448
End Caps	192
Total	640
No. of tubes	
Barrel	229,000
End Caps	119,000
Total	348,000
Tube Material	Aluminum
Tube Diameter	25.4 mm
Tube Wall Thickness	300 μm
Wire Diameter	100 μm
Wire Tension	1.2 kgm (g)
Operating Pressure	1-4 ATM
Gas Volume	
Barrel	460 kl
End Caps	160 kl
Total	620 kl
Detector Area	
Barrel	23,000 m^2
End Caps	8,000 m^2
Total	31,000 m^2
Tolerances	
σ(wire-fiducial),random	< 50 μm
σ(wire-fiducial), systematic	< 25 μm
σ(wire-tube axis@end of tube)	< 100 μm
σ(tube sagitta)	< 250 μm
σ(tube diameter)	< 100 μm
σ(wire tension)	< 100 gm (g)
Change in tube length (4.7 m tube)	
@ Δ(P) = 3 ATM	0.4 μm
@ Δ(T) = 10° C	1.1 μm
Est. Operating Voltage (LS mode)	
@ 1 ATM	5 kV
@ 4 ATM	10 kV
Max. Drift Time	350 ns
Radiation Length/Layer	
Tube	1.06 %
Gas(AR @ 4 ATM)	0.04 %
Wire	0.04%

Total	1.14 %
Radiation Length (10 Layer Chamber)	11.5 %
<u>Track Rate Limits (5% Occupancy)</u>	
Barrel Region (Avg. $0.1 < \eta < 1.3$)	120 Hz/cm^2
Endcap Region (Avg. $1.3 < \eta < 2.0$)	135 Hz/cm^2
Endcap Region (Avg. $2.0 < \eta < 2.5$)	330 Hz/cm^2
<u>Max. Wire Sag (4.7 m tube)</u>	
@0 V (gravity only)	370 μm
@ 10 kV	420 μm
Tube Capacitance	10 pf/m
Characteristic Impedance	330 Ω

Table 4.02

RDT AVERAGE CHAMBER ASSEMBLY:
16 SECTOR, 8+10+8; 25 mm DIA
544 Tubes

Operation	Persons	Unit Time (hrs.)	Total Manhrs.
Inspect tubes	2	0.02	21.8
Cut tubes to length	2	0.02	21.8
Debur tubes	1	0.02	10.9
Clean tubes	1	0.02	10.9
Flair tube ends	2	0.01	10.9
Inspect plugs	1	0.01	10.9
Put O-rings onto plugs	1	0.01	10.9
Crimp plugs into tubes	2	0.02	43.5
Pressure test tubes	1	0.05	27.2
Inspect Manifold Plates	2	2	4.0
Assemble Manifold Plates	2	5	20.0
Setup Assembly Table	2	8	16.0
Assemble tubes into Manifold	2	0.02	21.8
Insert Wires into tubes	2	0.1	108.8
Seal plug ends	1	0.02	10.9
Install gas fittings	1	1	1.0
Pressure test assembly	2	8	16.0
HV test	2	0.02	21.8
Test wire tension	2	0.02	21.8
Assemble Case	2	10	20.0
Prepare Readout Boards	1	1	17.0
Test Readout Boards	1	0.5	8.5
Assemble Power Buses	2	4	8.0
Assemble R.O. Boards	1	1	17.0
Assemble HV Boards	1	1	17.0
Final testing	2	8	16.0
Package for Shipping	2	8	16.0
Total			530
Time/Tube			0.76
Time/Chamber			117

Table 4.03

BARREL RDT COST ESTIMATE
8+10+8 ; 25 MM TUBES

NUMBER OF CHAMBERS: 448

NUMBER OF CHANNELS: 229376

ITEM	REQ'D (K)	COST ($)	NOTE	TOTAL ($K)
TUBES (Avg. 3.7 m)	229	26.12	1	5992
PLUGS	459	1.70	1	780
WIRE GUIDES	459	1.50	1	688
WIRE (m)	1147	0.20	2	229
MANIFOLD PLATES	0.896	2500	2	2240
CASE	0.448	300	2	134
R.O. BOARDS	7.168	50	3	358
TEST/ASSEMBLY EQUIP.			3	200
	TOTAL COMPONENTS			10622
LABOR (hrs)	228	25	4	5702
TOTAL PARTS + LABOR				16324

NOTES:

1. BASED ON ESTIMATE FROM SOURCE
2. BASED ON PROTOTYPE, NO ALLOWANCE FOR QUANTITY DISCOUNT OR ALTERNATE METHODS
3. ESTIMATE
4. ESTIMATE (Avg. 512 tubes/chamber @.76 hrs/ tube + 120 hrs/chamber)

R. J. MILLER 1/14/93

Table 4.04

END CAP RDT COST ESTIMATE
8+10+8 ; 25 MM TUBES

NUMBER OF CHAMBERS: 192

NUMBER OF CHANNELS: 118784

ITEM	REQ'D (K)	COST ($)	NOTE	TOTAL ($K)
TUBES (Avg. 2.7 m)	118.8	19.06	1	2264
PLUGS	237.6	1.70	1	404
WIRE GUIDES	237.6	1.50	1	356
WIRE (m)	475.1	0.20	2	95
MANIFOLD PLATES	0.384	2500	2	960
CASE	0.192	300	2	58
R.O. BOARDS	3.712	50	3	186
TEST/ASSEMBLY EQUIP.			3	200
	TOTAL COMPONENTS			4523
LABOR (hrs)	113	25	4	2830
TOTAL PARTS + LABOR				7353

NOTES:

1. BASED ON ESTIMATE FROM SOURCE
2. BASED ON PROTOTYPE, NO ALLOWANCE FOR QUANTITY DISCOUNT OR ALTERNATE METHODS
3. ESTIMATE
4. ESTIMATE (Avg. 618 tubes/chamber @.76 hrs/ tube + 120 hrs/chamber)

R. J. MILLER 1/14/93

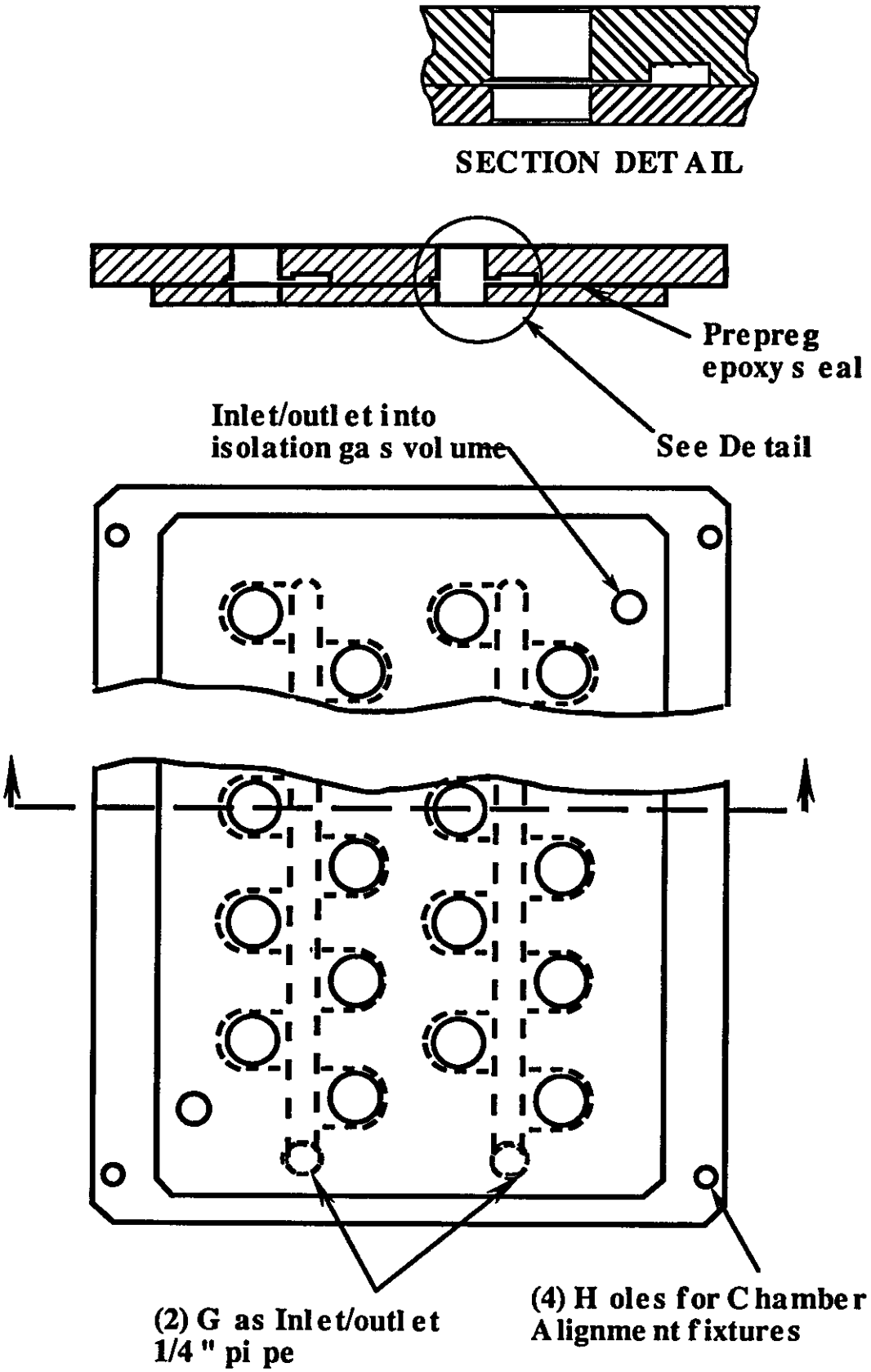
SECTION DETAIL
Prepreg
epoxy seal
Inlet/outlet into
isolation gas volume
See Detail
(2) Gas Inlet/outlet
1/4" pipe
(4) Holes for Chamber
Alignment fixtures

Fig. 4.0.1

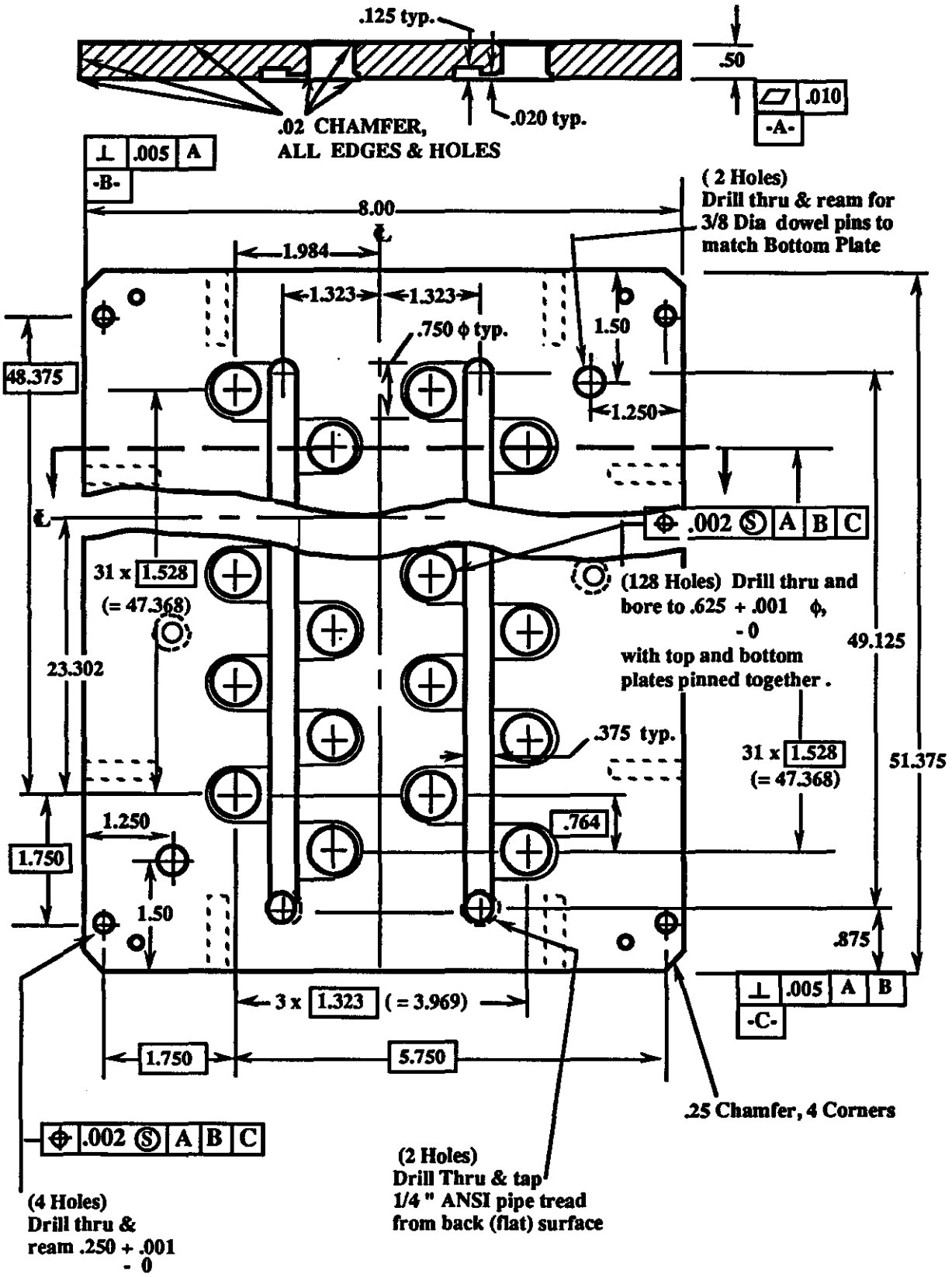
.125 typ.
.50
.010
-A-
.02 CHAMFER,
ALL EDGES & HOLES
.020 typ.
.005 A
-B-
8.00
1.984
1.323
1.323
.750 ϕ typ.
1.50
1.250
48.375
(2 Holes)
Drill thru & ream for
3/8 Dia dowel pins to
match Bottom Plate
.002 S A B C
31 x 1.528
(= 47.368)
(128 Holes) Drill thru and
bore to .625 + .001 ϕ,
- 0
with top and bottom
plates pinned together .
49.125
23.302
.375 typ.
31 x 1.528
(= 47.368)
51.375
1.250
.764
1.750
1.50
.875
.005 A B
-C-
3 x 1.323 (= 3.969)
1.750
5.750
.25 Chamfer, 4 Corners
.002 S A B C
(2 Holes)
Drill Thru & tap
1/4 " ANSI pipe tread
from back (flat) surface
(4 Holes)
Drill thru &
ream .250 + .001
- 0

Fig. 4.0.2

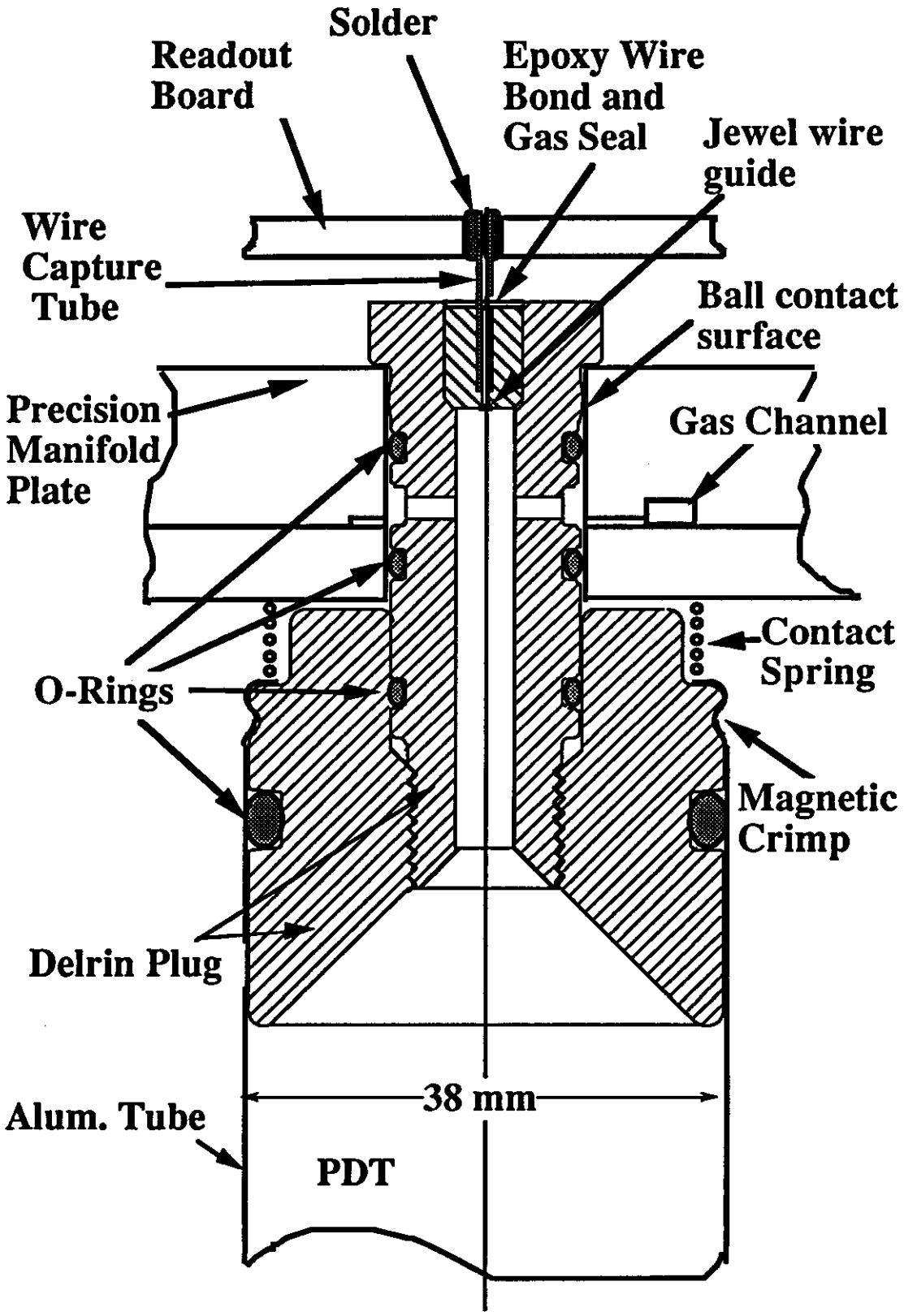
Solder
Readout Board
Epoxy Wire Bond and Gas Seal
Jewel wire guide
Wire Capture Tube
Ball contact surface
Precision Manifold Plate
Gas Channel
Contact Spring
O-Rings
Magnetic Crimp
Delrin Plug
38 mm
Alum. Tube
PDT

Fig. 4.0.3

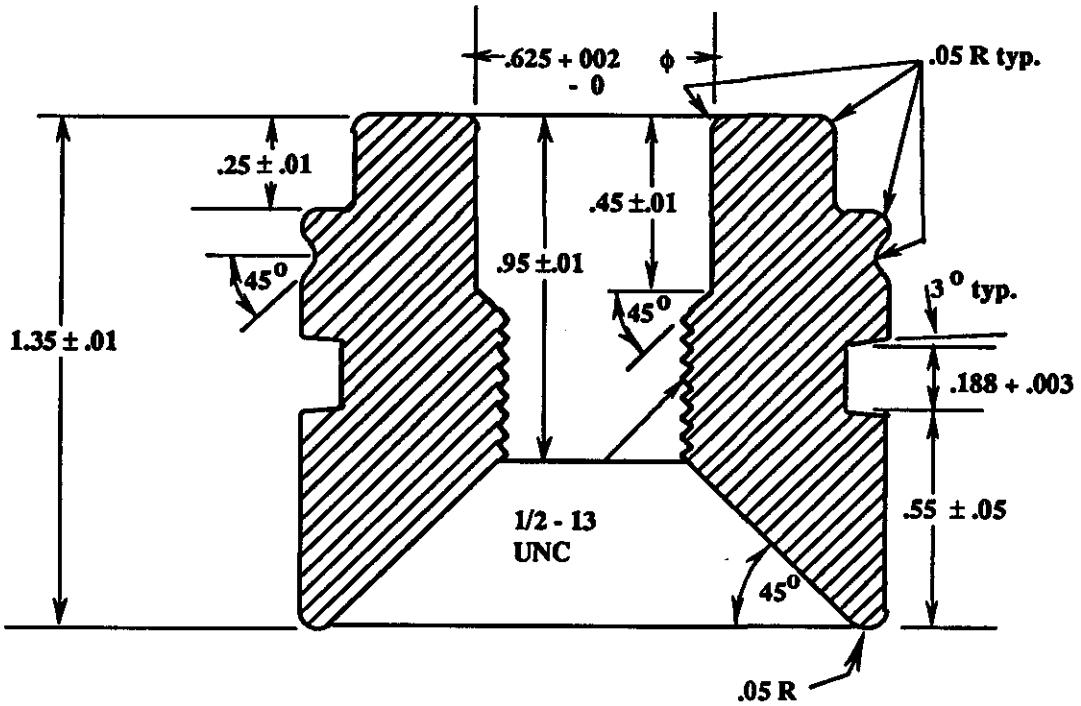
.625 + 002
- 0
ϕ
.05 R typ.
.25 ± .01
.45 ±.01
.95 ±.01
45°
45°
3° typ.
1.35 ± .01
.188 + .003
1/2 - 13
UNC
.55 ± .05
45°
.05 R

Fig. 4.0.4

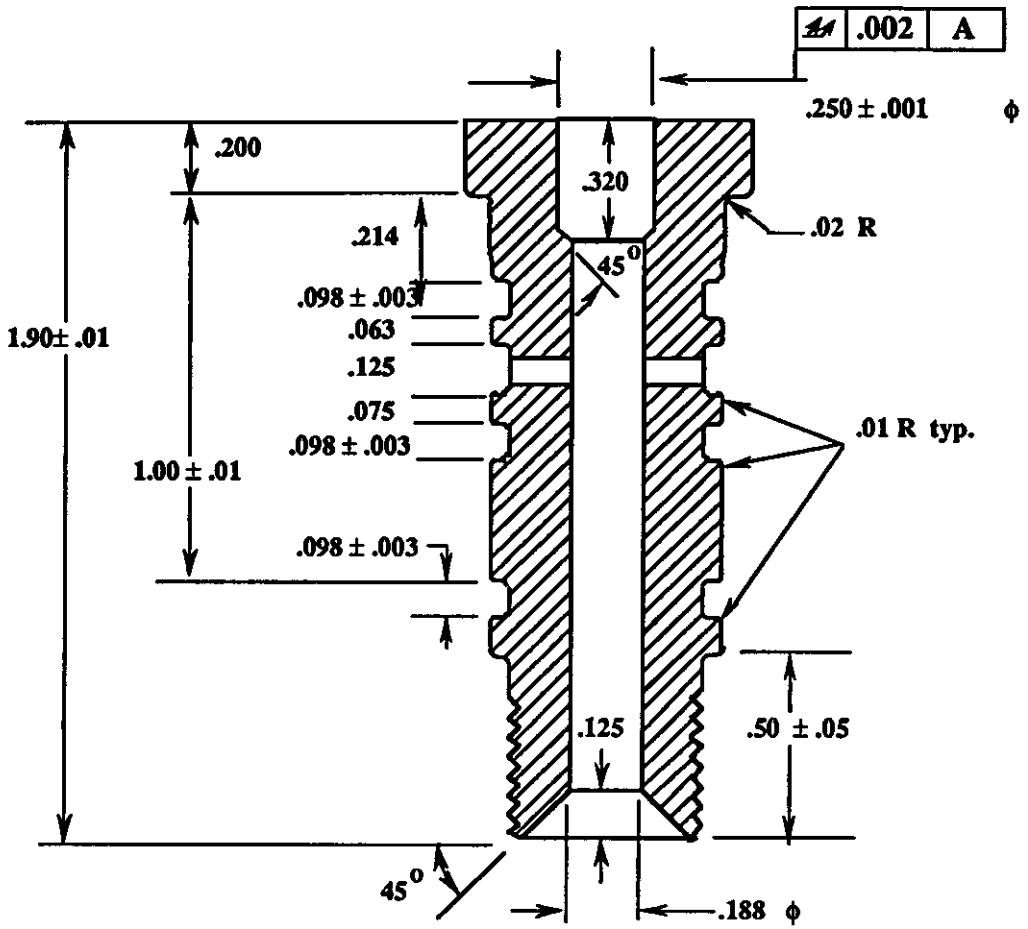
.002
A
.250 ± .001 ϕ
.200
.320
.02 R
.214
45°
.098 ± .003
.063
.125
.075
.098 ± .003
1.90± .01
1.00 ± .01
.01 R typ.
.098 ± .003
.125
.50 ± .05
45°
.188 ϕ

Fig. 4.0.5

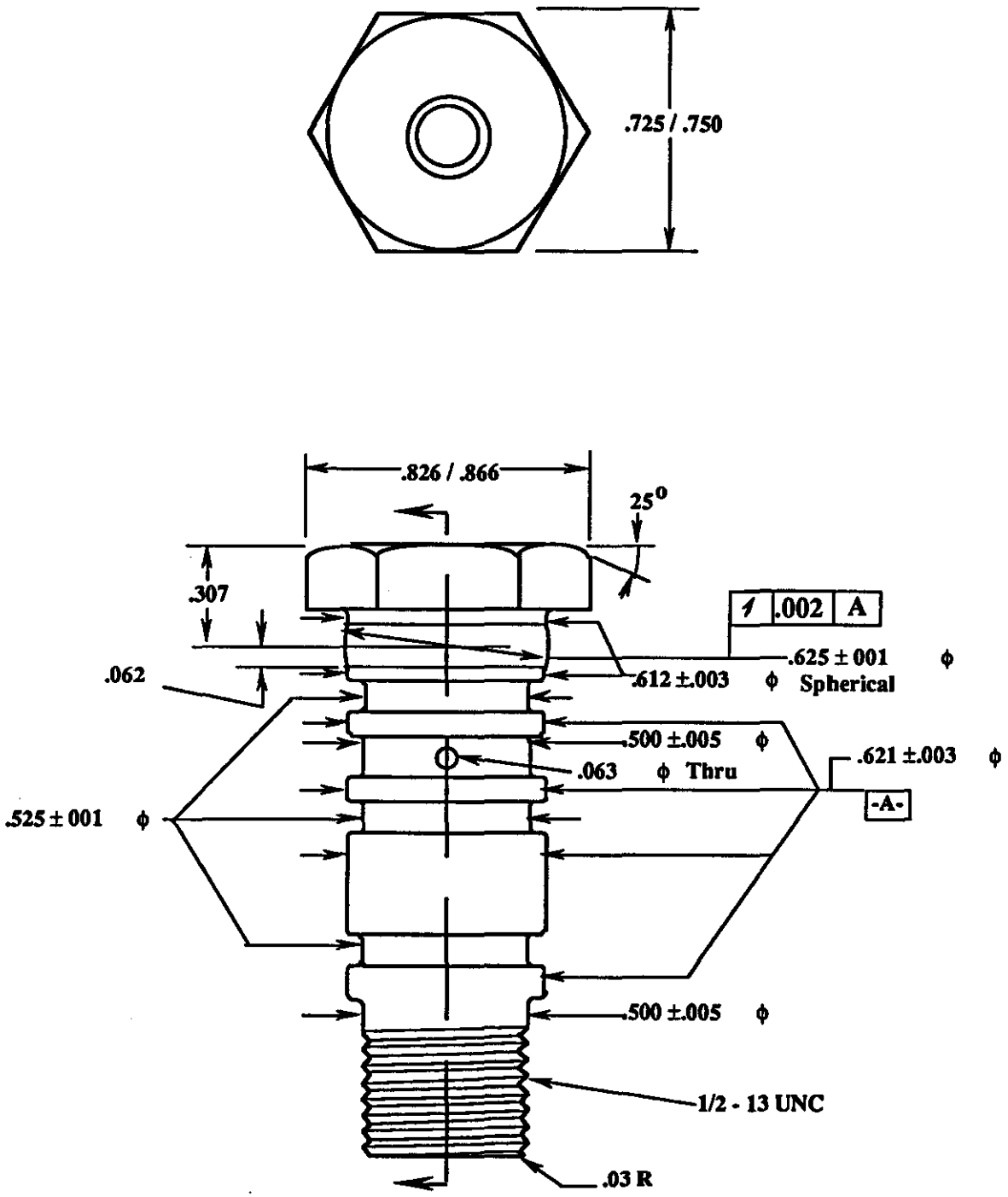
.725 / .750
.826 / .866
25°
.307
.002
A
.625 ± 001 ϕ
.062
.612 ±.003 ϕ Spherical
.500 ±.005 ϕ
.621 ±.003 ϕ
.063 ϕ Thru
-A-
.525 ± 001 ϕ
.500 ±.005 ϕ
1/2 - 13 UNC
.03 R

Fig. 4.0.6

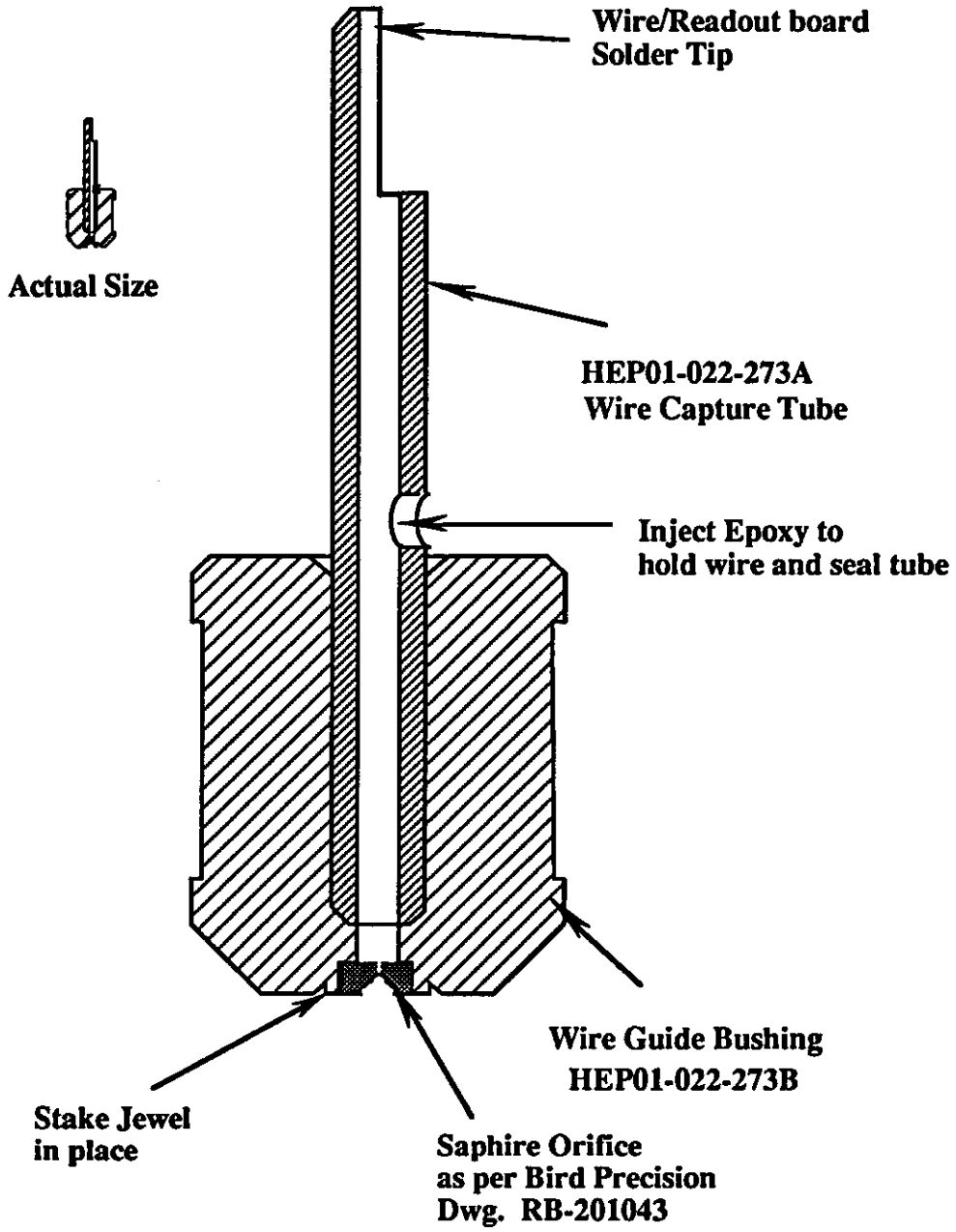
Wire/Readout board
Solder Tip
Actual Size
HEP01-022-273A
Wire Capture Tube
Inject Epoxy to
hold wire and seal tube
Wire Guide Bushing
HEP01-022-273B
Stake Jewel
in place
Saphire Orifice
as per Bird Precision
Dwg. RB-201043

Fig. 4.0.7

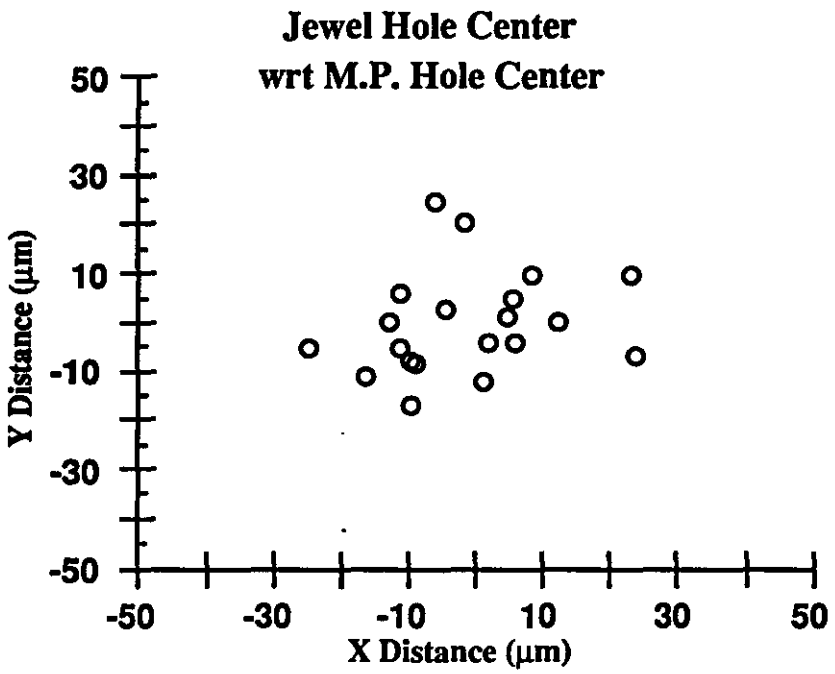
Jewel Hole Center
wrt M.P. Hole Center
Y Distance (μm)
50
30
10
-10
-30
-50
-50
-30
-10
10
30
50
X Distance (μm)

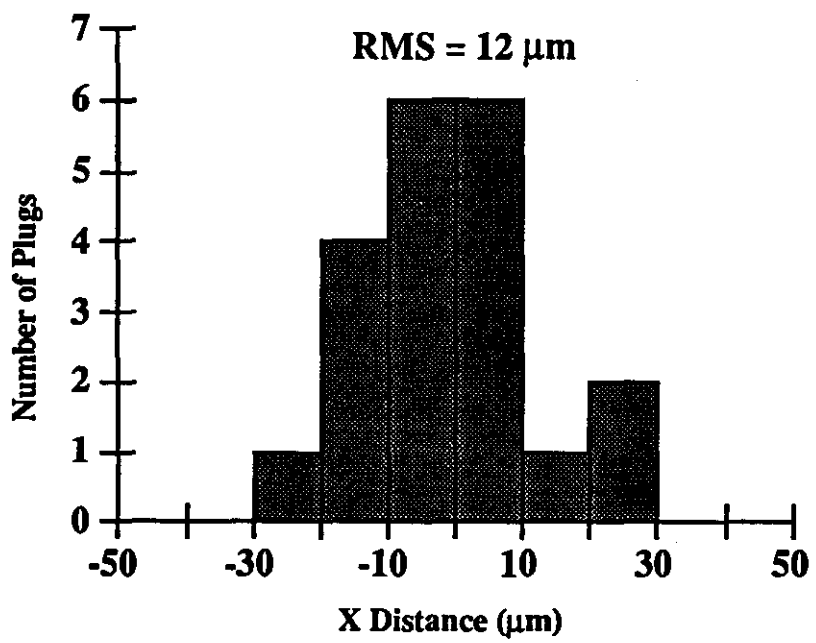
RMS = 12 μm
Number of Plugs
7
6
5
4
3
2
1
0
-50
-30
-10
10
30
50
X Distance (μm)

Fig. 4.0.8

(4.1) RDT Stereo Views

I. Tracks from Stereoscopic Measurements:

In a sector a local coordinate system is defined with the z-axis parallel to the beam, which is the direction of the wires in x-planes (axial), and with the x-axis in the plane of and perpendicular to the wires. Tracks are defined by the parameters: $x(r)$, $\theta(r)$, x_0, and z_0 (x and z at r=0), where the magnetic field is assumed to have only small components in the x, and r directions. For tracks of reasonable momentum the path along the helical trajectory is short enough to consider $\theta(r)$ = constant where the constant is called the θ-parameter of the track. Using the x-coordinate from the projection of the track determined from the X-planes and the stereo measurements from a U-U' or a U-V pair of planes the z-coordinate of the track as it passed through those planes can be determined as shown in Figure 4.1.1.

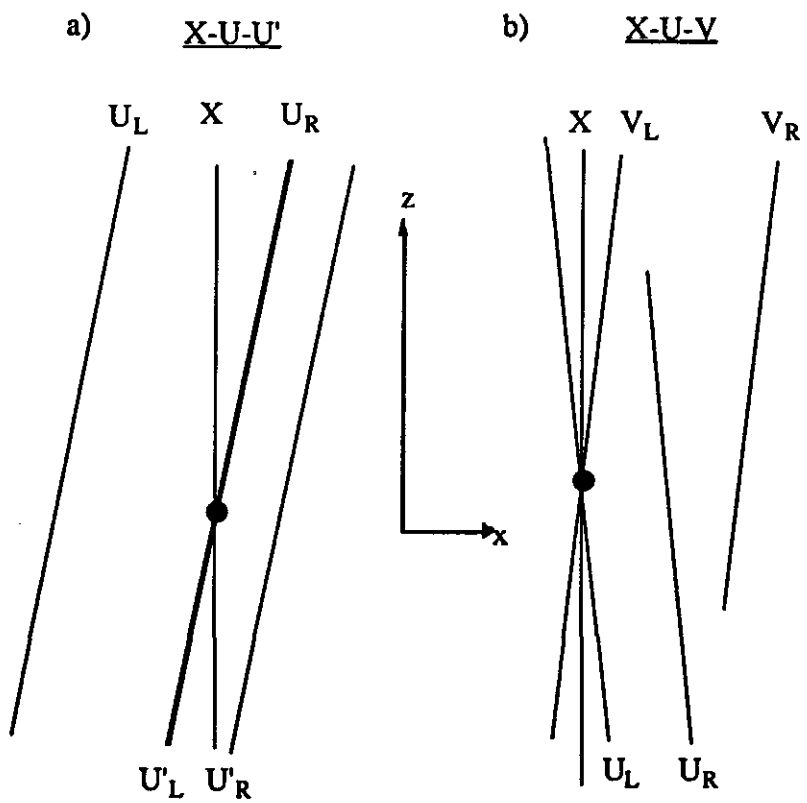

a) The z-coord. determined from the x-coord. and staggered U-U' drift tubes. b) The z-coord. determined from the x-coord. and a U-V pair of drift tubes.

Fig. 4.1.1

II. How many planes in total?

The RDT baseline has the planes arranged in an 8-10-8 layout in an 4-6-4 arrangement of axially oriented wires while the small angle stereo layers are 4-4-4 with a UU'-VV' quartet at each superlayer. The z_0 and θ-parameters can be determined either by generating space points in each superlayer or by reconstructing the track in any two of the three views (the axial and the two stereo views) and combining the results. The momentum resolution is optimized by a multi-parameter fit for the momentum, x_0 and z_0, and θ-parameters. The resolution obtained in this way from the 26 measurements along a track is nearly be indistinguishable from a purely axial system. If the number of planes must be reduced (cost) a system with only two views (reducing the number of stereo planes to 2 at each superlayer (but adding back 2 axial planes at superlayer 1) in an 8-8-6 would be only marginally worse in resolution due to the relative lack of stereo ambiguities in a small angle system, however, the redundancy would suffer considerably, making the system less robust at high luminosities.

III. What Stereo Angle?

A plane positioned so that its wires are at a small stereo angle ψ = 4 mr with respect to the axial wires will yield a z-measurement with a resolution of $\sigma_z = \sigma/\psi$ = 2.5 cm, where σ is the drift distance resolution (the x-coordinate is obtained accurately from the axial wires). A 4 mr stereo angle implies that the tubes displace by less than one tube diameter in the longest chambers. With 4 stereo planes at each station the resolution in z at each superlayer would be better than 1 cm after using the constraints of a straight line in the θ-view. Larger stereo angles should not be necessary since these resolutions are already much better than the requirements of the GEM muon system. At smaller stereo angles the z-coordinate resolution would be worsened but fewer stereo measurements would be subject to l-r ambiguities as shown in Figure 4.1.2.

l-r Ambiguities in Stereo Drift Systems

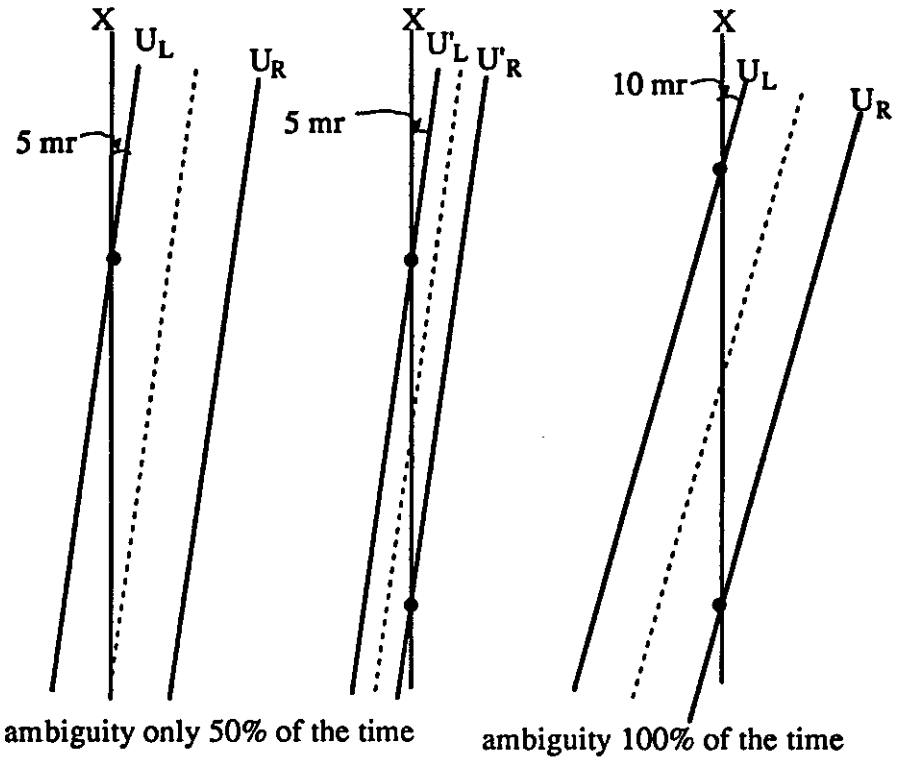

Small angle stereo (1/2 tube width over the full length) leads to l-r ambiguities only 50% of the time while a stereo angle twice as large (1 tube width over the full length) leads to l-r ambiguities 100% of the time

Fig. 4.1.2

(5.0) RPC Technology

Resistive Plate Chambers (RPCs) have many properties which make them an ideal technology for triggering a large muon system. The RPCs are intrinsically fast, easy to construct and operate, and inexpensive to build. The readout can be accomplished by pickup strips which inductively detect the avalanche induced by the muon upon traversal of the 2 mm chamber gas gap. We have demonstrated that RPCs have the required time and space resolution and can be operated simultaneously with the RDTs - validating our interest in this technology. The present difficulty is that the chambers have rate limitations which make them an uncertain choice for the high rate environment at GEM - especially for application in the endcaps. More R&D is needed to really be certain that they will meet the baseline requirements for GEM.

The following is a brief description of the RPC technology. More details can be found in the Appendix A.

A. Design

1. General Design Concept

The current standard (Italian) design is two meters long by one meter wide with a sensitive gas gap of 2 millimeters. There are no wires or conductors anywhere in the sensitive region. The walls of the chamber - in contact with the gas of the sensitive volume - consists of a semi-conductor (Bakelite, for example) with a bulk resistance of about 10^{11} Ω centimeters. The dimensional tolerances are modest. The thickness of the Bakelite plate is to first order not relevant for the proper operation of the RPC. The combined flatness and spacing requirements between the plates are $\pm$ 200 microns. This requirement is trivial to maintain over arbitrarily large areas by using PVC spacers 2 mm thick and 11 mm in diameter spaced on a 10 cm grid. An ionizing particle passing through the sensitive volume (2 m x 1 m x 2 mm) breaks down the gap and creates an electrical discharge. This discharge is very fast (a few nanoseconds). The discharge is capacitively coupled to pick-up strips which are located outside the semiconductor walls of the gas cell.

When the strip is terminated with a 50 Ω load the voltage pulses across the termination are typically 0.5 volts high with a rise time of 2-3 ns. A typical full width at half height (FWHM) is about 10 ns and the measured rise time jitter is less than 1.4 ns. Figure 5.1 is a schematic of the "standard" Italian RPC.

RPCs are used to perform the fast triggering necessary to identify the SSC beam bunch crossing associated with a particular physics event, as well as the muon momentum trigger (Level 1 trigger) for identifying muons of sufficient momentum. In the barrel region of the GEM Detector, bunch crossing identification is performed using straight line fits of tracks registered on projective strips oriented in the θ

direction (non-bend plane), with widths of 3.9, 6.5, and 8.9 cm, for inner, middle, and outer super-layers, respectively. Muon momentum measurements are made using strips of 1.3 cm width oriented along the z direction (bend plane). The strip widths are chosen to provide the necessary precision for track identification. In the case of the bunch-crossing identification, the wide strips are all that is necessary to identify a straight line track. In the case of the muon momentum identification, 1.3 cm strips are sufficient to provide sagitta measurements of the necessary precision to identify muons of particular momenta, for example, > 10 GeV/c, or > 50 GeV/c. This momentum identification is based on the measurement of the muon passage through a set of strips in the three super-layers and the strip displacement from a straight line as projected from the origin through the outer super-layer strip. The RPC strip widths in the end cap region are slightly different than in the barrel and the operation of the RPC trigger for both the barrel and end cap is described in greater detail in a later section.

Reading out an RPC is a simple matter of detecting the induced charge on the cathode strips, identifying the time of arrival of the charge, and the spatial coordinates of the strip. The RPC operation (spark chamber) implies that it is essentially a digital device. The critical conditions for RPC operation are 1) stability of materials used in the RPC, 2) stability and uniformity of the gas supplied to the RPC, 3) uniformity of the gas gap within the RPC that gives rise to the avalanche breakdown and the subsequent induced pulse on the pick-up strips, and 4) saturated rate capability in large particle fluxes, related to the bulk resistivity of the semiconducting material used for the resistive plates. The RPC system, being a somewhat less mechanically precise system than the proposed drift tube systems, uses much simpler manufacturing methods than the precision drift tube technologies being considered for the GEM Muon System.

3. High Rate RPC for GEM Muon Trigger System

The conditions in the GEM Detector environment demand that RPCs be capable of operating at higher rates than currently available with the standard Bakelite design. This is because there will be a large background of neutrons and charged particles in the barrel and end-cap regions of the detector. Neutron fluxes of about 10^4 Hz/cm^2 are expected, for example, in the barrel region first super-layer, with about a factor of 10 higher rate in the forward direction, at a luminosity of 10^{33} (not taking into account the possible addition of neutron shielding which could reduce the neutron flux by an additional factor of 20-30). Bakelite RPCs have been measured to have an efficiency for neutrons of about 0.5%, which implies an RPC singles rate due to neutrons of about 50 - 500 Hz/cm^2. Bakelite RPCs also have a measured rate capability at 97% plateaued efficiency of about 50-100 Hz/cm^2. Therefore, it is desired that RPCs used in the GEM Detector have higher rate capability by a factor of 10 - 100. Our R&D program indicates that this rate capability is now understood to be solely a function of the bulk resistivity of the resistive plate material.

Fig. 5.2 shows a SPICE model of a single layer RPC. The resistive plates are modeled as a resistor and capacitor in parallel, with the resistor determined by the measured bulk resistivity of the material and the thickness. The gas gap is modeled as a simple capacitor. A number of materials were studied for use in RPCs. Our model can be used to predict the dynamic behavior of the RPC when a spark discharge occurs in the gas gap. Fig. 5.3 shows that the model predicts a characteristic "recovery" time, associated with the re-establishment of the electric field in the plate after the discharge occurs, which varies widely for different materials. Note that the curves in Fig. 5.3 show the recovery time of a region around the spark discharge in the RPC and do not represent the signal pulse shape out of the RPC. We arbitrarily define the recovery time as the time between the 10% and 90% amplitude points on the curves shown in Fig. 5.3.

This recovery time is directly related to the saturated rate capability of the RPC as discussed below. The following is a simple model that lets one deduce the rate of a counter at a fixed efficiency given the saturation counting rate. This model usually underestimates the rate for high efficiencies.

Assume:

Rs = saturation rate
Re = rate at a fixed efficiency E

$$Re = Rs(1-E)$$

This equation is trivial to derive but it is only an approximation as it assumes a linear relation between saturation counting rate and the period of inefficiency of the counter. Note that this equation predicts that there is no rate for which a counter can be 100% efficient, which is true as every counter has to have a dead time and regardless of rate there is a non-zero probability to have two random counts within this dead time. If one assumes E = 0.95, which is the number that is normally used for this equation, then for Rs = 20,000 Hz we can assume that the counter will operate at 1,000 Hz. Because of the approximation previously mentioned, this derived rate is actually an underestimate of the real rate.

Fig. 5.4 shows the results for saturated rate measurements for different resistive materials compared to the inverse of the recovery time. The measured rates are seen to be proportional to the calculated time response of the material, indicating that we can understand the operation of the RPC based on this simple model and the knowledge of the bulk resistivity of the material. From Fig. 5.4 we see that two special plastics loaded with conducting polymer exhibit very high saturated rate capability compared to glasses and Bakelite, with rates approaching 15 kHz/cm^2. One plastic is an ABS-based plastic and the other is a PVC-based plastic. We have measured the dielectric strength of the ABS plastic to be superior to the PVC plastic. A number of RPCs constructed from ABS plastic have been built and tested (the largest being 1.2 m x 2.4 m).

R&D results (detailed in an Appendix) from measurements performed on a number of different RPCs indicate that plastic RPCs operate identically to Bakelite RPCs with regards to pulse width, pulse height, and rise-time jitter. In addition, noise measurements have been made and the best chambers exhibit a noise rate of about 0.5 Hz/cm^2 for a 15 mV discriminator threshold. This noise rate is achieved for plastic sheet without any special surface preparation, as compared to Bakelite chambers, which require a special coating of linseed oil on the inner surfaces in order to operate. The noise rate of 0.5 Hz/cm^2 is roughly a factor of two worse than the best Bakelite/linseed oil chambers and is about 20 times the cosmic ray rate.

The ABS plastic RPC appears to exhibit some variability in operation associated with initial turn-on and subsequent voltage changes. This variability is manifested as an increase in noise rate and exhibits a characteristic settling time of the order of hundreds of minutes. Once the RPC is stabilized the noise rate is reduced to the value quoted above. Another characteristic of the ABS plastic is a variability in saturated count rate associated with turn-on and subsequent voltage changes. This variability appears to be associated with a change in the bulk resistivity of this particular plastic and is possibly due to polarization effects. For example, it is observed that the saturated rate capability of RPCs constructed from ABS plastic is reduced from about 10 kHz/cm^2 to about 1 kHz/cm^2 over a period of a few hours. Also, the noise rate drops to a final value of about 0.5 Hz/cm^2. Once the RPC reaches this point it is stable, as shown by measurements of an RPC under constant voltage over a 6-day period.

There are a number of other semiconducting plastics that will be studied for use for high rate RPCs and it is expected that the variability discussed above will be overcome with the choice of the proper plastic. In addition, plastics with even lower bulk resistivities (in the range of 10^8 ohm-cm) have been identified. Based on our understanding of RPC operation, these lower resistivity plastics will provide RPC operation with correspondingly higher saturated rate capability – by as much as a factor of ten better than ABS plastics. In this event, sufficient rate capability for GEM will be insured even with small (less than a factor of ten) changes in resistivity. We will next describe the construction of RPCs based on these new plastic materials.

B. RPC Construction

1. Manufacturing

Our manufacturing philosophy is to build as large a chamber as possible for each super-layer following the same dimensions and lay-outs as for the RDT tracking chambers. The materials used in the individual chambers should be able to be assembled into a self-supporting structure that first and foremost maintains the gas gap dimensions with a tolerance of about $\pm$ 5%, or, in the case of a 2 mm gas gap, $\pm$ 100 μm. Similar dimensional tolerances are necessary for the distance between the pick-up strip electrodes and their ground plane, in order to control the strip

impedance. The gas gap is maintained by gluing 2 mm thick, 1 cm diameter disk spacers every 10 cm or so in between the laminated sheets. The strip-electrode-to-ground plane gap is maintained by using a rigid foam sheet to form the proper impedance transmission line. Because of this design flexibility the RPC can actually be deformed substantially from a flat plane and still operate correctly.

Similarly, the tolerance associated with the placement of the pick-up strips is defined by the desired measurements of timing (bunch crossing) and momentum (sagitta). This tolerance as we see it implies strips to be located also to about $\pm$ 500 μm, a not too difficult tolerance to achieve using standard commercially available techniques for metallization of mylar sheets.

Materials stability is an issue for long term performance of the RPCs. Plastics degrade over time due to out-gassing of plasticizers, interaction with ambient UV light, temperature fluctuations, radiation, and, in the case of RPCs, uniformity and stability of the bulk resistivity of the resistive plates and interaction of the plates with spark discharges. Proper materials choices and design will help to insure the long term stability of the RPCs. We can benefit from the experience of other RPC systems that show long term (years) operation of RPCs without degradation, albeit under lower rate conditions than that expected at the SSC. Aging tests are easily performed in R&D to determine the proper long term operation of RPC materials.

Fig. 5.5 shows a blow-up of a two-gap RPC design. The spacers produce about a 1% dead area; however, the size and spacing of these spacers has not been optimized and should be studied using finite element analysis to assess the minimal configuration required to maintain a gas gap to the required 2 mm $\pm$ 0.1 mm. The two-gap design we have chosen eliminates this 1% dead area by having two gas gaps with the spacers in one gap staggered with respect to the spacers in the second gap. This double gap construction also has the virtue of providing practically 100% redundancy for the RPC system. We are proposing to build a three-gap RPC stack, i.e., three independent RPCs within a single chamber. The three RPCs can be used to perform a two-out-of-three coincidence with a very tight timing window of about 20 ns by virtue of the inherent speed of the RPC. This provides a very low accidental trigger rate due to neutrons and charged particles conspiring to mimic a trigger. A discussion of the trigger will be presented in a later section. In a three-gap RPC system, spacers would be staggered in such a way as to allow clear passage of a muon in at least two of the three gas gaps.

The laminated plates consist of the resistive plastic coated on one side with a thin layer of graphite paint, commonly known as Aquadag. This coating serves as an electrically transparent high voltage electrode. A thin insulating mylar sheet with pick-up strips of aluminum or copper deposited on one side (available commercially) is bonded to the Aquadag-coated side of the resistive plastic sheet. Thus the high voltage electrode is insulated from the pick-up strips by the thickness of the mylar. A rigid low-density foam board (Last-A-Foam, density 0.029 g/cm^3) is used as a mechanical stiffener as well as a dielectric for the transmission line formed by the

pick-up strips and a thin foil ground plane placed on the opposite side of the foam. The foam is glued to the mylar and a thin metal foil of aluminum is glued on the opposite side. For 1.3 cm strips, such as those used in the bend plane in the barrel chambers, 5 mm thick foam is used to form a 50 ohm transmission line for each strip. This laminate process is repeated to form the four plates necessary for a two-layer RPC. Once the four plates are glued together with the spacers the laminate is quite rigid. For example, a single layer 1.2 m x 2.4 m RPC supported at its four corners sags about 1 cm at its center. A double layer RPC is expected sag even less.

2. Precision requirements

There are no precision requirements necessary for the RPC assembly. Standard tolerances on thicknesses of plastic sheet and other commercially available laminate materials are sufficient for the proper operation of the RPCs. The insulating disk spacers can be turned out using computerized machining with the necessary height tolerance of $\pm$ 100 μm ($\pm$ 4 mils) without difficulty. Pick-up strips can be laid out by commercial methods provided by the manufacturer of metallized mylars. Standard manufacturing processes are capable of providing the necessary dimensional tolerance of $\pm$ 100 μm.

Table 5.1 lists the breakdown of radiation lengths for the various materials in a three-gap RPC. A three-gap RPC of this construction has about 1.7% of a radiation length or about 0.55% per RPC layer.

Table 5.1

GEM RPC Radiation Lengths

Areal Mass: projected thickness = 0.55% X_0/layer

Material	Thickness	Rad. Length (cm)	% Rad. Length
Al	0.005″	8.9	0.14
Foam	5 mm	900	0.03
Mylar	0.005″	28.7	0.04
ABS plastic	0.020″	34.4	0.15
Gas	2 mm	Large	0
ABS plastic	0.020″	34.4	0.15
Mylar	0.005″	28.7	0.04
Foam	5 mm	900	0.03
Al	0.001″	8.9	0.03
Foam	5 mm	900	0.03
Mylar	0.005″	28.7	0.04
ABS plastic	0.020″	34.4	0.15
Gas	2 mm	Large	0
ABS plastic	0.020″	34.4	0.15
Mylar	0.005″	28.7	0.04
Foam	5 mm	900	0.03
Al	0.001″	8.9	0.03
Foam	5 mm	900	0.03
Mylar	0.005″	28.7	0.04
ABS plastic	0.020″	34.4	0.15
Gas	2 mm	Large	0
ABS plastic	0.020″	34.4	0.15
Mylar	0.005″	28.7	0.04
Foam	5 mm	900	0.03
Al	0.005″	8.9	0.14
Total:			**1.66 %**

Tables 5.2 and 5.3, GEM RPC Barrel Specifications and GEM RPC End-cap Specifications, contains, among many other items, the detailed breakdown of the weights. We have assumed 0.020″ (500 μm) thick ABS plastic sheet. Note that from Table 5.2 one can calculate that the weights of the individual barrel chambers are 99 lbs, 120 lbs, and 227 lbs for nominal radii of 4.0, 6.0, and 8.0 m (inner, middle and outer super-layers), respectively. Hence any chamber can be easily handled by four technicians (one for each corner) without the use of cranes or special hoisting apparatus.

Table 5.2

GEM RPC Barrel Specifications

Nominal Radius (m):	4.0	6.0	8.0
# of chambers	96	96	96
# of RPC layers/chamber	3	3	3
Width (cm)	167.0	255.0	342.0
Length (cm)	240.0	360.0	480.0
Total Length	720.0	1080.0	1440.0
# Bend-plane strips:	114	183	253
# Non-bend-plane strips:	166	166	166
Width of bend-plane strips (cm):	1.3	1.3	1.3
Width of non-bend-plane strips (cm):	3.9	6.5	8.9
Total number of channels - bend plane	17,696		
Total number of channels - non-bend-plane	15,936		
Total number of channels -	33,632		
Weights (lbs):			
ABS Plastic:	2496	6574	12,758
Aluminum perimeter frame:	1049	1472	2304
Cable:	385	641	963
Connectors, brackets:	1160	2855	5795
TOTAL/Super-layer	9561	11542	21820
TOTAL WEIGHT BARREL (TONS)	**21.5 TONS**		

Table 5.3

GEM RPC End-cap Specifications

Nominal Z (m):	6.0	11.0	16.0
# of chambers	64	64	64
# of RPC layers/chamber	3	3	3
Width (cm) (16 each)	150	260	370
(16 each)	140	250	370
(16 each)	70	120	180
(16 each)	75	130	190
Length (cm) (16 each)	190	330	470
(16 each)	180	310	460
(16 each)	71	130	180
(16 each)	76	130	190
# Bend-plane strips (30 degrees):	238	409	583
# Bend-plane strips (16 degrees):	186	320	486
# Non-bend-plane strips (30 degrees):	40	40	40
# Non-bend-plane strips (16 degrees):	26	26	26
Width of bend-plane strips (30 degrees) (cm):	0.6	0.6	0.6
Width of bend-plane strips (16 degrees) (cm):	0.44	0.44	0.44
Width of non-bend-plane strips (16 and 30 degrees) (cm):	3.8	6.5	9.3
Total number of channels - bend plane	71,104		
Total number of channels - non-bend plane	6,336		
Total number of channels - both end-caps	77,440		
Weights (lbs):			
ABS Plastic:	987	2600	5046
Aluminum perimeter frame:	415	582	911
Cable:	152	253	381
Connectors, brackets:	459	1129	2292
TOTAL/Super-layer	2013	4564	8630
TOTAL WEIGHT BOTH END CAPS (TONS)		**7.6 TONS**	

The chamber widths and lengths vary – 167 cm x 240 cm, 255 cm x 360 cm, and 342 cm x 480 cm, for inner, middle, and outer super-layer chambers, respectively in the barrel region. In the end cap region, there are two sets of chambers for coverage from theta = 9.75 - 16 degrees and from 16-30 degrees. The smallest end-cap chamber has dimensions of about 70 cm x 70 cm, and the largest end cap chamber has dimensions of 367 cm x 472 cm. These dimensions are identical to the dimensions of the corresponding RDT tracking chambers.

In summary, in the barrel there are 96 inner sector chambers, 96 middle sector chambers and 96 outer sector chambers with a total projected surface area of about 2,743 square meters. In the end cap there are 192 chambers grouped into 3 families of sizes distributed over the three super-layers. The total projected surface area is about 1,078 square meters.

8. Failure tolerance

As stated previously, the RPC is a very rugged reliable device without sense wires or regions of high fields. However, failures can occur. In case of a failure one half of the double RPC would fail. Because of this possibility, we operate each RPC gap as a separate chamber. The loss of one RPC gap means a decrease of efficiency of 1%. This is negligible from any practical point of view. Therefore we can state that the RPC system is, for practical purposes, 100% redundant and that any single failure has a negligible effect on the practical efficiency of the system.

Another way of looking at this situation is to suppose one gap fails per year. This is more than two orders of magnitude higher failure rate than is indicated by our current experience. Under this assumption one can show that the probability of two gaps failing in the same RPC chamber in ten years of operation is less than 10%.

5. Cost Uncertainties

The major cost uncertainty at this time is the structure cost, because the RPC may be incorporated into the drift tube structure and utilize its interface to the superstructure. In addition, the cost of machining and fabrication is somewhat uncertain. Also, electronics costs are not included in this review and estimates vary from about $11/channel to about $35/channel depending on the source of the electronics and whether the fabrication is in the US or overseas. Cost of materials is more certain, given the standard nature of the materials involved. Cost estimates for materials have been based on manufacturer's quotes or LLNL stock book prices for fittings, connectors, plastics, glues, etc. Details of costs have been presented in a number of reviews over the past year and can be found in various Cost Review proceedings.

In summary, it appears that a complete RPC system can be built for a less than $(5 to 10)M. This cost can perhaps be further reduced by a simplification of the structural requirements if the RPCs are incorporated in the drift tube support system.

H. Summary

We summarize this report by reiterating a number of important facts about RPCs:

A. They are the only Muon System technology currently made by industry. The standard sized RPC is one meter by two meters. In principle sizes much larger than this can be built.

B. They have the following pulse characteristics:

1. Pulse height about 0.5 volts without amplification into 50 ohms.
2. Pulse rise time less than 5 nanoseconds.
3. Pulse width about 10 nanoseconds.
4. Measured rise time jitter less than 1.4 nanoseconds (no other Muon System technology has this speed).

C. Lifetime is greater than 16.4 $\times 10^7$ pulses per square centimeter with no loss of efficiency within the 3% measuring error. This is equivalent to 8.2 standard SSC years (at luminosity 10^{33} and 2×10^7 seconds per year – the expected neutron flux is 2 Hz per square centimeter.)

D. Commercial RPCs have demonstrated essentially 100% efficiency at about 100 Hz per square centimeter using standard Bakelite resistive plates.

E. RPC prototypes built with new lower resistivity materials have demonstrated counting rates of about 20,000 Hz per square centimeter for short periods of time – in agreement with theoretical models based on bulk resistivity alone – prior to an observed increase in bulk resistivity that reduces the counting rate capability with a time constant on the order of hours. This indicates that with the proper choice of materials, i.e., with materials that exhibit stable resistive properties, we can expect RPCs with rate capabilities a factor of 1- 100 higher, with an added increase in rate capability achievable by utilizing thinner materials.

F. A number of candidate plastics have been identified and are under study, some with bulk resistivities of about 10^9 ohm-cm, which is about a factor of 100 lower than the ABS plastics currently used.

G. Refinement of the RPC design has led to an extremely low mass system with minimal muon scattering cross section of about 0.6% X_0/layer.

H. A series of cost reviews carried out over the past year indicate that the cost of the complete RPC system for GEM is about $5M including the cost of the electronics.

Based on the R&D we have performed, along with a detailed analysis of the cost of constructing a full RPC trigger system for GEM, we feel that the combination

of pressurized drift tubes (PDTs) for precision tracking coupled to RPCs for fast Level 1 triggering has the least risk, the highest muon resolution, the best beam crossing timing accuracy, and the lowest cost of all competing technologies.

I. General References

1. G. Battistoni, et al., "Plastic Spark Counters with PVC Electrodes," Nucl. Inst. Meth. **A270**, p. 190, 1988.

2. R. Cardarelli, et al., "Progress in Resistive Plate Counters," Nucl. Inst. Meth. **A263**, p. 20, 1988.

3. M. Della Negra, et al, "Study of Muon Triggers and Momentum Reconstruction in a Strong Magnetic Field for a Muon Detector at LHC," CERN/DRDC/90-36 DRDC/P7, August 30, 1990.

4. M. Anelli, et al., "Glass Electrode Spark Counters," Nucl. Inst. Meth. **A300**, p. 572, 1991.

5. "An Expression of Interest to Construct a Major SSC Detector," B. Barish, W. Willis, Co-spokespersons, pps. 3-38 - 3-40, July, 1991, unpublished.

6. C. Bacci, et al., "Muon Tracking and Hadron Punchthrough Measurements using Resistive Plate Chambers," Preprint ROM2F/91/18, July 22, 1991.

7. A. Bohrer, et al., "Status Report of the RD5 Experiment," CERN/DRDC/91-53, January 13, 1992.

8. M. Widgoff, et al., "Resistive Plate Chamber Technology Review" GEM-TN-92-206, October 6, 1992.

J. Figure Captions

5.1. Sketch of Italian (single layer design) Resistive Plate Chamber.

5.2. Equivalent circuit of the RPC used in SPICE to predict the operating characteristics of the RPC. The RPC is modeled as a capacitor and a resistor for each plate coupled via a capacitor, corresponding to the gas gap. The calculated RPC characteristics include recovery time, which is directly correlated to the saturated counting rate capability of the RPC.

5.3. SPICE calculation results for different RPC recovery times. In this figure we compare a number of different materials: Bakelite, glass, and plastics.

5.4. Comparison of SPICE calculated RPC rate capability with measured rates for a number of different RPCs. The RPCs plotted are, in order of increasing rate, the MIT glass, the LLNL glass, the Italian Bakelite, the Abstat-M310,

and the MiTech-411. The linear fit to the points is also indicated. The rate capability is defined as the inverse of the half-height time of the curves in Fig. 5.3.

5.5. Schematic layout of materials in the proposed two layer RPC for the GEM Muon System. See Table 5.1 for the corresponding radiation length fractions.

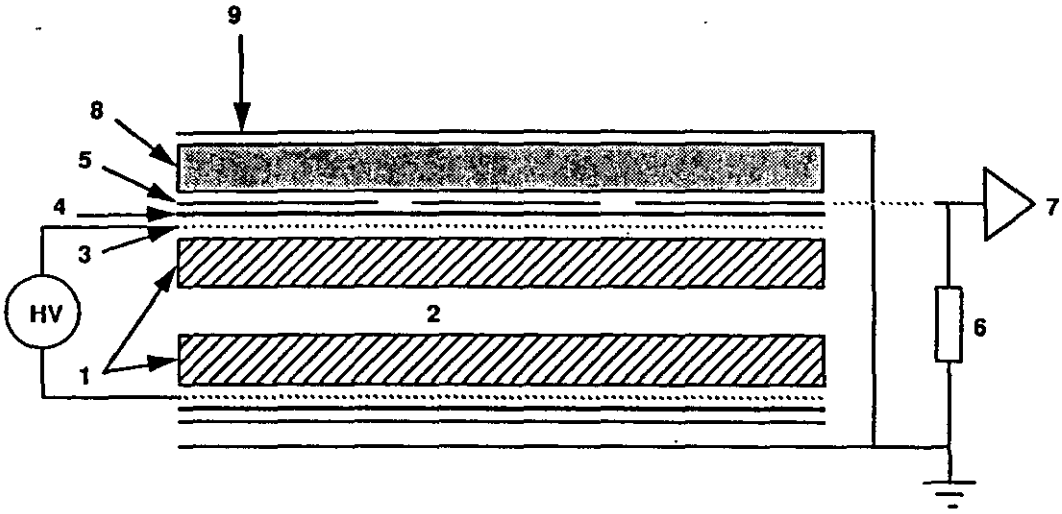

1 Bakelite plate
2 gas
3 graphite coating
4 insulating foil
5 aluminum strips
6 line termination
7 discriminator
8 foam
9 aluminum ground plane

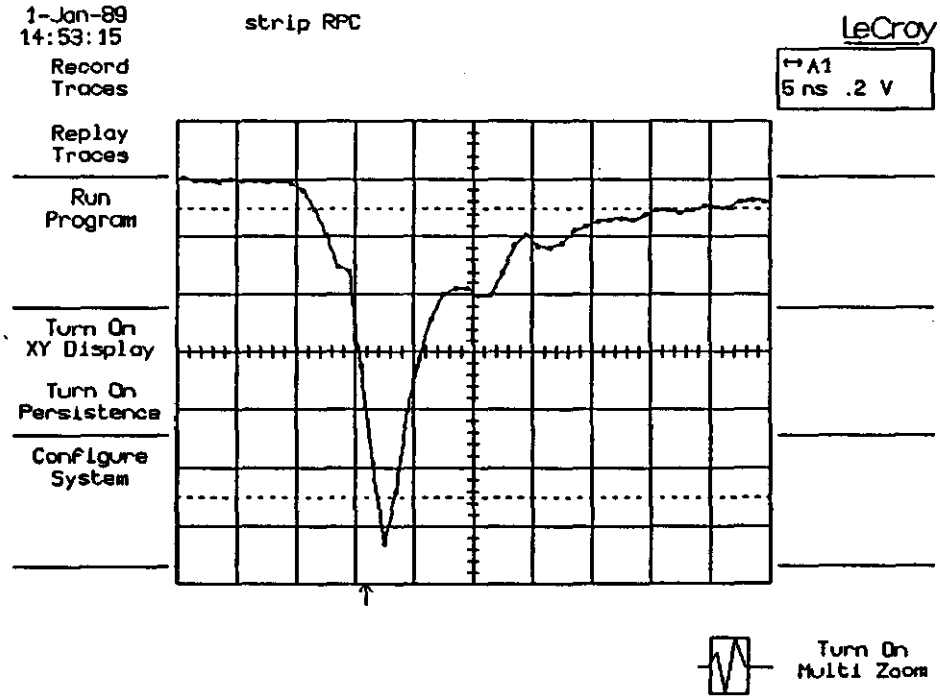

Fig. 5.1

Spice RPC Model

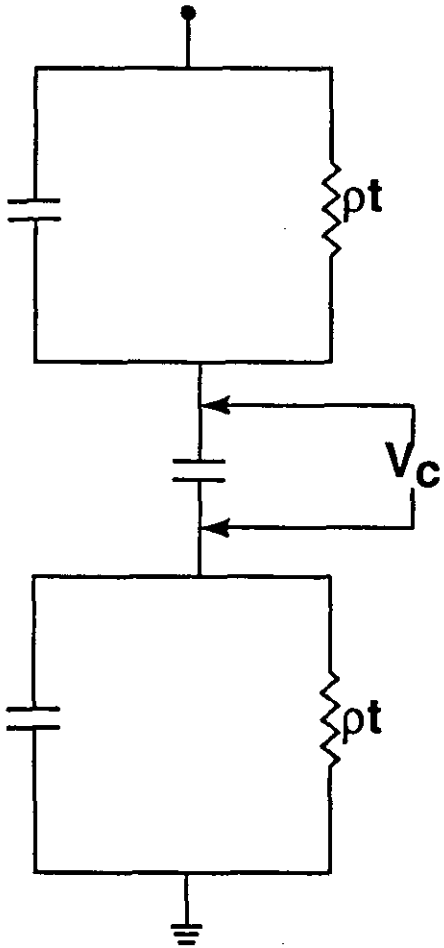

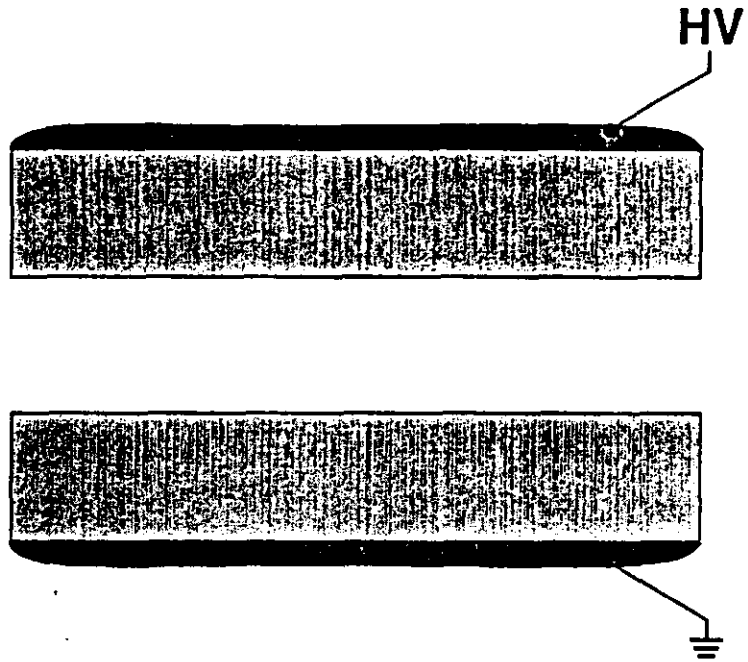

Fig. 5.2

BAK.KA-01/RMB

Spice Calculations of Recharge

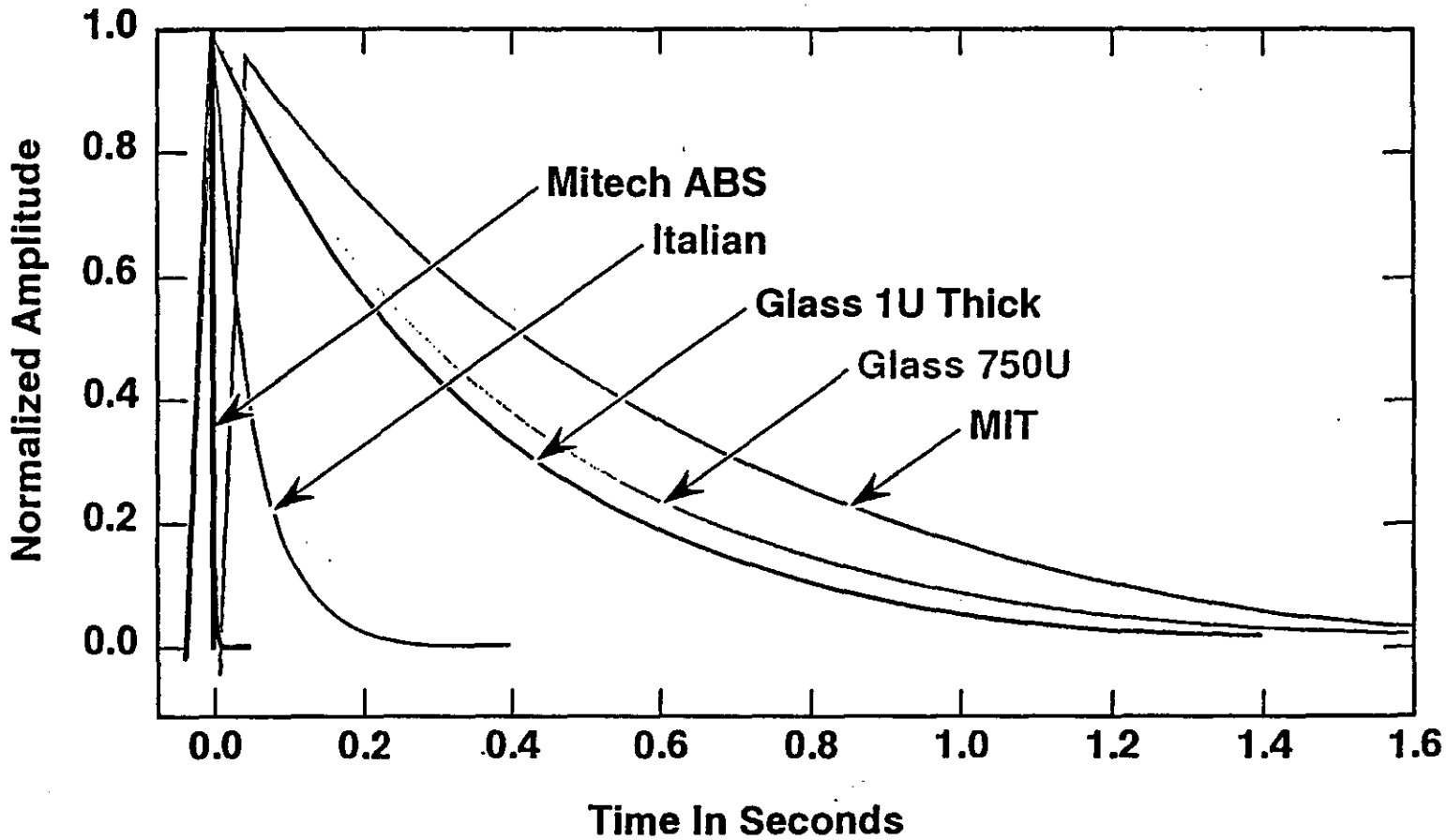

Fig. 5.3

BAK.KA-18/RMB

Saturated Singles Rate vs SPICE 1/tau

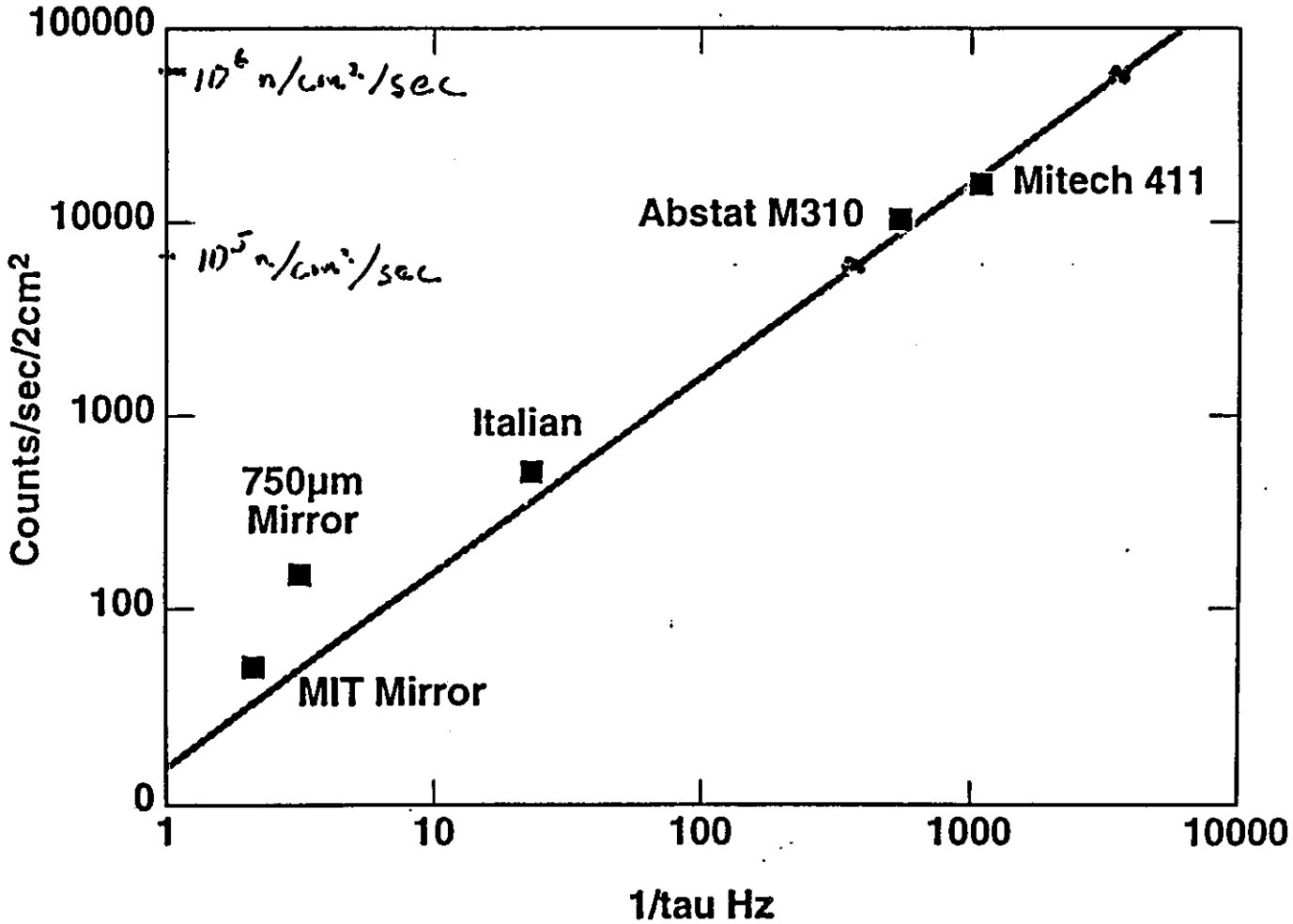

Fig. 5.4

BAK.KA-17/RMB

Fig. 5.5

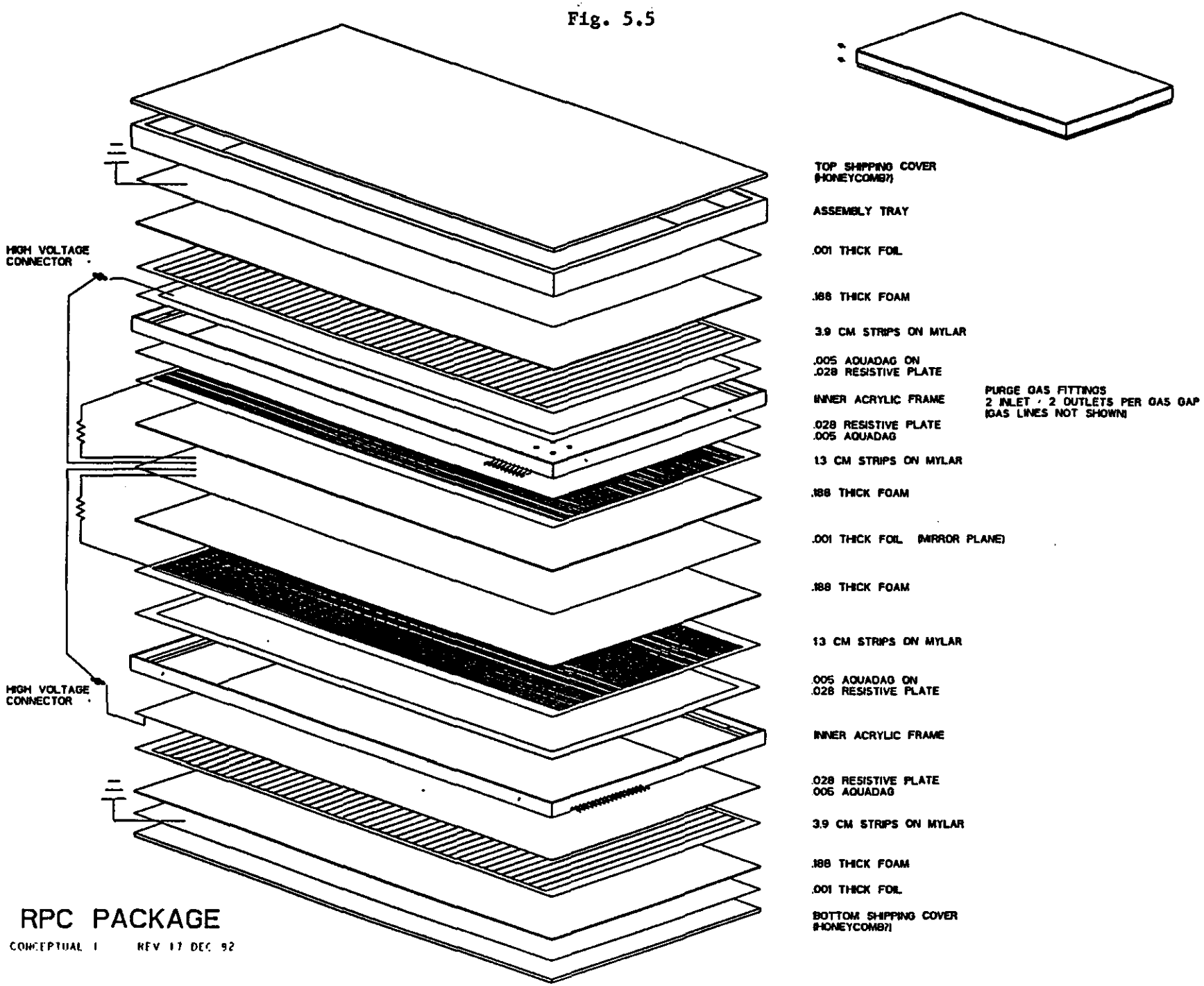
HIGH VOLTAGE CONNECTOR
HIGH VOLTAGE CONNECTOR
TOP SHIPPING COVER (HONEYCOMB?)
ASSEMBLY TRAY
.001 THICK FOIL
.188 THICK FOAM
3.9 CM STRIPS ON MYLAR
.005 AQUADAG ON .028 RESISTIVE PLATE
INNER ACRYLIC FRAME
PURGE GAS FITTINGS 2 INLET · 2 OUTLETS PER GAS GAP (GAS LINES NOT SHOWN)
.028 RESISTIVE PLATE .005 AQUADAG
13 CM STRIPS ON MYLAR
.188 THICK FOAM
.001 THICK FOIL (MIRROR PLANE)
.188 THICK FOAM
13 CM STRIPS ON MYLAR
.005 AQUADAG ON .028 RESISTIVE PLATE
INNER ACRYLIC FRAME
.028 RESISTIVE PLATE .005 AQUADAG
3.9 CM STRIPS ON MYLAR
.188 THICK FOAM
.001 THICK FOIL
BOTTOM SHIPPING COVER (HONEYCOMB?)
RPC PACKAGE
CONCEPTUAL I REV 17 DEC 92

(6.0) R&D Program

An active R&D program was carried out to determine the properties the RDT and RPC technologies. The program had two facets: (1) to understand the basic characteristics of the technologies, and (2) to certify the design concepts by building and operating full-scale prototypes. In the course of this program a variety of chambers were constructed - and tested with cosmic rays at the SSCL.

(6.1) Tests of Large Scale RDT Prototypes

Three large scale prototypes based on drift technology were constructed and tested at TTR:

- Dubna RDT Chamber.
- MSU RDT Chamber
- MIT LSDT Chamber.

These prototypes were designed to answer the crucial questions related to a performance of large detectors based on drift technology and to justify that the performance claimed in the baseline is achievable. It should be also noted that the tests are still underway and the results presented here must be treated as preliminary - more data are expected to follow.

1. Description of Prototypes

Dubna RDT Chamber:

This prototype consists of four staggered by half tube diameter planes of stainless steal tubes (3 cm diameter 4 m long tubes with wall thickness of .5 mm); Fig. 6.1.1(a). Actually, two separate chambers (4 m long and 0.5 m wide) are precisely joined to make the 1 m wide prototype. Each of these halves has 64 tubes so that the prototype consists of 128 tubes. Tubes are glued to each other without any special tolerances (however; certain stiffness of the structure is absolutely necessary to assure rigid wire support). Wire alignment was achieved by using high precision combs during chamber manufacturing (these combs, rather than the tube end-plugs, were determining wire position while they were soldered, as shown in Fig. 6.1.2; details may be found elsewhere [1]). Anode wires (50 μm, Au plated W) are stretched with tension of 300 g. Signals are amplified by low noise fast amplifiers mounted directly on tubes (the amplifiers allowed to set a threshold as low as 1mA, signal rise time being around 10 ns), then, after going through ~16 m long coaxial cables, they are discriminated and after additional 30 m flat cables fed to 12 bit 0.2 ns bin width TDC's (Philips7186H) . Chamber design allowed to use gas mixtures under high pressure up to 5-8 atm.

MSU RDT Chamber:

The MSU Prototype is a 4 m long 1.2 m wide chamber made of 4 staggered (by half tube diameter) planes of Al 3.8 cm diameter tubes with a wall thickness of 300 μm; Fig. 6.1.1(b). Total number of tubes is 128. Anode wires are the same as in Dubna RDT's, however; the alignment is achieved by a different method. The wires are fixed in the precise holes made in the chamber end-plates -- see Fig. 6.1.3. The accuracy of these end-plates was measured (Fig. 6.1.4) and found to satisfy the requirements. The tubes were glued to each other during manufacturing the prototype. This makes the prototype be very stiff. Details of the chamber design may be found elsewhere [2]. The chamber can be operated in both proportional and streamer modes. Drift times are measured by LeCroy 2277 TDC's operated in common stop mode (1 ns bin width, 50 μs depth, 16 hits per channel capability). Signals (can be amplified if the chamber operates in proportional mode) are discriminated and after not very long flat cable fed in TDC's. The chamber can operate at high pressure as well. So far, the chamber have been tested in streamer mode at 1 atm.

MIT LSDT Chamber:

This prototype is essentially different since it is assembled of U-shaped 10 mil Al profiles so that a drift cell has a square geometry; Fig. 6.1.1(c). Although, this design is not considered any more, many of the results obtained on this chamber are independent of cell geometry and provide important information to be discussed later on. The chamber is 1 m wide and 4 m long. Four profiles make four planes of square tubes with 2.5 cm cell size. Planes are staggered by half cell size. 100 μm wires (Au plated W, 1.2 kg tension) are supported each 2 m by precisely machined Mycalax bridges. Details of the design are in [3]. The chamber was tested in streamer mode only. The signals (no amplification) are shaped by discriminators mounted on the chamber and drift time digitization is performed by LeCroy 2277 TDC operated in common start mode (200 ft of flat cable between TDC and discriminators). The anode wires are connected in pairs at the rear end so that signal propagates in both directions and measured twice. The time difference provides the coordinate along the wire. Only 64 wires were actually instrumented with electronics.

2. Single layer resolution

The single layer resolution is a combination of an intrinsic resolution (determined by ionization density, diffusion and mode of operation: streamer vs. proportional), uniformity of gas through out the volume of chamber, alignment of wires in the chamber, wire droop (due to gravity and electrostatic forces) and, also, may include some multiple scattering.

Enormous amount of studies (both calculations and tests) devoted to high precision drift detectors have been done during recent decades. The <u>intrinsic spatial resolution under 100 μm</u> (even with rather simple electronics and at 1 atm gas pressure) has been demonstrated in many different drift detectors. Some of these results are shown

in Fig.6.1.5 [4]. Also, it should be noted that recent calculations have shown that the spatial resolution in proportional mode should not be much worse than that in streamer mode (degradation occurs only in the vicinity of the anode wire -- Fig.6.1.6 [5]).

Thus, the goal of R&D was to demonstrate that one can keep the good drift readout resolution in chambers of the proposed scale. The following is a summary of the most important results obtained by now.

Dubna RDT's

Just one half of the prototype has been analyzed by the time being, i.e. 64 wires. Fig.7 shows resolution achieved in a even smaller part of the prototype (6*4 wires) during preliminary tests outside of TTR. One can see that the resolution of 100 μm has been achieved both in proportional and streamer modes.

The two tables given in Fig.6.1.7 shows that a certain misplacement of planes has been found and, therefore, can be corrected for (it is absolutely reproducible!). The fact that the planes turned out to be misaligned is not surprising for this prototype as one can see from the way it was assembled. Fig.6.1.8 shows the residuals for 4 planes (now 32 wires per plane). One can clearly see asymmetrical tails which turned out to be a manifestation of incoherent wire misalignment. Fig.6.1.9(a) makes this fact obvious. All these observations resulted in the effort to understand if it is possible to extract geometrical corrections from the data. A standard software procedure has been formalized: first, plane-to-plane shifts should be corrected; then, individual wire shifts (see Fig.6.1.9(a) and Fig.6.1.9(b)) are to be taken into account; after that, one can look at plane rotations and correct on them (rotations are easily can be found by looking at residuals vs. track position along the wires -- Fig.6.1.10); and at the next and last step some small residual rotations of individual wires may be reconstructed. After this procedure, one gets number of small geometrical corrections which after having been applied make possible to reach the limit of intrinsic resolution, but over the large area of a chamber. The resolution of 85 ∝m with obvious bumps and humps have transformed in symmetrical peak with s=67 μm (at 1 atm!). To make sure that these corrections are really geometrical, they have been applied for analysis of data obtained many days later (different gas mixture, pressure also varied from 1 to 5 atm). Fig.6.1.11 shows that resolution of 50 μm has been easily achieved at 4.8 atm and no misalignment is visible at this level. The improvement of resolution with a pressure increase is presented in Fig.6.1.12.

Further analysis in this direction is expected to be done. It should finally prove that this procedure does not result in systematic errors.

The resolution is generally uniform across the chamber (no significant variations of resolution vs angles θ, φ and, also, along the wires have been found). The last confirms that a signal propagates along 4 m wires without significant distortion.

MSU RDT's

So far, this prototype has not been analyzed so thoroughly as the Dubna one. Obviously, to achieve a high resolution, one need to go through with calibrations. Unfortunately, this prototype does not provide a build-in calibration for electronic channels (hopefully, this problem will be overcome in the nearest future). It should be noted that despite the absence of proper calibration, the resolution for this prototype has been shown to be around 100 μm (Fig.6.1.13).

However, the already available information is important and complimentary to the Dubna prototype results. The real future muon chambers are now assumed to be constructed in the way this prototype had been made. Therefore, information about accuracy of wire placement in this prototype is essential. To determine wire positions, one really does not need to have accurate calibrations of electronics and delays. These errors would make residual distributions wider, but they can not shift mean values. One can see in Fig. 6.1.13 that there is no plane shifts in this prototype. Fig.6.1.14 shows that wires are located in places they are supposed to be, and Fig.6.1.15 shows that there are also no plane rotations with respect to each other. Thus, it is proven that this design has very high intrinsic mechanical accuracy.

MIT LSDT's

This prototype has demonstrated a high spatial resolution (Fig.6.1.16) and has not required any geometrical corrections on wire placement (i.e. similar results might be expected from MSU chamber after proper calibration of electronics). Fig.6.1.17 shows resolution vs. distance from a track to a wire. It is worth to show that these results are in agreement with truly intrinsic resolution which was obtained on a smaller chamber in high energy muon beam (Fig.6.1.18). One can see that resolutions close to a wire is essentially the same and determined by distance between clusters. Then, the small chamber actually had a flat resolution of 50-55 μm up to 12 mm away from a wire (maximum drift distance). However, the large scale prototype has a limit of 70 ∝m. When wire misalignment as measured during assembly (25 μm; Fig.6.1.19) and .6 ns intrinsic TDC time resolution (effectively 30 μm contribution) are taken into account, the expected value would be 50+30+25 ~ 65 μm. Some degradation of the resolution beyond 10 mm drift distances is apparently connected with a square cell geometry.

A summary of resolution dependence on track inclinations and position along a wire is presented in Fig.6.1.20. No significant dependence has been observed.

One more interesting result is presented in Fig.6.1.21. This figure shows an achievable accuracy of track localization along the wire as calculated from time difference between signals at a connected pair of wires. One can see that this technique allows to get about 10 cm accuracy (the tails come from TTR coordinate

predictions). This says that 8 m propagation of a signal along a wire does not result in significant signal distortions. Since this coordinate measured from the same wire, it provides a space-point measurement of a track in a single plane what significantly increases a pattern recognition capability.

3. Conclusions:

1. A 25 μm accuracy mechanical alignment of wires within a drift chamber has been demonstrated.

2. A spatial resolution of 50-100 μm is easily achievable through out the whole chamber - independent of the incident angle.

3. Non-flammable gas mixtures are available.

4. In case of unexpected misalignment there is possibly a way to find the geometrical corrections to restore the good resolution (some further studies are still needed).

5. Resolution of 10 cm along a wire is achievable by using a time difference technique.

References:

1. S. Movchan, in GEM TN-92-241

2. C. Bromberg, GEM TN-92-205

3. R. Sumner and et al., GEM TN-92-203

4. e.g. a) Filatova and et al., NIM 143 (1977) 17
   b) MIT group, "Tests of a LSDT chamber at .5 TeV muon beam", to be published
   c) Dubna group, (Tests of LSDT's at CERN beam presented by I.Golutvin, in GEM TN-92-218

5. A.Korytov, "One More Time about Spatial Resolution in Drift Chambers", to be published.

Figure Captions:

Fig. 6.1.1(a) Dubna Prototype Schematic.
Fig. 6.1.1(b) MSU Prototype Schematic.
Fig. 6.1.1(c) MIT Prototype Schematic.

Fig. 6.1.2 Concept of wire alignment in the Dubna Prototype:

(a) general view -- wires are supported by precise combs;
(b) wires do not touch end plugs during soldering.

Fig. 6.1.3 Concept of wire alignment in the MSU Prototype:
precision is determined by an accurately machined manifold plate and a tube end plug.

Fig. 6.1.4 Mechanical accuracy achieved in the manifold plate.

Fig. 6.1.5(a) LSDT spatial resolution [4b];
Fig. 6.1.5(b) LSDT spatial resolution [4b] - non-flammable gas, 1 atm;
Fig. 6.1.5(c) Drift Readout resolution [4a];
Fig. 6.1.5(d) LSDT spatial resolution [4c] - non-flammable gas, 3 atm.

Fig. 6.1.6. MC simulation of drift readout resolution with a fixed threshold: triggering on the first electron (streamer mode) is desirable but not necessary.

Fig. 6.1.7. First results from the Dubna Prototype: planes are misplaced but it is correctable in off-line.

Fig. 6.1.8 Dubna Prototype:
Residuals for all four planes -- some asymmetry is obvious.

Fig. 6.1.9 Dubna Prototype:
(a) incoherent wire misplacements are responsible for bumps and humps of residual distribution (Fig.6.1.8);
(b) wire positions have been corrected.

Fig. 6.1.10. Dubna Prototype:
Small rotations of planes could be also corrected.

Fig. 6.1.11. Dubna Prototype:
When all found geometrical corrections have been applied, the resolution at 4-5 atm is about 50 μm. (Notice that the corrections have been found from data obtained several days before in a different gas at 1 atm.)

Fig. 6.1.12. Dubna Prototype: Resolution vs. Pressure.

Fig. 6.1.13. MSU Prototype:
No systematic plane shifts have been discovered (mean values of residuals are of the order of 1 mm).

Fig. 6.1.14. MSU Prototype:
All wires in places where they are supposed to be.

Fig. 6.1.15. MSU Prototype: No plane rotations.

Fig. 6.1.16. MIT Prototype:
Resolution is 78 μm (all planes, no geometrical corrections!).

Fig. 6.1.17. MIT Prototype:
Resolution vs distance from a wire (~ 70 μm at plateau).

Fig. 6.1.18. MIT Prototype:
Intrinsic resolution as measured in a smaller prototype at Fermilab [4b] (~50 μm at plateau).

Fig. 6.1.19. MIT Prototype:
Wire misalignment as measured during assembly of the Prototype (RMS~25 μm).

Fig. 6.1.20(a) MIT Prototype: No wire misplacements.

Fig. 6.1.20(b) MIT Prototype:
Resolution vs coordinate along the chamber: no changes.

Fig. 6.1.20(c) MIT Prototype: Resolution vs q angle: no changes.

Fig. 6.1.20(d) MIT Prototype: Resolution vs j angle: no changes.

Fig. 6.1.21. MIT Prototype:
Resolution along a wire as obtained by time difference technique (s~10 cm).

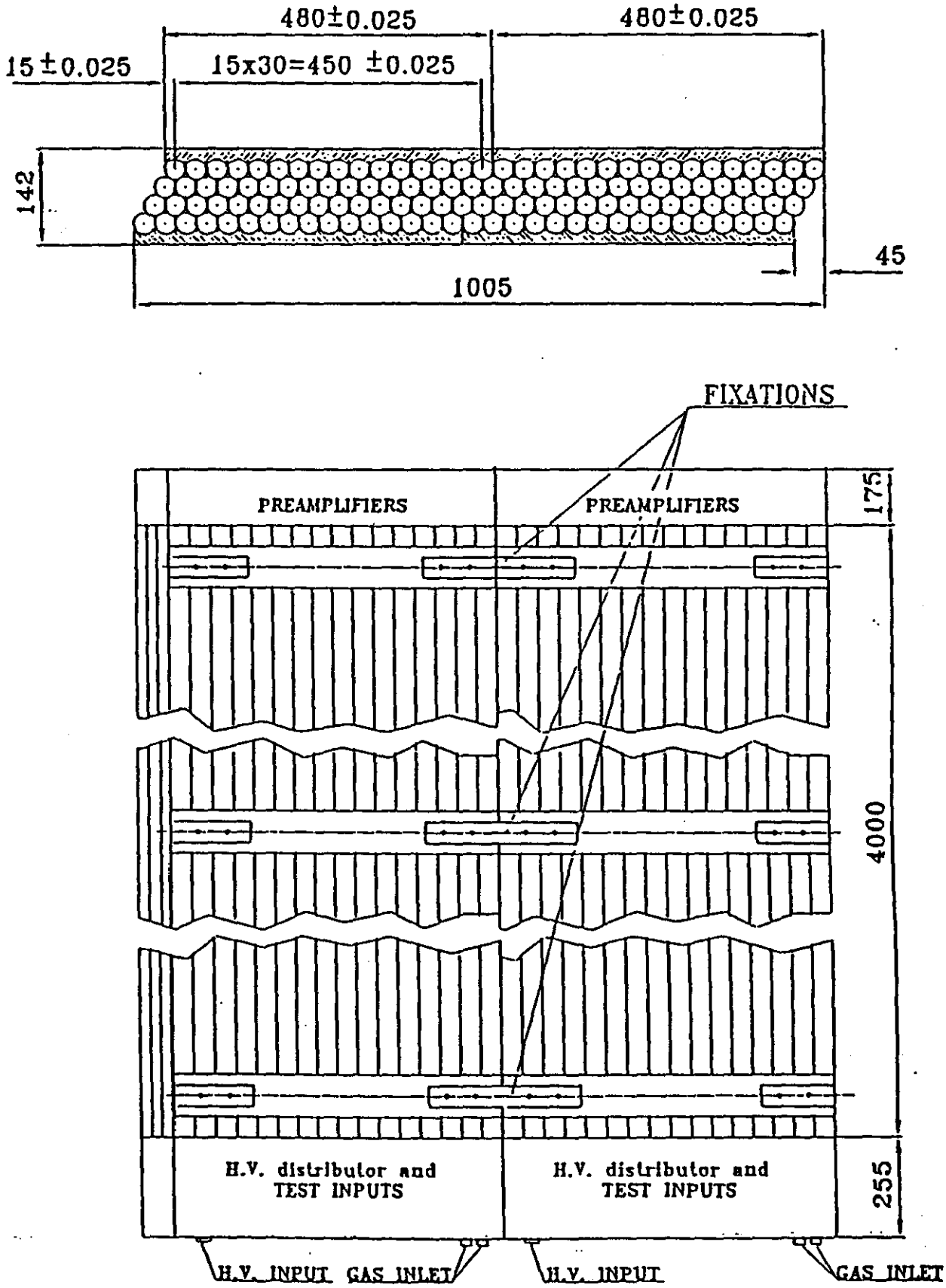
480±0.025
480±0.025
15±0.025
15x30=450 ±0.025
142
45
1005
FIXATIONS
PREAMPLIFIERS
PREAMPLIFIERS
175
4000
255
H.V. distributor and TEST INPUTS
H.V. distributor and TEST INPUTS
H.V. INPUT
GAS INLET
H.V. INPUT
GAS INLET

Fig. 6.1.1a

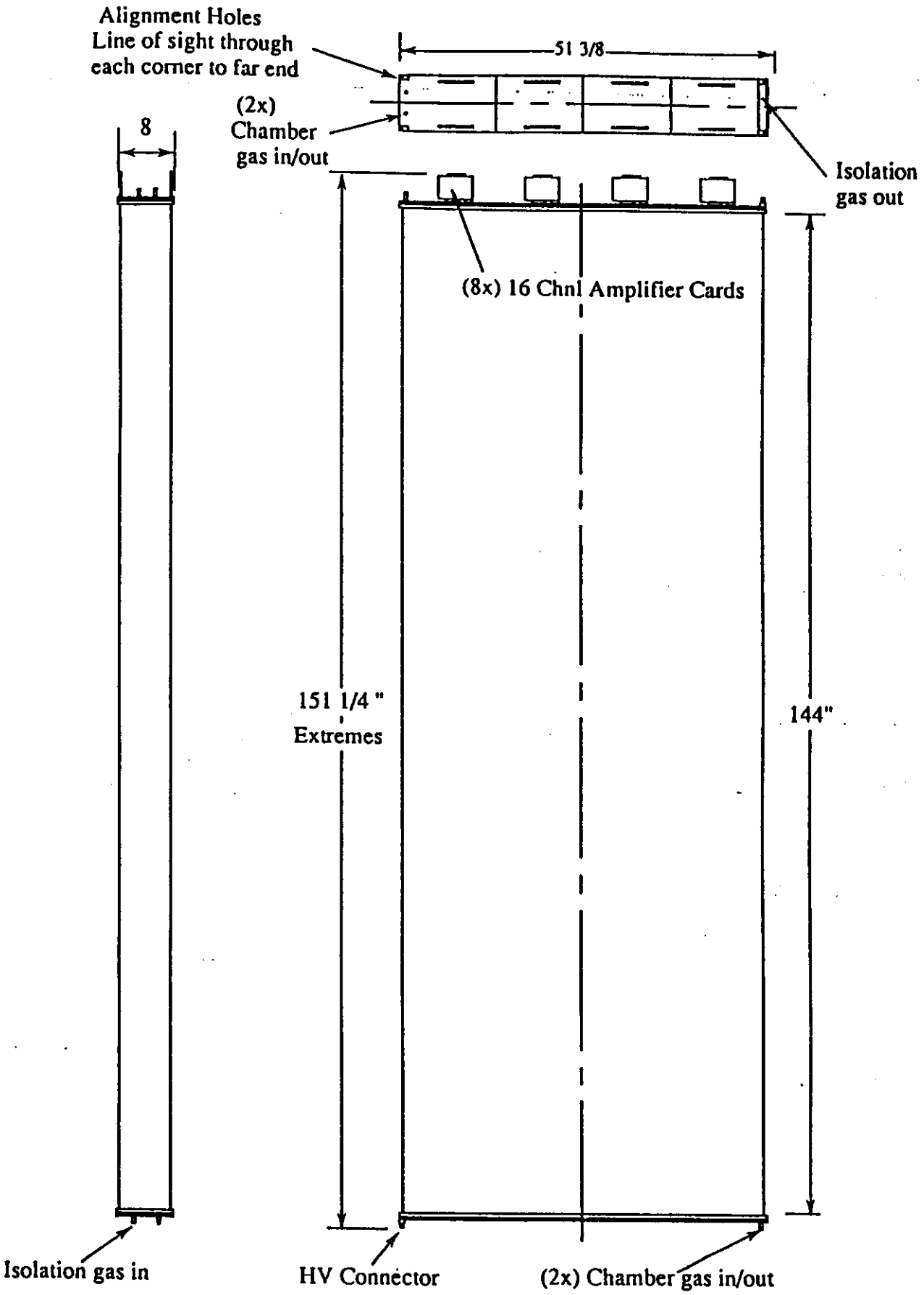

GEM PDT Prototype Assembly

HEP01-022-281-D R. Miller 5-14-92

Fig. 6.1.1b

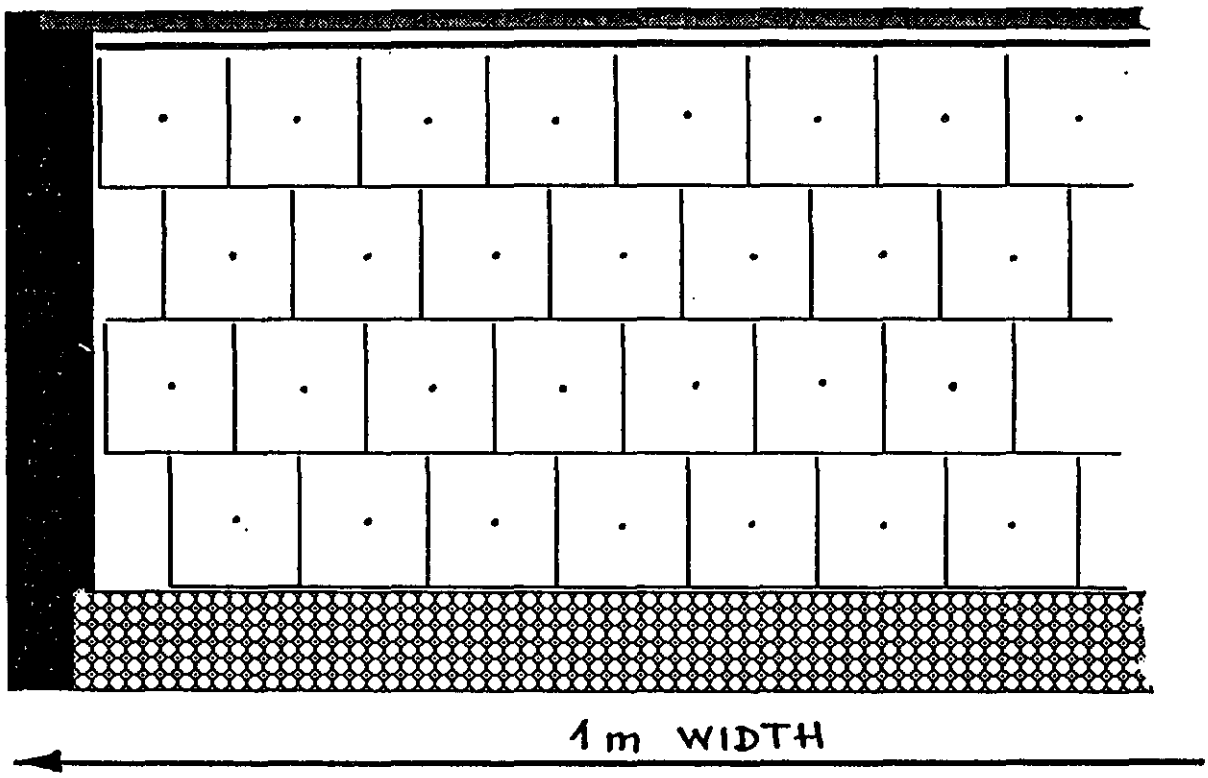

Fig. 6.1.1c

DUBNA PDT TECNOLOGY CONCEPT
(2)

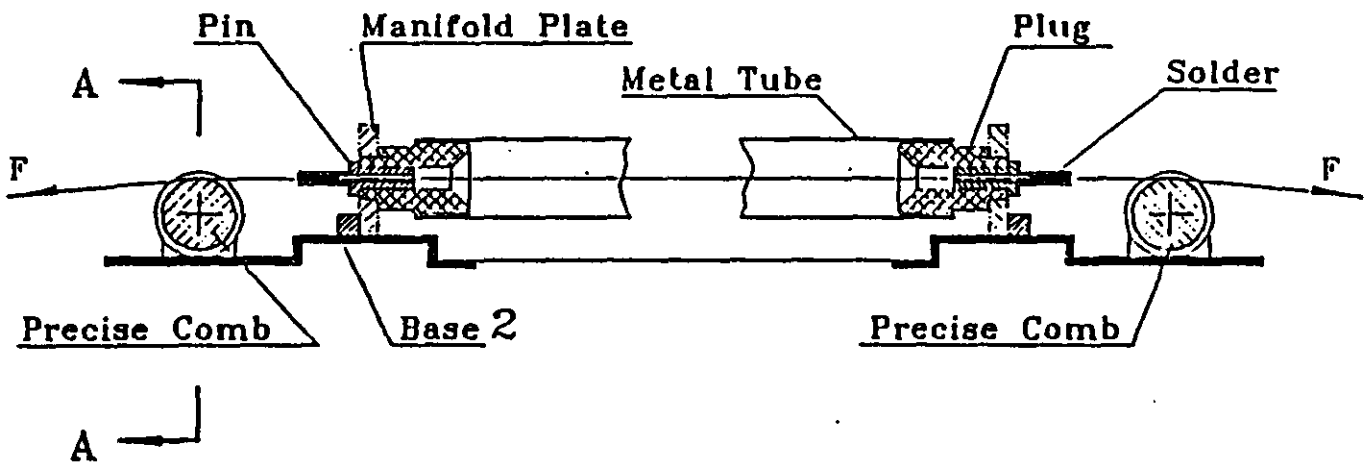

A–A

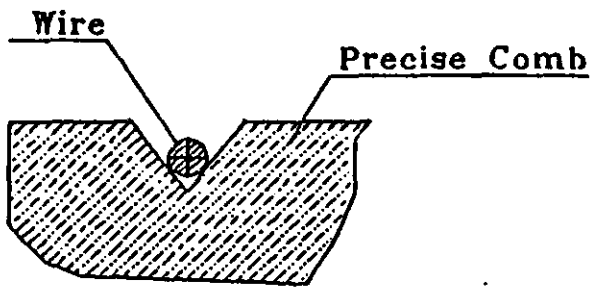

Fig. 6.1.2a

DUBNA TECNOLOGY CONCEPT

(3)

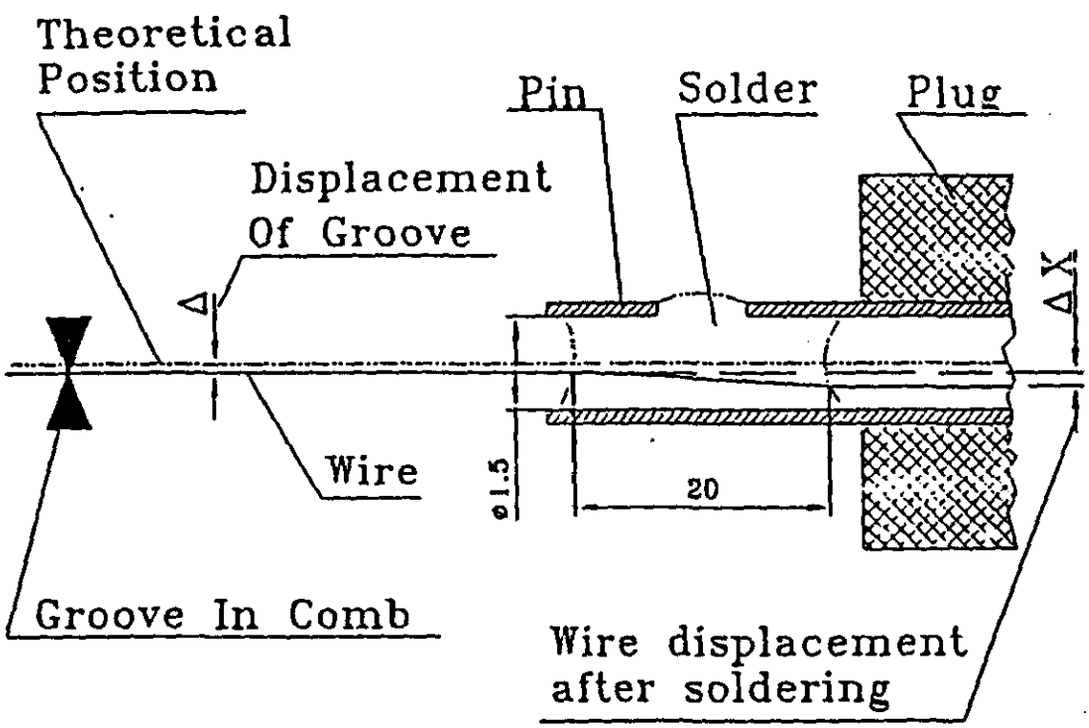

Fig. 6.1.2b

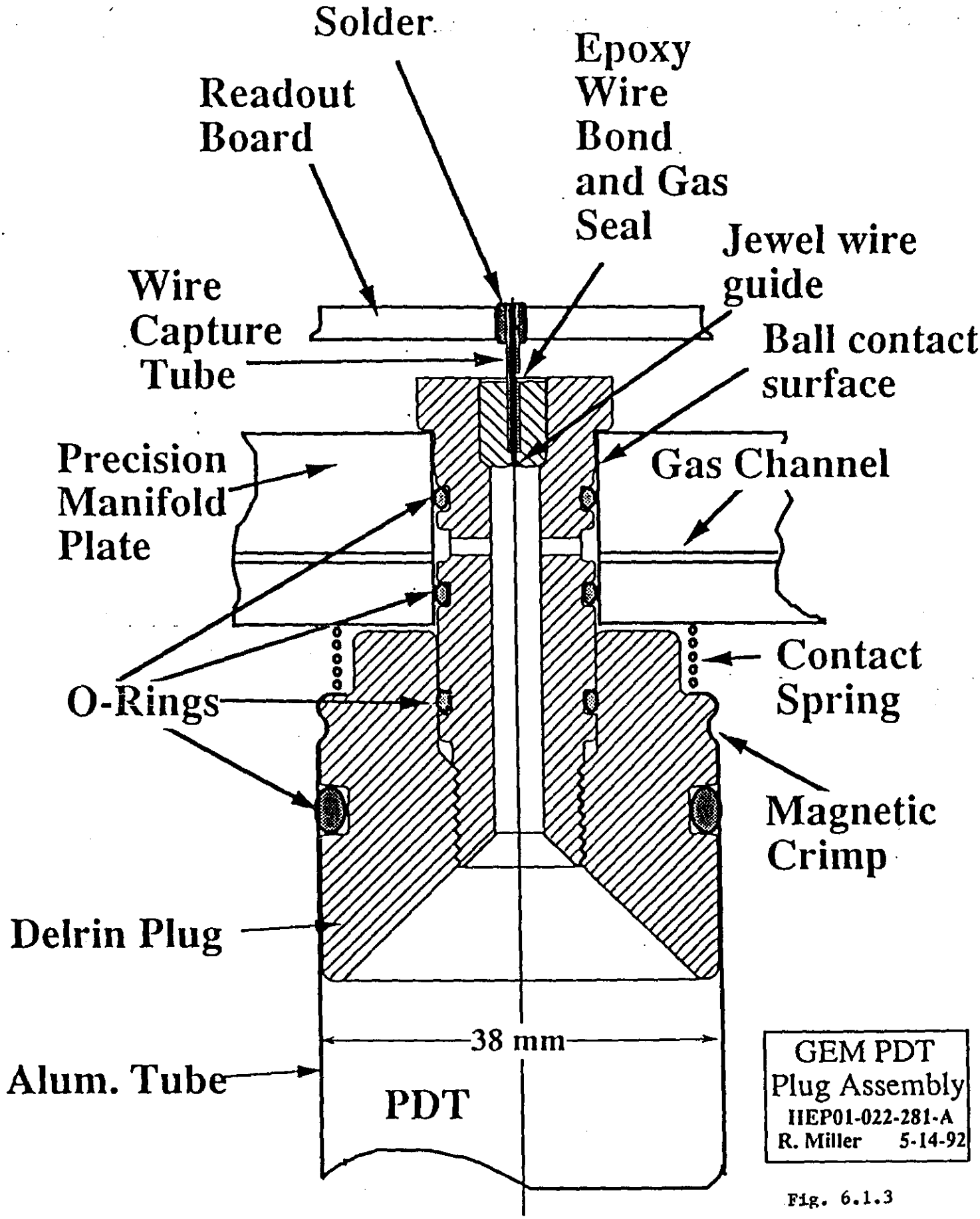
Solder
Epoxy
Wire
Bond
and Gas
Seal
Readout
Board
Jewel wire
guide
Wire
Capture
Tube
Ball contact
surface
Precision
Manifold
Plate
Gas Channel
Contact
Spring
O-Rings
Magnetic
Crimp
Delrin Plug
38 mm
Alum. Tube
PDT
GEM PDT
Plug Assembly
HEP01-022-281-A
R. Miller 5-14-92

Fig. 6.1.3

Manifold Plate Hole Placement

Aug. 4, 92

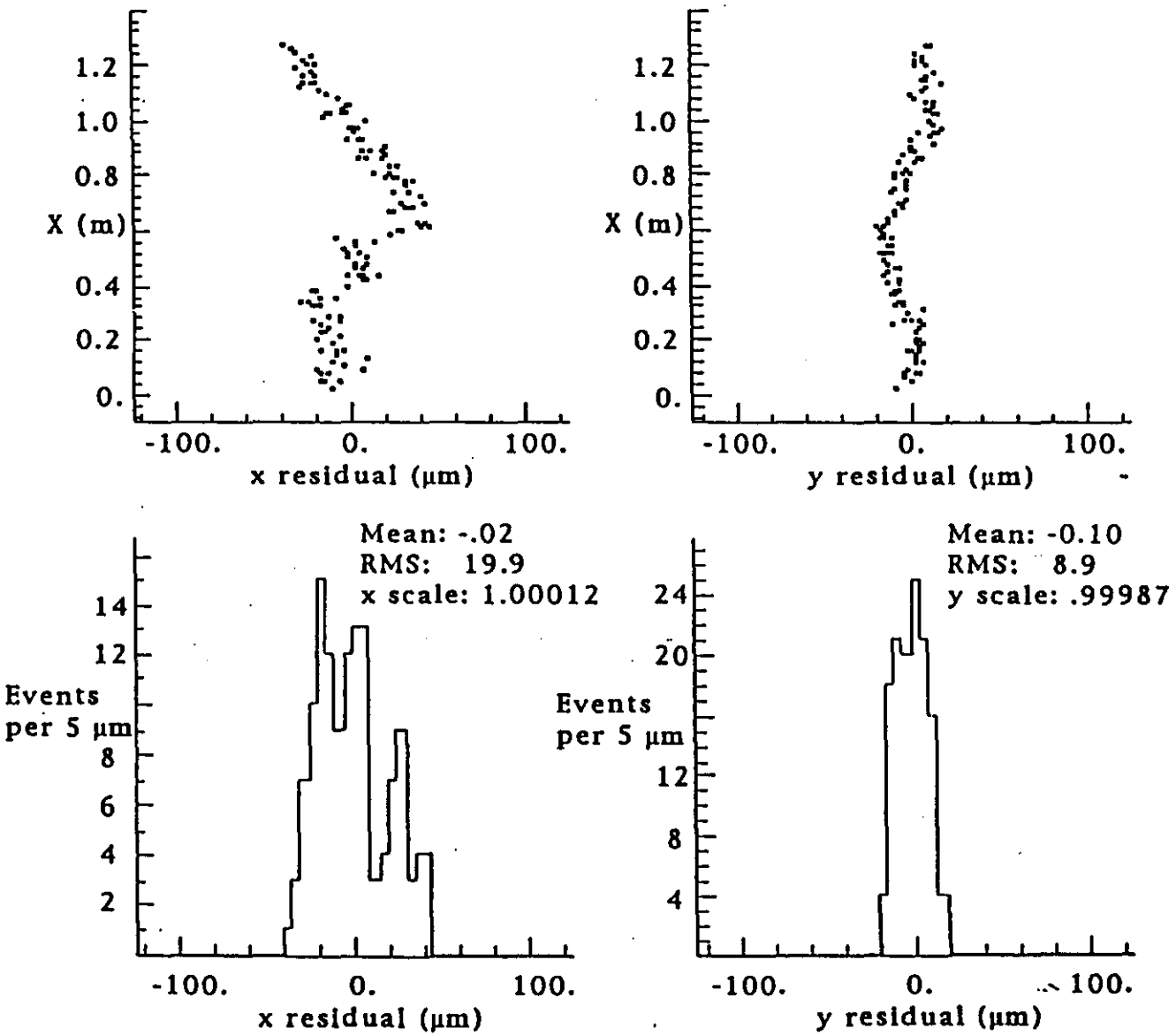

Fig. 6.1.4

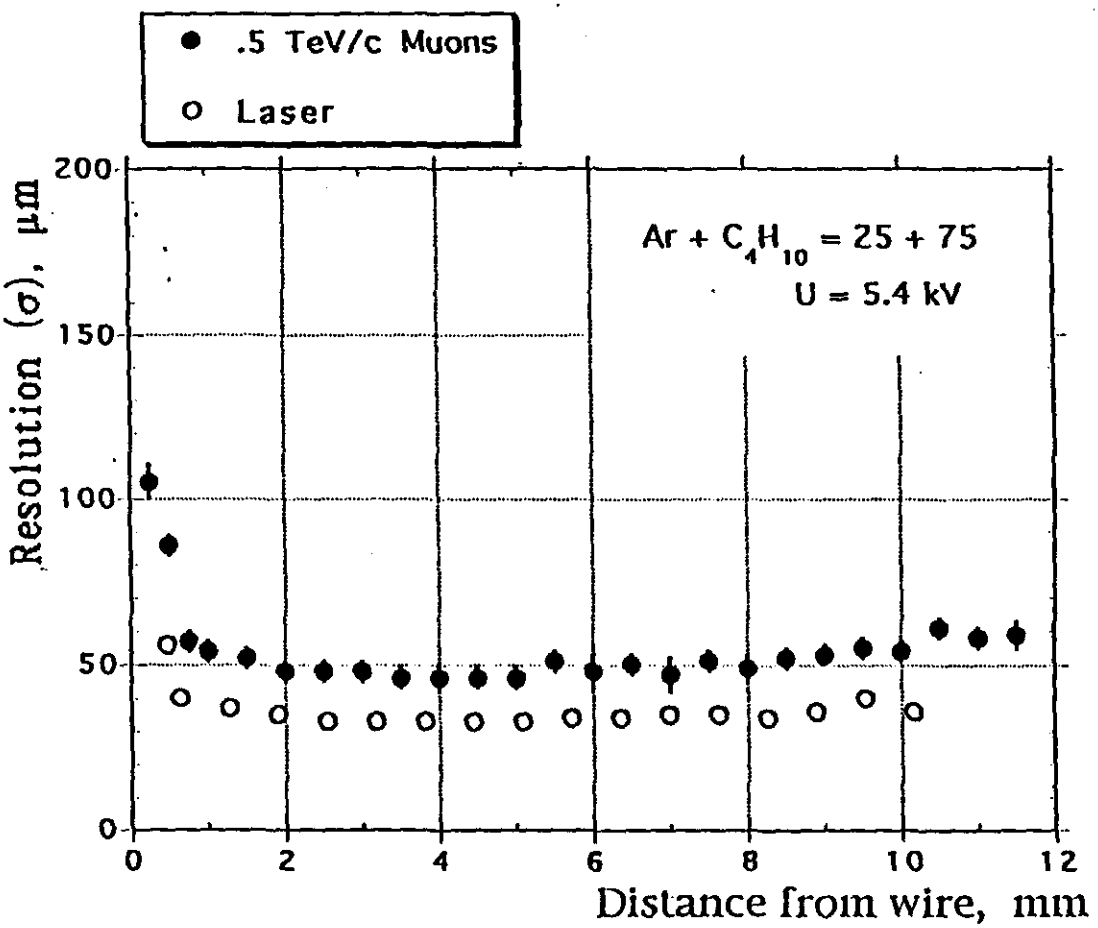
.5 TeV/c Muons
Laser
Ar + C4H10 = 25 + 75
U = 5.4 kV
Resolution (σ), μm
200
150
100
50
0
0
2
4
6
8
10
12
Distance from wire, mm

Fig. 6.1.5a

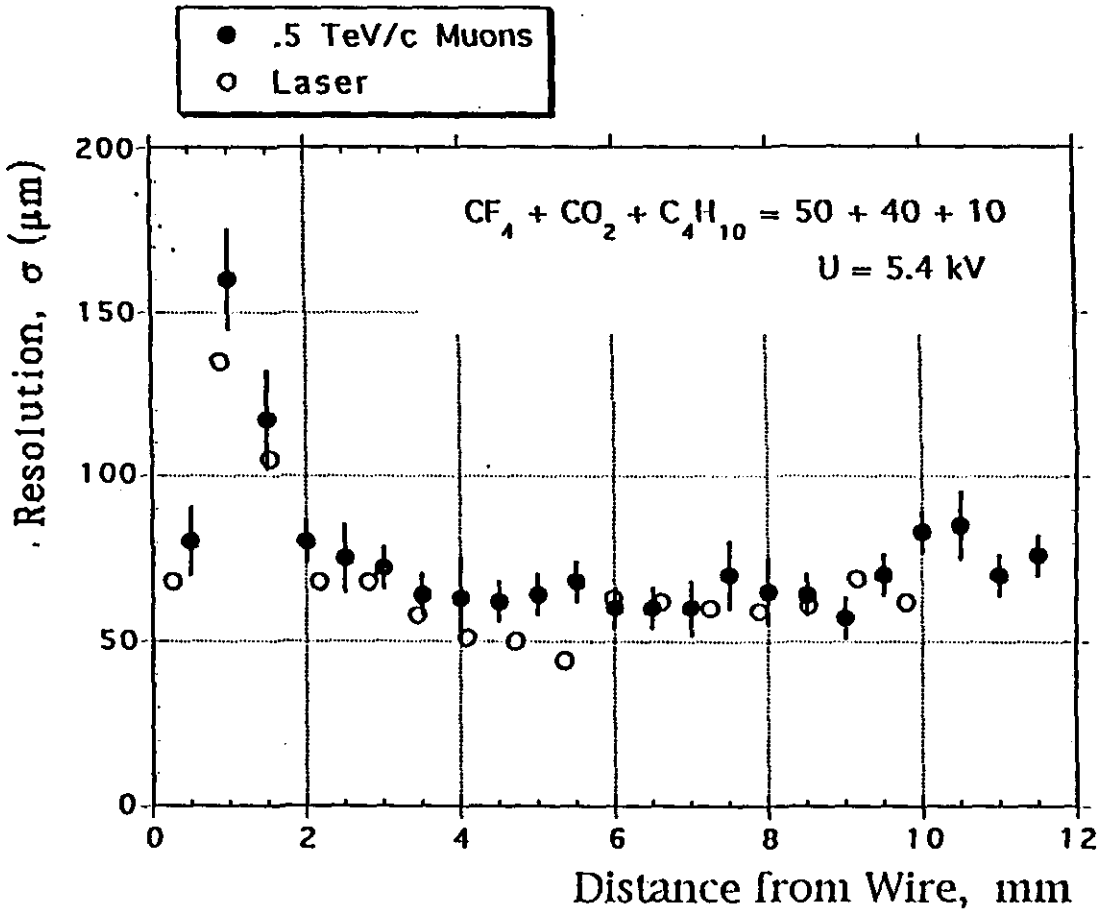
.5 TeV/c Muons
Laser
$CF_4 + CO_2 + C_4H_{10} = 50 + 40 + 10$
U = 5.4 kV
Resolution, σ (μm)
200
150
100
50
0
0
2
4
6
8
10
12
Distance from Wire, mm

Fig. 6.1.5b

NIM 143 (1977) 17

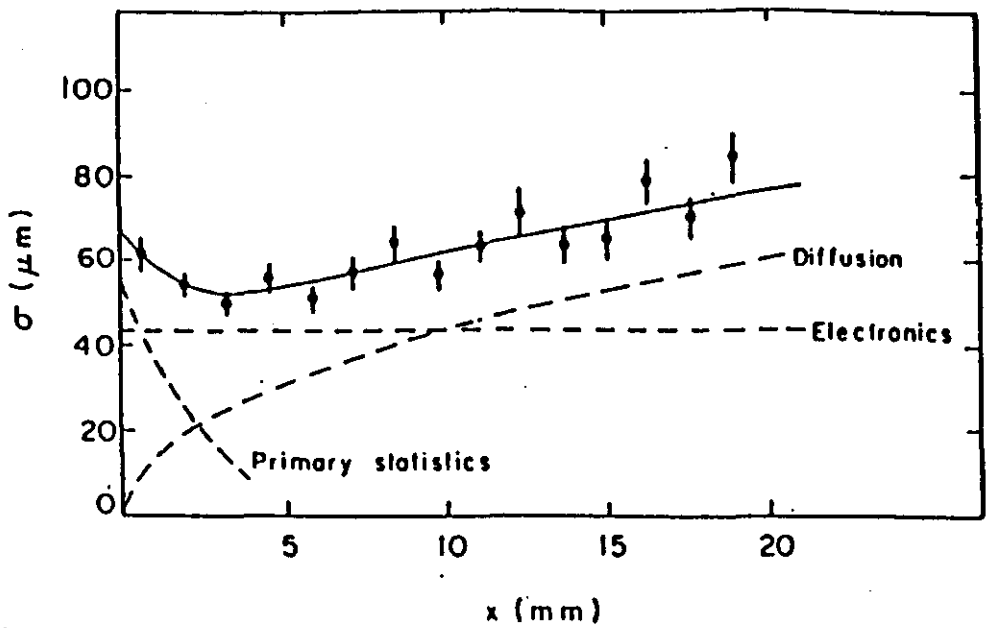

Fig. 6.1.5c

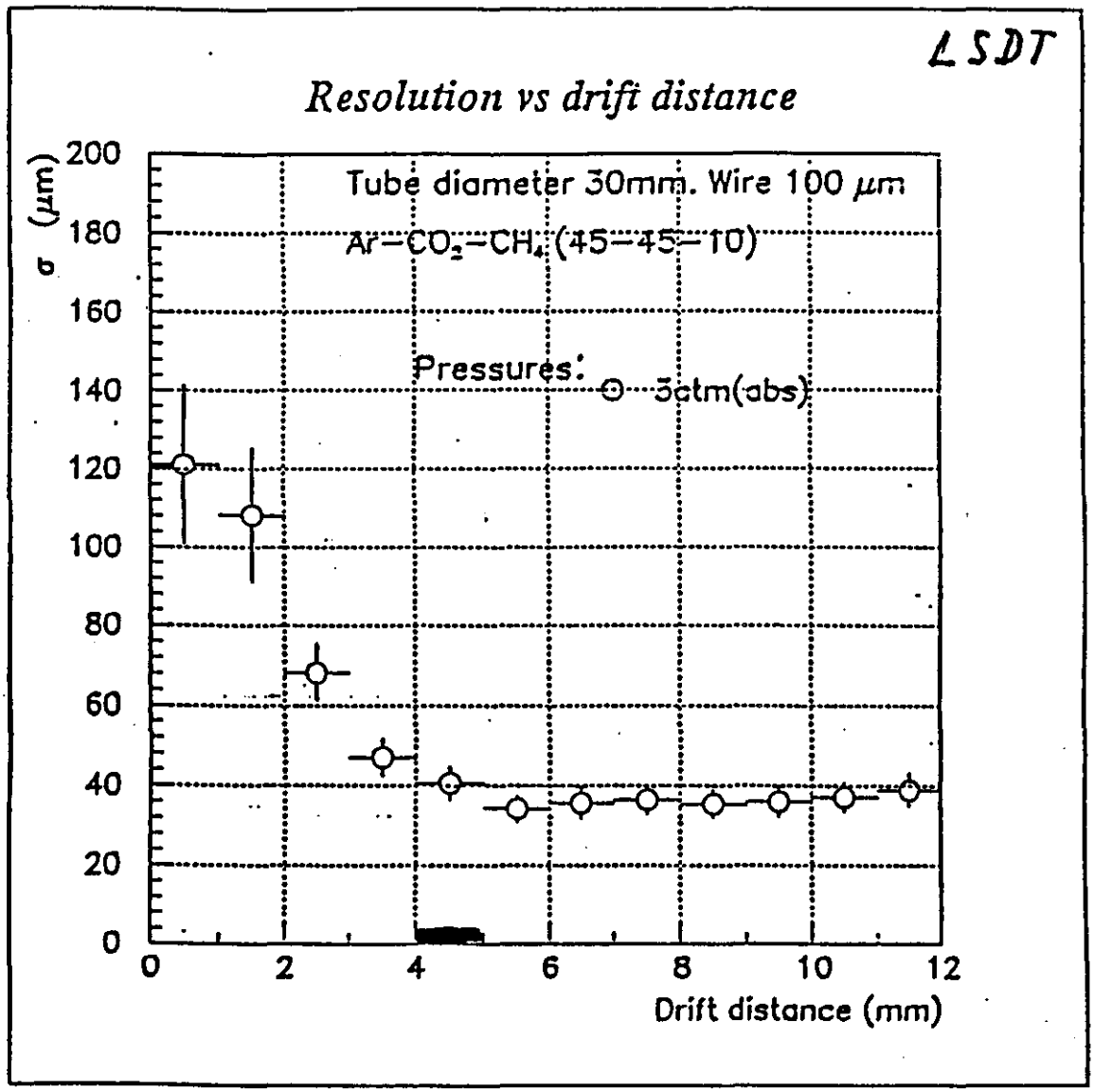
LSDT
Resolution vs drift distance
Tube diameter 30mm. Wire 100 μm
Ar–CO₂–CH₄ (45–45–10)
Pressures:
3atm(abs)
σ (μm)
200
180
160
140
120
100
80
60
40
20
0
0
2
4
6
8
10
12
Drift distance (mm)

Fig. 6.1.5d

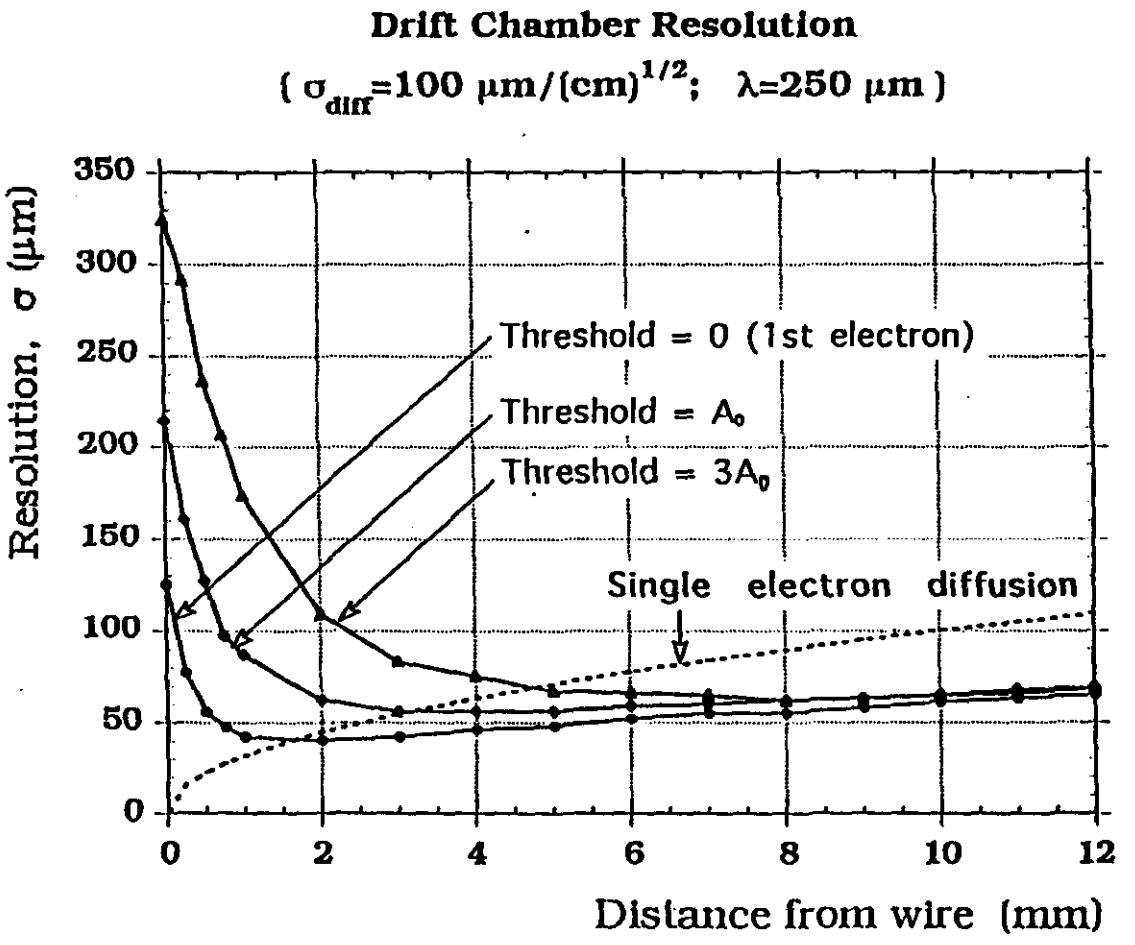
Drift Chamber Resolution
(σdiff=100 μm/(cm)^1/2; λ=250 μm)
Resolution, σ (μm)
350
300
250
200
150
100
50
0
0
2
4
6
8
10
12
Distance from wire (mm)
Threshold = 0 (1st electron)
Threshold = A0
Threshold = 3A0
Single electron diffusion

Fig. 6.1.6

$Ar - C_2H_6(50/50)$

PROP. MODE

U_A kV	Layer / P_{atm}	1	2	3	4	1...4
		Δ	Δ	Δ	Δ	σ
3.1	1	(+20)	(−47)	(+0)	(+10)	110
4.3	2	(+32)	(−52)	(+10)	(+10)	92
5.9	4	(+36)	(−59)	(+0)	(+10)	76

$Ar - C_4H_{10}(25/75)$

P = 1 atm

U_A kV	Layer / Mode	1	2	3	4	1...4
		Δ	Δ	Δ	Δ	σ
4.1	prop.	(+34)	(−52)	(+12)	(+10)	95
4.5	streamer	(+34)	(−57)	(+10)	(+12)	82

σ −space resolution (μm)

Δ −systematic shift (μm)

Fig. 6.1.7

DUBNA RDT: Ar-C_4H_{10} (25/75) at 1atm

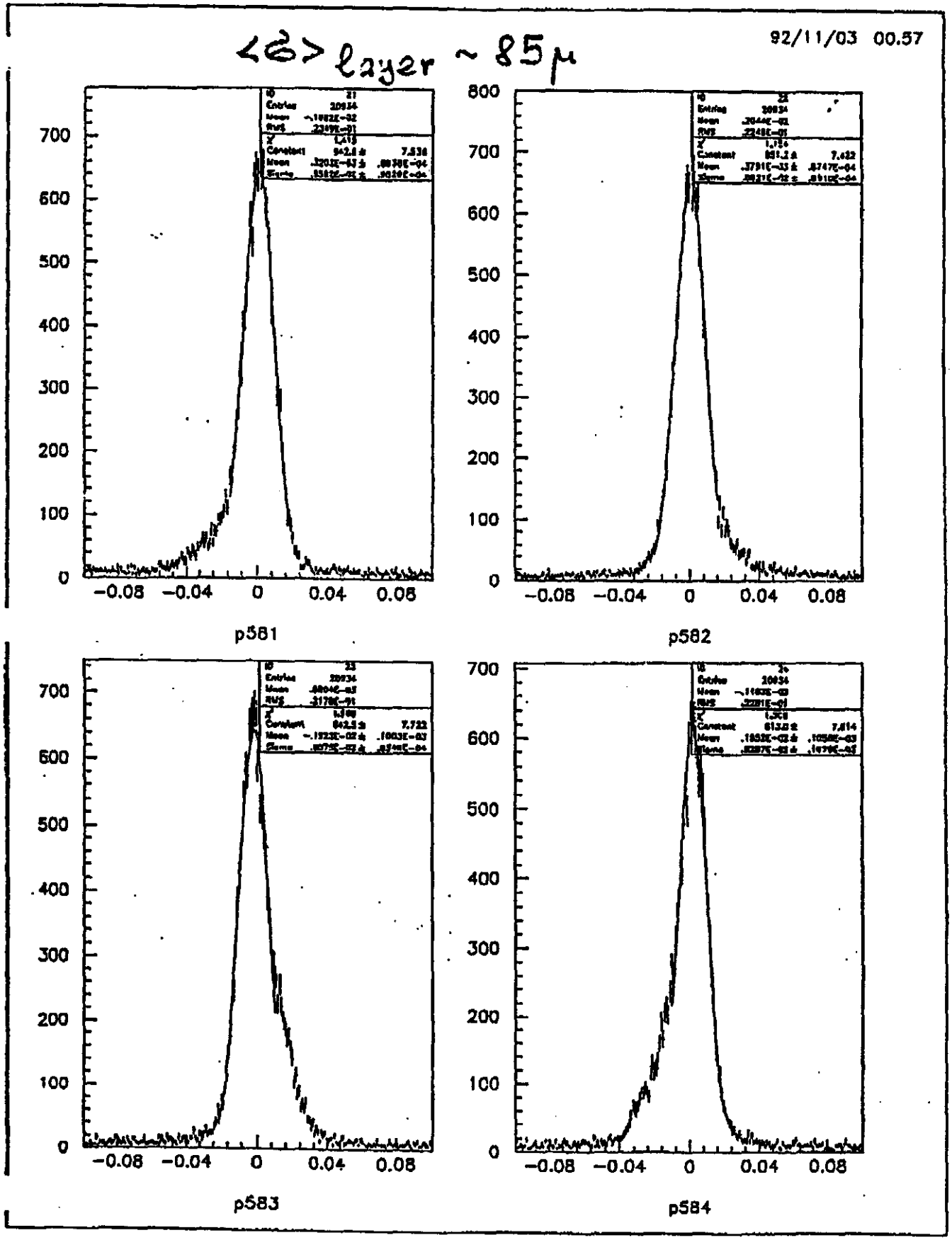

Fig. 6.1.8

ASYMMETRICAL TAILS ARE DUE TO

Residuals as a function of tube number

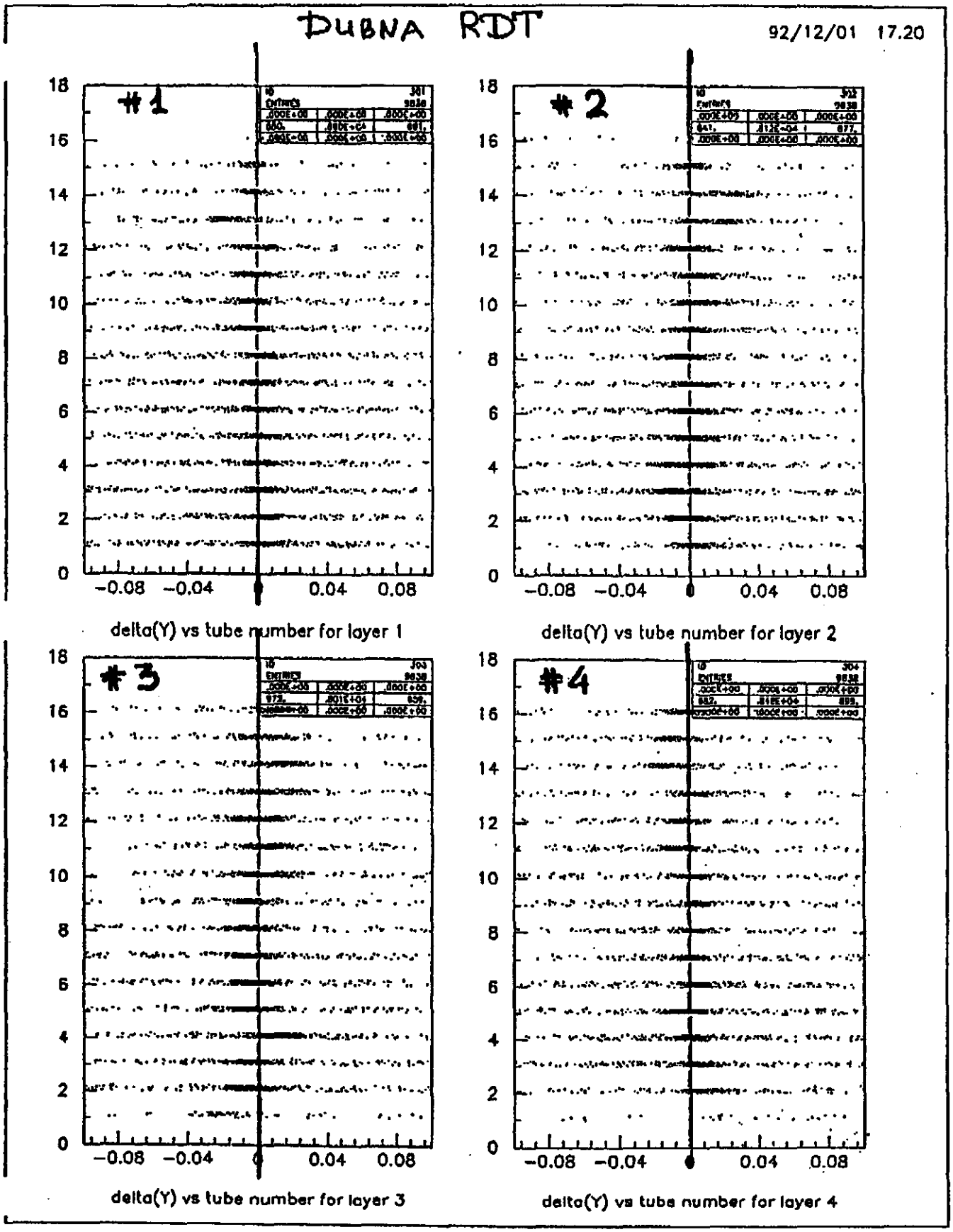

Fig. 6.1.9a

Residuals as a function of tube number

(after parallel shifts of wires)

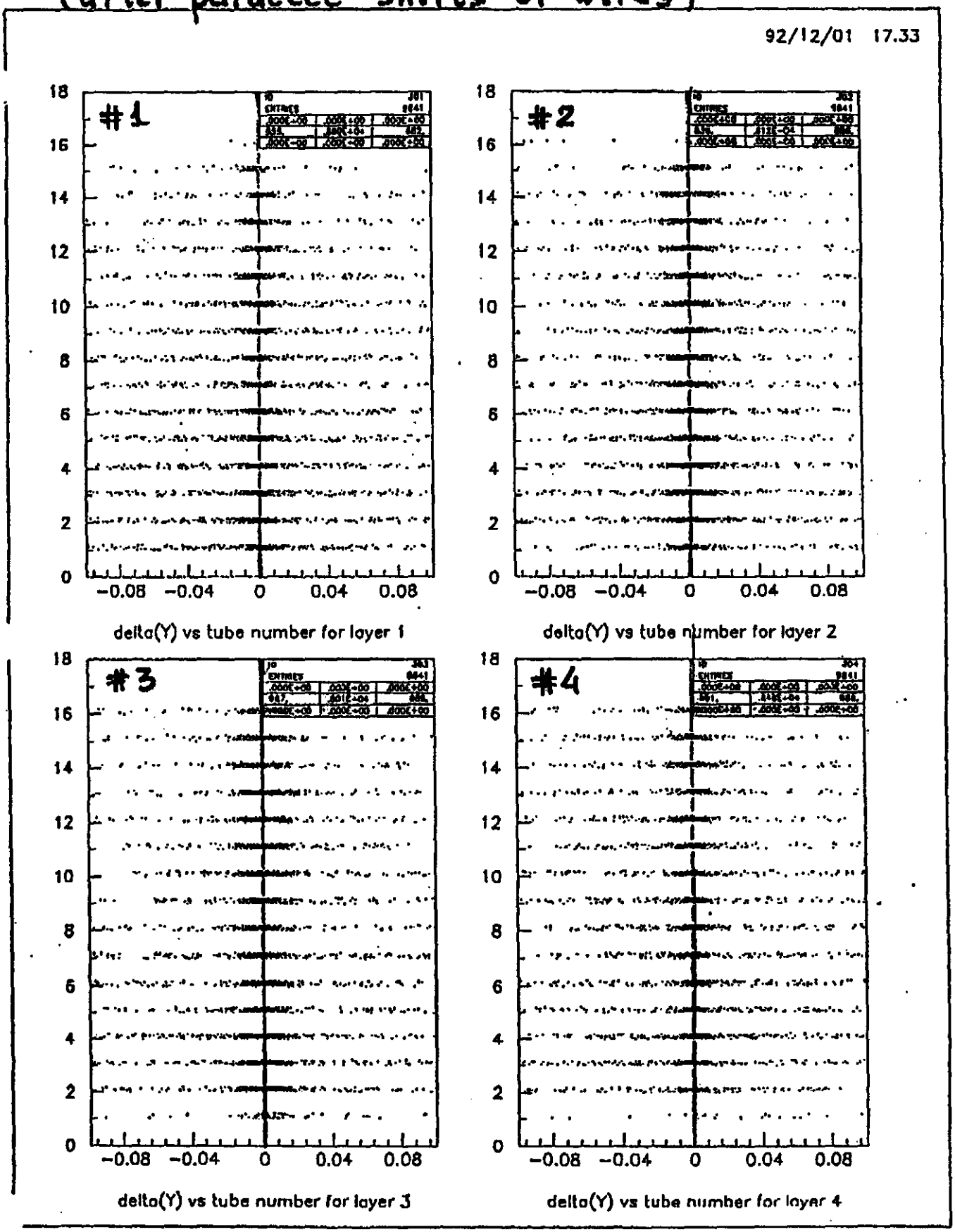

Fig. 6.1.9b

Rotation of layers

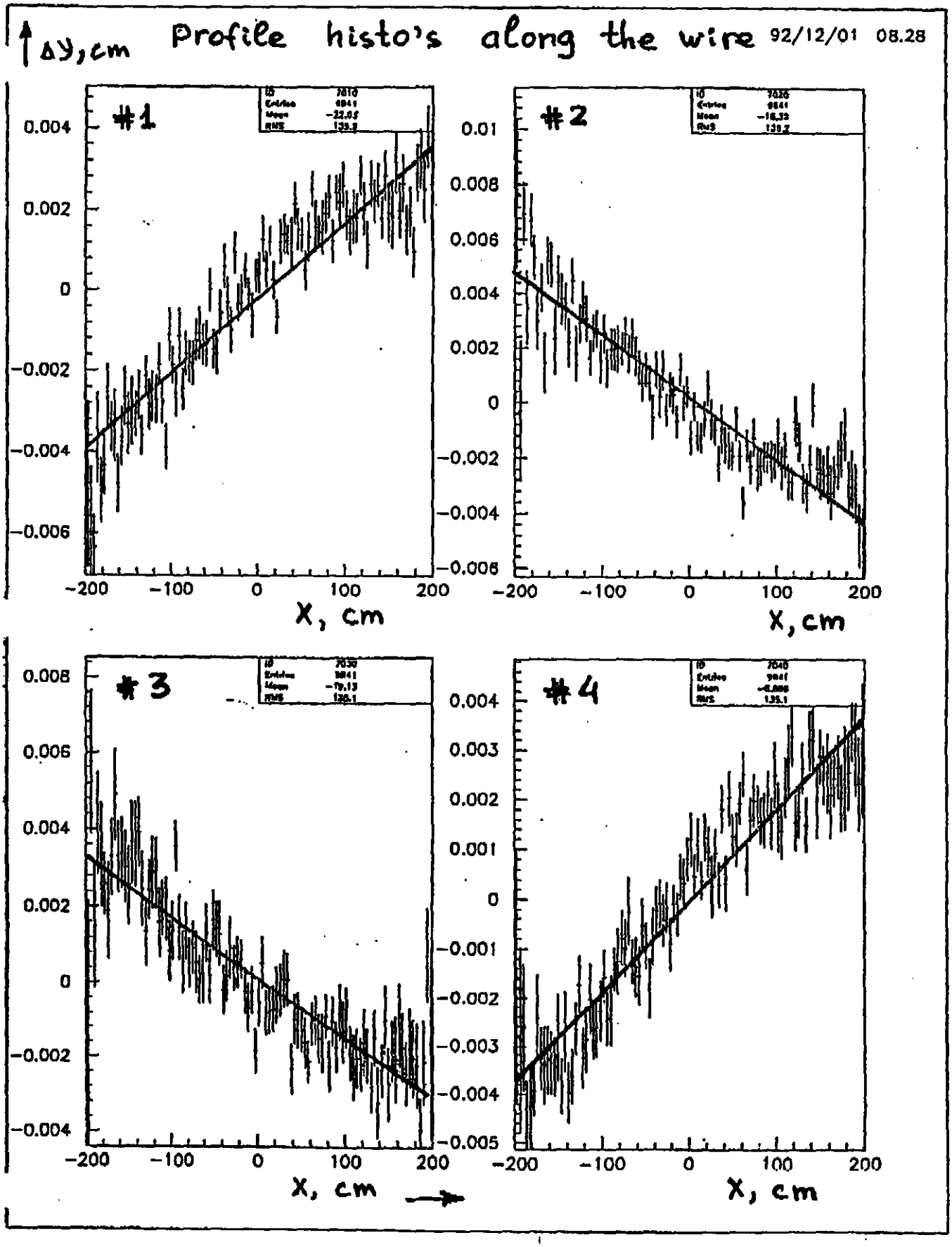

Fig. 6.1.10

RESIDUALS FOR DIFFERENT LAYERS

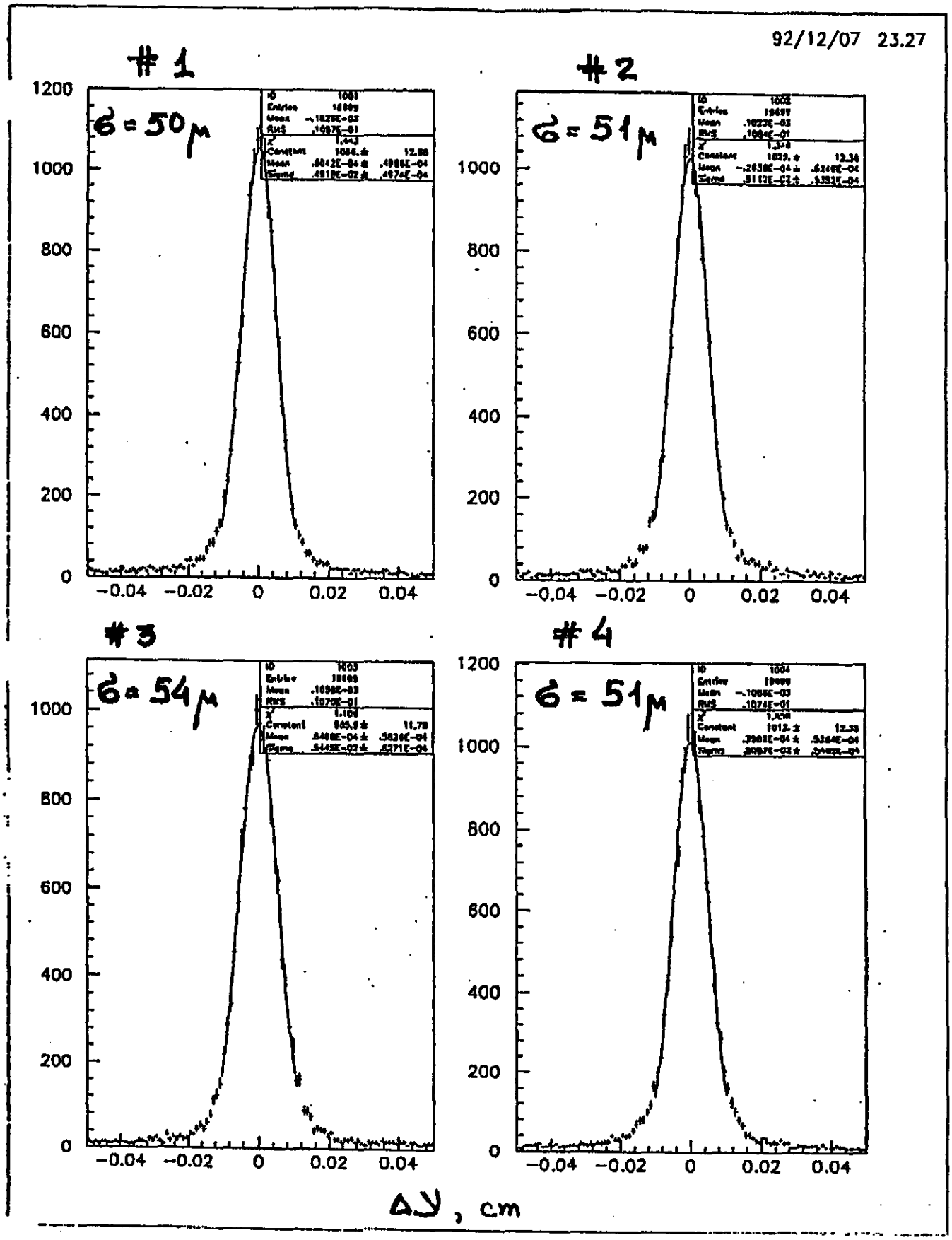

$Ar-C_2H_6$ at 4.8 atm

Fig. 6.1.11

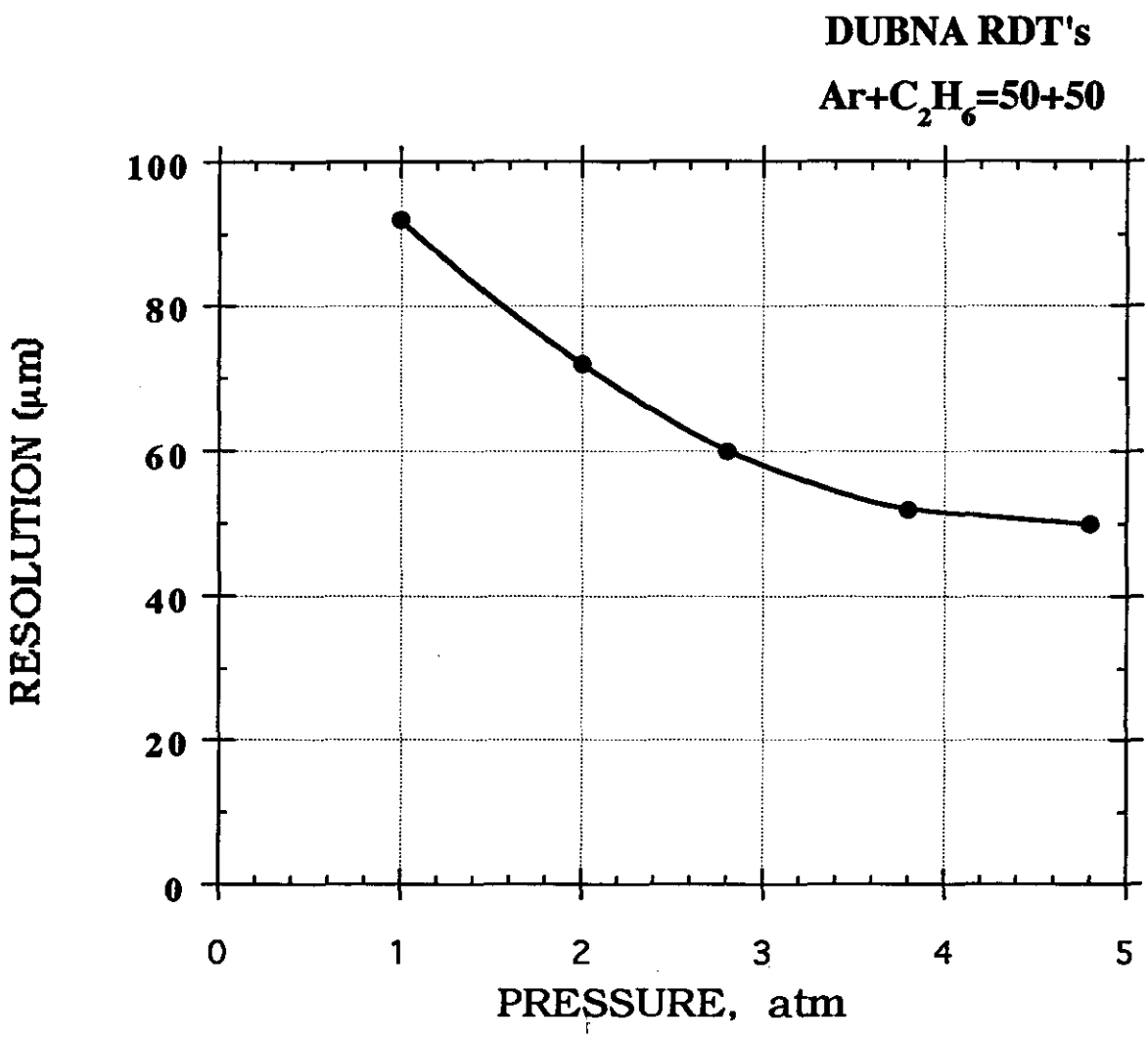
DUBNA RDT's
Ar+C2H6=50+50
RESOLUTION (μm)
100
80
60
40
20
0
0
1
2
3
4
5
PRESSURE, atm

Fig. 6.1.12

MSU PDT · AUN 388

RESOLUTION

92/12/10 23.59

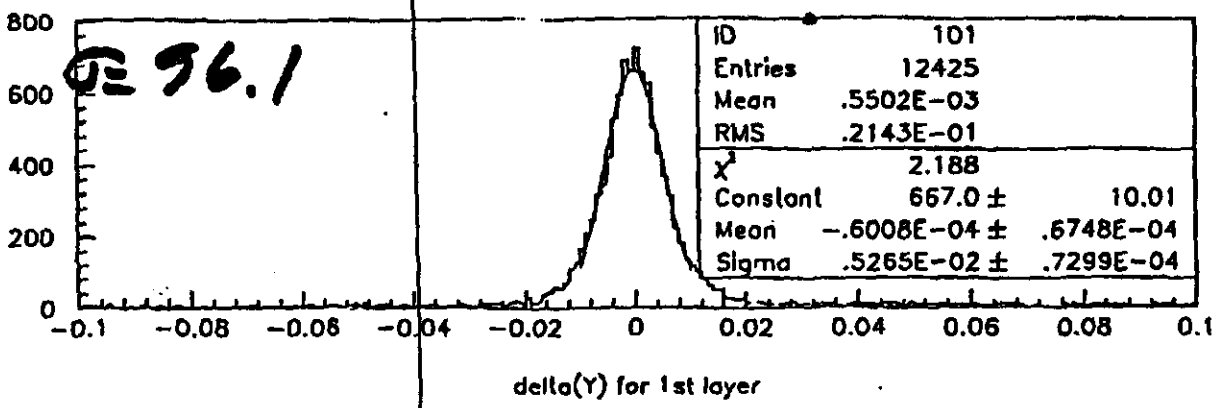

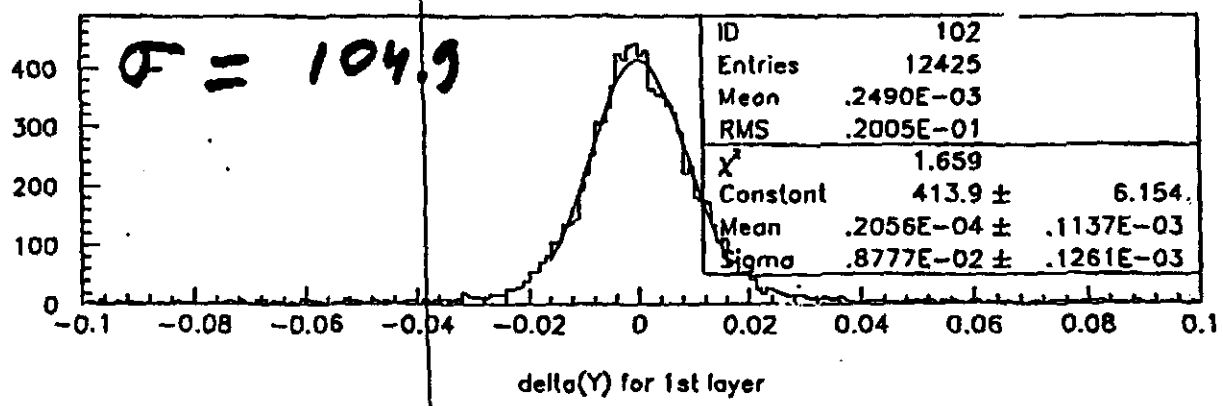

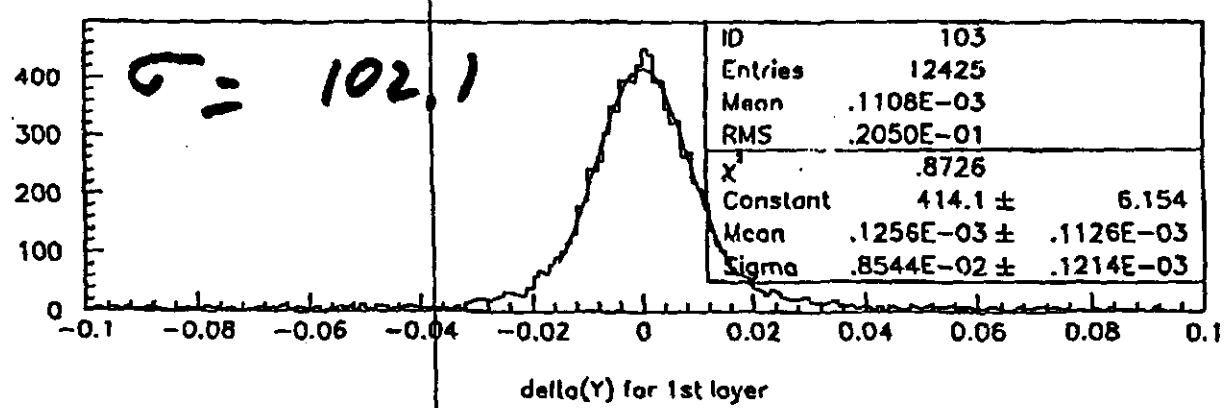

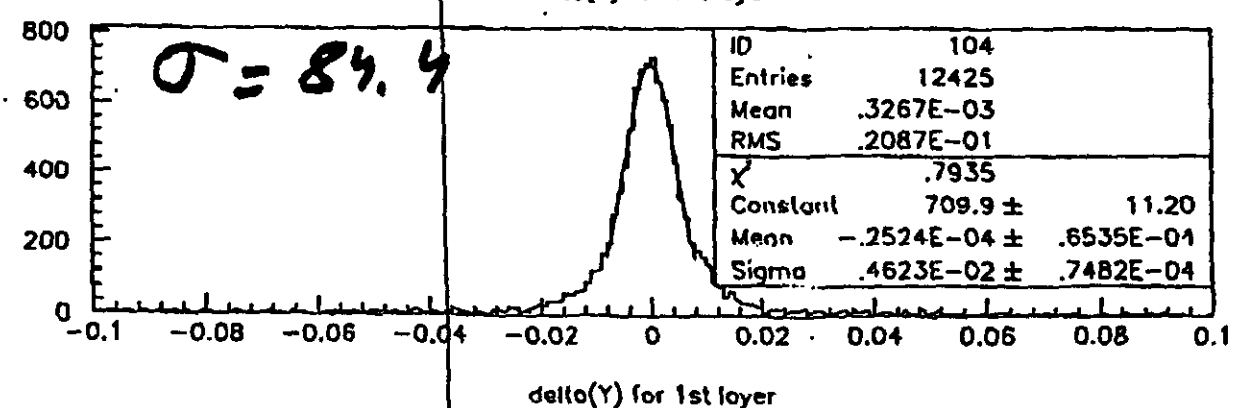

$\langle \sigma \rangle = 97 \pm 9\ \mu$

Fig. 6.1.13

RUN 388 Y-RESIDUALS FROM GLOBAL TRACK (PDTU)

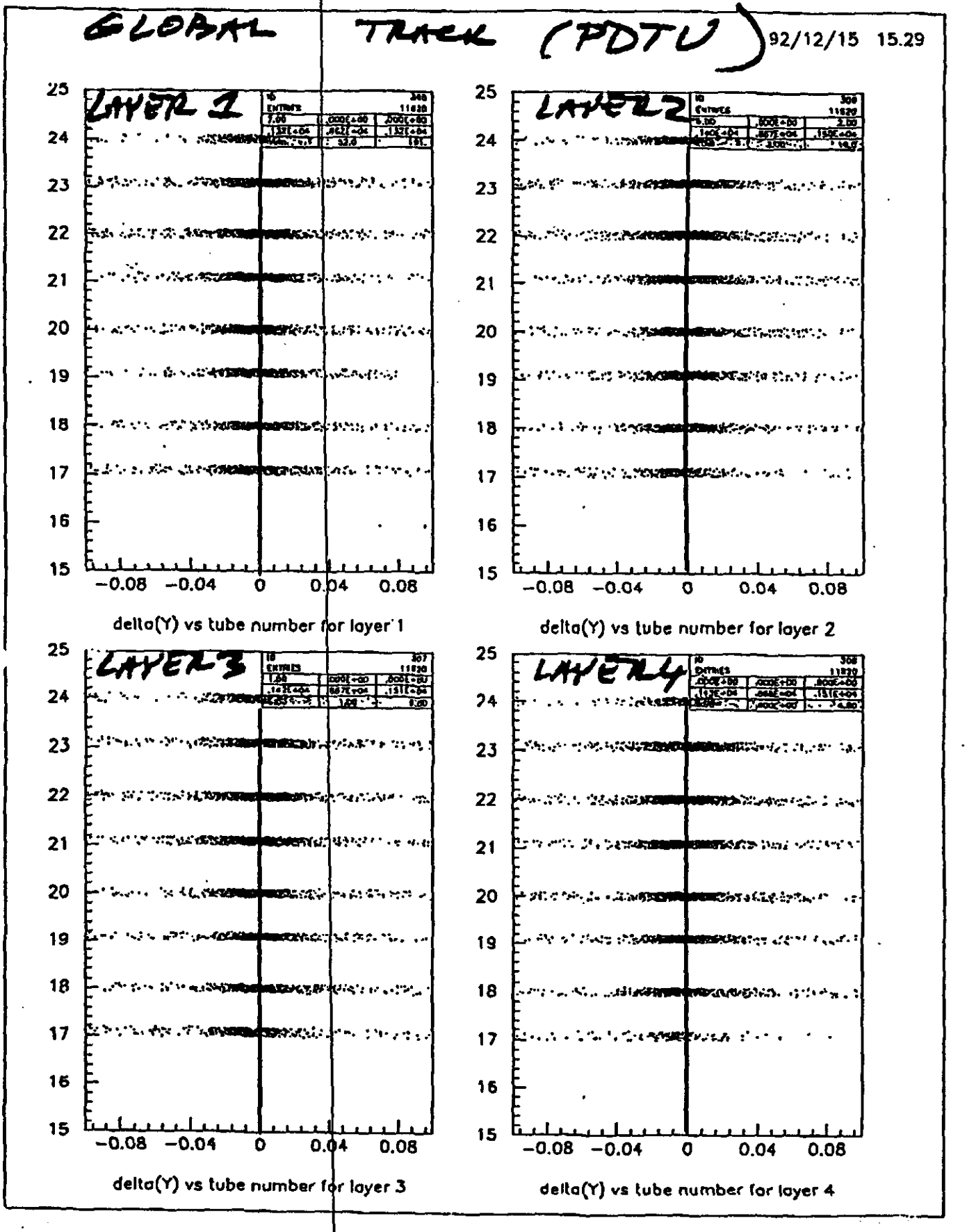

Fig. 6.1.14

MSU PROTOTYPE

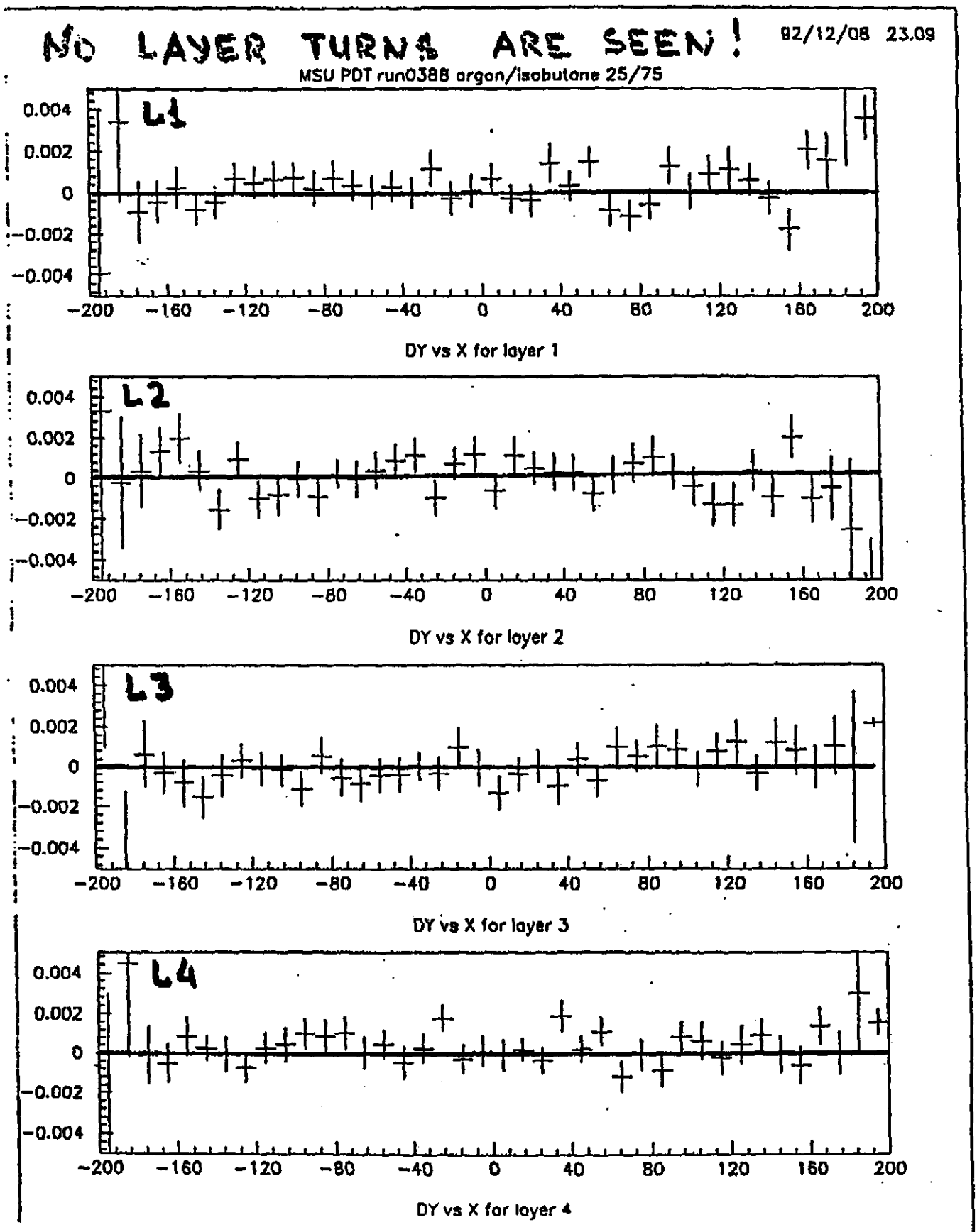

Fig. 6.1.15

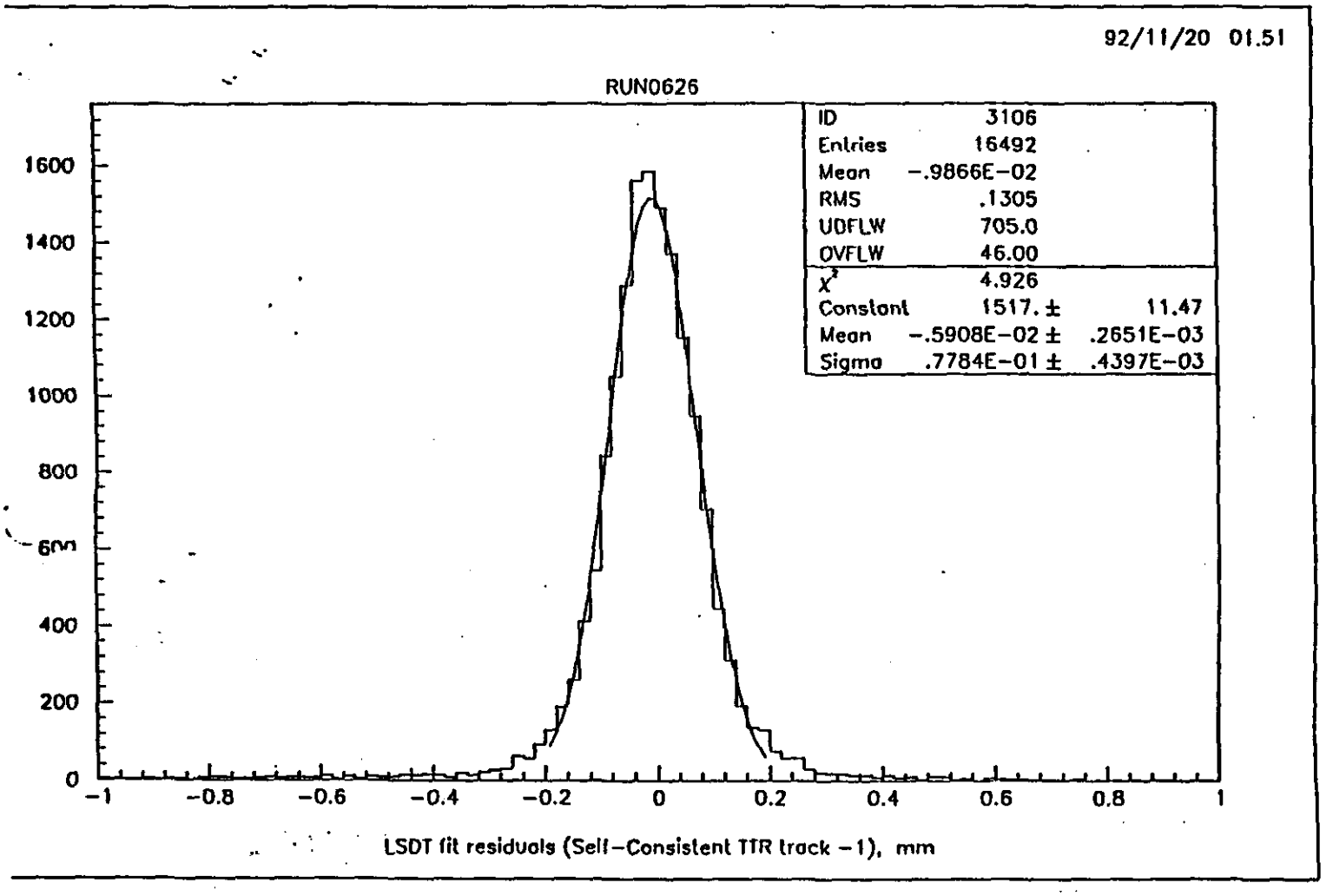
92/11/20 01.51
RUN0626
ID 3106
Entries 16492
Mean -.9866E-02
RMS .1305
UDFLW 705.0
OVFLW 46.00
χ² 4.926
Constant 1517. ± 11.47
Mean -.5908E-02 ± .2651E-03
Sigma .7784E-01 ± .4397E-03
1600
1400
1200
1000
800
600
400
200
0
-1
-0.8
-0.6
-0.4
-0.2
0
0.2
0.4
0.6
0.8
1
LSDT fit residuals (Self-Consistent TTR track -1), mm

Fig. 6.1.16

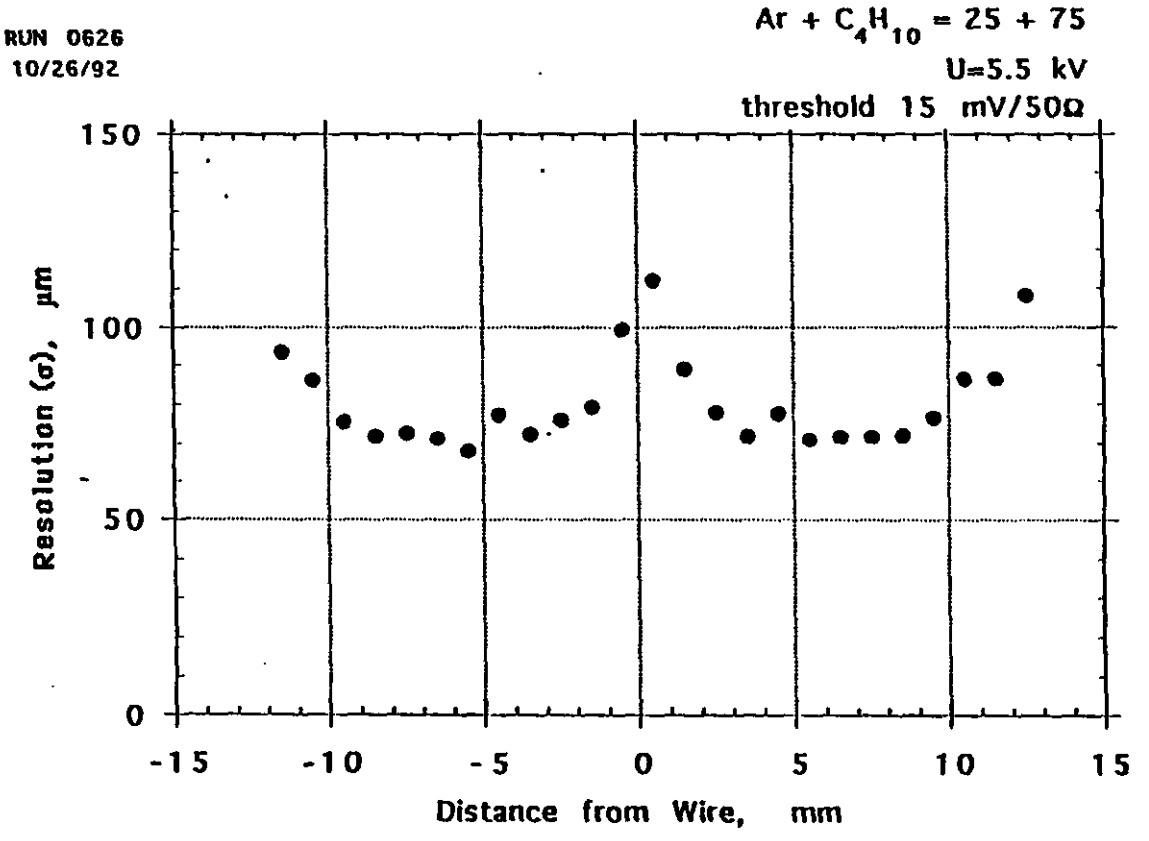
RUN 0626
10/26/92
Ar + C4H10 = 25 + 75
U=5.5 kV
threshold 15 mV/50Ω
150
100
50
0
Resolution (σ), μm
-15
-10
-5
0
5
10
15
Distance from Wire, mm

Fig. 6.1.17

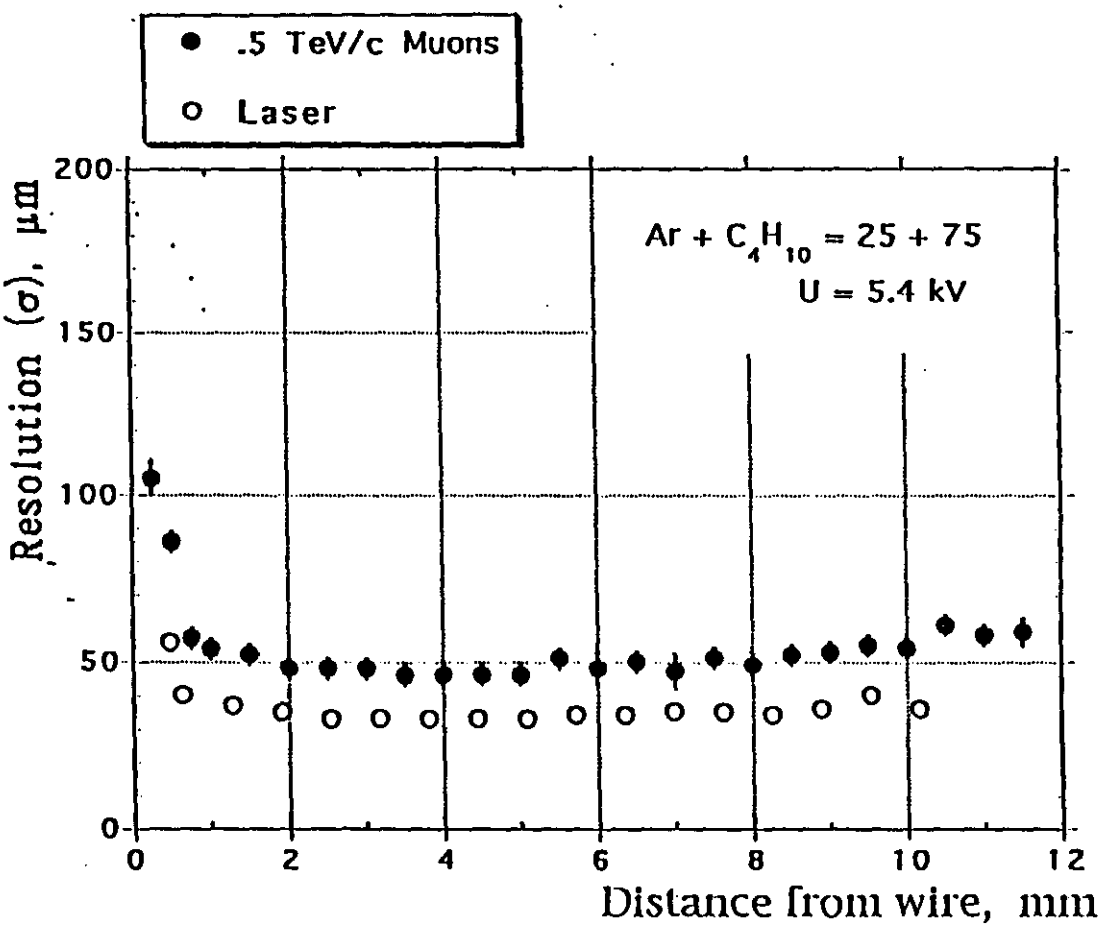
.5 TeV/c Muons
Laser
Ar + C4H10 = 25 + 75
U = 5.4 kV
Resolution (σ), μm
200
150
100
50
0
0
2
4
6
8
10
12
Distance from wire, mm

Fig. 6.1.18

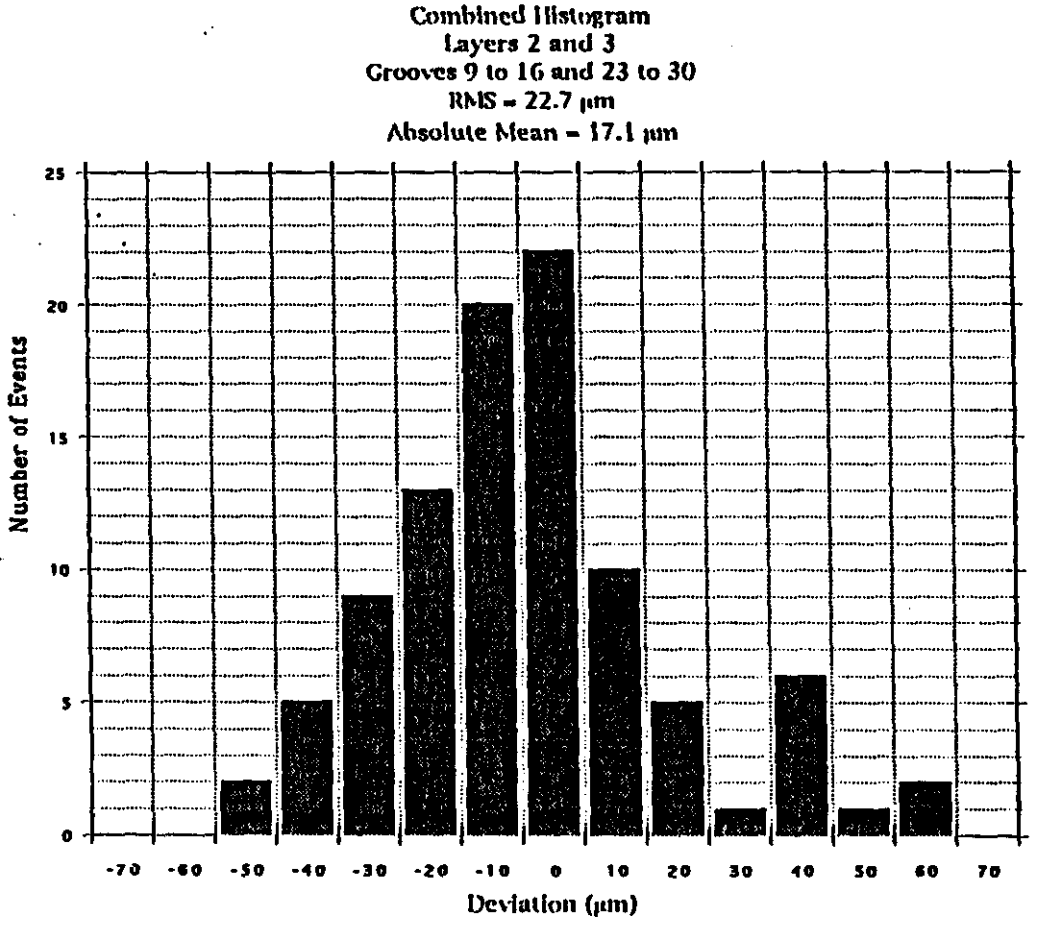
Combined Histogram
Layers 2 and 3
Grooves 9 to 16 and 23 to 30
RMS = 22.7 μm
Absolute Mean = 17.1 μm
Number of Events
0
5
10
15
20
25
-70
-60
-50
-40
-30
-20
-10
0
10
20
30
40
50
60
70
Deviation (μm)

Fig. 6.1.19

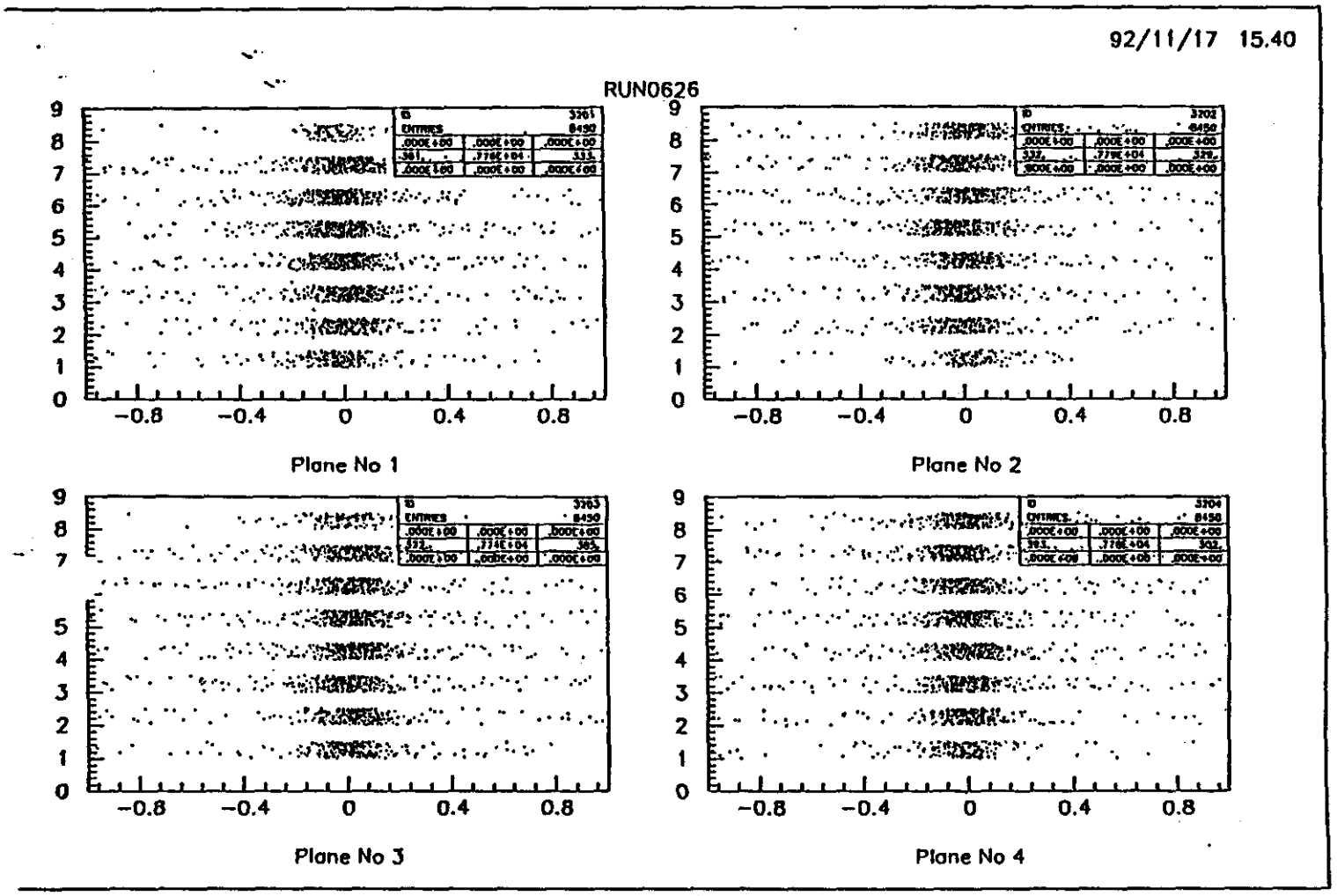

Fig. 6.1.20a

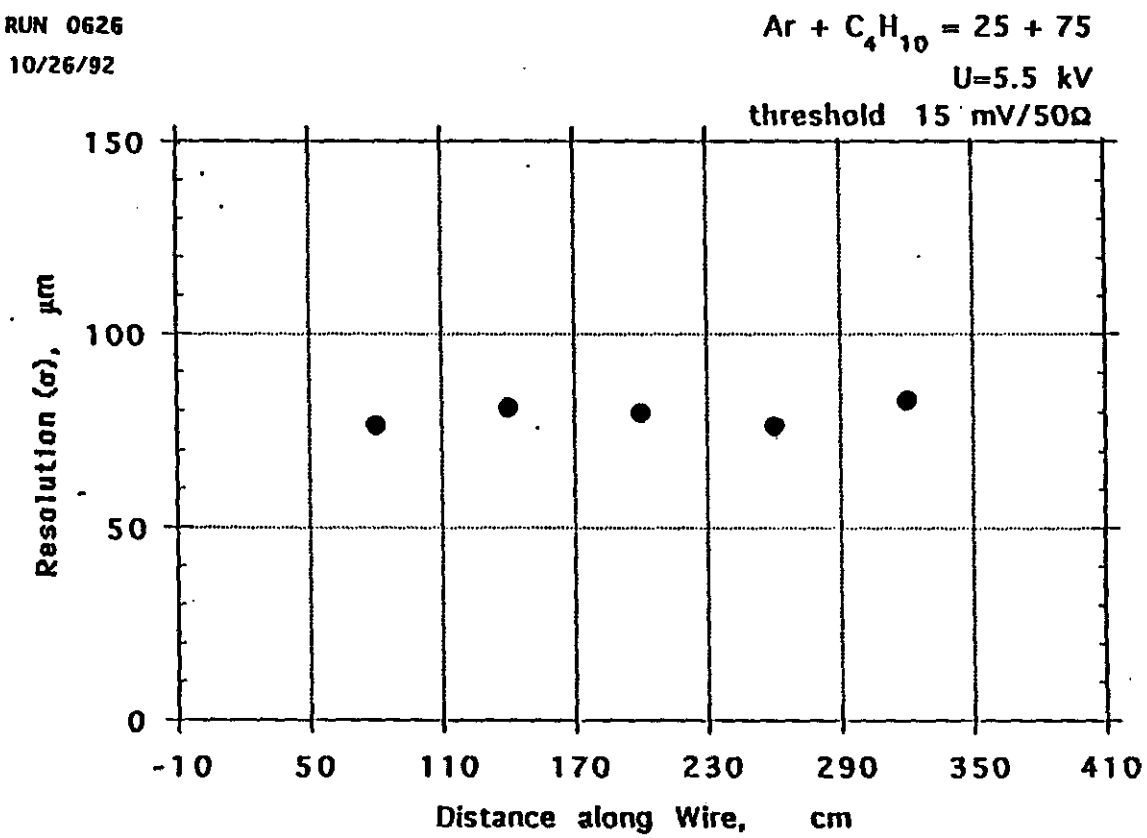
RUN 0626
10/26/92
Ar + C4H10 = 25 + 75
U=5.5 kV
threshold 15 mV/50Ω
150
100
50
0
Resolution (σ), μm
-10
50
110
170
230
290
350
410
Distance along Wire, cm

Fig. 6.1.20b

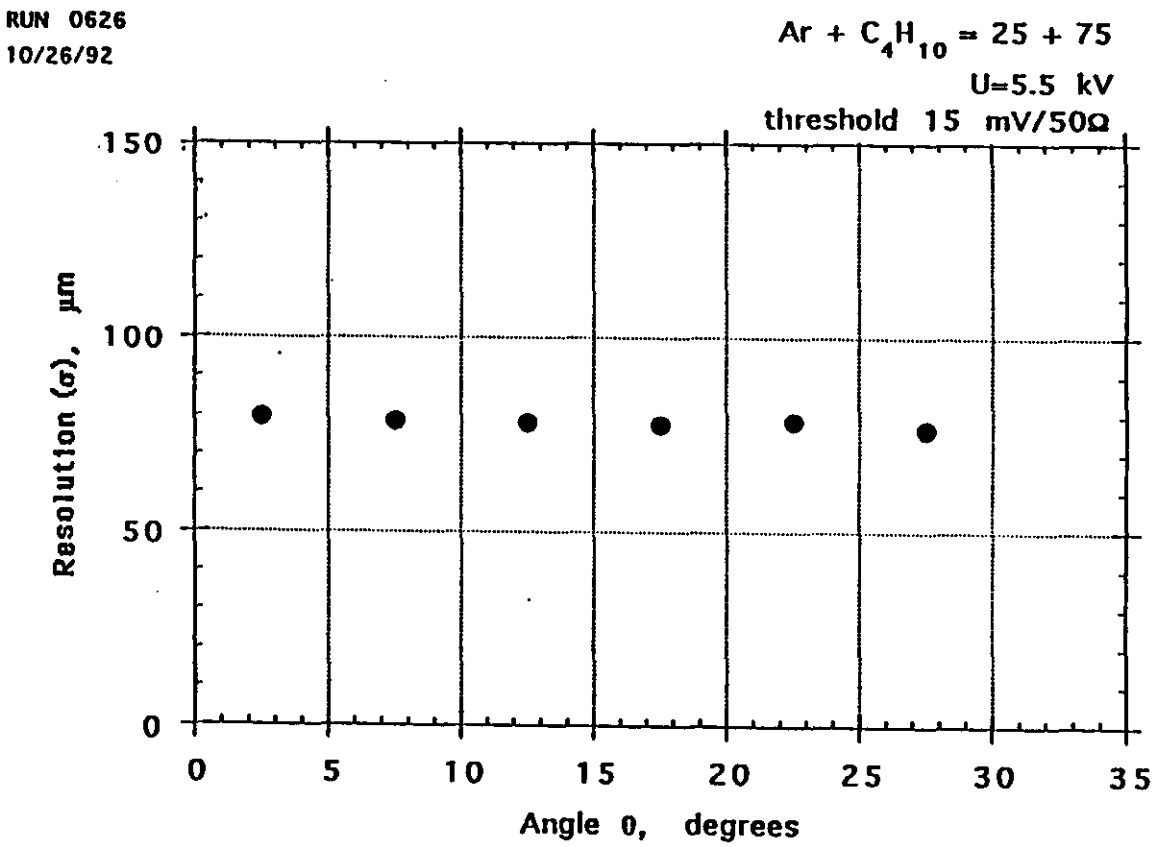
RUN 0626
10/26/92
Ar + C4H10 = 25 + 75
U=5.5 kV
threshold 15 mV/50Ω
150
100
50
0
Resolution (σ), μm
0
5
10
15
20
25
30
35
Angle θ, degrees

Fig. 6.1.20c

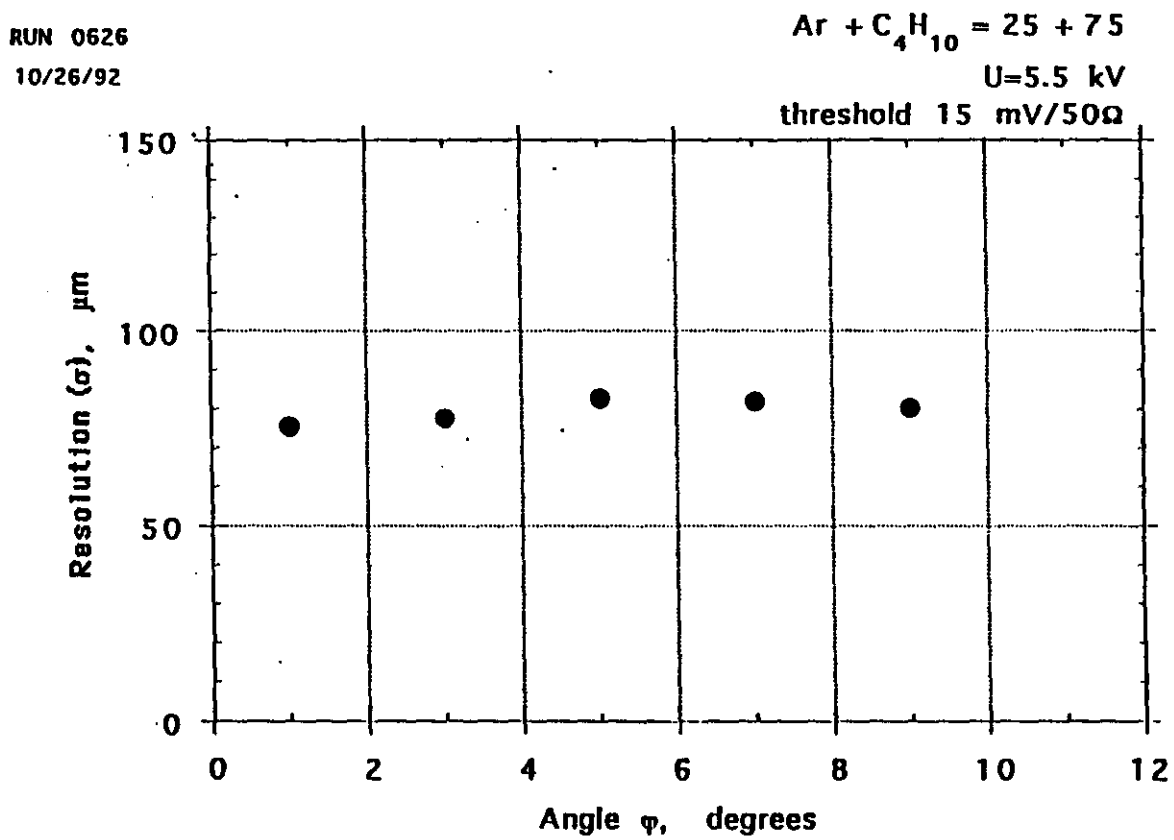
RUN 0626
10/26/92
Ar + C4H10 = 25 + 75
U=5.5 kV
threshold 15 mV/50Ω
150
100
50
0
Resolution (σ), μm
0
2
4
6
8
10
12
Angle φ, degrees

Fig. 6.1.20d

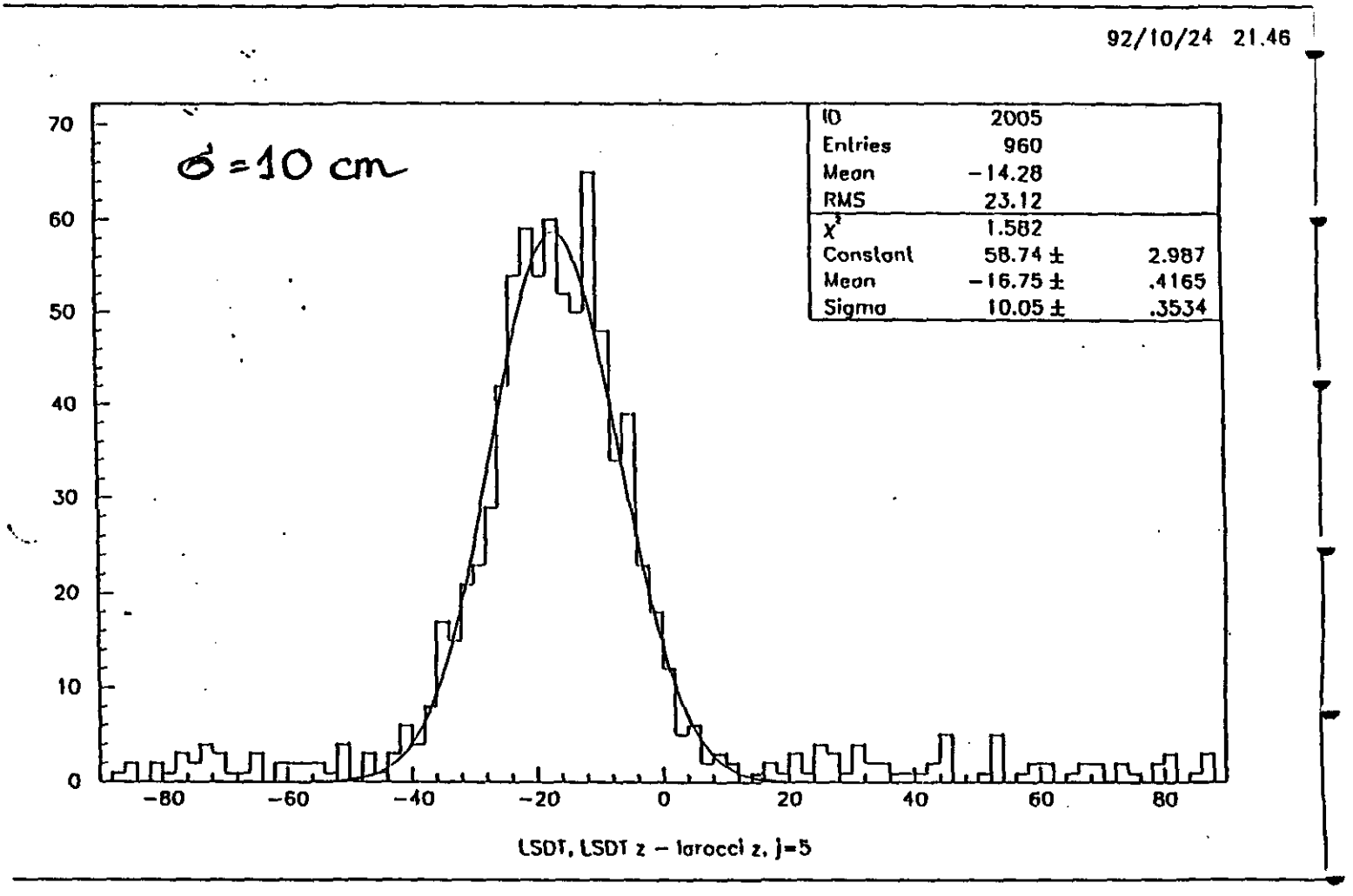
92/10/24 21.46
σ = 10 cm
ID 2005
Entries 960
Mean −14.28
RMS 23.12
χ² 1.582
Constant 58.74 ± 2.987
Mean −16.75 ± .4165
Sigma 10.05 ± .3534
70
60
50
40
30
20
10
0
−80
−60
−40
−20
0
20
40
60
80
LSDT, LSDT z − Iarocci z, j=5

Fig. 6.1.21

(6.1.1) Corrections to Precision Drift Measurements

(6.1.1.1) Lorentz Angle

Drift tubes determine the trajectory space point by measuring the drift time which is converted to a distance from the wire by knowing the drift velocity. The time (t)-to-space (r) function can be numerically evaluated as:

$$t=\int_{r_0}^{r} dr'/V_r(r'), \qquad (1)$$

where $V_r(r')$ is the radial component (i.e. parallel to the tube) of the mean drift velocity for electrons drifting in the gas under the combined influence of the electric and magnetic fields. If one assumes the average collision time between the electrons and the gas molecules is independent of the magnetic field, the drift velocity can be expressed analytically as a function of the magnetic field by the following:

$$V_r(r) = V_0(1 + (\omega_r\tau)^2)/(1 + (\omega\tau)^2), \qquad (2)$$

where V_0 is the drift velocity without magnetic filed, a quantity dependent on the gas properties and the electric field, and $\omega = |\omega|$ which depends on the gyration angular frequency for the electron circling in the magnetic field. The vector quantity $\omega = (\omega_r, \omega_T, \omega_Z) = (e/m)B$ denotes the gyration components: r in the radial direction of the wire, Z parallel to the wire, ant T is perpendicular to r and Z. The Lorentz angle θ is related to the magnetic field by the following relation:

$$\tan\theta = \omega\tau. \qquad (3)$$

By measuring:

- the drift velocity V_0 as a function of electric field for B=0
- the Lorentz angle to obtain $\omega\tau$

we can obtain the space-time function needed to correct for the Lorentz angle using eq. (1) above. Since the correction is small we need to know the B-field to only about 10%.

(a) Application in the Barrel Region:

The isochrons of the time-to-distance relation in the case of the B-field axial to the wire are circles concentric with the wire for the barrel case, or for the radial field component in the endcap. Hence the Lorentz angle correction in this case is independent of the angle of the muon incident to the plane of the muon chambers and is therefore especially simple. To study the influence of the magnetic field on V_r

in this case, a sample tube was operated in a 0.8 T magnetic field at MIT. The result is that for a typical gas (3:1 - argon-isobutane) the drift time is increased by about 8 ns out of about 250 ns for r=10 mm from the wire at B=0.8 T. This small change is easy to correct and has been shown not to degrade the resolution by more than 10 %.

(b) Application in the EndCaps:

In this case the ω_r term is not zero except in the case of normal incidence to the chamber plane. Letting ξ be the angle of incidence of the muon to an endcap chamber plane, we find that $\xi < 6.5^o$ and the term $\omega_r = (e/m)\, B_z \sin(\xi) < 25\%$ of the total Lorentz angle correction. In the off-line analysis the angle ξ will be reconstructed, and the more complicated electron trajectory calculated.

As a demonstration of this well-known correction, a cosmic ray experiment (PBAR) employed drift tubes in a 0.9T non-uniform field (30% variation) to precisely measure momentum. Fig. 6.1.1.1 shows the measured vs. calculated distance - time relation for the B-field parallel to the axis of the tube, and in Fig. 6.1.1.2 for the B-field perpendicular to the tube. Note that in both cases the measured distance-time relation agrees to within a few % of the calculated one. Hence the resolution should not be significantly degraded by this effect.

(6.1.2) Wire Sag

The present design of RDTs for the muon system is based on cylindrical Al tubes of various lengths up to about 4 meter long and 2.5 cm in diameter. The wires would be strung down the tube centers and would have their ends fixed at precision end-plates without using bridges. We have shown that allowing the wires to sag will be acceptable, even for 4 meter RDTs, and the wire position will be calculable to sufficient accuracy based on knowledge of the resonant frequency of the wire and the high voltage. It has also been shown that deviation of concentricity of the wire center from the tube center is at an acceptable level and that electrostatic instability will not be a problem.

Fig. 6.1.2.1 illustrates the basic components of a drift tube, and formulae for wire displacement due to gravity and electrostatic forces are also given. The critical voltage at which the electrostatic instability sets in, V(*critical*), is also given, which, for our application, is much larger than the voltage required for RDT operation.

Fig. 6.1.2.2 gives formulae for calculating the electrical field inside the drift tube, for the general case of a wire which is offset from the tube center. Using this formulae, it is possible to calculate tolerances acceptable for wire/tube a-concentricity (which contribute to tracking resolution errors due to deviation of the true space-time function from that assuming the wire and tube wall to be concentric). As examples, Fig. 6.1.2.3 shows the drift time error for the case of an offset of 1 mm, for a 2 cm

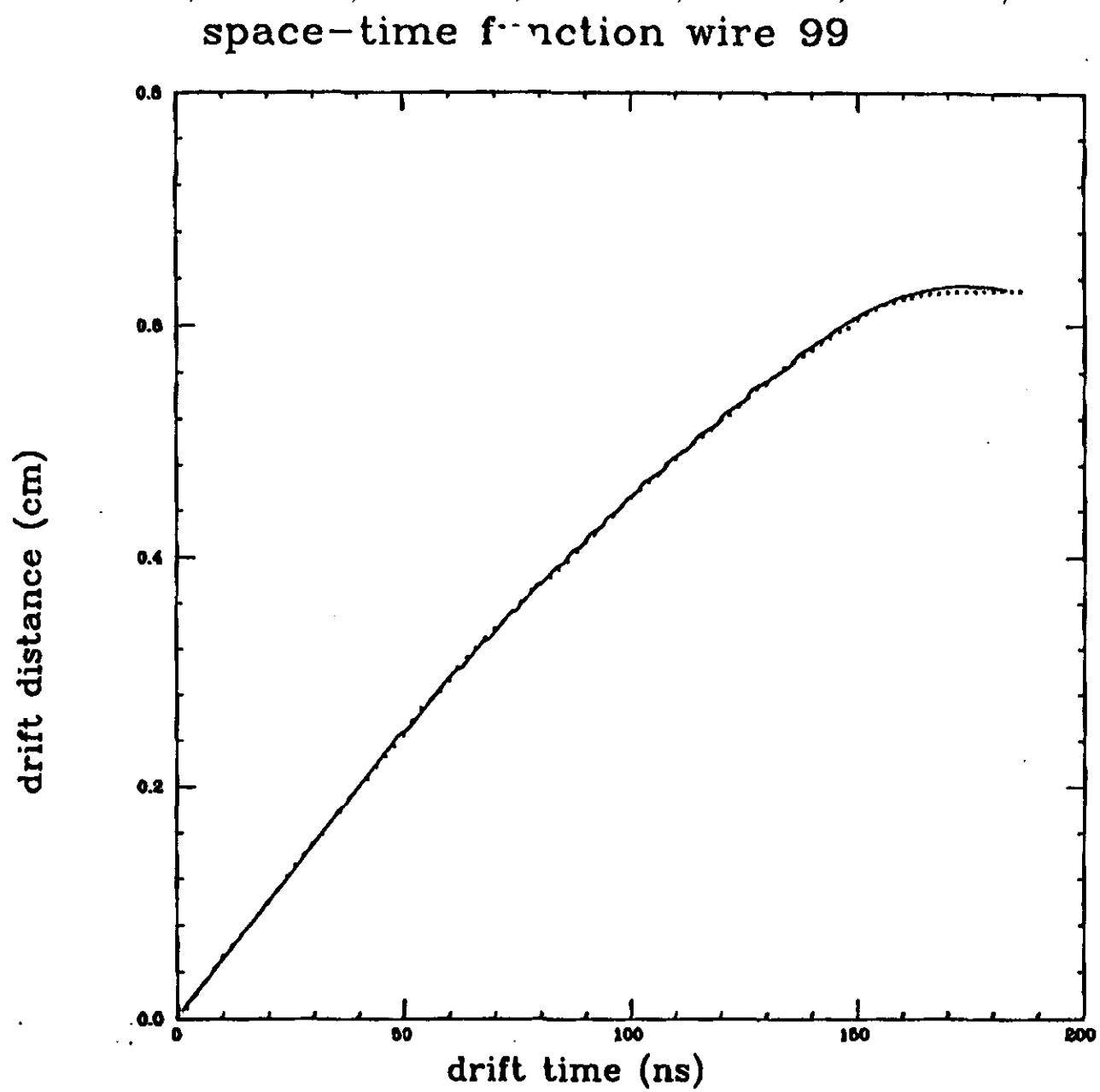

B 11 tube

Fig. 6.1.1.1

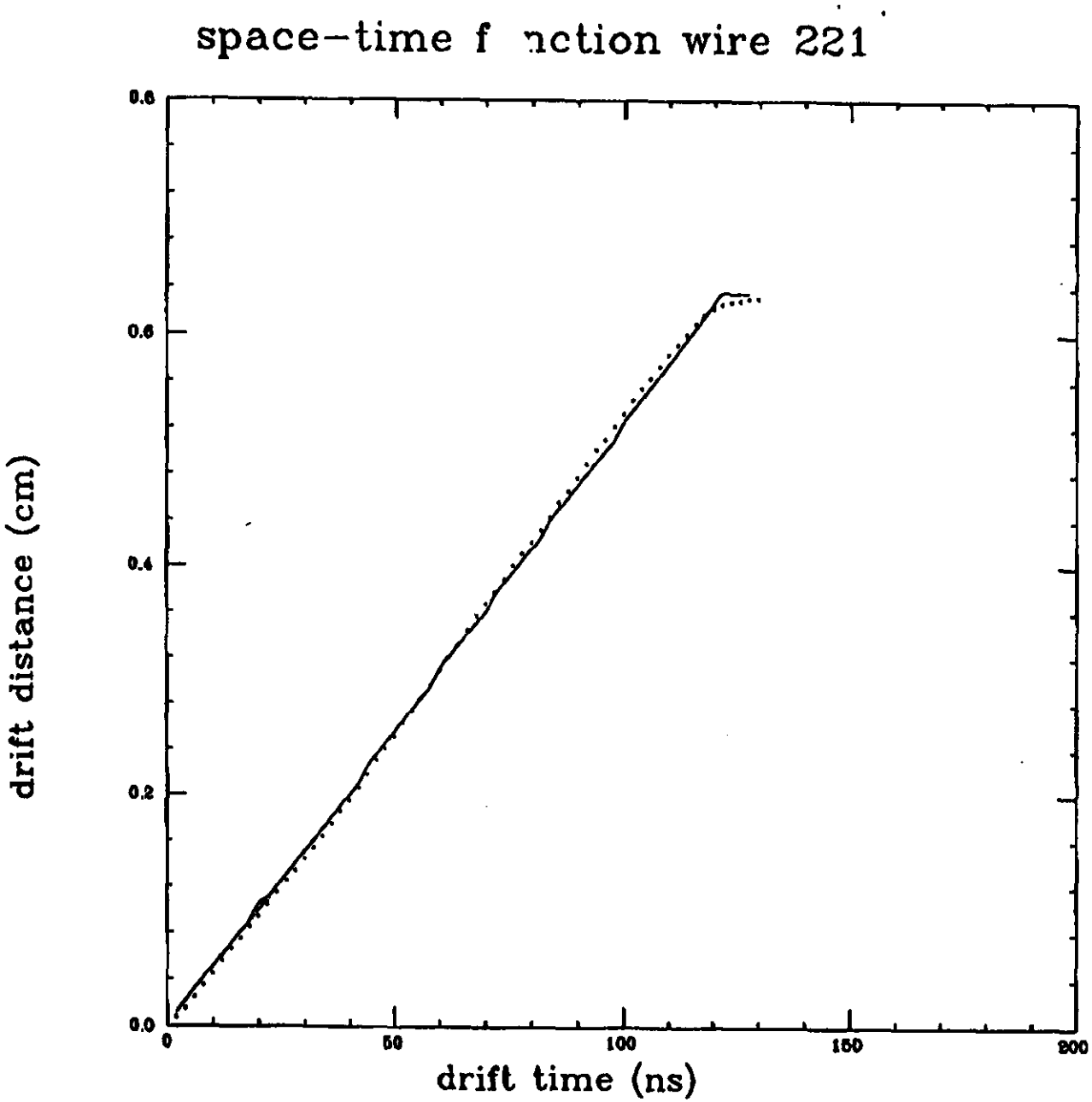

$\begin{cases} r_{offset} & 0.1 \\ t_{offset} & 20 \\ v_{fact} & 1.03 \end{cases}$

B ⊥ tube

Fig. 6.1.1.2

diameter tube and 25 micron wire, using the HRS gas (89% Ar, 10% CO_2, 1% CH_4) at 1atm and 2500 Volts. Fig. 6.1.2.4 shows the resulting tracking error. Fig. 6.1.2.5 shows the tracking error for a 0.5 mm offset, which amounts to an average error of less than 25 microns (since the error is random, and small compared to the 100 micron goal for single wire resolution, it is acceptable).

Another important parameter is the wire positioning accuracy based on knowledge of wire tension. The RDT technique requires that wire sag by an amount of about 250 microns be corrected for accurately to enable an overall single wire resolution of 100 micron or less. The tests done at Boston University are summarized in Fig. 6.1.2.6, which shows the set-up and the relevant formulae. The tension in the main length of the wire was determined from the fundamental resonant frequency, *f*. This was determined by passing a sinusoidal current of different frequencies through the wire in the presence of a magnetic field. The wire tension can be determined using the measured resonant frequency, and consequently the wire sag can be calculated (see Fig. 6.1.2.6 ; note that the sag can be determined solely from the resonant frequency). The calculated sags were compared with the actual sags measured with the microscope. Fig. 6.1.2.7 shows a comparison of the actual position of the wire with that determined through the frequency measurements for various wire tensions. Fig. 6.1.2.8 shows the differences of these numbers: a precision of the order of 5 microns is achievable. Fig. 6.1.2.9 shows the differences between the wire tensions T_1, T_2, and T3. Note that the wire tension is typically 10% lower than the weight, due to friction forces.

Fig. 6.1.2.10 shows the resonant frequency for the 7 different wire tensions. It is important to make sure that the vibration frequency spectra in the GEM experimental area are not such as to induce oscillations in the RDT wires. For comparison, it was observed at BU that large oscillation of the wires occurred at about 10 Hz, reflecting the dominant building vibration frequency there. Thus we expect no problems since the operation of drift tubes will occur at resonant frequencies of about 35 Hz. Fig. 6.1.2.11 shows the additional wire sag induced on a wire in a tube due to electrostatic forces. For 4kV for example, such sag is only of the order of 10 microns.

The Boston University group has participated in various accelerator and balloon-borne experiments using cylindrical drift tubes of various sizes and diameters. Among these, the HRS drift tube array, built 12 years ago, offered an excellent opportunity to study wire tension stability over a long period of time. The BU group was fortunate in being allowed to move one of the spare octants of HRS tubes (112 tubes, 3.5 m long, 2.54 cm diameter, 50 microns diameter wire) to Boston. They then used the technique described previously to measure tension. The results are shown in Fig. 6.1.2.12. Note that the wire tension, set for 250 g in 1980, varies typically by no more than several percent for all wires (average tension 248 g, standard deviation of 17 g, and a standard deviation of the wire sag of only 16 microns).

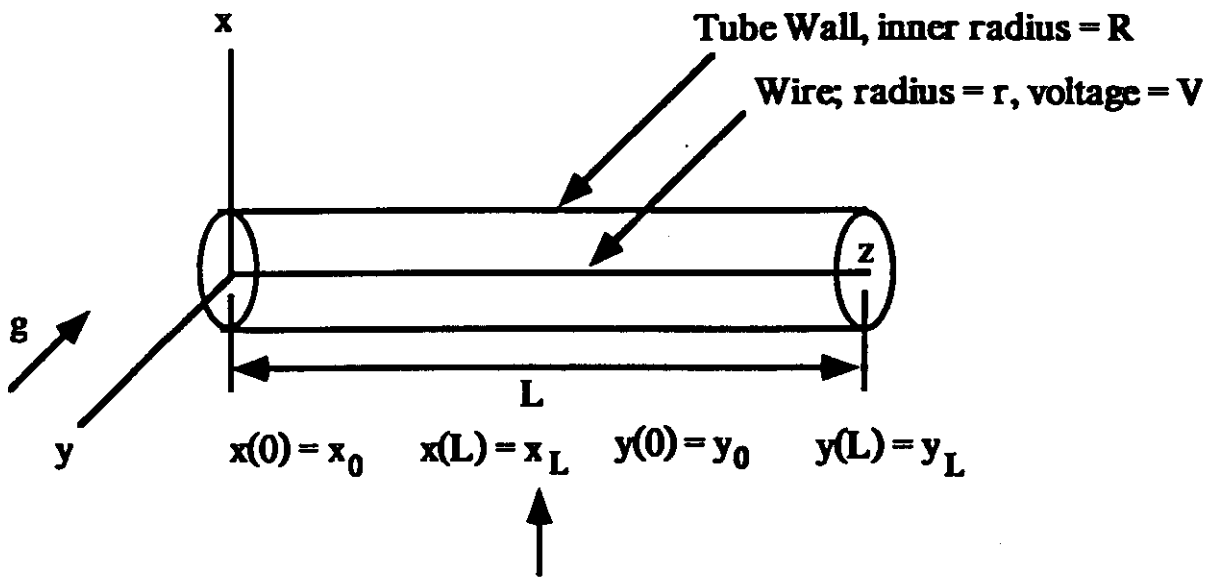

Coordinates of fixed ends of wire; tube center is along z axis

ρ = mass density of wire
T = tension of wire

$$K = 2\pi\varepsilon_0 V^2 / [R \ln(R/r)]^2$$

$$y_g = \rho \pi r^2 g / K$$

$$\omega^2 = K/T$$

$$\boxed{y(z) = (y_0 - y_g)\cos(\omega z) + y_g + [y_L + (y_g - y_0)\cos(\omega L) - y_g]\sin(\omega z)/\sin(\omega L)}$$

$$\boxed{x(z) = x_0 \cos(\omega z) + [x_L - x_0 \cos(\omega L)]\sin(\omega z)/\sin(\omega L)}$$

$$\boxed{V(\text{critical}) = 3611\ V\,(T/300\ g)^{0.5}\,(R/2\ \text{cm})\,(4\ m/L)\ln(R/r)}$$

Fig. 6.1.2.1

ELECTRIC FIELD IN DRIFT TUBE CAN BE EASILY CALCULATED PRECISELY

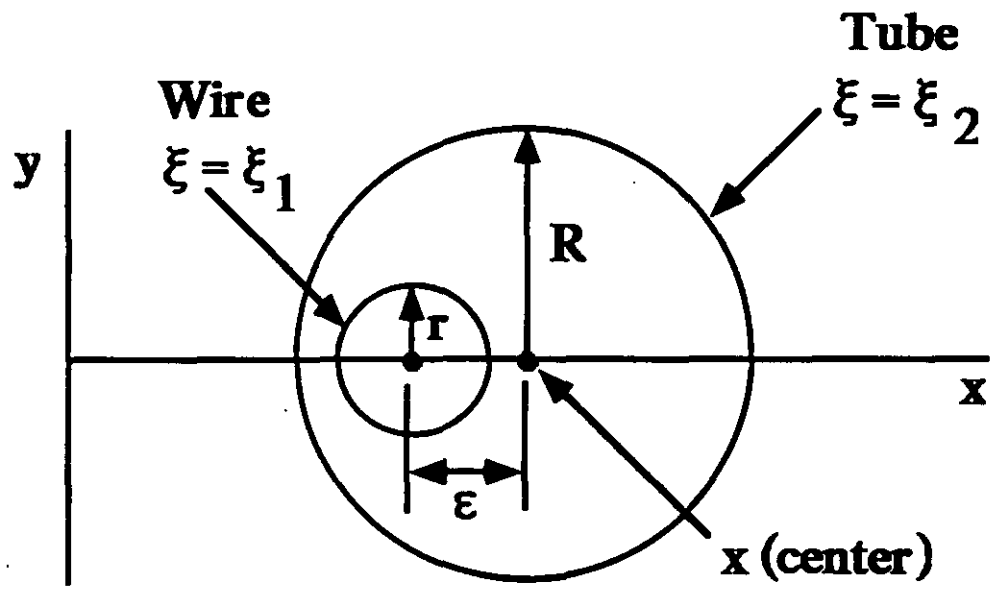

BIPOLAR COORDINATES

$$x = a \sinh(\xi) / (\cosh(\xi) + \cos(\theta))$$

$$y = a \sin(\theta) / (\cosh(\xi) + \cos(\theta))$$

$$\varepsilon = (R^2 + a^2)^{1/2} - (r^2 + a^2)^{1/2}$$

$$x\,(\text{center}) = a \coth(\xi_1)$$

$$r = a / \sinh(\xi_1)$$

$$R = a / \sinh(\xi_2)$$

$$E_x = -V (\cos(\theta) \cosh(\xi) + 1) / [a (\xi_1 - \xi_2)]$$

$$E_y = V (\sin(\theta) \sinh(\xi)) / [a (\xi_1 - \xi_2)]$$

Fig. 6.1.2.2

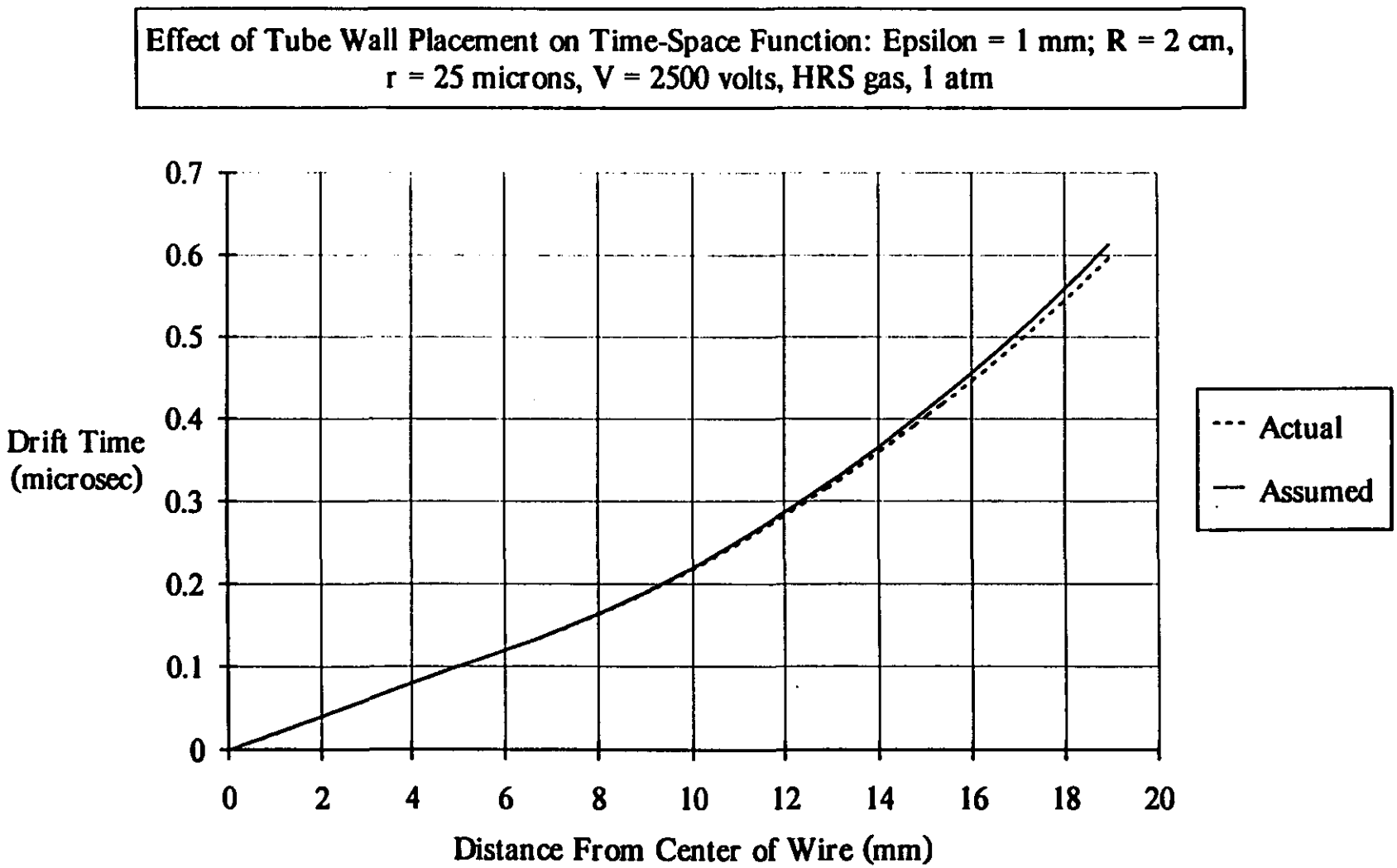
Effect of Tube Wall Placement on Time-Space Function: Epsilon = 1 mm; R = 2 cm, r = 25 microns, V = 2500 volts, HRS gas, 1 atm
Drift Time (microsec)
0.7
0.6
0.5
0.4
0.3
0.2
0.1
0
0
2
4
6
8
10
12
14
16
18
20
Distance From Center of Wire (mm)
Actual
Assumed

Fig. 6.1.2.3

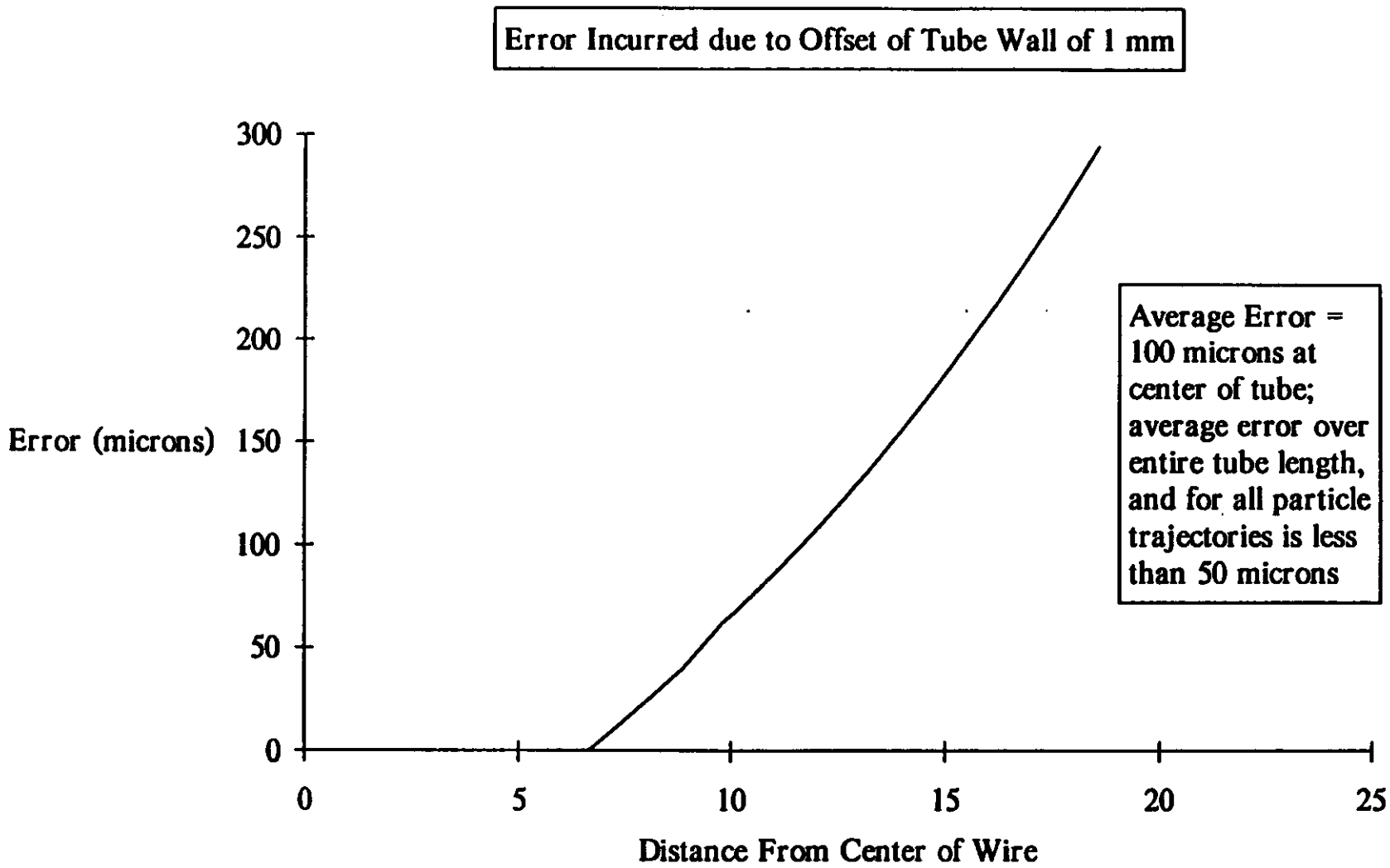
Error Incurred due to Offset of Tube Wall of 1 mm
Error (microns)
300
250
200
150
100
50
0
0
5
10
15
20
25
Distance From Center of Wire
Average Error = 100 microns at center of tube; average error over entire tube length, and for all particle trajectories is less than 50 microns

Fig. 6.1.2.4

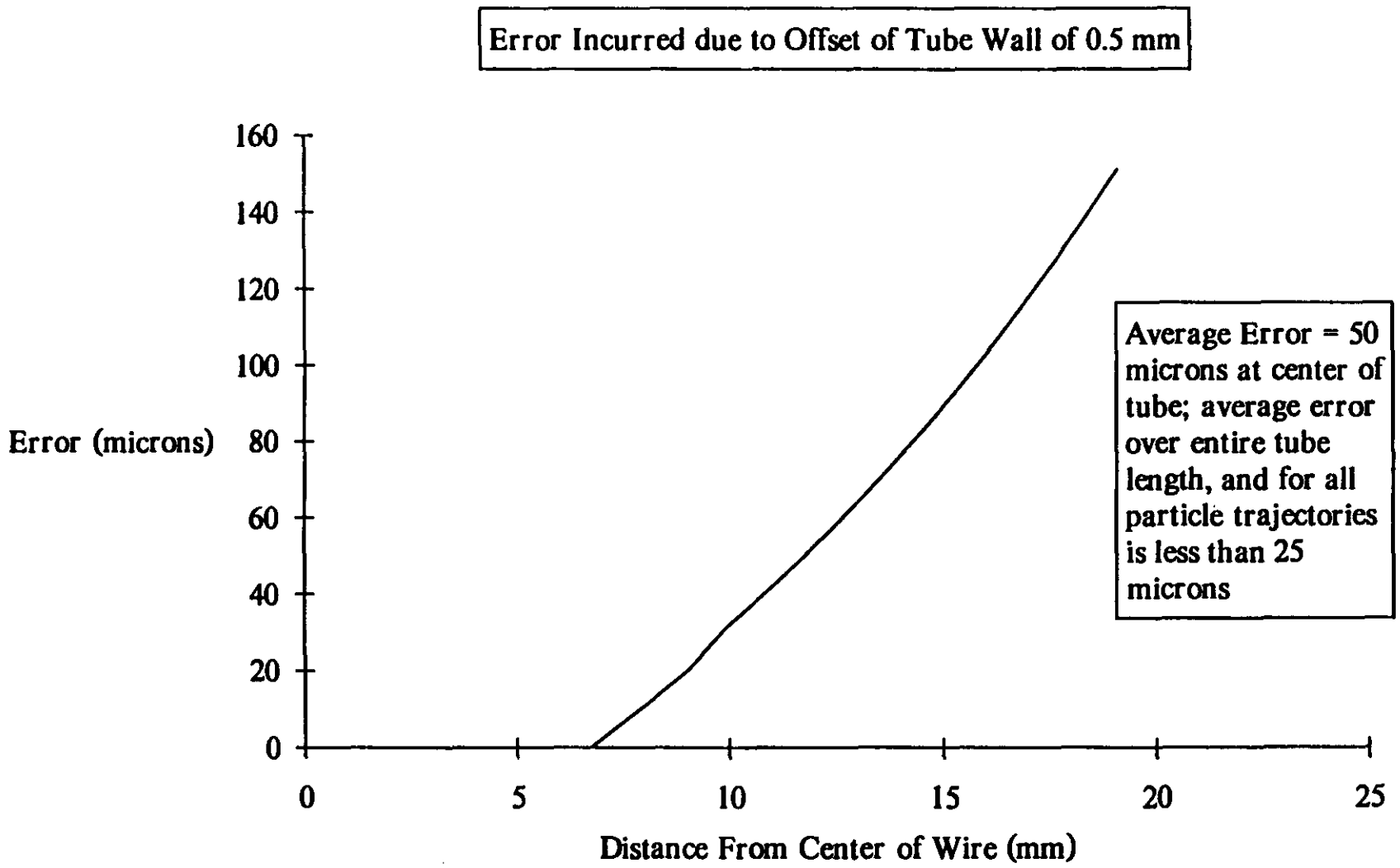
Error Incurred due to Offset of Tube Wall of 0.5 mm
Error (microns)
160
140
120
100
80
60
40
20
0
0
5
10
15
20
25
Distance From Center of Wire (mm)
Average Error = 50 microns at center of tube; average error over entire tube length, and for all particle trajectories is less than 25 microns

Fig. 6.1.2.5

Wire Tests

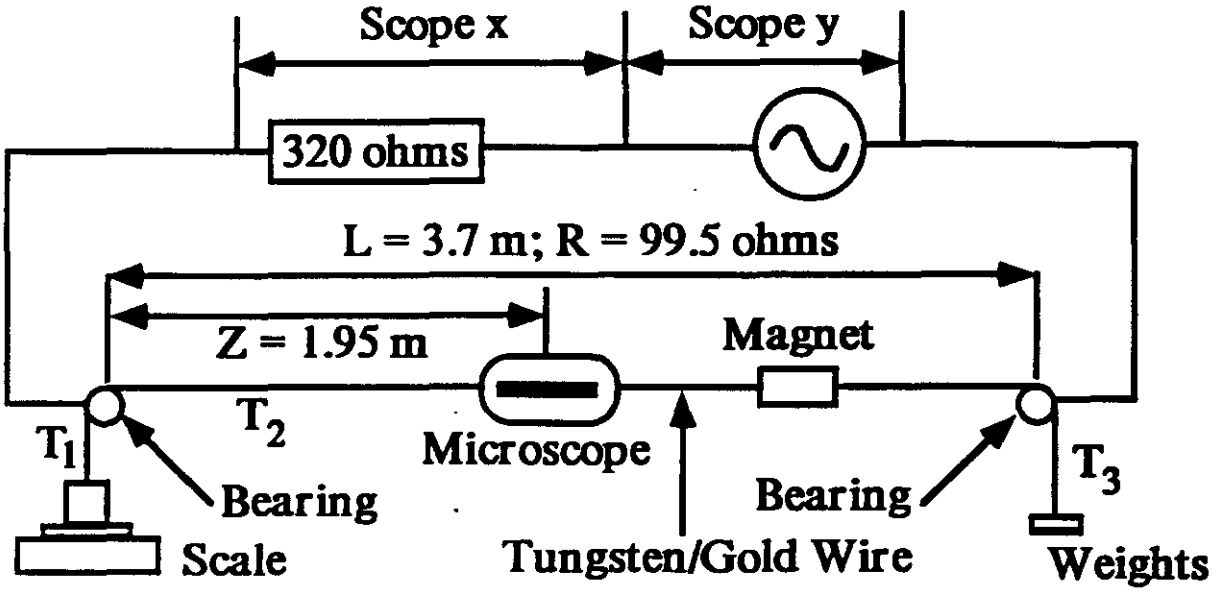

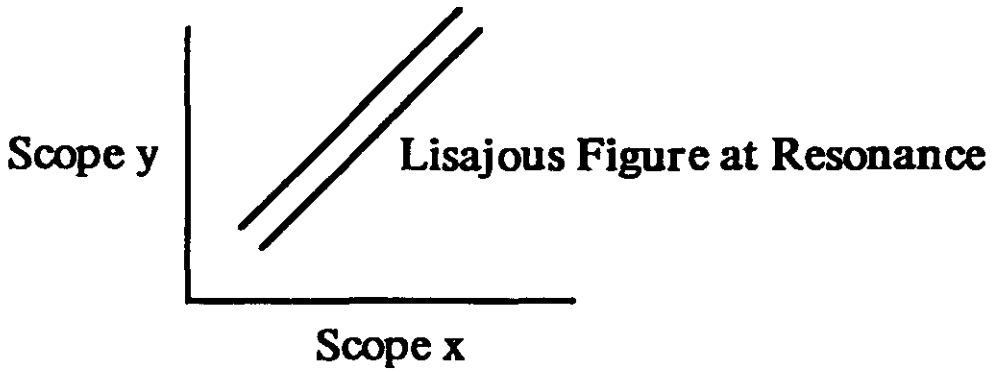

R = 99.5 ohms implies diameter = 2r = 49.6 microns (70 F)

S = wire sag
ρ = mass density = 19.3 g/cc (gold and tungsten)
g = gravitational acceleration
f = fundamental resonant frequency
T = tension in wire

$$T = \rho\pi r^2(2Lf)^2$$

$$\boxed{S = \rho\pi r^2 g(Z^2 - LZ)/(2T) = g((Z/L)^2 - (Z/L))/(8f^2)}$$

NOTE: S depends on f only, and has no additional dependence on T or r

Fig. 6.1.2.6

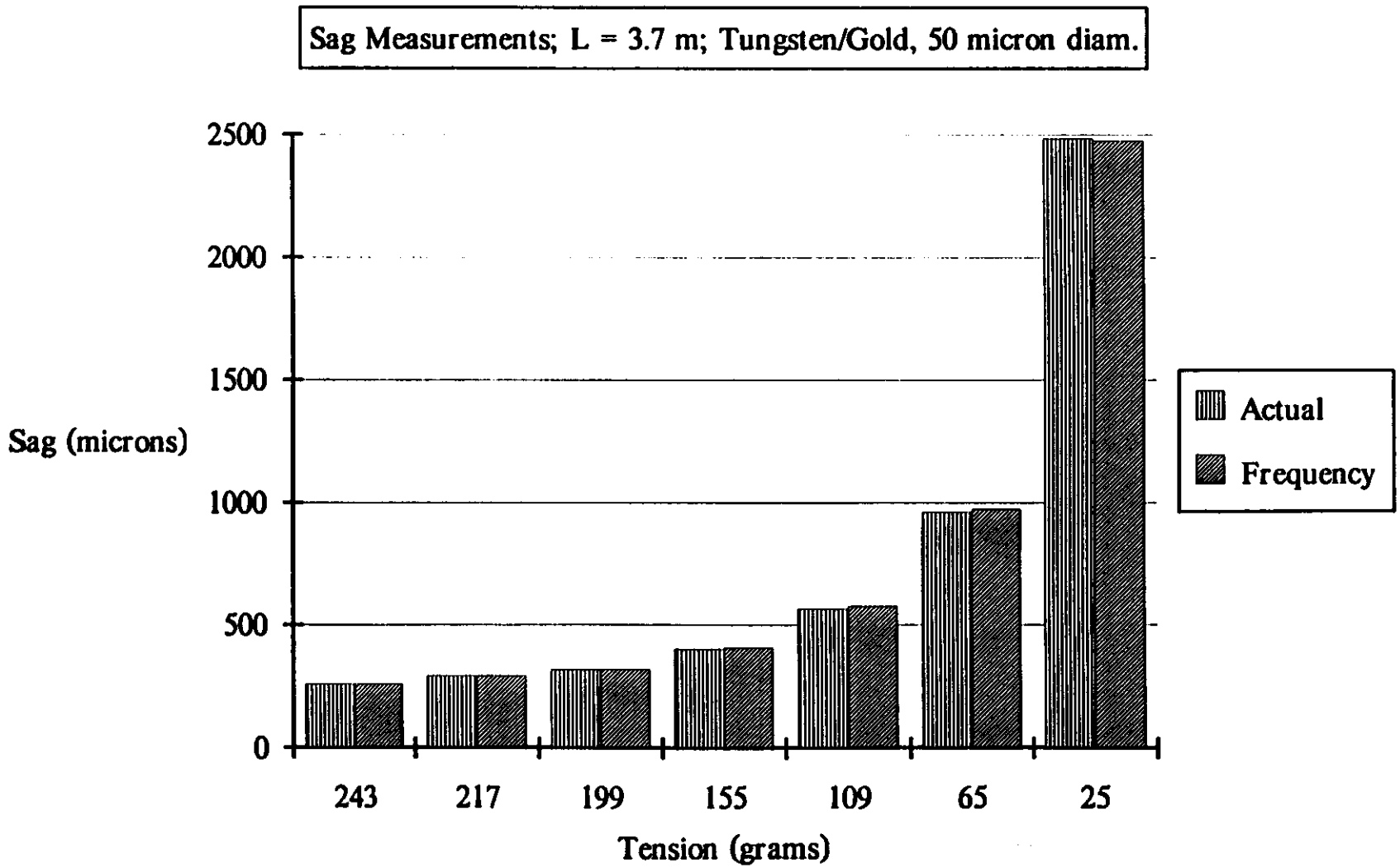
Sag Measurements; L = 3.7 m; Tungsten/Gold, 50 micron diam.
Sag (microns)
2500
2000
1500
1000
500
0
243
217
199
155
109
65
25
Tension (grams)
Actual
Frequency

Fig. 6.1.2.7

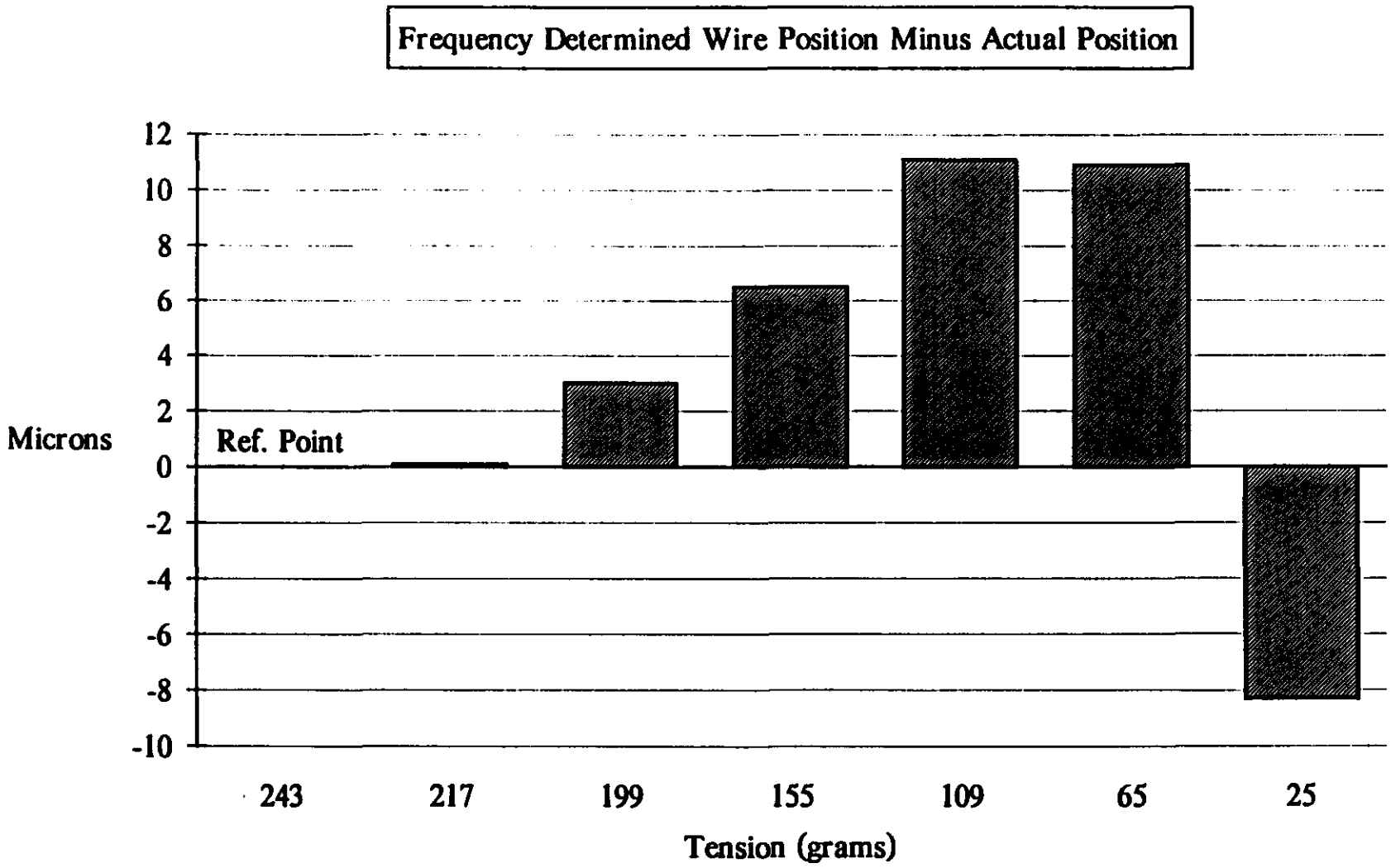
Frequency Determined Wire Position Minus Actual Position
Microns
12
10
8
6
4
2
0
-2
-4
-6
-8
-10
Ref. Point
243
217
199
155
109
65
25
Tension (grams)

Fig. 6.1.2.8

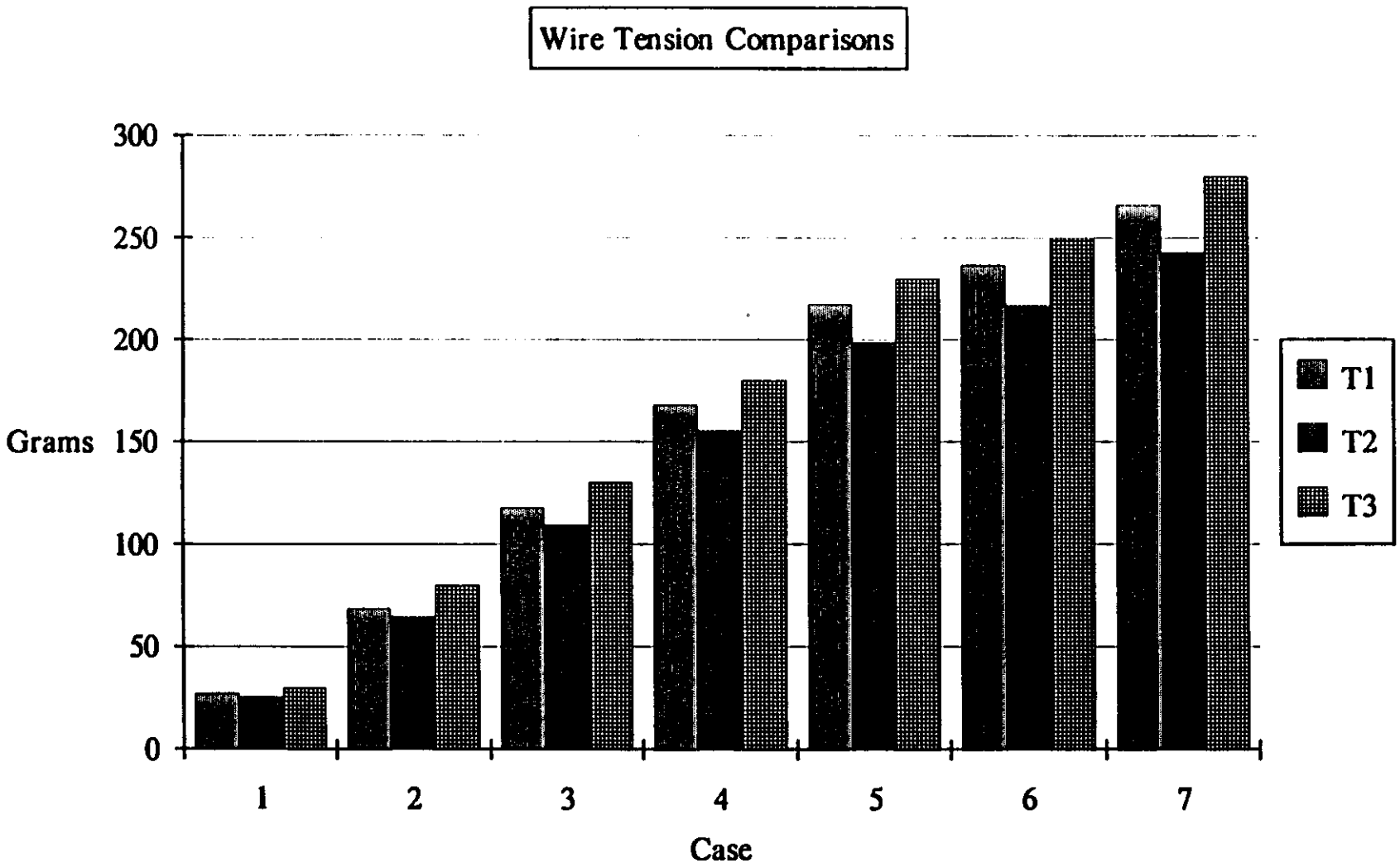
Wire Tension Comparisons
300
250
200
150
100
50
0
Grams
1
2
3
4
5
6
7
Case
T1
T2
T3

Fig. 6.1.2.9

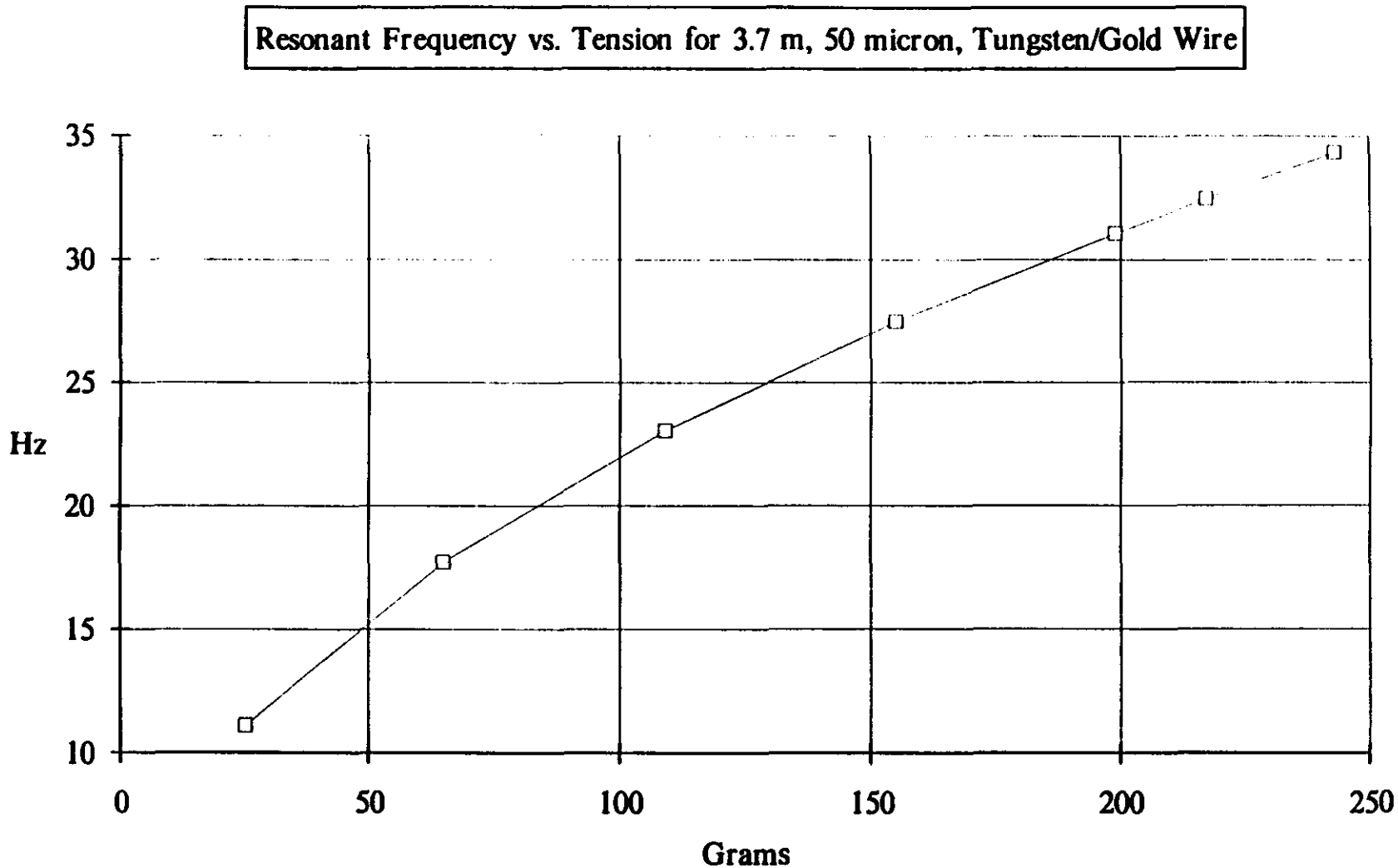
Resonant Frequency vs. Tension for 3.7 m, 50 micron, Tungsten/Gold Wire
35
30
25
20
15
10
Hz
0
50
100
150
200
250
Grams

Fig. 6.1.2.10

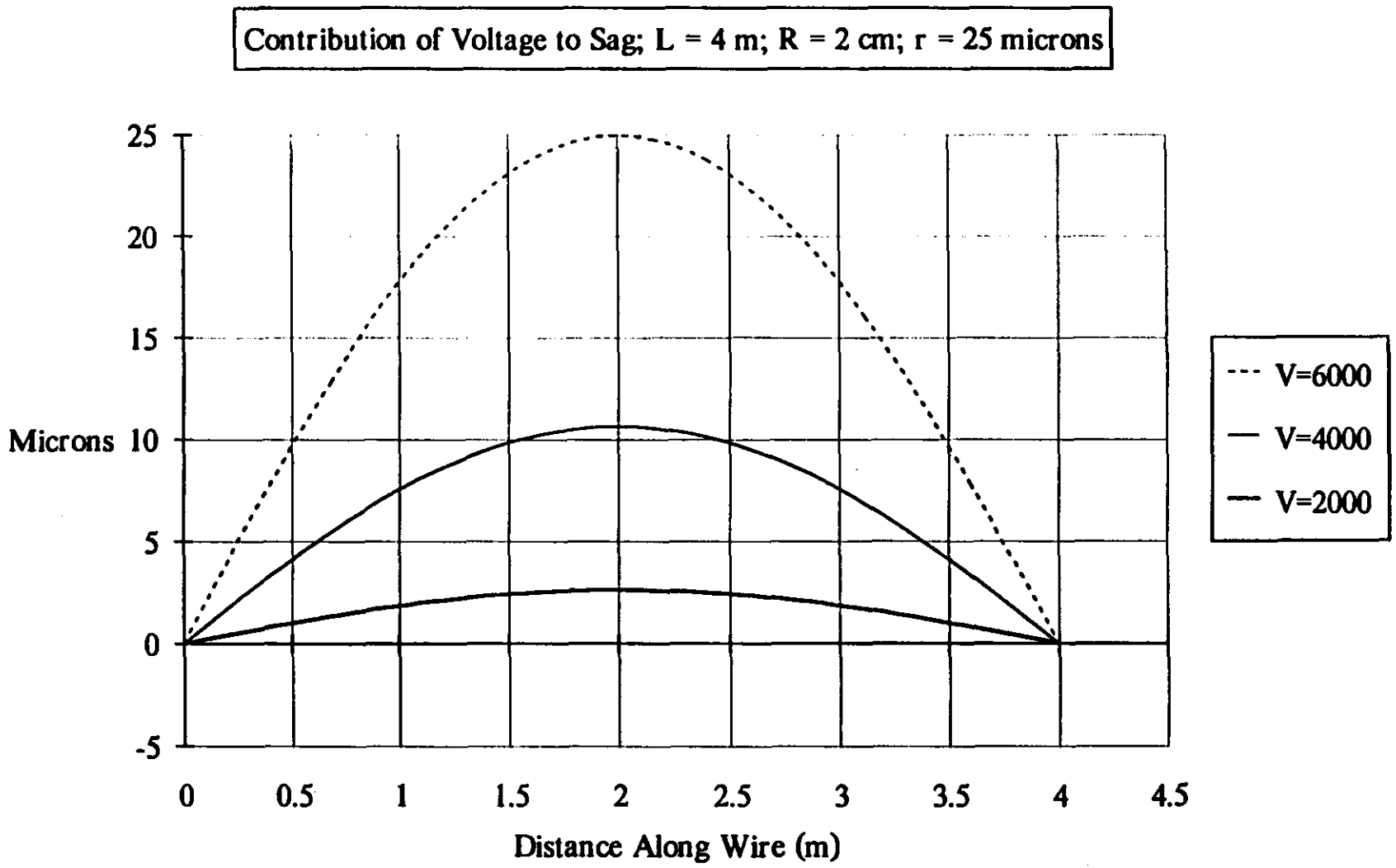
Contribution of Voltage to Sag; L = 4 m; R = 2 cm; r = 25 microns
Microns
25
20
15
10
5
0
-5
0
0.5
1
1.5
2
2.5
3
3.5
4
4.5
Distance Along Wire (m)
V=6000
V=4000
V=2000

Fig. 6.1.2.11

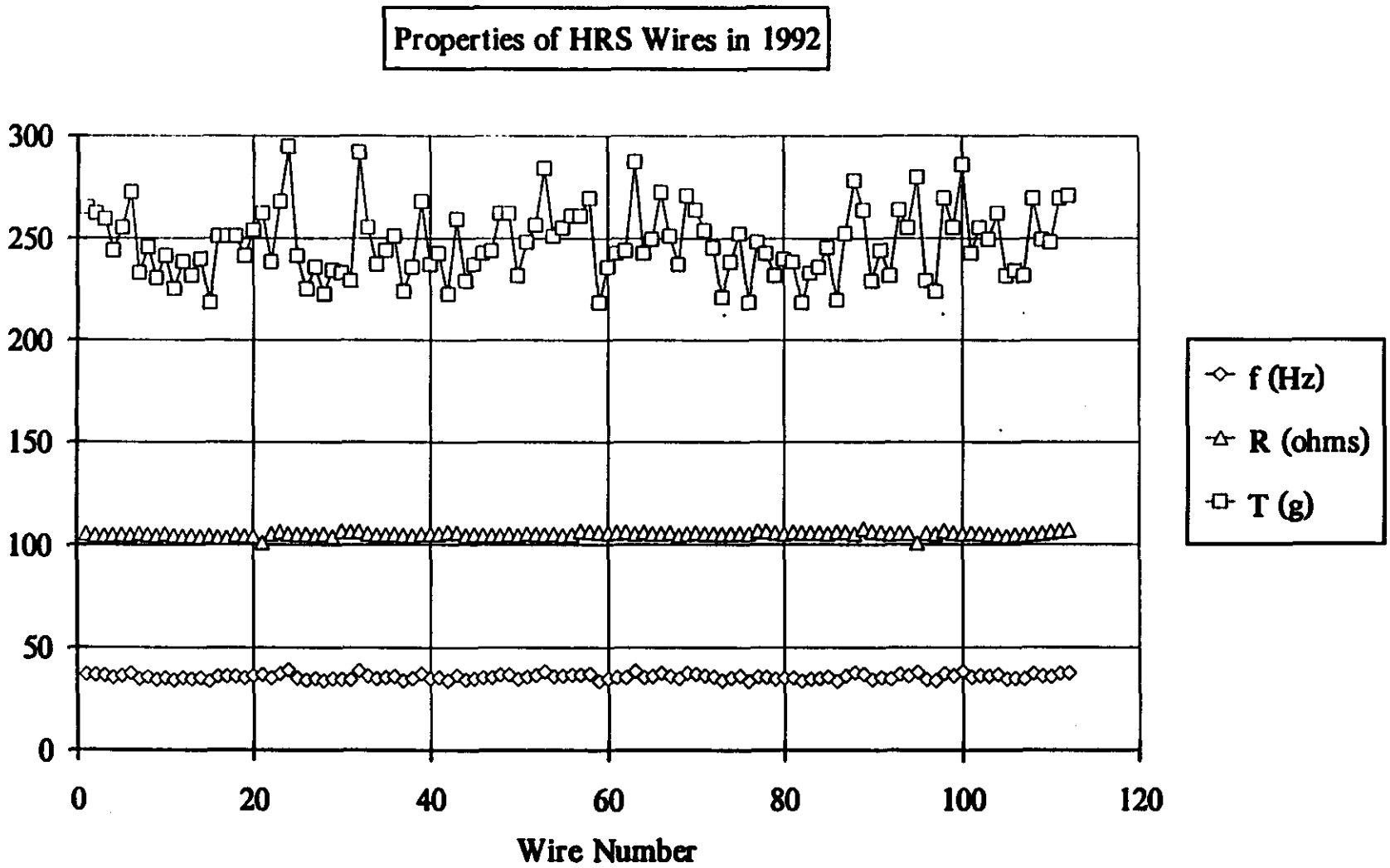
Properties of HRS Wires in 1992
300
250
200
150
100
50
0
0
20
40
60
80
100
120
Wire Number
f (Hz)
R (ohms)
T (g)

Fig. 6.1.2.12

(6.2) Tests of the RPC Technology:

The R&D program had the goal of a complete understanding of the operation and applicability of RPCs to the GEM Muon System. R&D has focused on studying the existing state-of-the-art as exemplified by the standard Italian design already described, as well as new RPCs using non-standard materials and fabrication methods, with an emphasis on reduced mass, stability and long term performance, and increased rate capability.

1. Standard Italian and Glass RPC Performance

MIT and LLNL have now studied a number of different RPC designs, including a 1 m x 2 m RPC provided by R. Santonico of the University of Rome, glass RPCs, cermet thin film RPCs and RPCs using a number of low resistivity materials such as static-dispersive plastics. Extensive testing of the Italian RPC, a custom built glass RPC, and, very recently, a plastic RPC, has been carried out at MIT, including measurements of efficiency, rise-time jitter, and response to neutrons, and the results of some of these tests are detailed in Appendix A. LLNL has also performed similar measurements on smaller glass RPCs.

In summary, the MIT and LLNL glass RPCs (resistivity = 5×10^{12} ohm-cm), with their relatively high bulk resistivity, exhibit a reduced rate handling capability and a reduced efficiency (70% for the MIT RPC with 2 mm glass and 90% for the LLNL RPC with 750 micron glass). The Italian Bakelite RPC (resistivity = $1\text{-}2 \times 10^{11}$ ohm-cm) exhibits about 95% efficiency using cosmic rays and a scintillator telescope for triggering. The Italian RPC has a measured saturated counting rate of about 560 Hz/cm^2 compared to a rate of about 50 Hz/cm^2 for the MIT glass RPC (75 Hz/cm^2 for the LLNL glass RPC). On the other hand, these different RPCs agree remarkably well in terms of pulse characteristics, e.g., pulse height, pulse width, rise time and pulse velocity along the strip.

2. Trigger Jitter

Trigger jitter measurements on the Italian RPC show time jitter on the order of 1 ns. The MIT glass RPC exhibits a larger jitter of about 7 ns due to the inability to achieve an adequate high voltage across the gas gap as detailed in Appendix A. Trigger jitter measurements have also been performed on plastic RPCs using strontium-90 betas (2.3 MeV endpoint energy). For a 6 cm x 6 cm RPC the jitter was measured to be 5 ns.

3. Neutron Sensitivity

Neutron sensitivity measurements were made using a strong Cf-252 source. The sensitivity of the RPC to 1-10 MeV neutrons is measured to be 4.8×10^{-3} and to 1-10 MeV photons to be 6.6×10^{-3}.

4. Alternative RPC Materials for High Rate RPCs

RPCs have been fabricated at LLNL using sputtered resistive cermet thin films on thin glass or plastic substrates. We have demonstrated that Cermets can function as RPCs, however the long term aging characteristics of these thin films is not clear. Indications are that the films are not strongly bonded to the substrate and are subject to sputtering effects because of ion bombardment. Alternative materials to Bakelites have been explored, concentrating on static-dispersive plastics with low bulk resistivities in the range 10^8 - 10^{11} ohm-cm. We have successfully demonstrated RPCs with a number of different plastics. Five 0.5 m x 0.5 m RPCs, and one 1.2 m x 2.4 m RPC have been built using low resistivity plastic materials. All RPCs are single dimension read-out with 1.3 cm strips, and one of the small RPCs, is built with 2 dimensional read-out. Table 6.2.1 summarizes the properties of

Table 6.2.1
RPC Resistive Materials Properties

Material	Thickness (cm)	Bulk Resistivity (W-cm)	Arc Resistivity (W-cm^2)
MIT mirror glass	0.300	5.00×10^{12}	1.50×10^{12}
LLNL mirror glass	0.066	4.90×10^{12}	3.23×10^{11}
Kodak projector glass	0.123	6.42×10^{11}	7.89×10^{10}
Italian RPC Bakelite	0.200	1.00×10^{11}	2.00×10^{10}
LLNL Bakelite	0.161	4.50×10^{9}	7.24 x 108
Abstat-M310 plastic	0.072	5.78×10^{9}	4.16×10^{8}
Abstat-M310 plastic	0.060	5.78×10^{9}	3.47×10^{8}
MiTech-411 plastic	0.090	2.03×10^{9}	1.83×10^{8}
MiTech-411 plastic	0.030	2.03×10^{9}	6.19×10^{7}
Corning 0211 glass	0.056	6.70×10^{7}	3.75×10^{6}
Boron film	0.0001	1.00×10^{6}	1.00×10^{2}

a number of materials used to make RPCs, including Bakelites and glasses.

We have measured the saturated counting rates from two different static-dispersive plastics, MiTech-411 and Abstat-M310. For the case of the MiTech-411 plastic, our SPICE model predicts a saturated counting rate capability of about 2.3×10^4 Hz/cm^2. We have assembled a number of RPCs with this material and in fact measure a count rate of approximately 1.5×10^4 Hz/cm^2. Fig. 6.2.1 plots the counting rate versus high voltage for an RPC made with MiTech-411 plastic. This rate has not been determined to be saturated and further work is in progress to determine the absolute saturated count rate of the RPC with this very interesting material.

This count rate is substantially larger than any other RPC materials measured to date, and constitutes a significant improvement in the state of the art. In addition,

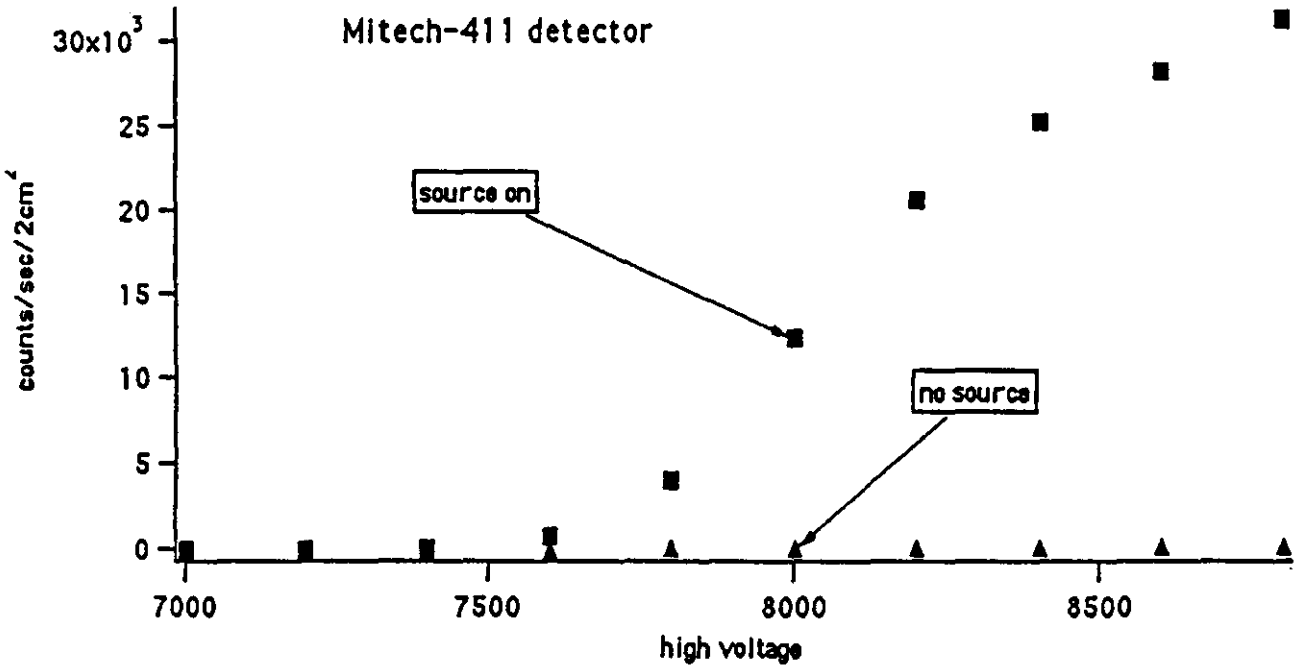
Mitech-411 detector
30x10^3
25
20
15
10
5
0
counts/sec/2cm^2
source on
no source
7000
7500
8000
8500
high voltage

Fig. 6.2.1

the Abstat M310 plastic has a significantly higher dielectric strength than the PVC-based MiTech-411 plastic. Large area RPCs have been constructed using thinner plastic sheets than those used initially (500 microns versus 720 microns), which could potentially give an increase of 5 - 10 times the rate of the earlier versions of the plastic RPCs. Measurements of efficiency of large area plastic RPCs show that they operate at or near the full geometric efficiency expected, about 98%. Also, systematic studies of gas mixtures on RPC performance (plateau voltage, efficiency, noise, pulse height, etc.) have been performed for large area plastic RPCs.

5. Lifetime Testing of the Italian RPC

Lifetime (aging) tests have also been performed using the Italian 1 m x 2 m Bakelite RPC. We chose an area of this RPC approximately 5 cm x 10 cm which was irradiated with a radioactive source. The counting rate on this area was approximately 250 Hz/cm^2. We placed a cosmic ray scintillation counter telescope which had approximately the same 5 cm x 10 cm area over the chosen area of the RPC. We chose the RPC region so that one of the PVC spacers was contained in the area.

We define one SSC year (at a luminosity of 10^{33}) to be 2×10^7 counts per square centimeter. This is the expected neutron interaction rate at the 10^{33} luminosity. We accumulated 16.4×10^7 counts per square centimeter in our test, which is equivalent to 8.2 SSC standard years. The data is shown in Fig. 6.2.2.

Before irradiation the chosen area had an efficiency of $93.6 \pm 3\%$. The fact that the measured efficiency is not about 97% is a reflection of the mismatch between the cosmic ray hodoscope and the RPC area. After an irradiation equivalent to 8.2 SSC years of operation, we measured the efficiency of this area to be $92.4 \pm 3\%$. As can be seen from Fig. 6.2.2, within the 3% errors, we find no change in efficiency for the equivalent 8.2 SSC year exposure at a luminosity of 10^{33}.

6. Measurements of RPC-induced Noise on RDT Systems

A number of measurements of RDT sensitivity to RPC signals have been made at the Texas Test Rig (TTR) at SSCL. Measurements have been made using both the Italian 1m x 2m RPC installed in the TTR and 0.5 m x 0.5 m plastic RPCs. Both MSU (4 cm diameter) and Dubna (2.5 cm diameter) RDT systems have been measured as well as the UH cathode strip chambers. Measurements of signals induced on RDT wires were made by examining the signals off the wires on an oscilloscope while triggering on RPC signals. The MSU RDT system contained amplifiers with x1000 gain, whereas the Dubna RDT system was unamplified. The RPC was placed approximately 1 m, and 2 m from the MSU and Dubna RDTs, respectively. Under these conditions, no induced signals were observed at a level of 5 microvolts and 2 millivolts for the MSU and Dubna RDTs, respectively. Also, no induced signals were observed on the UH CSC system at a level of 5 microvolts.

Fig. [illegible].2

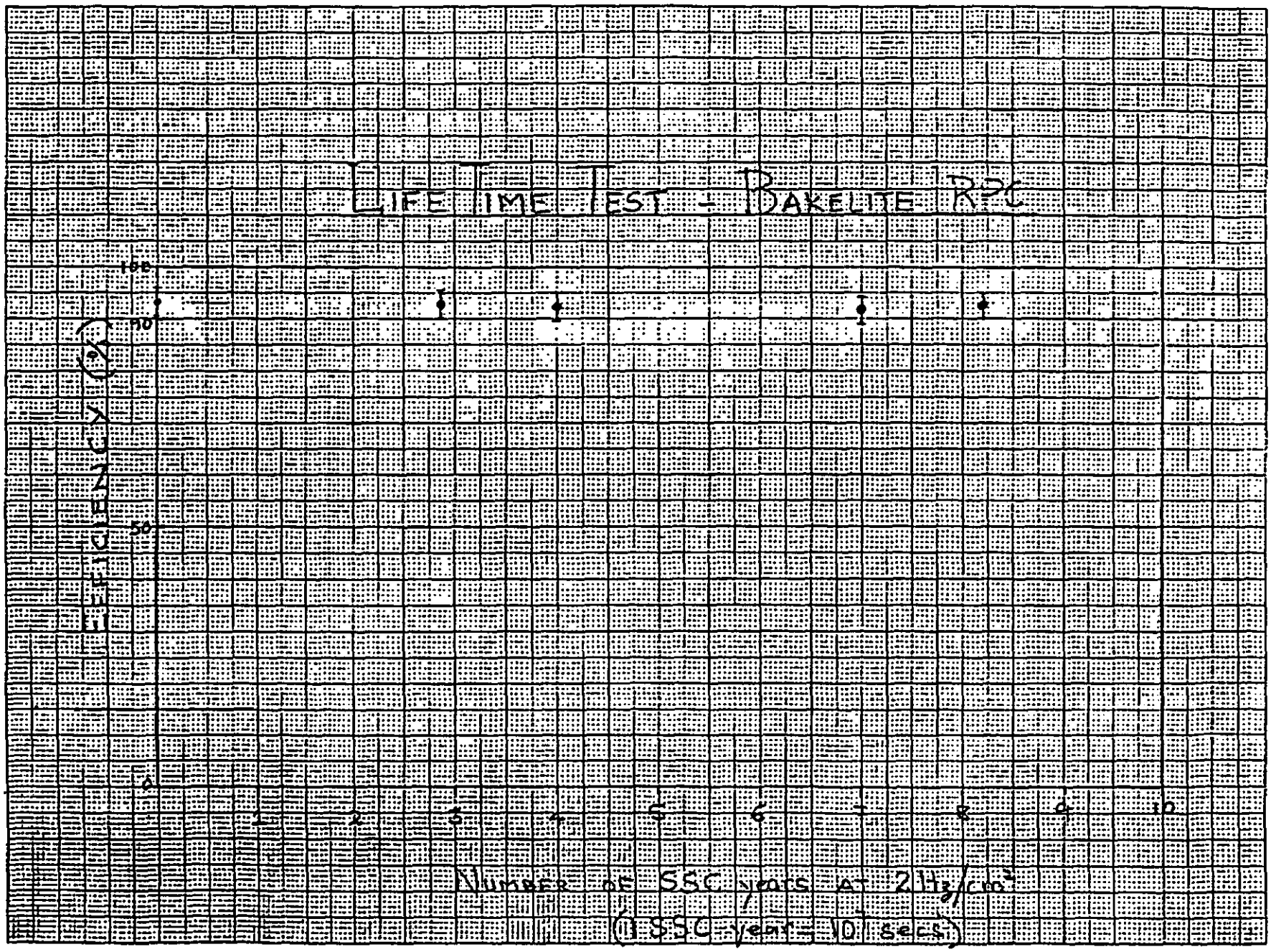
LIFE TIME TEST - BAKELITE RPC
EFFICIENCY (%)
100
90
50
10
1
2
3
4
5
6
7
8
9
10
Number of SSC years at 2Hz/cm²
(1 SSC year = 10⁷ secs)

Another measurement was made by measuring the effect of RPC operation on RDT singles rates. In the case of the MSU RDTs, no increase in singles rate was observed for either the Italian RPC or the LLNL RPC as these RPCs had their voltages increased. In this case the singles rates of the RPCs increased by three and five orders of magnitude, respectively, as their voltages were increased from 6 kV to 8 kV. Similar measurements were made for the Dubna RDT and the UH CSC for the Italian RPC only. Again, no increase in singles rates were observed for a wide range of RPC operating voltages.

(7.0) Pipeline Muon Trigger based on RPCs

The basis for the proposed muon trigger is the resistive plate technology. The properties of this technology are:

1. Pulse rise time jitter ≤ 1.4 nanoseconds.
2. Pulse full width, half height ≤ 20 nanoseconds.
3. Pulse height @ 500 millivolts into 50 ohms.

A PWC instrumented with the same segmentation will provide a trigger in essentially the same manner.

II. SIMPLIFIED LOGIC FOR THE BARREL TRIGGER

A. Introduction

The barrel trigger is based on 250 megahertz shift register logic. One can adjust cable lengths and gate widths so that all relevant signals from the non-bend strips and the bend strips can be loaded synchronously into shift registers. The outputs of these shift resistors can be put into simple logic to form the trigger and beam crossing tag. The trigger is formed in 100 nanoseconds. At a neutron flux of 10^5 Hertz per square centimeter per second the accidental trigger rate in the barrel is about 29 Hertz. In the end cap the accidental rate is even less. The dead time is about 6% for a gate width of 100 nanoseconds.

Geometry of an RPC Barrel Plane

In Fig. 7.0.1 is the typical X and Y strip lay out. The crucial thing to note is that a hit anywhere on the plane generates signals on an X strip and Y strip that arrive at the collection point in coincidence. Another point to note is that half the bend plane strips are in coincidence with the lower half of the non-bend plane strips while the other half of the bend plane strips are in coincidence with the upper half of the non-bend plane strips. This division has two virtues, the first it reduces the time resolution in tagging the beam crossing by about a factor two and it also reduces the ambiguity of double hits by a factor two. Note that this is achieved without increasing the electronic channel count. These points will be discussed in detail in later sections of this paper.

It should be noted that each RPC super layer consists of three identical RPC counters with the requirement that two out of three strips fire when a track passes through the super layer. This increases the low rate efficiency of the RPC trigger system from about 90% to essentially 97% without increasing the electronic channel count. It does, however, increase the total number of signal cables and electronic inputs. This is discussed in detail in Appendix B.

B. Geometry of an RPC Sector

Fig. 7.0.2 is a simplified sketch of the three RPC super layer chambers that form an RPC sector.

As can be seen from Fig. 7.0.2, there is an outer RPC super layer which we will label SL3, a central RPC super layer which we will label SL2, and an inner RPC super layer which we will label SL1 in accordance with the GEM Base Line 1 notation.

The non-bend strips form projective towers with respect to the interaction point. The non-bend plane strip widths are:

SL1 (A and B)	= 3.9 cm
SL2 (A and B)	= 6.5 cm
SL3 (A and B)	= 8.9 cm

The number of non-bend plane chambers per sector are given below:

Non-bend plane channel count:

SL1	= 166 channels
SL2	= 166 channels
SL3	= 166 channels

All bend plane strips are each 1.3 cm wide. The number of bend plane strips per sector are given below:

Bend plane channel count:

SL1	= 345 channels
SL2	= 552 channels
SL3	= 762 channels

The total number of electronic channels we have for each sector is:

Non-bend plane	= 498 electronic channels
Bend plane	= 1659 electronic channels

As we stated above, note, that we have more cables and connectors than we have electronic channels.

The total number of electronic channels is 69,024.

C. Simplified Trigger and Beam Crossing Logic

The bend plane logic for the barrel is the most difficult to work out. Hence we will discuss this case first. It can be shown that with proper choice of cable lengths

between SL1 and SL3; and SL2 and SL3, corresponding strips in the three super layers can be placed in coincidence using predetermined delays as inputs to the shift registers. This is discussed in Appendix B.

The proposed trigger is a three layer trigger. Due to the multiple scattering in the calorimeter, a number of possibilities must be considered. Fig. 7.0.3 illustrates this.

For each pair of strips in SL3 and SL1 there is a range of strips in SL2 that determine the momentum of the track.

For a given strip in SL3 and a given strip in SL1 there is a shift register logic for forming a trigger.

A trigger can be formed under computer control. The trigger momentum for each strip in SL3 that forms a trigger is chosen by which strips in SL1 are selected, and then for each selected strip in SL1 which strips in SL2 are selected. Fig. 7.0.4 illustrates the situation for a 20 GeV/c track.

As a specific example we consider a trigger for momentum greater than 30 GeV/c. In this case, for each sign of charge, three strips in SL1 must be selected for each strip in SL3. In addition, for each strip selected in SL3, two strips must be selected for SL2. If we consider both possible charges, then we activate six similar sets of shift register logic. We define the following symbols:

SL3i	The strip in super layer three that has been struck
SL1j (j = 1 to 6)	The strip in super layer one that has been struck. The six possible strips are determined by the 30 GeV/c sagitta at super layer 1 with respect to an infinite momentum track that passes through SL3i and the interaction point and the multiple scattering due to a 30 GeV/c muon passing through the calorimeter.
SL2k (k = 1 to 3)	The strip in super layer two that has been struck. The three strips are determined by the 30 GeV/c sagitta at super layer 2 with respect to an infinite momentum track that passes through strips SL3i and SL1j.

The shift register logic for this situation is shown in Fig. 7.0.4.

Every four nanoseconds the first eight shift registers are loaded with the eight bit address of strip SL3i. The next shift register is the input of SL3i, which we have assumed has been hit. The next 3 shift registers contain the hit pattern in SL2. The following 8 shift registers contain the eight bit address of SL1j. The following shift

register is the input of SL1j, which we have assumed has been hit. The last shift register is the local trigger flag for this logic circuit. Note that we have allowed five clock ticks to fan out all strips to their required logic. Clock ticks 6 and 7 form an or of the SL2 strips. Clock ticks 8 and 9 form a triple coincidence between SL3i, SL1j, and the or of the SL2 strips. This is the actual trigger. Clock ticks 10 and 11 form a fanout of the trigger. Clock tick 12 sets the local trigger flag and feeds the pipelined 256 or circuit, one for each strip of SL3. Clock ticks 13 through 16 form this or. The output at clock tick 18 is the bend plane master trigger. Clock tick 18 and 19 form the coincidence between the bend plane master trigger and the non-bend plane master trigger. The formation of the non-bend plane master trigger is discussed later in this paper. Clock ticks 20 and 21 open a 64 line data bus. Clock ticks 22 and 23 activate the 64 line data bus. Clock ticks 24 and 25 load the data bus. Note that the local trigger addresses the bus in the usual memory fashion. Clock ticks 24 and 25 send the trigger and the complete information to the second level trigger. We use a 64 bit data bus so that we can transfer 22 bits of bend plane and 42 bits of non-bend plane information. Hence at the end of 25 clock ticks we have the decoded addresses of the SL3 and SL1 hit strips and the SL2 hit strips. The same is true for the non-bend plane. The non-bend plane also furnishes the clock time of the beam crossing. The complete trigger is accomplished in 100 nano seconds.

Triggers for 20 GeV/c and 10 GeV/c can be produced in similar fashions. By including appropriate gates, which are under computer control, one can select the desired trigger.

D. Non-Bend Plane Trigger Logic and Beam Crossing Tag

Fig. 7.0.5 shows the geometry of the non-bend plane. The projective strip design has been optimized to account for multiple scattering.

As indicated in Fig. 7.0.5 for each strip in SL3 there is only one strip in SL2 and three possible hits in SL1. Hence only strips in SL1 are shared by other logic. Each strip in SL1 is fanned out to three logic circuits.

For the non-bend plane, the logic is the same for all momentum. Also for the non-bend plane we only need the 8 bit address of SL3i. SL2j has the same address. The SL1k strips have addresses one less than SL3i, the same as SL3i and one more than SL3i. As we have noted earlier each non-bend strip is effectively divided in half. The uncertainty in time is therefore given by:

SL1 = 1.485/2 x 5 = 3.7 nanoseconds

SL2 = 2.390/2 x 5 = 6.0 nanoseconds

SL3 = 3.296/2 x 5 = 8.3 nanoseconds

Since we have a four nanosecond clock and a 1.5 nanosecond pulse rise time jitter, all three super layers can uniquely determine the beam crossing time. However, since we will be using cable and electronic delays to place the relevant strips in coincidence, only one superlayer can be kept in absolute synch with the beam crossing time. We chose SL1 as the beam crossing timing superlayer. The gate widths of superlayer 1 channels will be four nanoseconds, while the gate widths of the other two superlayers will be larger. This is discussed in Appendix B. Fig. 7.0.6 is a sketch of the non-bend plane logic.

The first shift register indicates whether or not the hit in SL3 is on the lower half of SL3i. In this example we assume the lower half of SL3i was hit. The second shift register indicates whether or not the upper half of SL3i was hit. The next 8 shift registers contain the eight bit address of SL3i. The next shift register indicates whether or not SL3i was hit. In this example we assume SL3i was hit. The next three shift registers contain the hit pattern in SL1. In this example we assume only SL(i + 1) was hit. The following 10 shift registers contain the 10 least significant bits of the master beam crossing clock which is loaded every clock tick. The next 6 bits contain the fixed, known delay time from strip SL2i to the master clock. This includes all cable delays and flight time delays from the interaction point. Any delays to the master beam clock from the interaction point can be included in these six bits. The next 10 shift registers contain the beam crossing time. The final shift register contains the non-bend plane trigger.

On clock tick 1 all data is loaded into the 42 shift registers. There is no fan out delay as there is in the bend plane trigger. On clock ticks 2 and 3 we perform the subtraction between the clock 10 bits and SL2i Dt six bits. Also on clock ticks 2 and 3 we perform the or between SL1 (i - 1), SL1 (i), and SL1 (i + 1). On clock tick 4 we deposit the ten bit beam crossing time. Hence in four clock ticks we have the unique beam crossing time. On clock ticks 4 and 5 we form the and between SL3i, SL2i and the or of the three strips centered on SL1i. This forms the non-bend plane trigger. Hence in 5 clock ticks we have the non-bend plane trigger. On clock ticks 6 and 7 we fan out the non-bend trigger to the trigger bit and to the 166 fan in system. On clock ticks 8 and 14 we generate the non-bend plane trigger. Clock tick 16 - 18 places the master non-bend trigger in coincidence with the master bend plane trigger. Clock ticks 19 to 25 places the non-bend plane information on the 64 bit bus to the level 2 trigger. As indicated in the discussion of the bend plane trigger, the complete muon trigger is formed in 25 ticks or 100 nanoseconds.

It should be noted that the beam crossing tag is now at this level with a maximum error of 3.7 + 4.0 + 4 = 11.7 nanoseconds. The 3.7 comes from the effective strip length of SL1, the 4.0 is the clock period and the 4 is the three sigma error of the rise time jitter. This can be verified to within a maximum error of 5 nanoseconds at the second level.

III. END CAP MUON TRIGGER

Fig. 7.0.7 is the calculated sagitta including the energy loss in the calorimeter for the GEM muon system for different transverse momenta. We see from Fig. 7.0.7 that the sagitta at 16° is about 6 mm for 50 GeV/c transverse momentum. Therefore to resolve 50 GeV/c in the endcaps we must choose our strip width for the region 16° to 29° to be 6 mm. In the region of 9.75° the sagitta is roughly 4.4 millimeters for 50 GeV/c transverse momentum. Thus we must take our strip width to be 4.4 mm in the region between 9.75° and 16°. The performance of the trigger with this segmentation is discussed in a later section.

For the non-bend plane, the strip width has to be consistent with multiple scattering and the precision we wish to know the non-bend coordinate. For the barrel, SL2 determines the non-bend coordinate and that was chosen as 6.5 cm which about matched the multiple scattering requirement. For the end cap it seems 6.5 cm will match the requirement for the non-bend plane. It also seems that the 6.5 cm will also about match the multiple scatter requirement. Hence we will choose a tower geometry with the width at SL2 = 6.5 centimeters. Table 7.1 lists the strip widths and the number of strips for the six chambers in the end cap.

TABLE 7.0.1

Strip Information for the End Caps

SL3 Non-Bend Plane				SL3 Bend Plane		
CHAMBER WIDTH	STRIP NUMBER	STRIPS	WIDTH	NUMBER STRIPS		STRIP
29°	93	mm	40	6	mm	583
16°	93	mm	26	4.4	mm	486

SL2 Non-Bend Plane				SL2 Bend Plane		
CHAMBER WIDTH	STRIP NUMBER	STRIPS	WIDTH	NUMBER STRIPS		STRIP
29°	65	mm	40	6	mm	409
16°	65	mm	26	4.4	mm	320

SL1 Non-Bend Plane				SL2 Bend Plane		
CHAMBER WIDTH	STRIP NUMBER	STRIPS	WIDTH	NUMBER STRIPS		STRIP
29°	38	mm	40	6	mm	238
16°	38	mm	26	4.4	mm	186

Total number non-bend strips = 198 per sector.

Total number of bend strips = 2,222 per sector.

Total number of channels per sector = 2,420.

Total number of channels for GEM = 77,440.

This is about 2.4 times the number of channels in the barrel.

The trigger logic for each bend plane set of 3 chambers (three 29° chambers and three 16° chambers) is identical to the barrel bend plane trigger logic. The same is true for the non-bend plane. Since there are two separate sets of chambers in the end cap, there will be two 64 bit data buses to carry the information to the second level trigger. The accidental rate and dead time calculation, however, are different. These calculations are discussed in Appendix B.

The layout and wiring of each endcap RPC chamber will be similar to the layout and wiring of the RPC chamber in the barrel.

IV. Electronics

The electronics for the trigger has to have the following features:

- Four momentum ranges - each range programmable
- Relative positions of each RPC plane programmable.
- Correction for interaction point programmable.

In addition the electronics must determine the centroid of the hit cluster - especially important in the endcaps. The beam crossing time must be determined, the strips which participated in the trigger must be isolated and recorded at Level 2, and multiple triggers - with their strip numbers are stored in memory for access at Level 2. Fig. 7.0.8 is a schematic of the electronics.

V. SUMMARY

The RPC trigger scheme has the following properties:

Barrel

1.	Number of Channels			
	Non-bend plane	498 x 32	=	15,936
	Bend plane	1659 x 32	=	53,088
	TOTAL			69,024
	Strip Widths			
	Non-bend plane			
	SL1	3.9	cm	
	SL2	6.5	cm	
	SL3	8.9	cm	
	Bend plane			
	SL1	1.3	cm	
	SL2	1.3	cm	
	SL3	1.3	cm	
	Strip Length			
	Non-bend plane			
	SL1	148.5	cm	
	SL2	239.0	cm	
	SL3	329.6	cm	
	Bend plane			
	SL1	631.9	cm	
	SL2	1,042.6	cm	
	SL3	1,475.0	cm	
Trigger acquisition time		100	nanoseconds	

Beam crossing error		
First level trigger	11.7	nanoseconds
Second level trigger	5.0	nanoseconds
Accidental rate at $L = 10^{34}$		
(transverse momentum > 50 GeV/c	29	Hertz
Dead time at a neutron flux of 10^5 neutrons per square centimeters per second (transverse momentum > 50 GeV/c		
Signal dead time gate = 100 nanoseconds	6%	
Signal dead time due to possible high rate inefficiency	16 %	

End Cap

Detailed strip information is in Table 1.

Total number of end cap channels	77,440
Trigger acquisition time	100 nanoseconds
Beam crossing error	
First level trigger	11.7 nanoseconds
Second level trigger	5 nanoseconds

All accidental rates and dead times are less than the barrel by more than an order of magnitude except if we assume each RPC chamber is only 90% efficient due to the high rate. In that case, the dead times in the barrel and end caps are the same.

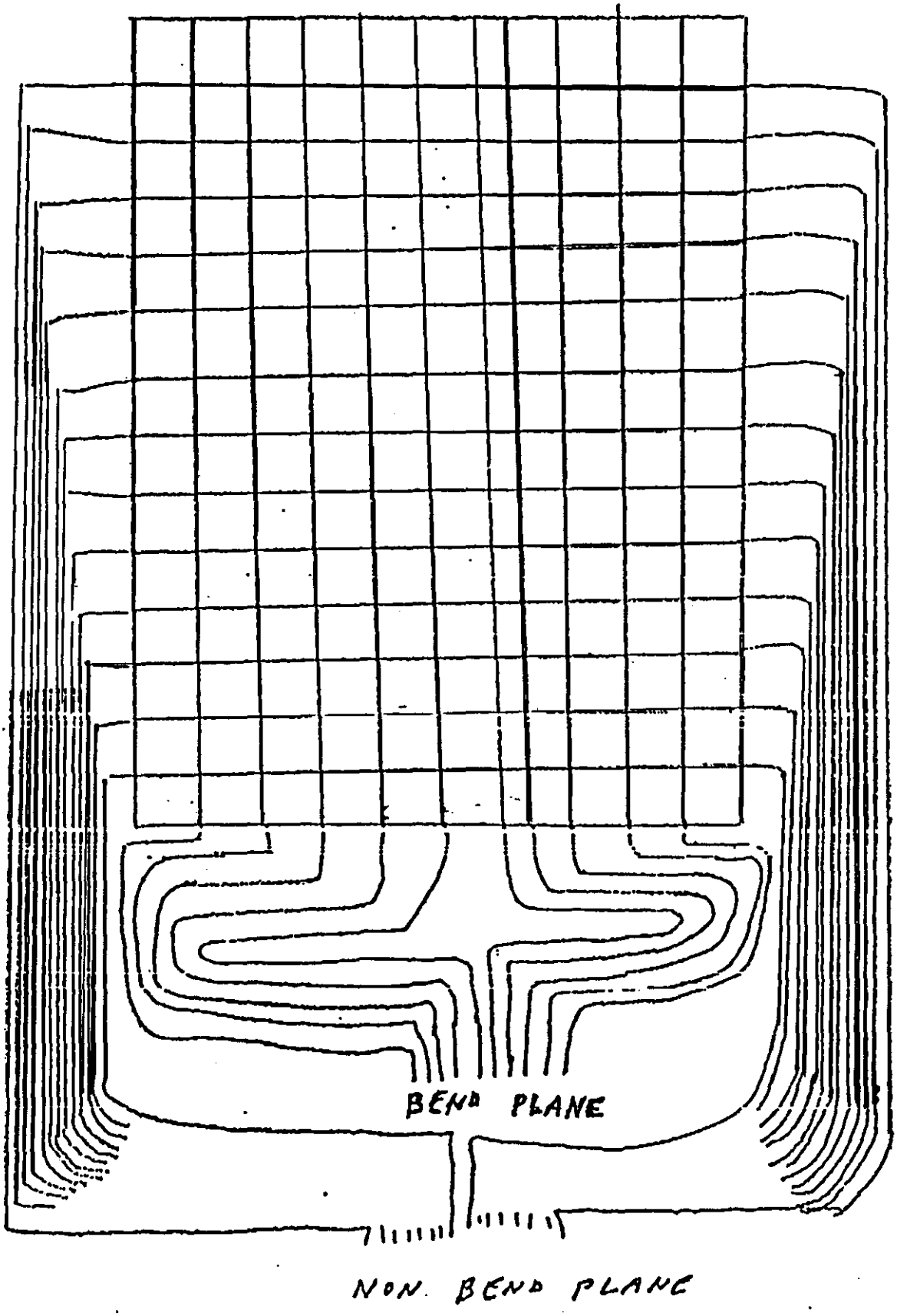

Fig. 7.0.1

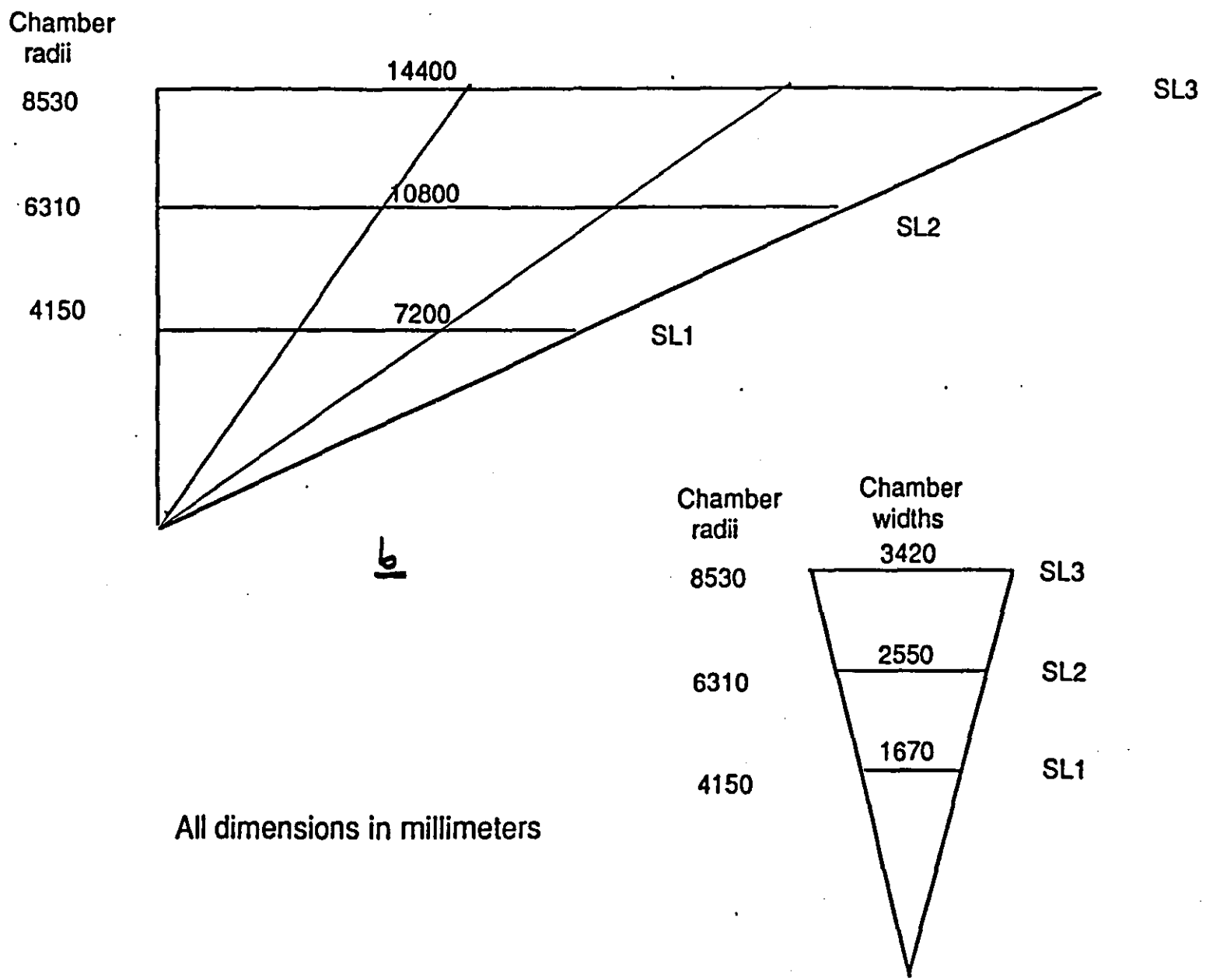
Chamber radii
8530
6310
4150
14400
10800
7200
SL3
SL2
SL1
Chamber radii
Chamber widths
3420
2550
1670
8530
6310
4150
SL3
SL2
SL1
All dimensions in millimeters

Fig. 7.0.2

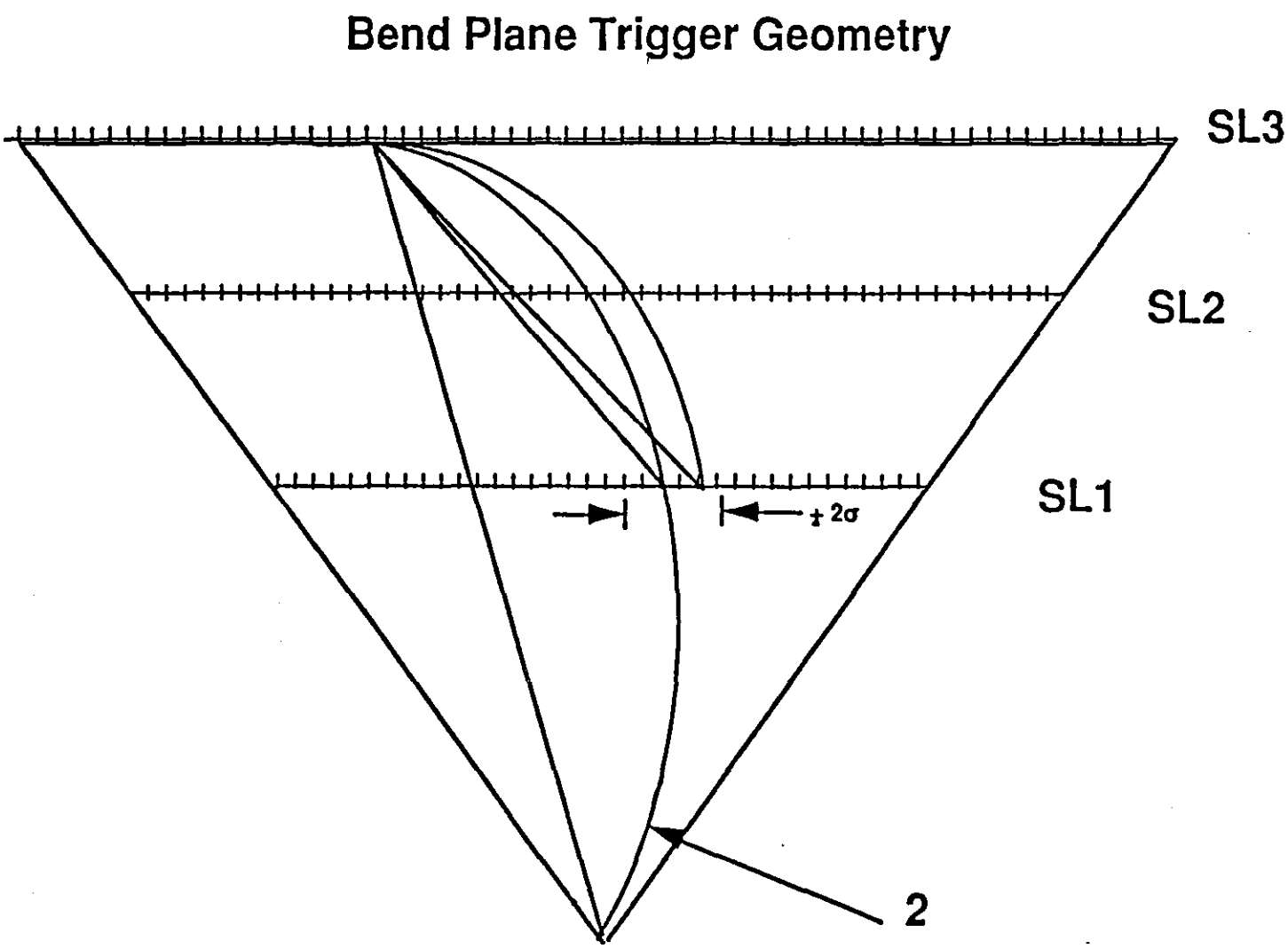

Fig. 7.0.3

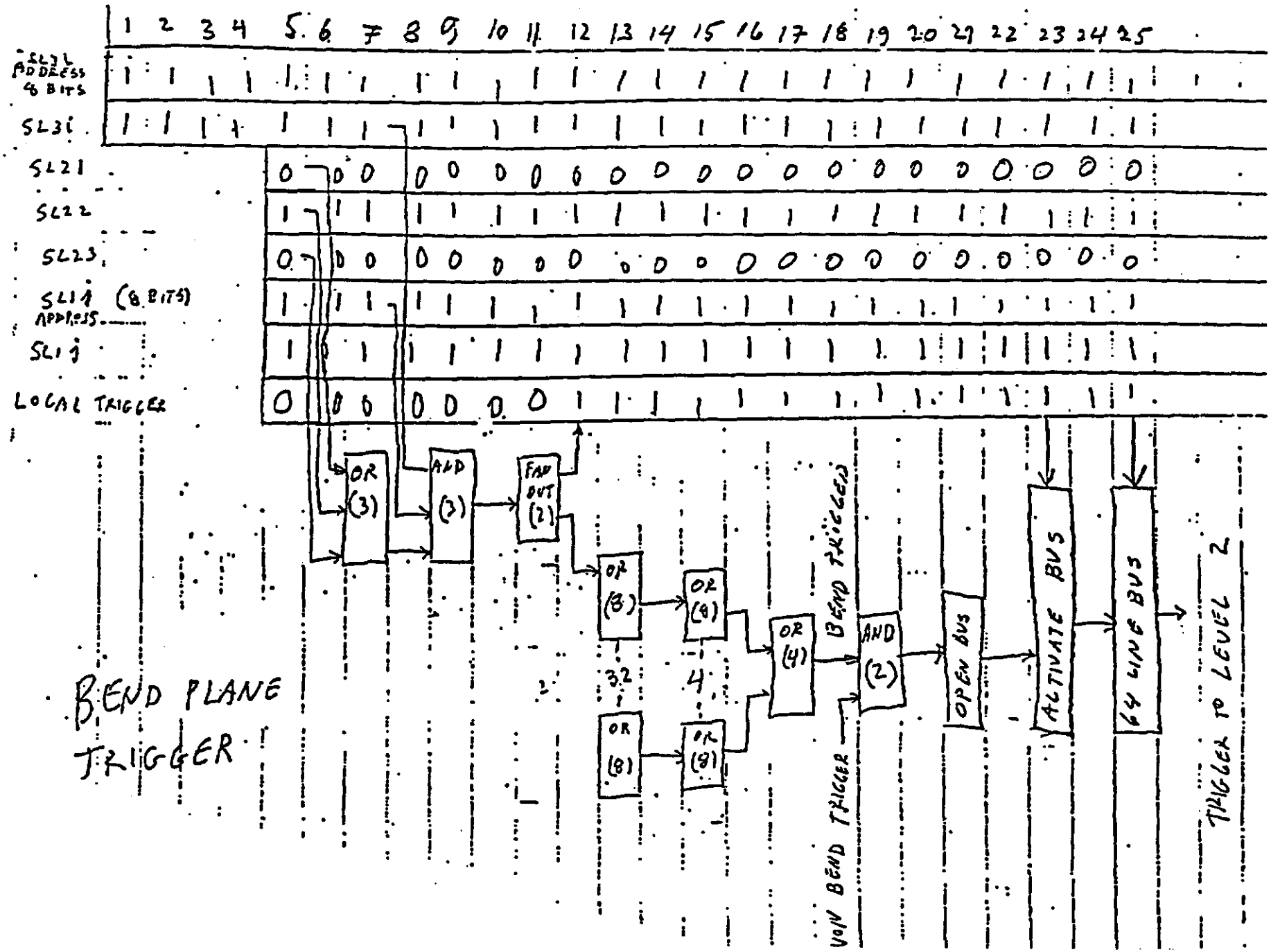
1 2 3 4 5 6 7 8 9 10 11 12 13 14 15 16 17 18 19 20 21 22 23 24 25
SL31 ADDRESS 4 BITS
SL31
SL21
SL22
SL23
SL14 (8 BITS) ADDRESS
SL13
LOCAL TRIGGER
OR (3)
AND (3)
FAN OUT (2)
OR (8)
OR (8)
OR (8)
OR (8)
32
4
OR (4)
BEND TRIGGER
AND (2)
V0/V BEND TRIGGER
OPEN BUS
ACTIVATE BUS
64 LINE BUS
TRIGGER TO LEVEL 2
BEND PLANE TRIGGER

Fig. 7.0.4

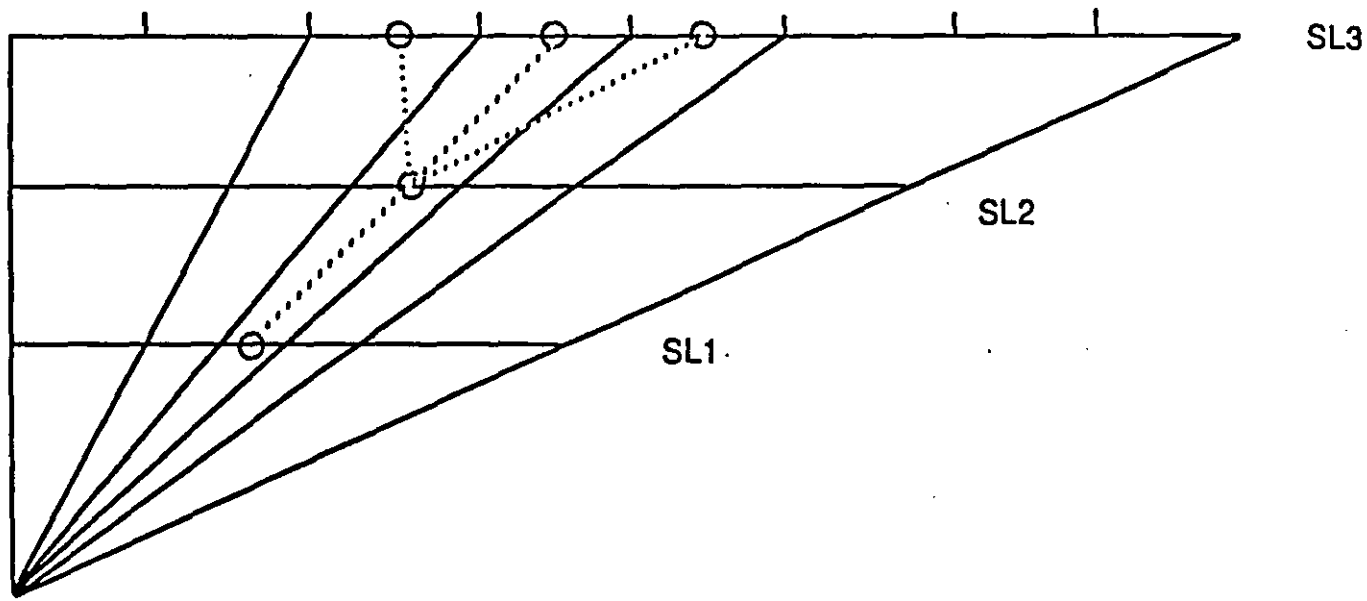

Fig. 7.0.5

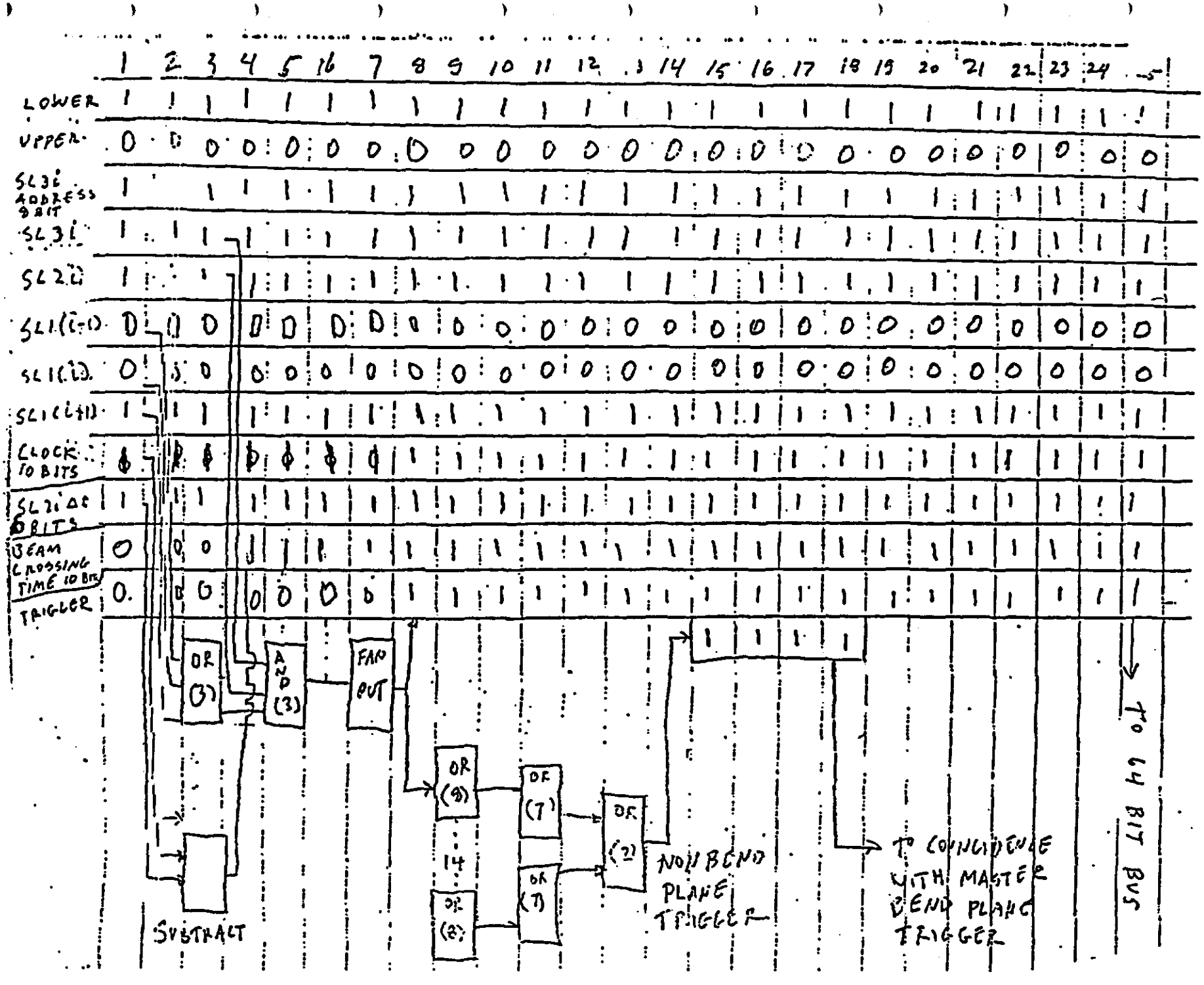
LOWER
UPPER
SL3i ADDRESS 9 BIT
SL3i
SL2i
SL1i(i-1)
SL1i(i)
SL1i(i+1)
CLOCK 10 BITS
SL2i Δt 8 BITS
BEAM CROSSING TIME 10 BITS
TRIGGER
OR (3)
AND (3)
FAN OUT
OR (9)
14
OR (8)
OR (7)
OR (7)
OR (2)
SUBTRACT
NO BEND PLANE TRIGGER
TO COINCIDENCE WITH MASTER BEND PLANE TRIGGER
TO 64 BIT BUS

Fig. 7.0.6

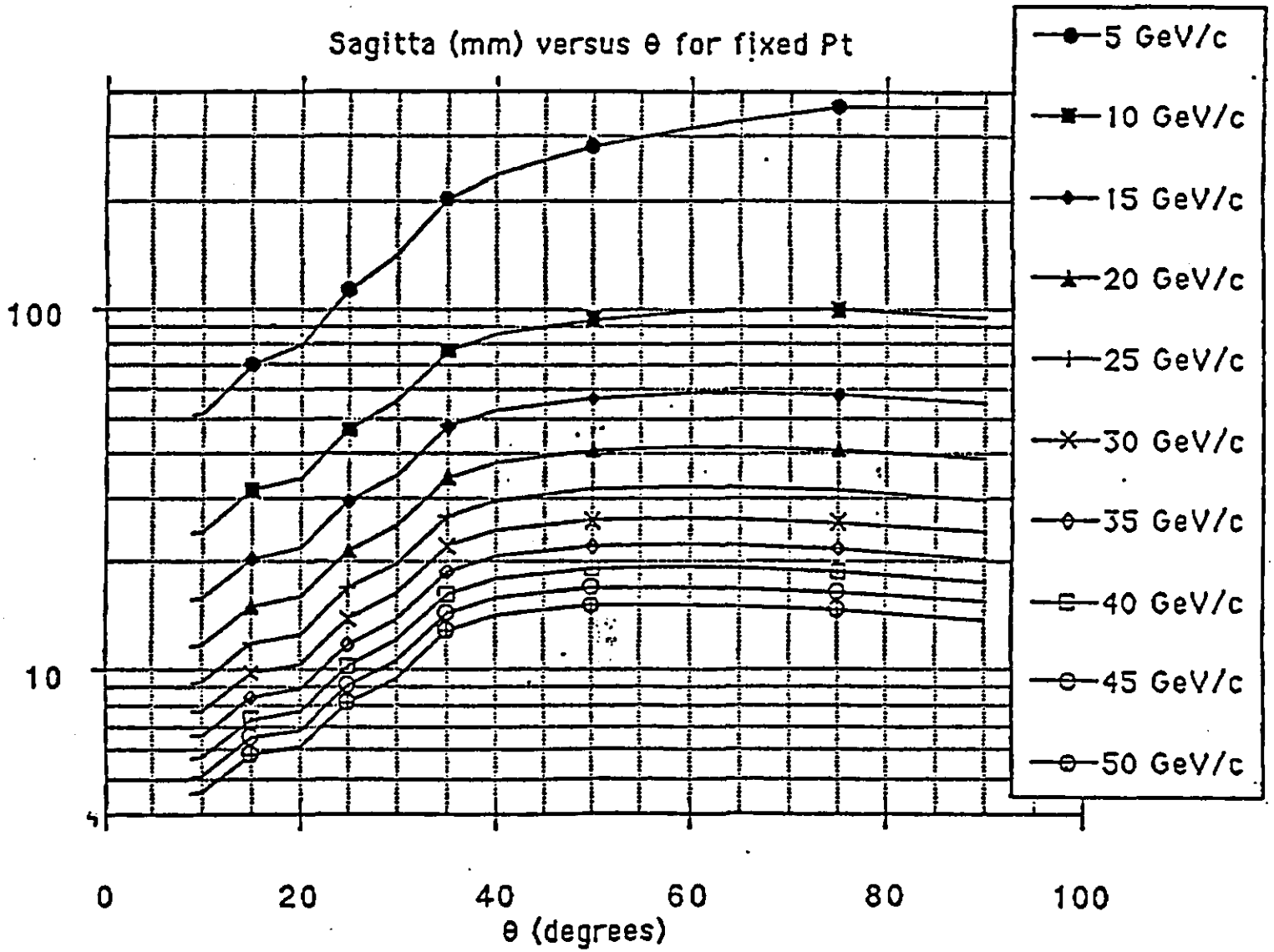
Sagitta (mm) versus θ for fixed Pt
100
10
0
20
40
60
80
100
θ (degrees)
5 GeV/c
10 GeV/c
15 GeV/c
20 GeV/c
25 GeV/c
30 GeV/c
35 GeV/c
40 GeV/c
45 GeV/c
50 GeV/c

Fig. 7.0.7

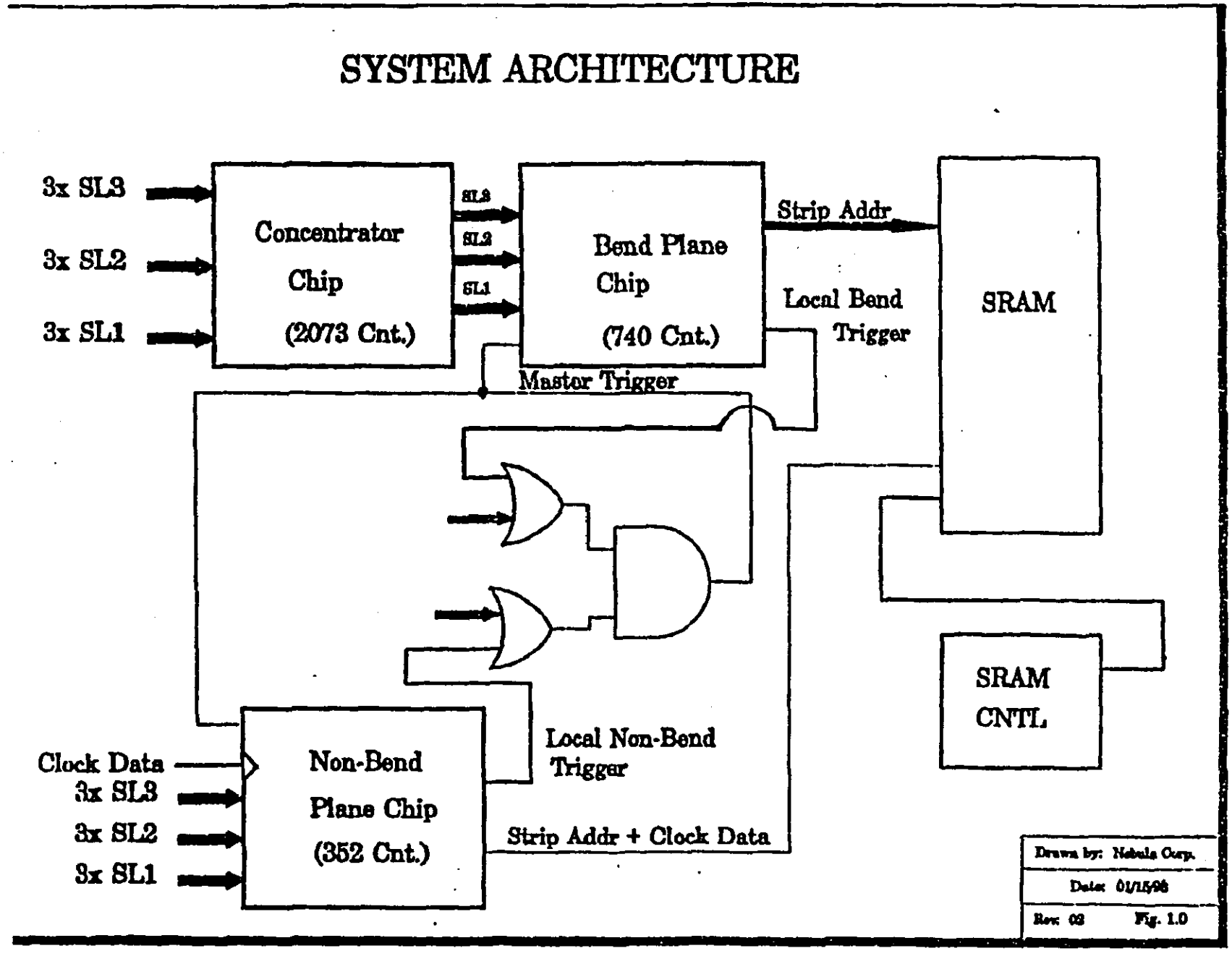
SYSTEM ARCHITECTURE
3x SL3
3x SL2
3x SL1
Concentrator Chip (2073 Cnt.)
SL3
SL2
SL1
Bend Plane Chip (740 Cnt.)
Strip Addr
Local Bend Trigger
SRAM
Master Trigger
SRAM CNTL
Local Non-Bend Trigger
Clock Data
3x SL3
3x SL2
3x SL1
Non-Bend Plane Chip (352 Cnt.)
Strip Addr + Clock Data
Drawn by: Nebula Corp.
Date: 01/15/98
Rev: 02
Fig. 1.0

Fig. 7.0.8

(7.1) RDT Data Acquisition

It is proposed that the readout of the RDT chamber data of a Level-1 trigger be track driven; only tubes which are part of a local track segment (3-of-4 tubes) are readout. Each super-layer contains two packages of either 4 or 6-tube layers that are grouped into sections with at most 24 tubes per section as shown in the figure below (i.e. 6 tubes/layer, the package with 6 x-layers will have two such groups with two layers in common).

Superlayer Track Sections

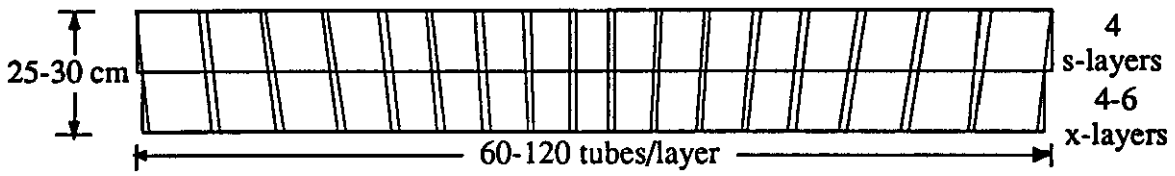

There is one tube/layer overlap between sections to allow a track to cross between sections or for stereo angle effects. The fast pattern logic shown below determines if a track segment exists in a section.

Track-Segment Pattern Logic

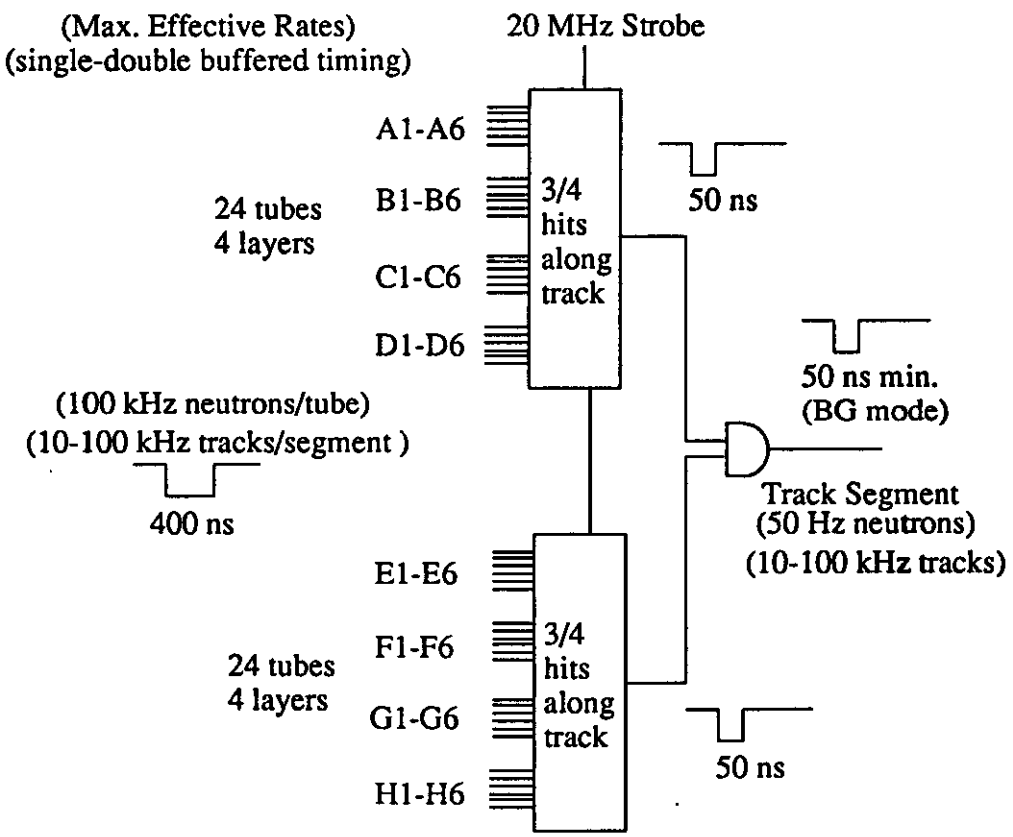

The 6 tubes/layer in each section are grouped into two 16M-bit memories (2^{24}). A 3-of-4 requirement is coded into the memories. A 1-bit in the memory signifies a legal track pattern is formed by the 24 tubes (address lines of the memory) in a section. If the upper(A-D) and lower(E-H) sections when strobed (every 50 ns) both satisfy the 3-of-4 requirement a track signal is formed.

This logic will reduce the neutron rate to well below the true track rate. This means that only true tracks will be readout on a Level-1 trigger and the large number of random neutron hits will be suppressed. The dead time of this logic is not serious if the subsequent timing is double buffered. In the event that two tracks cross a section within a drift-time the width of the Track Segment output will signify when it is safe to stop the second buffer. In this manner two tracks with any relative timing within the 2 msec Level-1 trigger delay can be recorded for readout. Dead-time can be incurred only if there are three tracks within a section within the Level-1 trigger delay.

The time of the most recent hit is latched via a common stop signal generated soon after a Track Segment signal is transmitted from the pattern logic. The stop time is referenced to a fixed phase of the accelerator clock to better than 1 nsec.

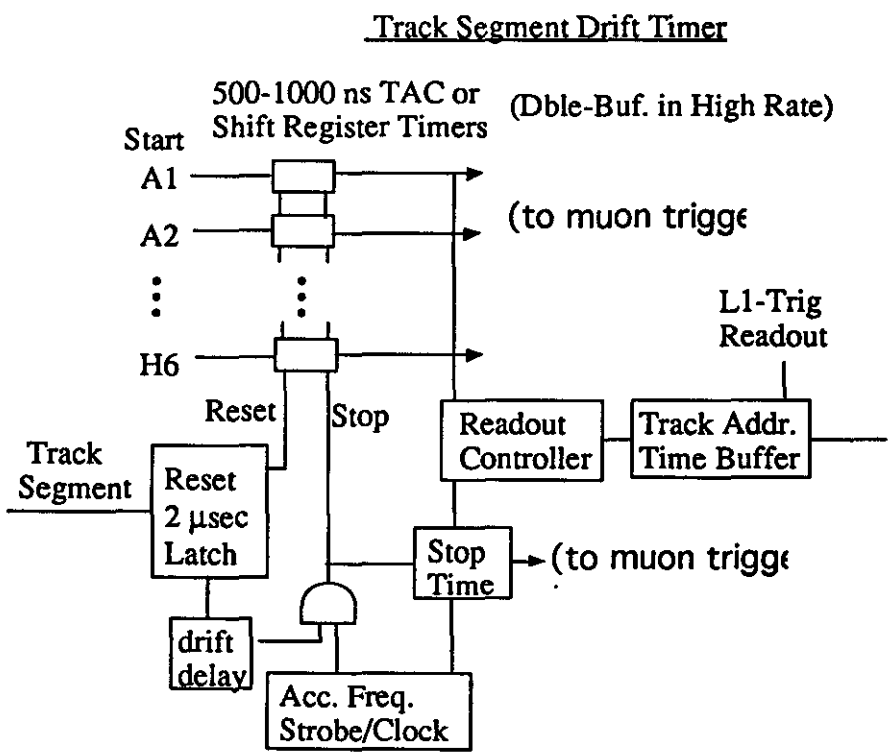

The timing element will be a shift-register or a time-to-amplitude converter. In either case the common stop time from an absolute bucket scaler is also latched by the stop signal. In less than 1.5 μsec while a Level-1 trigger from any source is being formed

the non-zero times and tube addresses are loaded into a buffer. If a level-1 trigger does not arrive by 2.0 μsec the timing elements are reset. The timing elements will be double buffered in regions where the track-rate is high enough to cause significant dead-time. The individual times and the stop time are also made available to a RDT stand-alone trigger system.

The common stop time is relevant only for the track in this section. Each track segment will have its own stop time recorded. In the chambers at the smallest angles to the beam the expected track rate in a section may exceed 10kHz (2% dead time for the Timers). For these chambers and any other region where the rate exceeds 10 kHz/section the Timer circuitry will be double buffered to allow two tracks within 2 μsec to be latched. Since a small loss of trigger efficiency can be tolerated at small angles it does not seem necessary to duplicate the trigger logic for the second track.

In the RDT baseline there are 26 tubes which will lie along a track in either the barrel or the endcap. The time of these signals relative to the stop time is known off-line to better than 1 nsec and can be determined on-board the chambers quickly to better than ± 5 nsec.

(7.2) P_T-Trigger Based on RDT

A number of viable T_0 and P_T -triggering schemes have been discussed within the RDT group. The RDT system can be auto-triggered, as in the scheme of A. Korytov and B. Barabash (see Appendix E). Another scheme is to use the scintillators of the tail catcher of the calorimeter or a standalone PWC system (as a substitute to the RPCs) to generate a T0 signal needed for the drift trigger.

A description of one of these auto-triggering schemes is presented here. Track segments in the three superlayers consistent with the trigger P_T determine the slope of the track b_0 at each superlayer to better than 10 mrad. At most one hit tube in each layer is then identified with the track from the observed hit-pattern. Shown below are a set of hit patterns and typical track limits defined by the b_0 constraint. The b_0 constraint can also be used to resolve the small number of ambiguous cases. The object here is to identify the direction of the drift in each tube which is needed to determine t_0 .

4 Tube Patterns and Range of Track Solutions

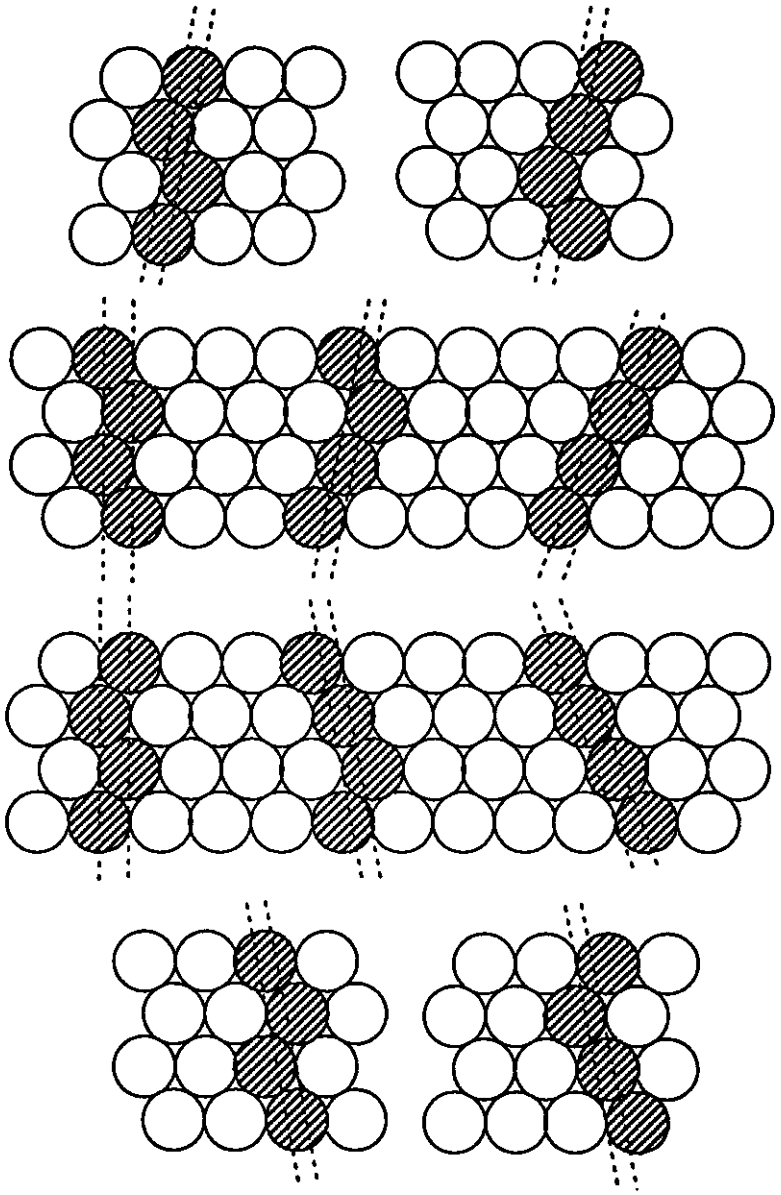

Of course if t_0 is determined by another device, such as a PWC, the a measurement of the transverse momentum can be made from these patterns alone.

An improved superlayer crossing point α and a preliminary interaction time t_0 can then be calculated in each package using a constant drift velocity. The example shown below has a l-r-l-r pattern of drifts, however, only the signs change in algorithm for other patterns. For less than 4 good hits the averaging is done only over the good hits.

Let: $Z_i = (+3,+1,-1,-3)\Delta Z$, $\Delta Z = 1$ cm, $v_i = \pm v$, and $c_i = n_i t_i + b_o Z_i$. Then superlayer crossing point and the estimator of the interaction time is given by:

$$\alpha = \langle c \rangle = \frac{v(-t_1+t_2-t_3+t_4)}{4} \text{ for } v_i = -v, +v, -v, +v$$

$$\tau_0 = \frac{\langle vc \rangle}{\langle v^2 \rangle} = \frac{(t_1+t_2+t_3+t_4)}{4} + \frac{b_0 \Delta Z}{v}$$

Once t_0 and α are determined the correct velocities using the true time-to-distance relationship can be used to obtain the precise interaction time t_0, crossing point α, and slope b. Each of these computations is performed via table lookups rather than a true calculation. With 26 tubes the identification of the true bucket crossing for the track and the momentum seem assured.

(8.0) System Performance

In this section the resolutions of the trigger, momentum reconstruction, and angle reconstruction are described. All have been calculated from the parameters of the system given in Section (3) above.

(8.1) Trigger Performance:

(8.1.1) Momentum Resolution:

The trigger algorithm is based on a measurement of the sagitta in the barrel and the projected sagitta (within a small-angle cosine correction equal to the true sagitta). This method has been adapted over the $\Delta\phi$ method since it has superior resolution which will be crucial in limiting the Level 1 trigger rate at high luminosity. A typical set of parameters for this trigger scheme is shown in the table below:

Table 8.1

RPC Trigger Parameters for Pt = 10 GeV/c

Region number	angle limits	element size	η limits	sagitta cuts
1	57 to 90	1.3 cm	0 to 0.6	9.0 cm
2	39 to 57	1.3 cm	0.6 to 1.04	9.0 cm
3	29 to 39	1.3 cm	1.04 to 1.35	8.0 cm
4	22.5 to 29	0.6 cm	1.35 to 1.61	7.5 cm
5	16 to 22.5	0.6 cm	1.61 to 1.96	5.0 cm
6	9.75 to 16	0.44 cm	1.96 to 2.46	2.7 cm

The trigger threshold performance was simulated by computing the (projected) sagitta as would be measured with the finite trigger elements of system. Multiple scattering and energy loss with fluctuations were included in the calculation. But note that the sagitta method is not sensitive to the multiple scattering in the calorimeter. The muon was allowed to have the full ϕ range of a given chamber (11.5^o for the barrel and 22.5^o for the endcaps). The results are shown in Fig. 8.1.1(a), 8.1.1(b), 8.1.1(c) for (primordial) Pt = 10, 25, 50 GeV/c, respectively. Note that the projected sagitta in the endcaps leads to a small additional smearing of the trigger threshold. However the thresholds are still quite good even with this effect. To reduce (but is not needed) the ϕ smearing arising from the rectangular chambers in the endcaps the following strategy may be adapted. If a track penetrates the overlap region, the coincidence can be detected and trigger cut be made on the larger of the

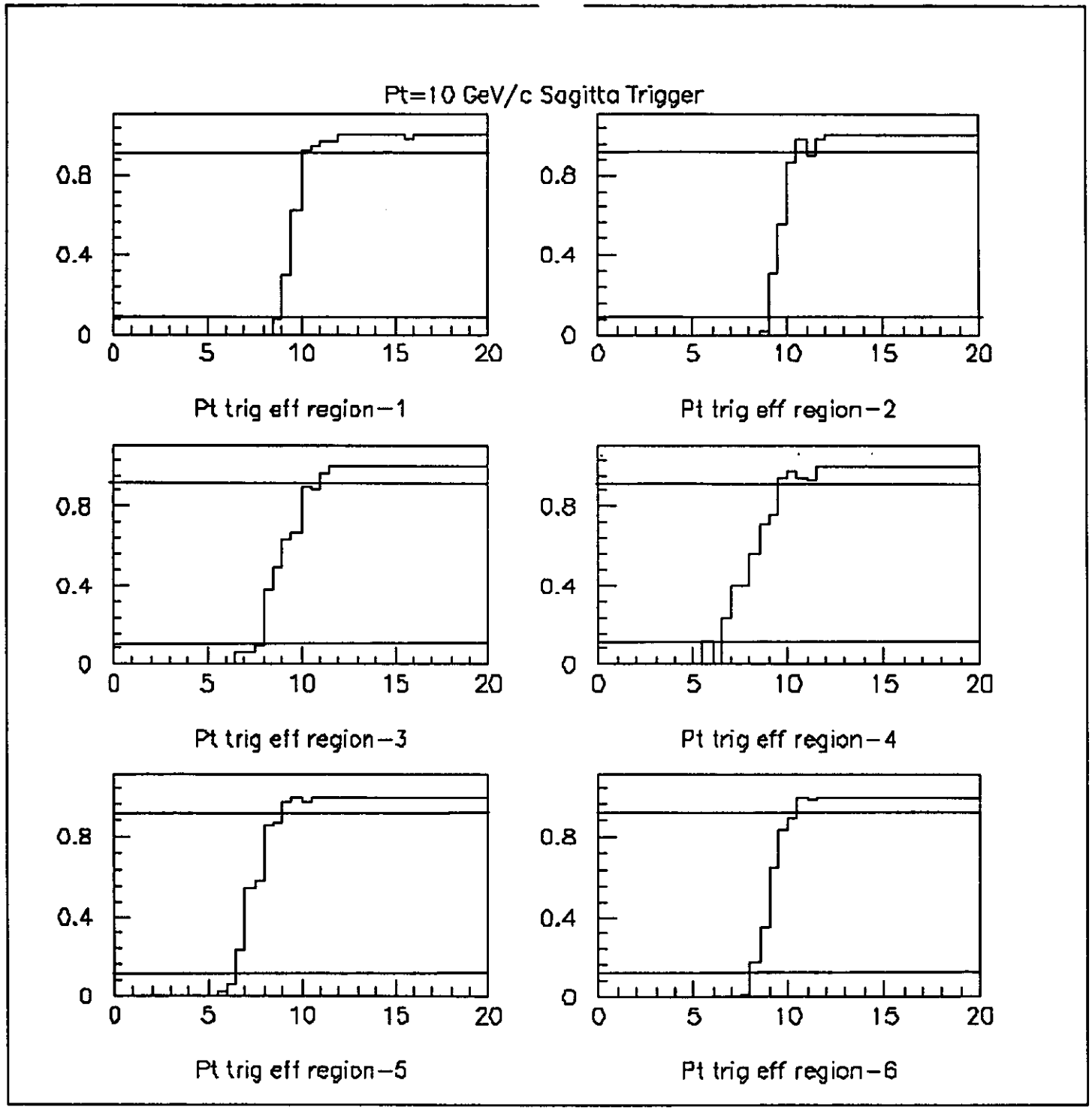
Pt=10 GeV/c Sagitta Trigger
0.8
0.4
0
0
5
10
15
20
Pt trig eff region−1
Pt trig eff region−2
Pt trig eff region−3
Pt trig eff region−4
Pt trig eff region−5
Pt trig eff region−6

Fig. 8.1.1a

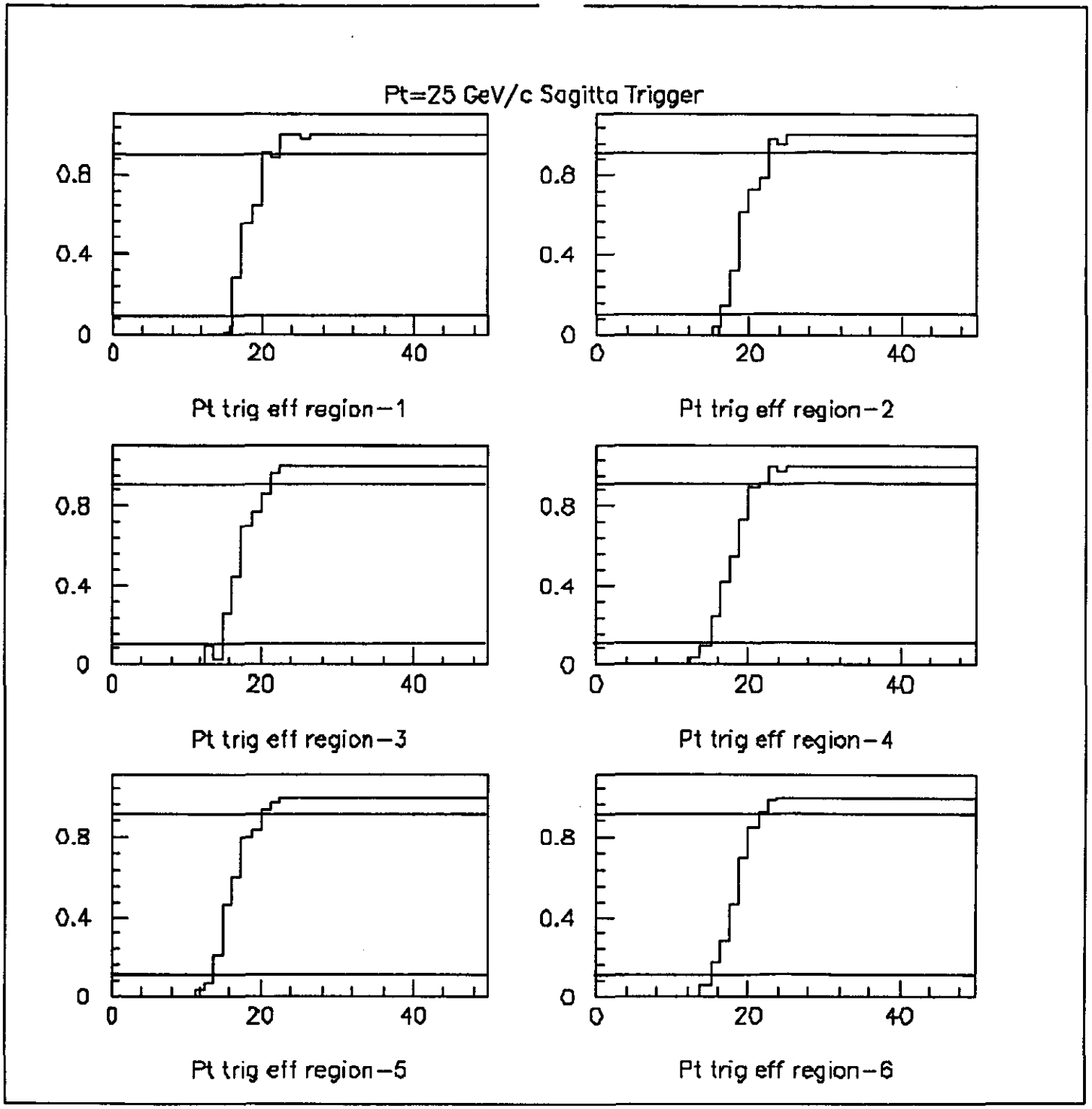
Pt=25 GeV/c Sagitta Trigger
0.8
0.4
0
0
20
40
Pt trig eff region-1
Pt trig eff region-2
Pt trig eff region-3
Pt trig eff region-4
Pt trig eff region-5
Pt trig eff region-6

Fig. 8.1.1b

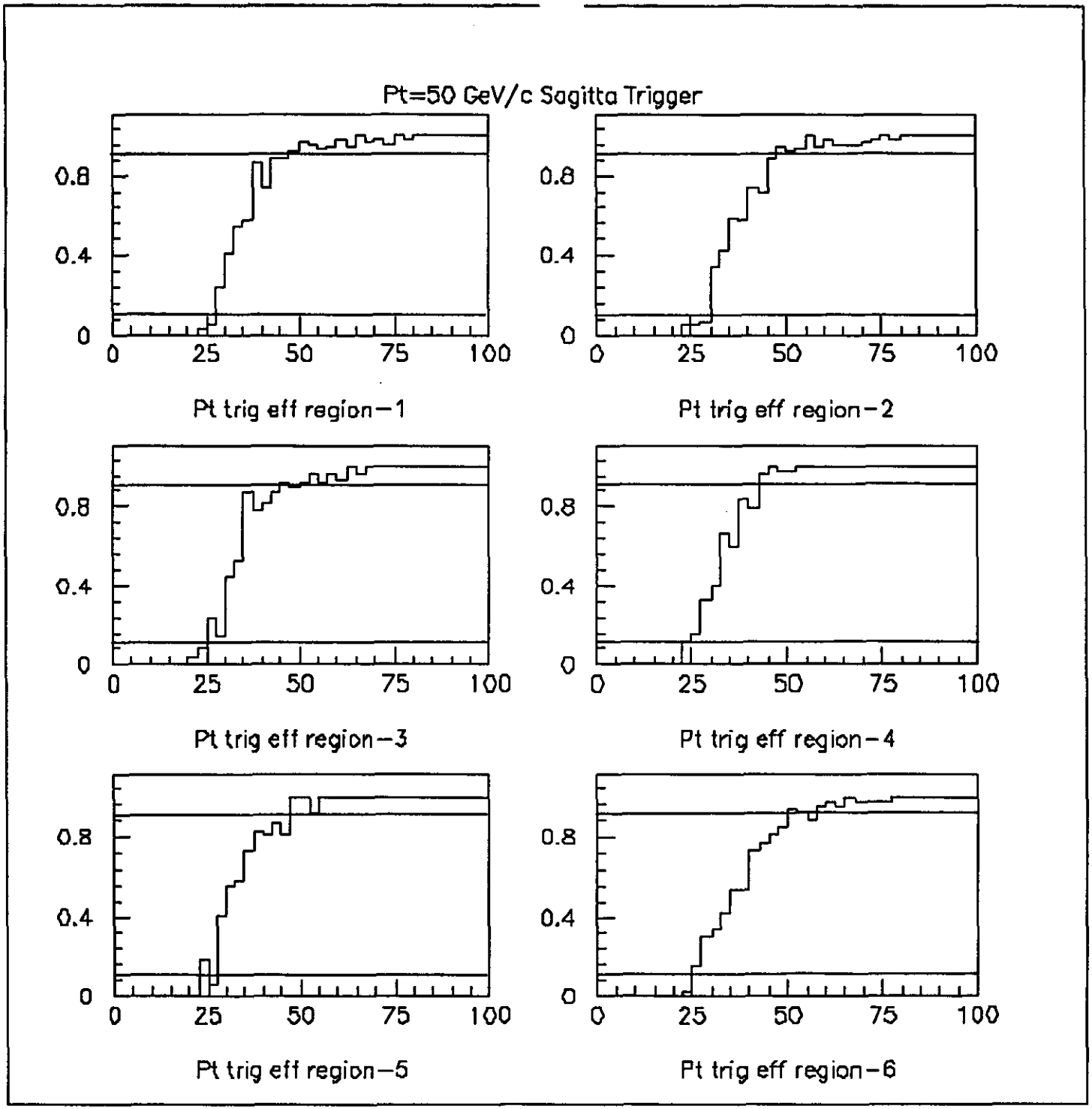
Pt=50 GeV/c Sagitta Trigger
0.8
0.4
0
0
25
50
75
100
Pt trig eff region−1
Pt trig eff region−2
Pt trig eff region−3
Pt trig eff region−4
Pt trig eff region−5
Pt trig eff region−6

Fig. 8.1.1c

two projected sagitta values. Where the ϕ smearing is large in one chamber it is small in the other.

In contrast to the sagitta method adapted here, the $\Delta\phi$ method with radial strips in the endcaps as applied between superlayers 2 and 3 as presently proposed has considerably less resolution since it is dominated by multiple scattering in the calorimeter. A typical threshold curve computed by this scheme is shown in Fig. 8.1.2. This trigger method will not achieve the needed low P_T-rejection at high luminosities.

(8.1.2) Rate Performance:

The difficulty with the present RPC trigger arises from the rate limitation (97% efficient for rates < 50 Hz/cm^2) of the present version of this technology. Neutron fluences of order 10^4 /cm^2 sec are expected in the barrel region at L = 10^{33}/cm^2 sec and roughly 10 times higher in the endcaps. At these rates and with the measured sensitivity of the RPC to neutrons of 0.5%, we find the neutron rate "burden" in the barrel to be 50 Hz/cm^2 and 500 Hz/cm^2 in the endcaps. The barrel environment is then just at the rate limit of the Italian RPC and the endcaps severely beyond. The charged particle flux in the very forward angle region is calculated to be < 50 Hz/cm^2 at L= 10^{33}. Hence the RPC in its present design is marginal at L= 10^{33} in the barrel region and not viable in the endcaps.

The neutron fluence calculations are very uncertain and there is some reason to believe that shielding will mitigate the problem. Furthermore there have been promising results in finding new materials for the RPC resistive layer which would withstand much higher rates (Peskov - FNAL private communication). Major uncertainties remain however and it is for these reasons that we propose a PWC trigger system to replace the RPCs. Such a device could be an inexpensive version of the present CSC design where roughly 80% of the costs go into high precision elements. At the present pricing of chambers a 4-3-3 trigger system would cost roughly $8M. See the Cost Appendix C.

The random hit occupancy for a typical drift tube (where two tubes are tied together at one end) is about 5% for a neutron fluence of 10^4 Hz/cm^2. Roughly the same numbers pertain to a CSC system with an integration time of 500 ns.

(8.2) Momentum Reconstruction:

The momentum resolution of the system is determined by the number of chamber layers, the layer resolution, the multiple scattering in the middle superlayer, and the fluctuations of the energy loss in the calorimeter. The event reconstruction of two important processes drive the specification of the system.

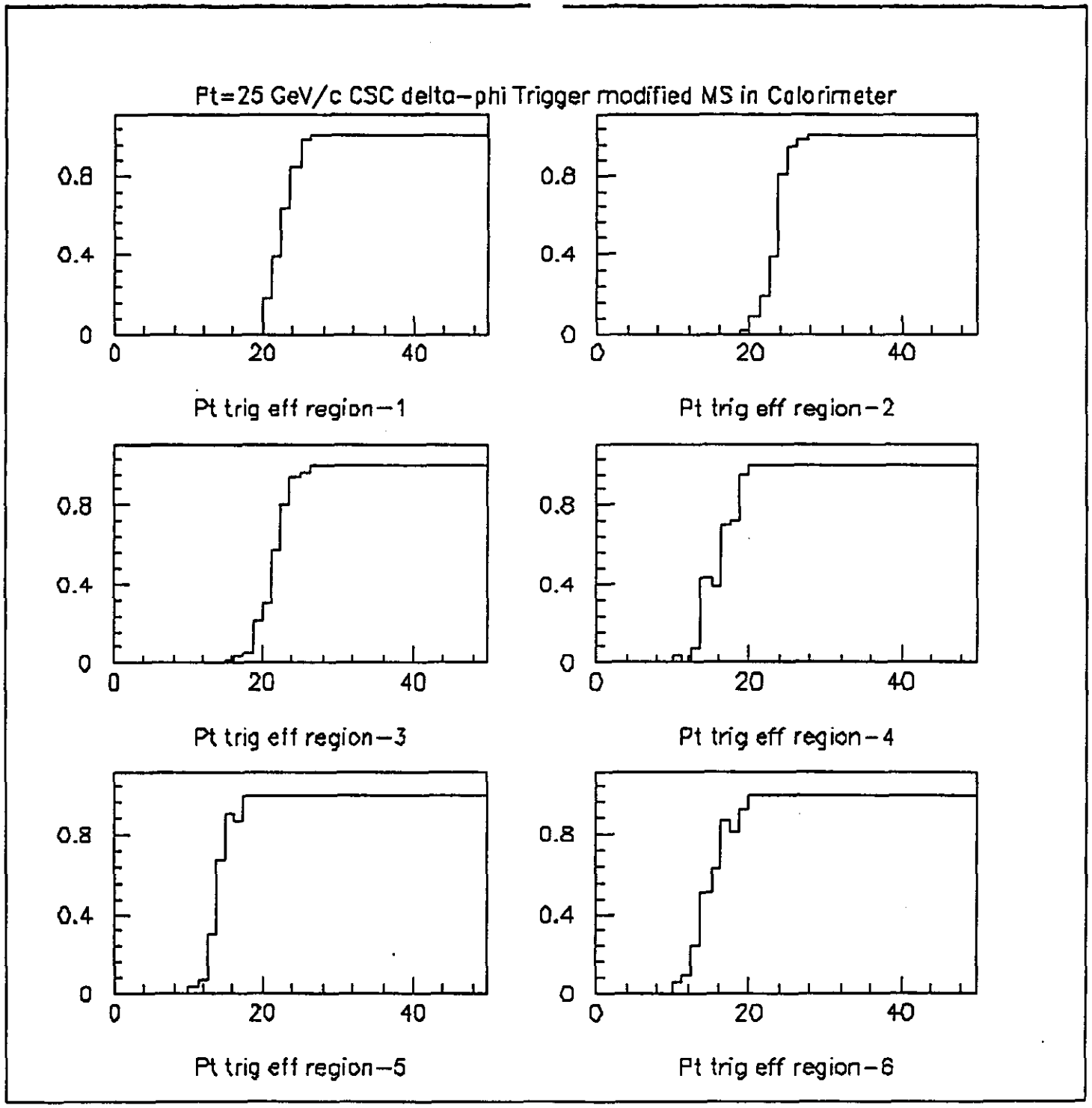
Pt=25 GeV/c CSC delta-phi Trigger modified MS in Calorimeter
0.8
0.4
0
0
20
40
Pt trig eff region-1
Pt trig eff region-2
Pt trig eff region-3
Pt trig eff region-4
Pt trig eff region-5
Pt trig eff region-6

Fig. 8.1.2

• Low mass Higgs boson M_H = 130 GeV/c^2 where the transverse momenta of the decay muons range from 10 GeV/c to 100 GeV/c.

• High mass Z' boson $M_{Z'}$ = 1 TeV/c^2, where the analysis of muons in 0.5 to 1 TeV/c range is needed.

In the low momentum region, the fluctuations of the energy loss of the muons traversing the calorimeter is the dominate factor. The energy loss of the muon in the calorimeter can in principle be reconstructed, but would require isolating the muon energy loss ($\Delta E\mu$ = 5 to 10 GeV) from a noisy background of much greater energy deposition and resolving the $\Delta E\mu$ with an error of $20\%/\sqrt{(\Delta E\mu)}$. Less important is the multiple scattering of the muon in the middle superlayer.

Key to the reconstruction of high energy momenta is to have enough chamber planes with clean hits. This is why we have exploited the economic chamber construction of this system to allow for high redundancy. We believe that this is an important design parameter of the system. To illustrate this point Table 8.2 give the fraction of clean events observed for a 1 TeV/c muon traversing the detector at 90 degrees. These parameters have been used in a fast simulation of the high energy system performance. We have assumed that the single layer resolution of the RDT system is 100 μm even though full-scale prototypes have demonstrated a resolution as good as 60 μm.

Table 8.2

Ratio of good hits (golden hits) for 1 TeV/c Muons at 90 degrees

hits required	Inner	Middle	Outer
3/4	0.873 (0.825)	0.918 (0.888)	0.943 (0.910)
4/4	0.743 (0.703)	0.810 (0.785)	0.835 (0.813)
4/6	0.893 (0.830)	0.928 (0.900)	0.958 (0.928)
5/6	0.810 (0.760)	0.888 (0.855)	0.893 (0.863)
6/6	0.675 (0.638)	0.758 (0.730)	0.745 (0.728)
4/8	0.933 (0.880)	0.910 (0.925)	0.968 (0.948)
6/8	0.870 (0.795)	0.858 (0.880)	0.940 (0.913)
8/8	0.630 (0.605)	0.700 (0.683)	0.710 (0.700)

We note that at least 8 layers are required in the inner superlayer for at least 4 good hits > 90 % time, and at least 6 layers are required in the outer superlayer for the same criterion. Our 8:10:8 chamber configuration meets this requirement. Both the small angle stereo planes and axial layers determine [within a very small effect of order 1/cos(4mr)] the same coordinate for the momentum reconstruction. In addition

the U-V planes are paired to determine the Y coordinate with a resolution indicated in Section 2.1 of this Baseline.

The momentum resolution in the P_T = 10 to 100 GeV/c region is given in Fig. 8.2.1a. (The worse resolution sector of the endcaps was chosen for this calculation - see below.) Note that the resolution improves with increasing momentum in this region since the dominate effect is the un-reconstructed energy fluctuations in the calorimeter. The resolution is computed in the overlap region of the endcaps in Fig. 8.2.1b. There the chamber configuration is effectively 16-20-16 and the multiple scattering in the middle superlayer will be a larger effect. That we observe in the 25 to 50 GeV/c range where the resolution is degraded from 2.5% to 3%.

The high energy performance, where the energy fluctuations in the energy loss in the calorimeter can be neglected, is shown in Fig. 8.2.2a and 8.2.2b for the two angle sectors of the endcaps. For this calculation we have assumed that all the chamber planes provide unspoiled hits. The resolution in the overlap region of the endcaps is somewhat better. In that region the number of planes in the middle superlayer is effectively 20 providing a better resolution, or equivalently there are two determinations of the momentum which can be treated as independent measurements, but with 2x multiple scattering. The resolution in that region is indicated in Fig. 8.2.2c. Roughly 30% of the single muons will traverse this region.

From the table above we note that the resolutions of Fig. 8.2 are optimistic and do not account for spurious hits associated with a high energy muon track. The get a measure of this effect the probabilities of the Table 8.2 were converted to a binomial distribution to provide an estimator (uncorrelated) of the number of good hits participating in the track reconstruction. These probabilities are illustrated in Fig. 8.2.3a,b for the barrel and endcaps, respectively. Putting these into the computation of the resolutions Fig. 8.2.3c indicates that the resolution degrades from only about 23.3% to 24% for η= 2.5 for an 8-10-8 at 1 TeV/c. A muon system with fewer planes degrades more rapidly, again illustrating the need for a large number of planes in the muon system.

The angle resolutions are shown in Figs. 8.2.4a and 8.2.4b. We have used the Y resolution obtained by the small angle stereo to achieve the θ resolutions shown. The RPC also determines this angle and will be used as a redundant measurement. At low momentum the polar angle resolution is dominated by the multiple scattering in the calorimeter and at high momenta by the spatial resolution of the system. The ϕ resolution is dominated by the multiple scattering in the superlayers at low momentum and by the spatial resolution of the precision coordinate measurement at high momentum.

In summary the RDT system proposed has good performance and a high redundancy of chamber planes - needed for a good muon system at the SSCL.

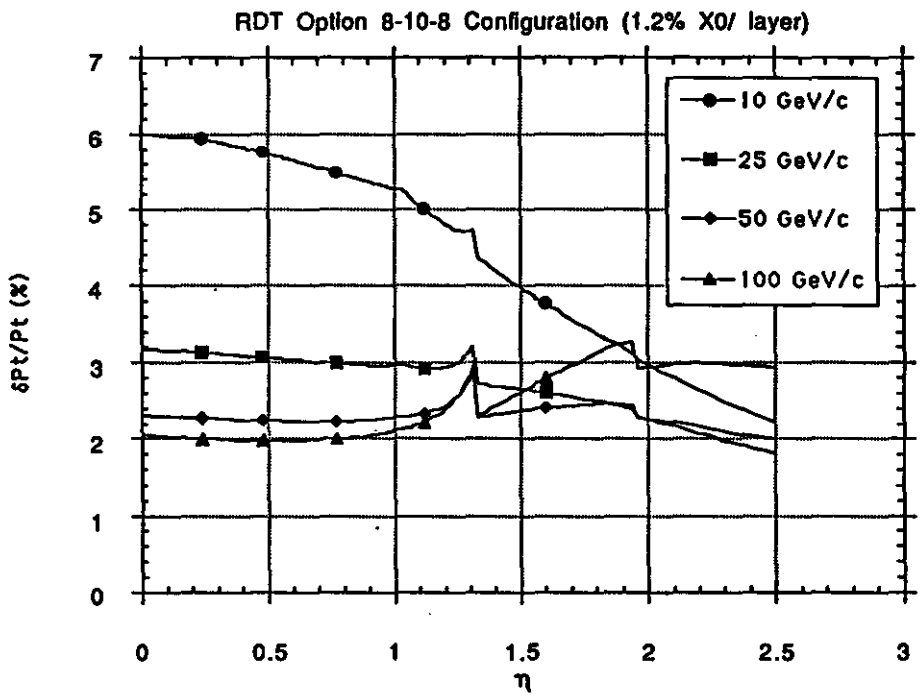

Fig. 8.2.1a

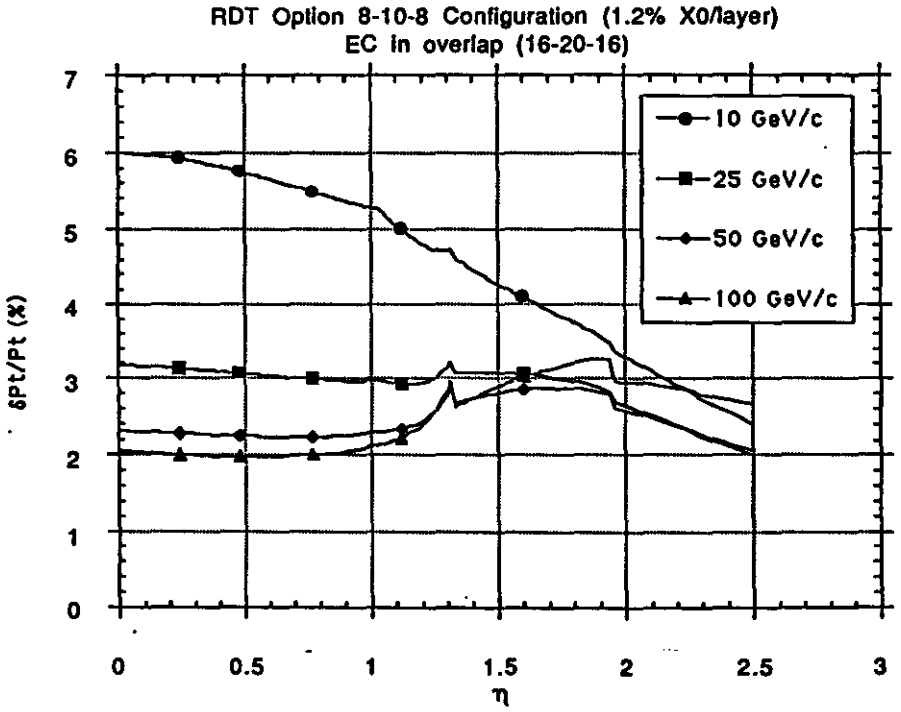

Fig. 8.2.1b

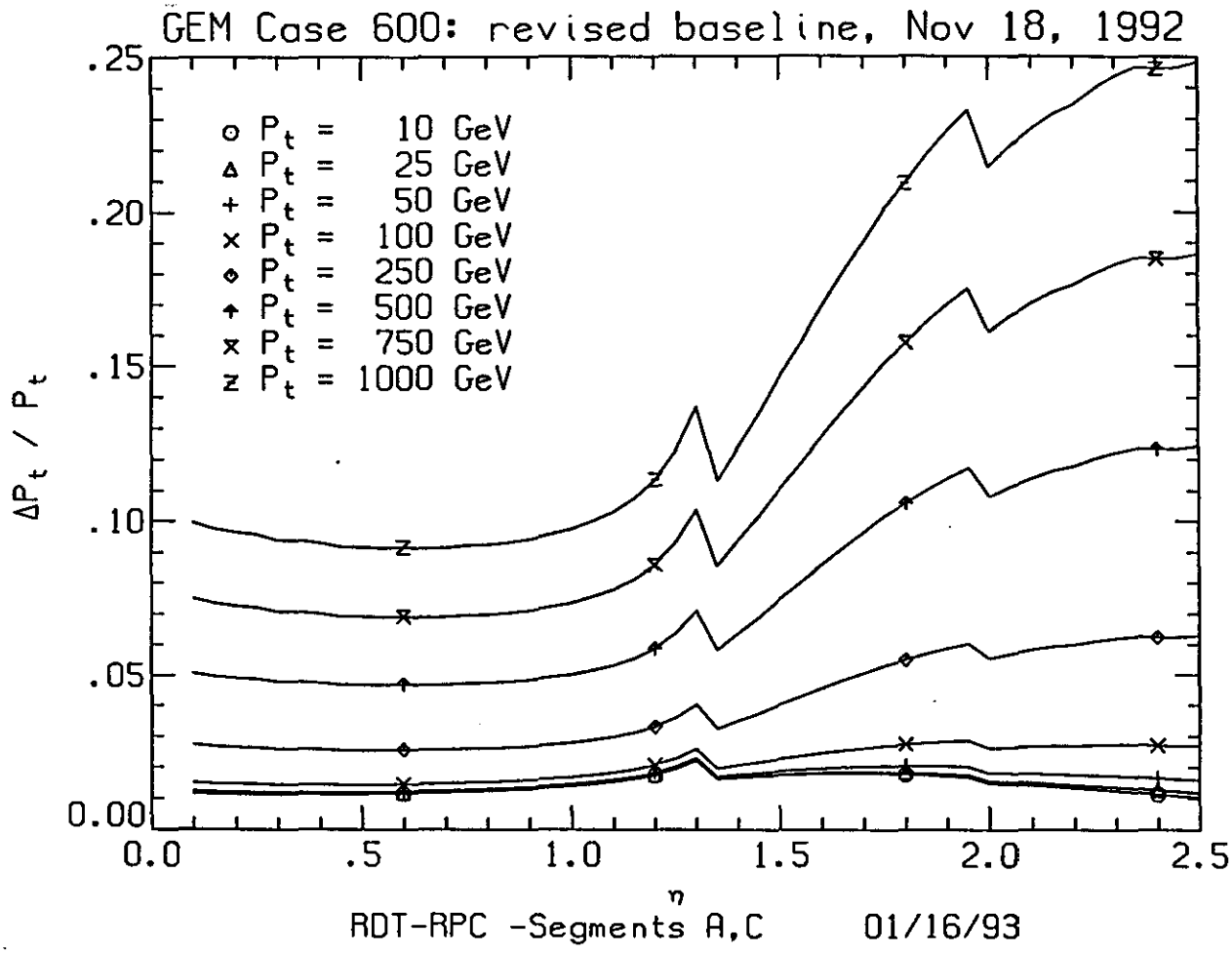

Fig. 8.2.2a

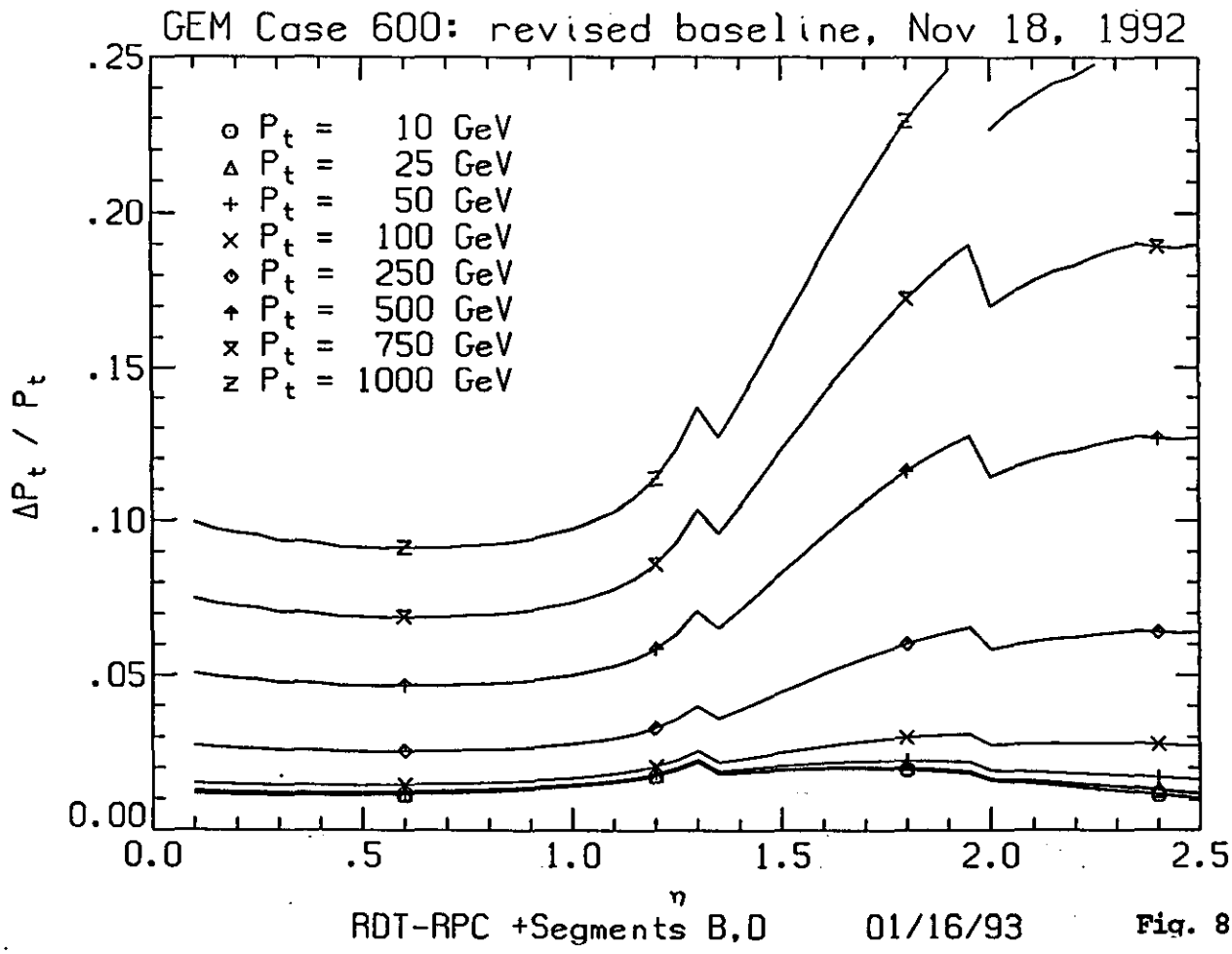

Fig. 8.2.2b

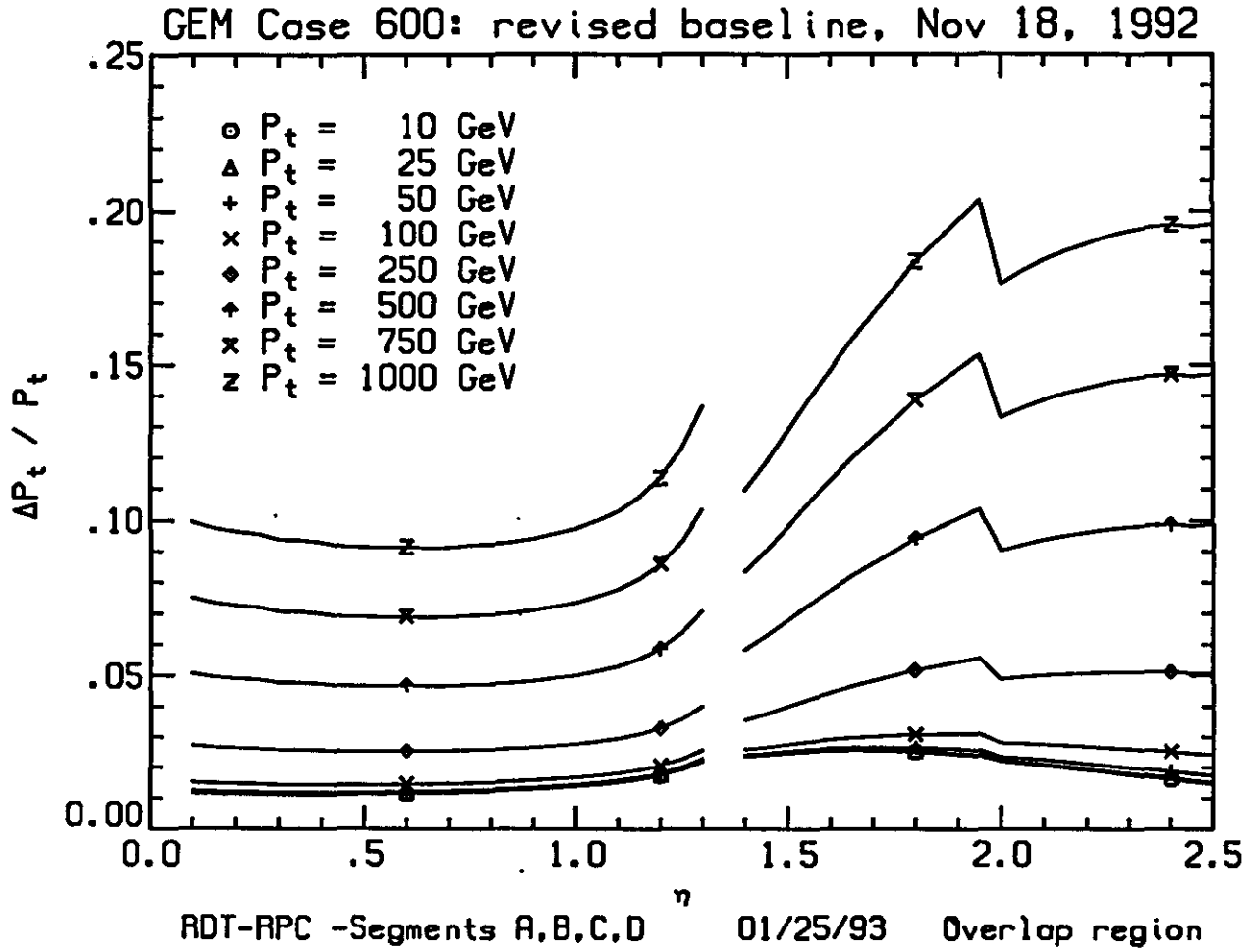
GEM Case 600: revised baseline, Nov 18, 1992
o Pt = 10 GeV
Δ Pt = 25 GeV
+ Pt = 50 GeV
× Pt = 100 GeV
◆ Pt = 250 GeV
♦ Pt = 500 GeV
✖ Pt = 750 GeV
z Pt = 1000 GeV
ΔPt / Pt
.25
.20
.15
.10
.05
0.00
0.0
.5
1.0
1.5
2.0
2.5
η
RDT-RPC -Segments A,B,C,D
01/25/93
Overlap region

Fig. 8.2.2c

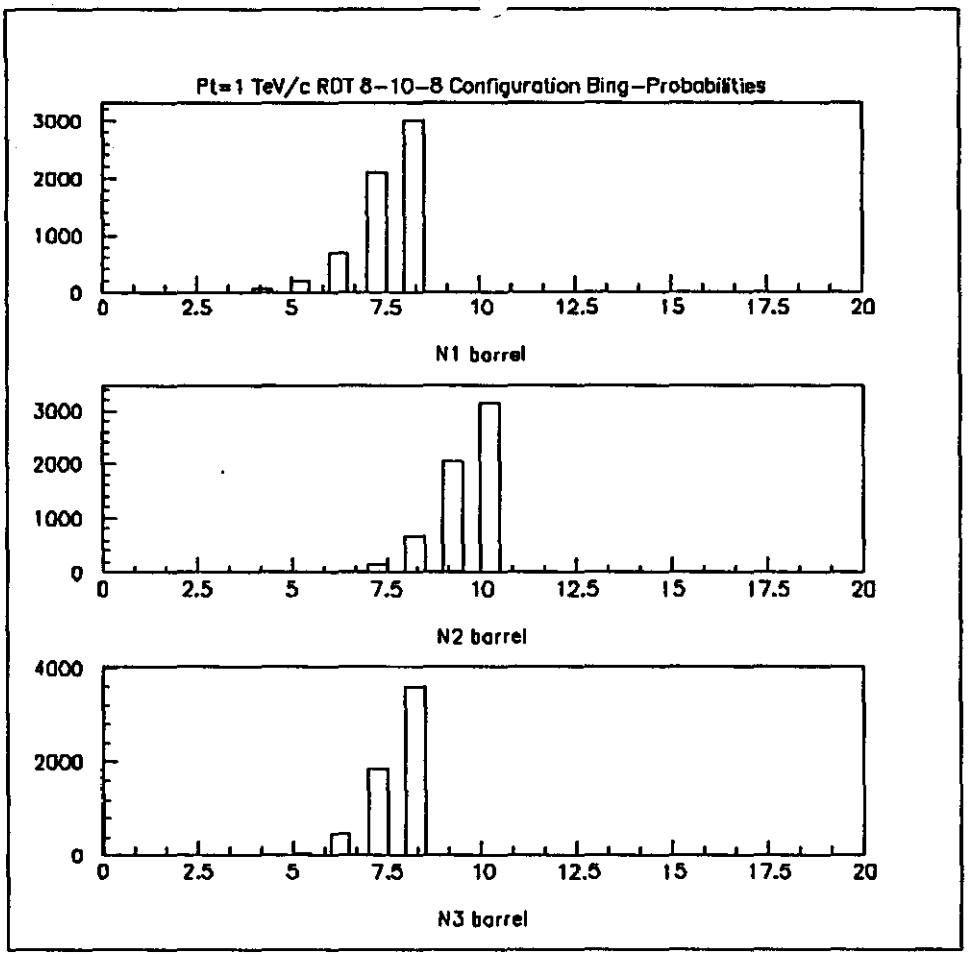

Fig. 8.2.3a

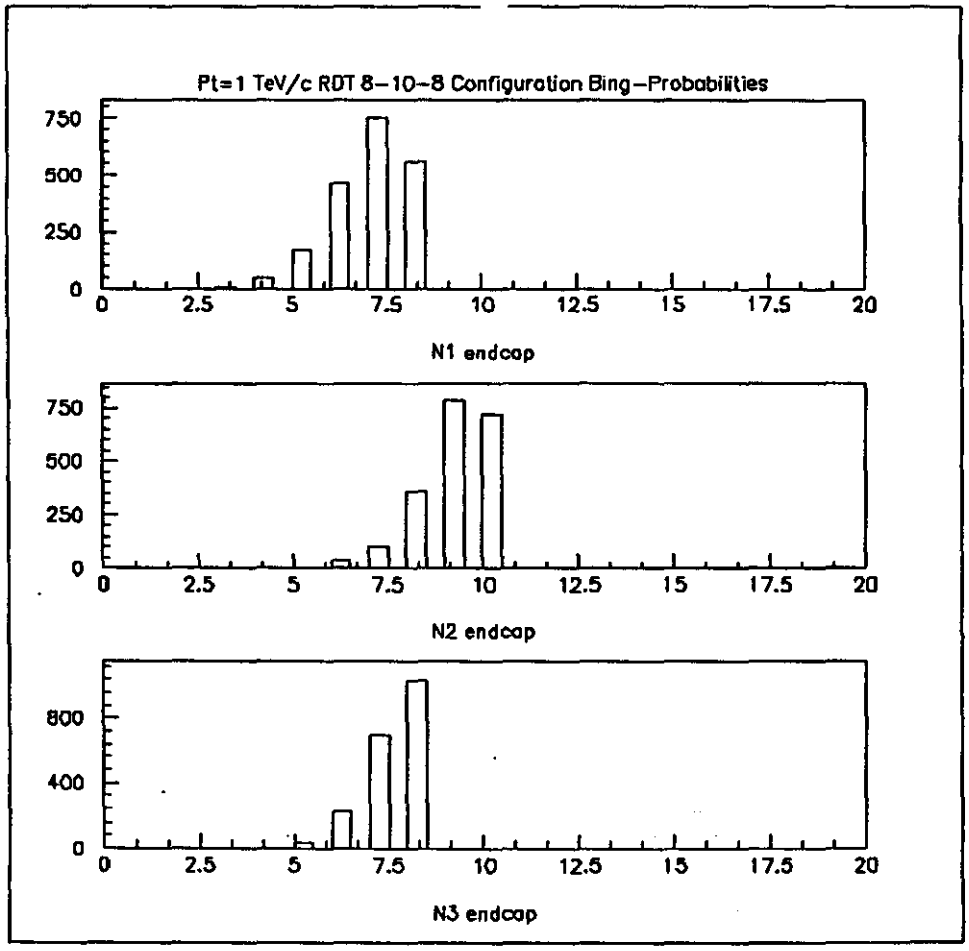

Fig. 8.2.3b

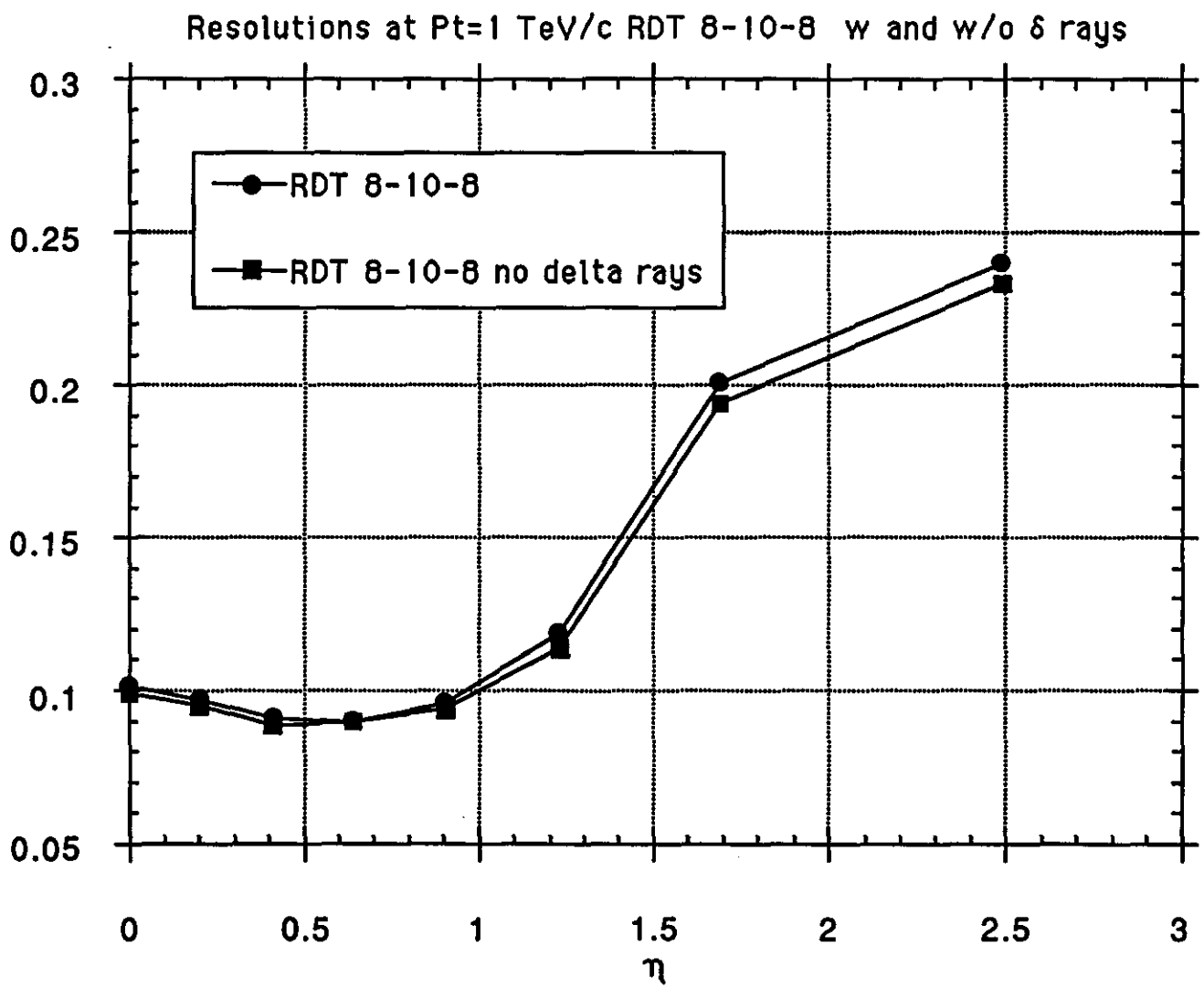
Resolutions at Pt=1 TeV/c RDT 8-10-8 w and w/o δ rays
RDT 8-10-8
RDT 8-10-8 no delta rays
0.3
0.25
0.2
0.15
0.1
0.05
0
0.5
1
1.5
2
2.5
3
η

Fig. 8.2.3c

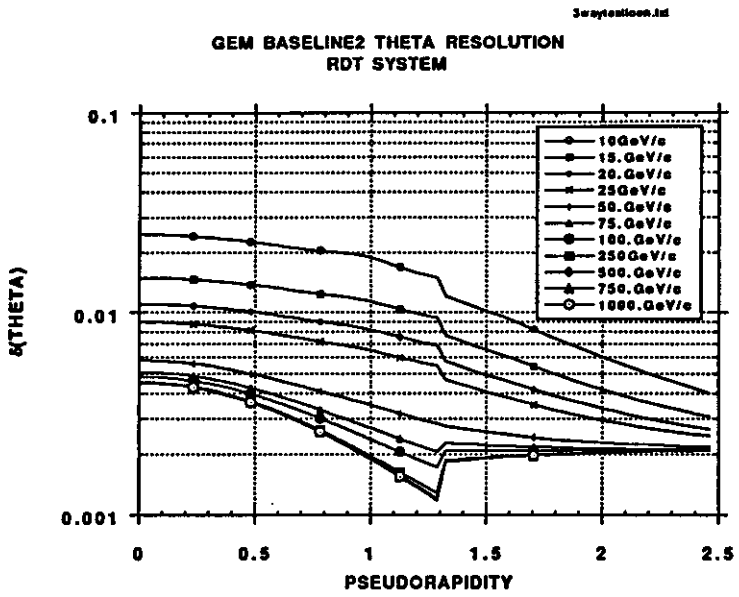

Fig. 8.2.4a

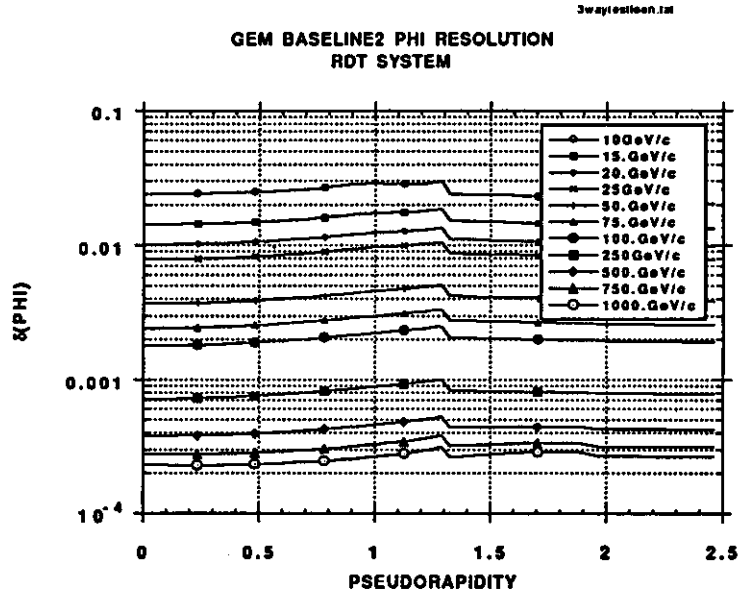

Fig. 8.2.4b

APPENDIX A

Resistive Plate Chambers for the GEM Detector Muon Trigger System

January 18, 1993

Craig R. Wuest
Richard M. Bionta
Irwin A. Pless

Lawrence Livermore National Laboratory

Massachusetts Institute of Technology

Table of Contents

A. Design 1
1. General Design Concept 1
2. Standard RPC 2
3. High Rate RPC for GEM Muon Trigger System 2

B RPC Construction 4
1. Manufacturing approach/philosophy 4
2. Component fabrication 5
3. Precision requirements 5
4. Construction procedure 6
5. Impact on truss structure design 8
6. Super-layer configuration 9
7. Electronic Packaging Requirements 10
8. Failure tolerance 10

C. RPC R&D Results 11
1. Standard Italian and Glass RPC Performance 11
2. Trigger Jitter 11
3. Neutron Sensitivity 11
4. Alternative RPC Materials for High Rate RPCs 12
5. RPC Gas Mixture Studies 13
6. Lifetime Testing of the Italian RPC 13
7. Measurements of RPC-induced Noise on RDT Systems 14
8. Measurement of RDT signals with an RPC Trigger at the TTR 14

D. Alignment 14

E. Structural Performance 15

F. Cost 15
1. Assumptions, basis 15
2. Vendor availability 16
3. Equipment, material and labor 16
4. Development, engineering, procurement/fabrication, installation/assembly 23
5. Cost Uncertainties 23

G. Strength of Supporting Group 23

H. Summary 24

I. General References 26

J. Figure Captions 27

A. Design

1. General Design Concept

Resistive Plate Chambers (RPCs) have been in operation since 1981. The current standard (Italian) design is two meters long by one meter wide with a sensitive gas gap of 2 millimeters. There are no wires or conductors anywhere in the sensitive region. The walls of the chamber - in contact with the gas of the sensitive volume - consists of a semi-conductor (Bakelite, for example) with a bulk resistance of about 10^{11} ohm-centimeters. An ionizing particle passing through the sensitive volume (2 m x 1 m x 2 mm) breaks down the gap and creates an electrical discharge. This discharge is very fast (a few nanoseconds). The discharge is capacitively coupled to pick-up strips which are located outside the semi-conductor walls of the gas cell.

When the strip is terminated with a 50 ohm load the voltage pulses across the termination are typically 0.5 volts high with a rise time of 2-3 ns. A typical full width at half height (FWHM) is about 10 ns and the measured rise time jitter is less than 1.4 ns. Figure 1 is a schematic of the "standard" Italian RPC.

RPCs are used to perform the fast triggering necessary to identify the SSC beam bunch crossing associated with a particular physics event, as well as the muon momentum trigger (Level 1 trigger) for identifying muons of sufficient momentum. In the barrel region of the GEM Detector, bunch crossing identification is performed using straight line fits of tracks registered on projective strips oriented in the phi direction (non-bend plane), with widths of 3.9, 6.5, and 8.9 cm, for inner, middle, and outer super-layers, respectively. Muon momentum measurements are made using strips of 1.3 cm width oriented along the z direction (bend plane). The strip widths are chosen to provide the necessary precision for track identification. In the case of the bunch-crossing identification, the wide strips are all that is necessary to identify a straight line track. In the case of the muon momentum identification, 1.3 cm strips are sufficient to provide sagitta measurements of the necessary precision to identify muons of particular momenta, for example, > 10 GeV/c, or > 50 GeV/c. This momentum identification is based on the measurement of the muon passage through a set of strips in the three super-layers and the strip displacement from a straight line as projected from the origin through the outer super-layer strip. The RPC strip widths in the end cap region are slightly different than in the barrel and he operation of the RPC trigger for both the barrel and end cap is described in greater detail in a later section.

Identification of tracks in an RPC is a simple matter of reading the induced charge on the cathode strips, identifying the time of arrival of the charge, and the spatial coordinates of the strip. The RPC operation (spark chamber) implies that it is essentially a digital device. The critical conditions for RPC operation are 1) stability of materials used in the RPC, 2) stability and uniformity of the gas supplied to the RPC, 3) uniformity of the gas gap within the RPC that gives rise to the spark breakdown and the subsequent induced pulse on the pick-up strips, and 4) saturated rate capability in large particle fluxes, related to the bulk resistivity of the semiconducting material used for the resistive plates. The RPC system, being a somewhat less mechanically precise system than the proposed drift tube systems, uses much simpler manufacturing methods than the precision drift tube technologies being considered for the GEM Muon System.

2. Standard RPC

The Bakelite plates in a standard Italian RPC are 2 mm thick. As stated above, the gas gap is also 2 mm thick. The edges are sealed with a strip of PVC 1 cm in width. The dimensional tolerances are modest. The thickness of the Bakelite plate is to first order not relevant for the proper operation of the RPC. The combined flatness and spacing requirements between the plates are $\pm$ 200 microns. This requirement is trivial to maintain over arbitrarily large areas by using PVC spacers 2 mm thick and 11 mm in diameter spaced on a 10 cm grid. In a test of chamber robustness, the 1 m x 2 m chamber has been operated with one corner raised by 10 cm with respect to the three opposite corners. There was no measurable change in the performance in this warped geometry as compared to the performance when the chamber is flat. This chambers has also been stood up on end with the 2 m edge vertical and then allowed to fall flat. After this mishandling the chamber worked exactly as before the fall.

Hundreds of these chambers have been produced and are operating in experiments all over the world. A set of these chambers have operated at Frascati for 7 years. Such chambers are currently being used in E-771 at Fermilab. Recently L3 at CERN has ordered 400 of these chambers from General Technica, Colli, Italy, which is a company that is a commercial supplier of RPCs.

This history has been related here to emphasize that we are not talking about a new technology, but rather a mature technology which is well understood and for which the manufacturing technology has already been transferred to industry.

3. High Rate RPC for GEM Muon Trigger System

The conditions in the GEM Detector environment demand that RPCs be capable of operating at higher rates than currently available with the standard Bakelite design. This is because there will be a large background of neutrons and charged particles in the barrel and end-cap regions of the detector. Neutron fluxes of about 10^4 Hz/cm^2 are expected, for example, in the barrel region first super-layer, with about a factor of 10 higher rate in the forward direction, at a luminosity of 10^{33} (not taking into account the possible addition of neutron shielding which could reduce the neutron flux by an additional factor of 20-30). Bakelite RPCs have been measured to have an efficiency for neutrons of about 0.5%, which implies an RPC singles rate due to neutrons of about 50 - 500 Hz/cm^2. Bakelite RPCs also have a measured rate capability at 97% plateaued efficiency of about 50-100 Hz/cm^2. Therefore, it is desired that RPCs used in the GEM Detector have higher rate capability by a factor of 10 - 100. Our R&D program indicates that this rate capability is now understood to be solely a function of the bulk resistivity of the resistive plate material.

Figure 2 shows a SPICE model of a single layer RPC. The resistive plates are modeled as a resistor and capacitor in parallel, with the resistor determined by the measured bulk resistivity of the material and the thickness. The gas gap is modeled as a simple capacitor. Table 4 (p. 12) gives a number of parameters for materials studied for RPCs. This model is used to predict the dynamic behavior of the RPC when a spark discharge occurs in the gas gap. Figure 3 shows that the model predicts a characteristic "recovery" time, associated with the re-establishment of the electric field in the plate after the discharge occurs, which varies widely for different materials. The curves in Figure 3 show the recovery time of a

region around the spark discharge in the RPC and do not represent the signal pulse shape out of the RPC. We arbitrarily define the recovery time as the time between the 10% and 90% amplitude points on the curves shown in Figure 3.

This recovery time is directly related to the saturated rate capability of the RPC as discussed below. The following is a simple model that lets one deduce the rate of a counter at a fixed efficiency given the saturation counting rate. This model usually underestimates the rate for high efficiencies.

Assume:

Rs = saturation rate
Re = rate at a fixed efficiency E

$$Re = Rs(1-E)$$

This equation is trivial to derive but it is only an approximation as it assumes a linear relation between saturation counting rate and the period of inefficiency of the counter. Note that this equation predicts that there is no rate for which a counter can be 100% efficient, which is true as every counter has to have a dead time and regardless of rate there is a non-zero probability to have two random counts within this dead time. If one assumes E = 0.95, which is the number that is normally used for this equation, then for Rs = 20,000 Hz we can assume that the counter will operate at 1,000 Hz. Because of the approximation previously mentioned, this derived rate is actually an underestimate of the real rate.

Figure 4 shows the results for saturated rate measurements for different resistive materials compared to the inverse of the recovery time. The measured rates are seen to be proportional to the calculated time response of the material, indicating that we can understand the operation of the RPC based on this simple model and the knowledge of the bulk resistivity of the material. From Figure 4 we see that two special plastics loaded with conducting polymer exhibit very high saturated rate capability compared to glasses and Bakelite, with rates approaching 15 kHz/cm^2. One plastic is an ABS-based plastic and the other is a PVC-based plastic. We have measured the dielectric strength of the ABS plastic to be superior to the PVC plastic. A number of RPCs constructed from ABS plastic have been built and tested (the largest being 1.2 m x 2.4 m). PVC-based RPCs have also been built and tested.

R&D results (detailed in a later section) from measurements performed on a number of different RPCs indicate that plastic RPCs operate identically to Bakelite RPCs with regards to pulse width, pulse height, and rise-time jitter. In addition, noise measurements have been made and the best chambers exhibit a noise rate of about 0.5 Hz/cm^2 for a 15 mV discriminator threshold. This noise rate is achieved for plastic sheet without any special surface preparation, as compared to Bakelite chambers, which require a special coating of linseed oil on the inner surfaces in order to operate. The noise rate of 0.5 Hz/cm^2 is roughly a factor of two larger than the best Bakelite/linseed oil chambers and is about 20 times the cosmic ray rate.

The ABS plastic RPC appears to exhibit some variability in operation associated with initial turn-on and subsequent voltage changes. This variability is manifested as a decrease in noise rate over time and exhibits a characteristic settling time of the order of hundreds of minutes. Once the RPC is stabilized the noise rate is reduced to the value quoted above. Another characteristic of the ABS plastic is a variability in saturated count rate associated

with turn-on and subsequent voltage changes. This variability appears to be associated with a change in the bulk resistivity of this particular plastic and is possibly due to polarization effects. For example, it is observed that the saturated rate capability of RPCs constructed from ABS plastic is reduced from about 10 kHz/cm^2 to about 1 kHz/cm^2 over a period of a few hours. Also, the noise rate drops to a final value of about 0.5 Hz/cm^2. Once the RPC reaches this point it is stable, as shown by measurements of an RPC under constant voltage over a 6-day period.

Figure 5 shows results of measurements of bulk resistivity as a function of time for different plastics with 1000 volts/mm applied across them. In general the plastics show an initial rise to a limiting value of resistivity. The ABS plastic in this figure shows a very rapid rise in resistivity compared to other plastics. Figure 6 shows measurements of saturated count rate for ABS and PVC plastic RPCs of identical construction as a function of time. The ABS count rate is reduced substantially from its initial value of about 15 KHz/cm^2, whereas the PVC count rate is reduced to a final value of about 10 KHz/cm^2. This indicates that it is possible to use plastics such as PVC in high rate RPCs and provide the necessary count rate capability for the GEM Detector.

There are a number of other semiconducting plastics that will be studied for use for high rate RPCs and it is expected that the variability discussed above will be overcome with the choice of the proper plastic. In addition, plastics with even lower bulk resistivities (in the range of 10^8 ohm-cm) have been identified. Based on our understanding of RPC operation, these lower resistivity plastics will provide RPC operation with correspondingly higher saturated rate capability – by as much as a factor of ten better than ABS plastics. In this event, sufficient rate capability for GEM will be insured even with small (less than a factor of ten) changes in resistivity. We will next describe the construction of RPCs based on these new plastic materials.

B. RPC Construction

1. Manufacturing approach/philosophy

Our manufacturing philosophy is to build as large a chamber as possible for each superlayer following the same dimensions and lay-outs as for the RDT tracking chambers. The materials used in the individual chambers should be able to be assembled into a self-supporting structure that first and foremost maintains the gas gap dimensions with a tolerance of about $\pm$ 5%, or, in the case of a 2 mm gas gap, $\pm$ 100 microns. Similar dimensional tolerances are necessary for the distance between the pick-up strip electrodes and their ground plane, in order to control the strip impedance. The gas gap is maintained by gluing 2 mm thick, 1 cm diameter disk spacers every 10 cm or so in between the laminated sheets. The strip-electrode-to-ground plane gap is maintained by using a rigid foam sheet to form the proper impedance transmission line. Because of this design flexibility the RPC can actually be deformed substantially from a flat plane and still operate correctly.

As an extreme case, the RPC could be formed into a series of concentric cylindrical shells rather than the flat sectors envisioned in GEM and theoretically provide the same operating characteristics. Thus the structural support for the RPCs can be minimized to help reduce muon scattering. The RPCs in GEM can be allowed to deform by as much as 10 cm over the largest dimensions without affecting the overall operation of the muon trigger sys-

tem, although proper support structure design can probably minimize this sag to less than 1 cm. Because materials associated with the RPC should be minimized, the addition of support frames will probably not be allowed. Also, depending on the design, RPCs could be integrated into the drift tube structure, utilizing this structure to minimize sags.

Similarly, the tolerance associated with the placement of the pick-up strips is defined by the desired measurements of timing (bunch crossing) and momentum (sagitta). This tolerance as we see it implies strips to be located also to about ± 500 microns, a not too difficult tolerance to achieve using standard commercially available techniques for metallization of mylar sheets.

Materials stability is an issue for long term performance of the RPCs. Plastics degrade over time due to out-gassing of plasticizers, interaction with ambient UV light, temperature fluctuations, radiation, and, in the case of RPCs, uniformity and stability of the bulk resistivity of the resistive plates and interaction of the plates with spark discharges. Proper materials choices and design will help to insure the long term stability of the RPCs. We can benefit from the experience of other RPC systems that show long term (years) operation of RPCs without degradation, albeit under lower rate conditions than that expected at the SSC. Aging tests are easily performed in R&D to determine the proper long term operation of RPC materials.

2. Component fabrication

Component fabrication will be based on commercially available materials of more-or-less standard sizes in order to keep costs to a minimum. For example, MiTech Corporation (manufacturers of static-dispersive plastics) can provide plastic sheet of a standard width of 48 inches (or less – they can cut to any specified width in this range) and with a length of many hundreds of meters. Plastic sheets would be cut to the necessary lengths for the particular RPC chamber dimension and then heat-welded together using a commercial process, while cross laminated with rigid foam and mylar sheet for strength. The assembly of RPC chambers is a relatively simple process of laminating layers of material together into a final structure that is then incorporated into a perimeter frame containing gas and electrical connections. In addition this frame allows for attachment points for the RPCs to the precision tracking chambers or to the superstructure of the Muon System.

Other components for the RPCs include rigid foam board, metallized mylar, glues, insulating spacers (1 cm diameter, 2 mm height) for maintaining the gas gap, gas fittings (Swage-lok), electrical connectors (LEMO or Kings K-lok, or 100 ohm twist-and-flat), high voltage connectors (SHV or GHV), and extruded aluminum channel. All these components are commercially available. Fabrication of the RPC laminates requires large area benches of approximately 4 m x 5 m at the largest for the outer super-layer.

3. Precision requirements

There are no precision requirements necessary for the RPC assembly. Standard tolerances on thicknesses of plastic sheet and other commercially available laminate materials are sufficient for the proper operation of the RPCs. The insulating disk spacers can be turned out using computerized machining with the necessary height tolerance of ± 100 microns (± 4 mils) without difficulty. Pick-up strips can be laid out by commercial methods provided

by the manufacturer of metallized mylars. Standard manufacturing processes are capable of providing the necessary dimensional tolerance of $\pm$ 100 microns.

4. Construction procedure

The chamber construction will follow the well-tested and proven Italian design. The chamber will be made up of various layers glued together to form a single self-supporting laminated plate. Spacers, consisting of 2 mm thick, 10 mm diameter Lucite disks are placed on a 10 cm square grid and serve three functions. First, they mechanically separate the two laminated plates and keep the plates flat with respect to one another. Second, they insulate the resistive plates from each other. Third, they transmit the mechanical stresses from one side of the plate to the other.

Figure 7 shows a blow-up of a two-gap RPC design. The spacers produce about a 1% dead area; however, the size and spacing of these spacers has not been optimized and should be studied using finite element analysis to assess the minimal configuration required to maintain a gas gap to the required 2 mm $\pm$ 0.1 mm. The two-gap design we have chosen eliminates this 1% dead area by having two gas gaps with the spacers in one gap staggered with respect to the spacers in the second gap. This double gap construction also has the virtue of providing practically 100% redundancy for the RPC system. We are proposing to build a three-gap RPC stack, i.e., three independent RPCs within a single chamber. The three RPCs can be used to perform a two-out-of-three coincidence with a very tight timing window of about 20 ns by virtue of the inherent speed of the RPC. This provides a very low accidental trigger rate due to neutrons and charged particles conspiring to mimic a trigger. A discussion of the trigger will be presented in a later section. In a three-gap RPC system, spacers would be staggered in such a way as to allow clear passage of a muon in at least two of the three gas gaps.

The laminated plates consist of the resistive plastic coated on one side with a thin layer of graphite paint, commonly known as Aquadag. This coating serves as an electrically transparent high voltage electrode. A thin insulating mylar sheet with pick-up strips of aluminum or copper deposited on one side (available commercially) is bonded to the Aquadag-coated side of the resistive plastic sheet. Thus the high voltage electrode is insulated from the pick-up strips by the thickness of the mylar. A rigid low-density foam board (Last-A-Foam, density 0.029 g/cm^3) is used as a mechanical stiffener as well as a dielectric for the transmission line formed by the pick-up strips and a thin foil ground plane placed on the opposite side of the foam. The foam is glued to the mylar and a thin metal foil of aluminum is glued on the opposite side. For 1.3 cm strips, such as those used in the bend plane in the barrel chambers, 5 mm thick foam is used to form a 50 ohm transmission line for each strip. This laminate process is repeated to form the four plates necessary for a two-layer RPC. Once the four plates are glued together with the spacers the laminate is quite rigid. For example, a single layer 1.2 m x 2.4 m RPC supported at its four corners sags about 1 cm at its center. A double layer RPC is expected sag even less.

Table 1 lists the breakdown of radiation lengths for the various materials in a three-gap RPC. A three-gap RPC of this construction has about 1.7% of a radiation length or about 0.55% per RPC layer.

Table 1. GEM RPC Radiation Lengths

Areal Mass: projected thickness = 0.55% X_0/layer

Material	Thickness	Rad. Length (cm)	% Rad. Length
Al	0.005"	8.9	0.14
Foam	5 mm	900	0.03
Mylar	0.005"	28.7	0.04
ABS plastic	0.020"	34.4	0.15
Gas	2 mm	Large	0
ABS plastic	0.020"	34.4	0.15
Mylar	0.005"	28.7	0.04
Foam	5 mm	900	0.03
Al	0.001"	8.9	0.03
Foam	5 mm	900	0.03
Mylar	0.005"	28.7	0.04
ABS plastic	0.020"	34.4	0.15
Gas	2 mm	Large	0
ABS plastic	0.020"	34.4	0.15
Mylar	0.005"	28.7	0.04
Foam	5 mm	900	0.03
Al	0.001"	8.9	0.03
Foam	5 mm	900	0.03
Mylar	0.005"	28.7	0.04
ABS plastic	0.020"	34.4	0.15
Gas	2 mm	Large	0
ABS plastic	0.020"	34.4	0.15
Mylar	0.005"	28.7	0.04
Foam	5 mm	900	0.03
Al	0.005"	8.9	0.14
Total:			**1.66**

The edges of the RPCs will be sealed by gluing 1 cm wide, 2 mm thick Lucite strips between the plastic plates. This stiffens the edges mechanically so that the plate is self-supporting. In addition, there will be an aluminum U-channel frame that will encompass the chamber on all four sides. This aluminum U-channel frame will be glued to the completed RPC body. The purpose of this frame is, first, to protect the edges of the RPC during shipping, handling and installation; second, to stiffen the edges so that the RPC can be mounted by four corners (if necessary); and third, to furnish the base to mount the high voltage connectors, the gas connectors, and the signal connections to the pick-up strips.
All the above technology is well understood and presents no engineering or manufacturing problems. There is a problem of availability of wide sheets of plastic. Plastic sheet comes in arbitrarily long lengths, but the standard width is 48 inches. Industrial contacts have indicated that plastic sheet such as PVC, ABS, etc. is easily joined together using heat to weld edges to each other.

Tables 2 and 3, GEM RPC Barrel Specifications and GEM RPC End-cap Specifications, contains, among many other items, the detailed breakdown of the weights. We have assumed 0.020" (500 micron) thick ABS plastic sheet. Note that from Table 2 one

Table 2. GEM RPC Barrel Specifications

Nominal Radius (m):	4.0	6.0	8.0
# of chambers	96	96	96
# of RPC layers/chamber	3	3	3
Width (cm)	167.0	255.0	342.0
Length (cm)	240.0	360.0	480.0
Total Length	720.0	1080.0	1440.0
# Bend-plane strips:	114	183	253
# Non-bend-plane strips:	166	166	166
Width of bend-plane strips (cm):	1.3	1.3	1.3
Width of non-bend-plane strips (cm):	3.9	6.5	8.9
Total number of channels - bend plane	17,696		
Total number of channels - non-bend-plane	15,936		
Total number of channels -	33,632		
Weights (lbs):			
ABS Plastic:	2496	6574	12,758
Aluminum perimeter frame:	1049	1472	2304
Cable:	385	641	963
Connectors, brackets:	1160	2855	5795
TOTAL/Super-layer	9561	11542	21820
TOTAL WEIGHT BARREL (TONS)	**21.5 TONS**		

can calculate that the weights of the individual barrel chambers are 99 lbs, 120 lbs, and 227 lbs for nominal radii of 4.0, 6.0, and 8.0 m (inner, middle and outer super-layers), respectively. Hence any chamber can be easily handled by four technicians (one for each corner) without the use of cranes or special hoisting apparatus.

It is worth noting that there are no sense wires in this technology. The pick-up strips are formed on the aluminized or copper coated mylar and is available commercially. The required precision for the strips is $\pm$ 100 microns. Once the mylar is glued into the RPC stack, the strip positions need to be known with respect to an outside fiducial with a precision of $\pm$ 2 mm. Thus the RPC is a robust device with modest precision manufacturing requirements.

5. Impact on truss structure design

The weight of the largest RPC Chamber is 227 lbs. This weight should have a negligible impact on the truss structure design. Because the dimensional tolerances of the RPC are so loose, the RPC can be fastened directly to the drift chamber systems. Hence, they should introduce no geometrical impact on the truss structure design.

Table 3. GEM RPC End-cap Specifications

Nominal Z (m):	6.0	11.0	16.0
# of chambers	64	64	64
# of RPC layers/chamber	3	3	3
Width (cm) (16 each)	150	260	370
(16 each)	140	250	370
(16 each)	70	120	180
(16 each)	75	130	190
Length (cm) (16 each)	190	330	470
(16 each)	180	310	460
(16 each)	71	130	180
(16 each)	76	130	190
# Bend-plane strips (30 degrees):	238	409	583
# Bend-plane strips (16 degrees):	186	320	486
# Non-bend-plane strips (30 degrees):	40	40	40
# Non-bend-plane strips (16 degrees):	26	26	26
Width of bend-plane strips (30 degrees) (cm):	0.6	0.6	0.6
Width of bend-plane strips (16 degrees) (cm):	0.44	0.44	0.44
Width of non-bend-plane strips (16 and 30 degrees) (cm):	3.8	6.5	9.3

Total number of channels - bend plane	71,104
Total number of channels - non-bend plane	6,336
Total number of channels - both end-caps	77,440

Weights (lbs):			
ABS Plastic:	987	2600	5046
Aluminum perimeter frame:	415	582	911
Cable:	152	253	381
Connectors, brackets:	459	1129	2292
TOTAL/Super-layer	2013	4564	8630

TOTAL WEIGHT BOTH END CAPS (TONS) 7.6 TONS

6. Super-layer configuration

The RPC system is broken up into three levels: the RPC itself, the RPC chamber, which encloses three layers of the RPC, and the RPC super-layer, of which there are three – inner, middle, and outer. The inner, middle and outer RPC super-layers form a complete RPC sector, with 16-fold symmetry in phi, and mirror symmetry about the z-axis of the GEM detector. The RPC itself consists of three layers of detectors, slightly staggered within a single chamber enclosure. This staggering is necessary to prevent trigger ineffi-

ciency due to the presence of spacers and other hardware that contribute to dead area in the RPC.

The RPC chamber is a laminate which encloses the two layers of RPC and is envisioned as an aluminum frame with thin 0.005" aluminum sheet covers. RPC chamber widths and lengths vary – 167 cm x 240 cm, 255 cm x 360 cm, and 342 cm x 480 cm, for inner, middle, and outer super-layer chambers, respectively in the barrel region. In the end cap region, there are two sets of chambers for coverage from theta = 9.75 - 16 degrees and from 16-30 degrees. The smallest end-cap chamber has dimensions of about 70 cm x 70 cm, and the largest end cap chamber has dimensions of 367 cm x 472 cm. These dimensions are identical to the dimensions of the corresponding RDT tracking chambers.

In summary, in the barrel there are 96 inner sector chambers, 96 middle sector chambers and 96 outer sector chambers with a total projected surface area of about 2,743 square meters. In the end cap there are 192 chambers grouped into 3 families of sizes distributed over the three super-layers. The total projected surface area is about 1,078 square meters.

Tables 2 and 3 provides estimates of the weight of the chambers in each super-layer sector including the RPC itself, the RPC chamber enclosure with aluminum perimeter frame, RPC perimeter cable weight with an additional 10% added in each super-layer for connectors, brackets, etc.

Summarizing, the inner super-layer weight is 9561 lb., the middle super-layer weight is 11542 lb., and the outer super-layer weight is 21820 lb. The total weight for the RPC subsystem is 21.5 tons for the barrel RPC system, or about 1.3 tons per sector. In the end-cap region the total weight for both end-caps is about 7.6 tons.

7. Electronic Packaging Requirements

As presently designed, there will be no electronics inside the magnet. All that is required is high voltage connectors, gas connectors and connectors for strip signals to be carried on cable. One possibility is to configure the strips for 50 ohm impedance and to carry the signals on RG-174/U 50 ohm coaxial cable. Another possible configuration is to use 100 ohm strips coupled to 100 ohm twisted wire pairs (commonly available in ribbon cable called twist-and-flat cable). This configuration could significantly reduce cable weight and volume as well as cost, however it has not yet been tested in an RPC.

8. Failure tolerance

As stated previously, the RPC is a very rugged reliable device without sense wires or regions of high fields. However, failures can occur. In case of a failure one half of the double RPC would fail. Because of this possibility, we operate each RPC gap as a separate chamber. The loss of one RPC gap means a decrease of efficiency of 1%. This is negligible from any practical point of view. Therefore we can state that the RPC system is, for practical purposes, 100% redundant and that any single failure has a negligible effect on the practical efficiency of the system.

Another way of looking at this situation is to suppose one gap fails per year. This is more than two orders of magnitude higher failure rate than is indicated by our current experience. Under this assumption one can show that the probability of two gaps failing in the same RPC chamber in ten years of operation is less than 10%.

C. RPC R&D Results

RPC R&D has been carried out using a multi-faceted approach with the goal being to completely characterize the RPC operation and applicability to the GEM Muon System. R&D has focused on studying the existing state-of-the-art as exemplified by the standard Italian design already described, as well as new RPCs using non-standard materials and fabrication methods, with an emphasis on reduced mass, stability and long term performance, and increased rate capability.

1. Standard Italian and Glass RPC Performance

MIT and LLNL have now studied a number of different RPC designs, including a 1 m x 2 m RPC provided by R. Santonico of the University of Rome, glass RPCs, cermet thin film RPCs and RPCs using a number of low resistivity materials such as static-dispersive plastics. Extensive testing of the Italian RPC, a custom built glass RPC, and, very recently, a plastic RPC, has been carried out at MIT, including measurements of efficiency, rise-time jitter, and response to neutrons, and the results of some of these tests are detailed in Reference [8]. LLNL has also performed similar measurements on smaller glass RPCs.

In summary, the MIT and LLNL glass RPCs (resistivity = 5×10^{12} ohm-cm), with their relatively high bulk resistivity, exhibit a reduced rate handling capability and a reduced efficiency (70% for the MIT RPC with 2 mm glass and 90% for the LLNL RPC with 750 micron glass). The Italian Bakelite RPC (resistivity = $1\text{-}2 \times 10^{11}$ ohm-cm) exhibits about 95% efficiency using cosmic rays and a scintillator telescope for triggering. The Italian RPC has a measured saturated counting rate of about 560 Hz/cm^2 compared to a rate of about 50 Hz/cm^2 for the MIT glass RPC (75 Hz/cm^2 for the LLNL glass RPC). On the other hand, these different RPCs agree remarkably well in terms of pulse characteristics, e.g., pulse height, pulse width, rise time and pulse velocity along the strip.

2. Trigger Jitter

Trigger jitter measurements on the Italian RPC show time jitter on the order of 1 ns. The MIT glass RPC exhibits a larger jitter of about 7 ns due to the inability to achieve an adequate high voltage across the gas gap as detailed in Appendix 3. Trigger jitter measurements have also been performed on plastic RPCs using strontium-90 betas (2.3 MeV endpoint energy). For a 6 cm x 6 cm RPC the jitter was measured to be 5 ns.

3. Neutron Sensitivity

Neutron sensitivity measurements were made using a strong Cf-252 source. The sensitivity of the RPC to 1-10 MeV neutrons is measured to be 4.8×10^{-3} and to 1-10 MeV photons to be 6.6×10^{-3}.

Table 4. RPC Resistive Materials Properties

Material	Thickness (cm)	Bulk Resistivity (Ω-cm)	Arc Resistivity (Ω-cm^2)
MIT mirror glass	0.300	5.00×10^{12}	1.50×10^{12}
LLNL mirror glass	0.066	4.90×10^{12}	3.23×10^{11}
Kodak projector glass	0.123	6.42×10^{11}	7.89×10^{10}
Italian RPC Bakelite	0.200	1.00×10^{11}	2.00×10^{10}
LLNL Bakelite	0.161	4.50×10^{9}	7.24 x 108
Abstat-M310 plastic	0.072	5.78×10^{9}	4.16×10^{8}
Abstat-M310 plastic	0.060	5.78×10^{9}	3.47×10^{8}
MiTech-411 plastic	0.090	2.03×10^{9}	1.83×10^{8}
MiTech-411 plastic	0.030	2.03×10^{9}	6.19×10^{7}
Corning 0211 glass	0.056	6.70×10^{7}	3.75×10^{6}
Boron film	0.0001	1.00×10^{6}	1.00×10^{2}

4. Alternative RPC Materials for High Rate RPCs

RPCs have been fabricated at LLNL using sputtered resistive cermet thin films on thin glass or plastic substrates. We have demonstrated that Cermets can function as RPCs, however the long term aging characteristics of these thin films is not clear. Indications are that the films are not strongly bonded to the substrate and are subject to sputtering effects because of ion bombardment. Alternative materials to Bakelites have been explored, concentrating on static-dispersive plastics with low bulk resistivities in the range 10^8 - 10^{11} ohm-cm. We have successfully demonstrated RPCs with a number of different plastics. Five 0.5 m x 0.5 m RPCs, and one 1.2 m x 2.4 m RPC have been built using low resistivity plastic materials. All RPCs are single dimension read-out with 1.3 cm strips, and one of the small RPCs, is built with 2 dimensional read-out. Table 4 summarizes the properties of a number of materials used to make RPCs, including Bakelites and glasses.

We have measured the saturated counting rates from two different static-dispersive plastics, MiTech-411, a PVC plastic and Abstat-M310, an ABS plastic. For the case of the MiTech-411 plastic, our SPICE model predicts a saturated counting rate capability of about 2.3×10^4 Hz/cm^2. We have assembled a number of RPCs with this material and in fact measure a count rate of approximately 1.5×10^4 Hz/cm^2. Figure 8 plots the counting rate versus high voltage for an RPC made with MiTech-411 plastic. This rate has not been determined to be saturated and further work is in progress to determine the absolute saturated count rate of the RPC with this very interesting material.

This count rate is substantially larger than any other RPC materials measured to date, and constitutes a significant improvement in the state of the art. In addition, the Abstat M310 plastic has a significantly higher dielectric strength than the PVC-based MiTech-411 plastic. Large area RPCs have been constructed using thinner plastic sheets than those used initially (500 microns versus 720 microns), which could potentially give an increase of 5 - 10 times the rate of the earlier versions of the plastic RPCs. Measurements of efficiency of large area plastic RPCs show that they operate at or near the full geometric efficiency expected, about 98%.

5. RPC Gas Mixture Studies

Also, systematic studies of gas mixtures on RPC performance (plateau voltage, efficiency, noise, pulse height, etc.) have been performed for large area plastic RPCs. RPC operation is highly dependent on the gas that is used. Standard RPC gas mixes are a mix of argon, isobutane and freon in a ratio of about 60%/38%/2%, respectively. We have begun a detailed study of RPC operation for different gas mixtures. For example in Figure 9 we see the efficiency of an RPC as a function of the percentage of isobutane, in an argon/isobutane mix without freon. The efficiency and position of the plateau is seen to be sensitive to the amount of isobutane. Figure 10 shows the effect of isobutane concentration on pulse amplitude. For isobutane concentrations above about 40%, there is no difference in pulse height, indicating RPC operation in limited streamer mode. Figure 11 shows the effect of adding Freon 13B1 (2.5%) to a mix with argon with 40% isobutane. The effect of adding Freon is to increase the efficiency to nearly 100% and to flatten the plateau. Figure 12 shows that the pulse height is decreased somewhat when Freon is added.

As part of the R&D program, we have continued these gas studies with the goal finding a gas that is nonflammable and contains no freon. This is important for safety reasons and also because it is unlikely that Freon 13B1 will available in the future due to its high environmental ozone depleting characteristics. Figure 13 compares RPC pulse shapes for a 0.5 m x 0.5 m ABS plastic RPC with flammable and non-flammable gas mixtures. The gas mixtures are 66% argon/30 % isobutane/ 4% Freon (flammable) and 55% argon/31% CO_2/10% isobutane/4% Freon. The latter gas mixture is considered non-flammable because of the low isobutane concentration. As can be seen from Figure 13, there is little difference in pulse shape or height. Figure 14 shows a set of efficiency plateaus for different discriminator thresholds for the non-flammable gas mixture. The efficiency is near 100% and is essentially the same as for RPCs run with flammable gas mixtures. Figure 15 shows a comparison of time jitter measured for 4 strips on the RPC with the flammable and non-flammable gas mixures. The time jitter is slightly worse – 6 ns versus 5 ns – for the non-flammable gas mixture, compared to the flammable gas mixture. The tails in the distribution are due to pulses on adjacent strips inducing signals on the strip in the cosmic ray telescope area and would be eliminated by fully instrumenting all the strips on the RPC with TDCs and tagging all cosmic rays.

6. Lifetime Testing of the Italian RPC

Lifetime (aging) tests have also been performed using the Italian 1 m x 2 m Bakelite RPC. We chose an area of this RPC approximately 5 cm x 10 cm which was irradiated with a radioactive source. The counting rate on this area was approximately 250 Hz/cm^2. We placed a cosmic ray scintillation counter telescope which had approximately the same 5 cm x 10 cm area over the chosen area of the RPC. We chose the RPC region so that one of the PVC spacers was contained in the area.

We define one SSC year (at a luminosity of 10^{33}) to be 2 x 10^7 counts per square centimeter. This is the expected neutron interaction rate at the 10^{33} luminosity. We accumulated 16.4 x 10^7 counts per square centimeter in our test, which is equivalent to 8.2 SSC standard years. The data is shown in Figure 16.

Before irradiation the chosen area had an efficiency of 93.6 $\pm$ 3%. The fact that the measured efficiency is not about 97% is a reflection of the mismatch between the cosmic ray hodoscope and the RPC area. After an irradiation equivalent to 8.2 SSC years of operation, we measured the efficiency of this area to be 92.4 $\pm$ 3%. As can be seen from Figure 16, within the 3% errors, we find no change in efficiency for the equivalent 8.2 SSC year exposure at a luminosity of 10^{33}.

7. Measurements of RPC-induced Noise on RDT Systems

A number of measurements of RDT sensitivity to RPC signals have been made at the Texas Test Rig (TTR) at SSCL. Measurements have been made using both the Italian 1m x 2m RPC installed in the TTR and 0.5 m x 0.5 m plastic RPCs. Both MSU (4 cm diameter) and Dubna (2.5 cm diameter) RDT systems have been measured as well as the UH cathode strip chambers. Measurements of signals induced on RDT wires were made by examining the signals off the wires on an oscilloscope while triggering on RPC signals. The MSU RDT system contained amplifiers with x1000 gain, whereas the Dubna RDT system was unamplified. The RPC was placed approximately 1 m, and 2 m from the MSU and Dubna RDTs, respectively. Under these conditions, no induced signals were observed at a level of 5 microvolts and 2 millivolts for the MSU and Dubna RDTs, respectively. Also, no induced signals were observed on the UH CSC system at a level of 5 microvolts.

Another measurement was made by measuring the effect of RPC operation on RDT singles rates. In the case of the MSU RDTs, no increase in singles rate was observed for either the Italian RPC or the LLNL RPC as these RPCs had their voltages increased. In this case the singles rates of the RPCs increased by three and five orders of magnitude, respectively, as their voltages were increased from 6 kV to 8 kV. Similar measurements were made for the Dubna RDT and the UH CSC for the Italian RPC only. Again, no increase in singles rates were observed for a wide range of RPC operating voltages.

8. Measurement of RDT signals with an RPC Trigger at the TTR

A 0.5 m x 0.5 m ABS RPC has been used to provide the start time trigger for the MSU RDT system at the TTR. In this test, the RPC was positioned directly above the RDT system. RPC signals were used to form the start time for the RDT system in a similar manner to the TTR scintillator trigger system. RDT signals were used to generate stop times for the cosmic ray muon tagged by the RPC. Figure 17 shows a distribution of stop times with respect to the RPC trigger. The distribution shows an uncorrected sigma of 6.9 ns. The data is uncorrected for difference in transit time from the RPC to the RDT due to the different entry angles of the cosmic ray muons.

D. Alignment

Because of the previously mentioned performance criteria for RPCs as a Muon System trigger, precision alignment is not necessary for these chambers. The RPCs can be mounted either separately from the precision drift tube technology, or co-located with the drift tubes. It is assumed during construction that sufficient care in fabrication will allow strips to be located with an accuracy of about 0.1 mm with respect to a fiducial placed on

the edge of the RPC support frame. Sag in the RPC will be within the limits imposed for proper muon timing and momentum determination so that monitoring of the sag will not be necessary.

In-situ RPC alignment can be performed using cosmic rays or physics events at the SSC. In addition, if the RPC system is incorporated into the drift tube structure, alignment will be coupled to the drift tube alignment system without added cost. This is because the RPC strip readout is referenced to a fiducial that can be referenced to the drift tube alignment system. In any event, RPC location to 2 mm in Z and Φ, and 1 cm in R is sufficient to insure proper operation for Level 1 triggering.

E. Structural Performance

A first attempt at modeling the RPC structural performance has been made at LLNL. A double layer plastic RPC was modeled using the following assumptions:

1. RPC sandwich assumed to be 3500 mm x 5500 mm x 0.20 inch plastic sheets with 10 mm diameter, 2 mm thick disk spacers every 10 cm. Last-a-foam sheet, 5 mm thick on bend plane side, 35 mm thick on non-bend plane side.

2. Lucite frame.

3. Support fixed at four corners.

4. Sandwich bonded to frame and stiffeners.

5. FEA model has stiffeners on one side only but with 2x section modulus.

6. Plastic properties: $E = 1.239 \times 10^4$ N/mm^2, density = 1.87×10^{-5} N/mm^3

Deflection under the RPC's own weight is 1.09 cm. Frame stress is less than 25 ksi. The fundamental frequency is estimated to be less than 10 Hz. In addition, there is ample room to increase stiffener cross-sections and to increase frame heights. If the RPC is mounted on the drift chamber, then calculations will be needed to establish the deflection of the drift chamber due to the added load of the RPC. It is likely that this added load will not adversely effect a properly designed drift chamber system.

F. Cost

1. Assumptions, basis

The cost of the RPC system has undergone a series of refinements starting with studies begun in October, 1991. In this time three additional cost studies have been performed, culminating in the Cost Estimate prepared on September 11, 1992 as part of an engineering review of the muon system technologies held at SSCL in September, 1992. This costing was performed for both the Bakelite design and an alternative Cermet thin film design that held promise for reduced weight. R&D on the Cermet concept is continuing; however there

is now sufficient data to indicate that plastic sheets of the proper resistivity can offer the desired performance and weight reductions without resorting to the exotic thin film technologies needed to fabricate Cermets. The September 11 costing reflected a Bakelite system using 15 mil thick sheets of Bakelite material for the resistive plates. The costing presented here assumes 20 mil plastic sheet bonded to rigid polyurethane foam board. We assume a cost of $300/m^2 for structures associated with RPCs although a detailed design for the structure has not yet been made.

2. Vendor availability

RPCs have been manufactured in large quantities by Italian University groups for many years. In fact, we have performed a large part of our R&D on an Italian RPC with dimensions 1 m x 2 m at MIT. A factory to build these RPCs is already in place and is capable of building RPCs to our specifications with minor modifications to their manufacturing process to take into account our new materials. If the need arises the manufacturing of RPCs could be carried out in the US at LLNL or MIT or also in China. Tsing Hua University in Beijing has written a Letter of Intent with the GEM Detector Collaboration to perform a number of manufacturing services for the various sub-systems including electronics for calorimeter and muon systems, as well as structural component assembly for calorimetry and the muon system. In addition, the Institute for High Energy Physics (IHEP), also in Beijing, has expressed interest in manufacturing Resistive Plate Chambers for GEM.

3. Equipment, material and labor

Based on our experience with the various cost reviews held in 1992, we have attempted to revise our cost estimate to reflect new design changes and also to incorporate more "realistic" cost estimates based on vendor quotes.

Design changes have occurred that radically alter the RPC concept. This is based on new experience with the "Italian" RPC now in testing at SSCL, and with the construction of a number of large area plastic counters at LLNL. It has been realized that a rigid, gas-tight box of aluminum honeycomb is not necessary. In addition, a new cabling scheme has cut the amount of cabling substantially.

In the process of revising the cost estimates, manufacturer's quotes were used for the resistive plastic sheet and for rigid foam board. ABS plastic sheet is priced at $6/lb and foam sheet is $2/lb. For all estimates we have now included stainless steel tubing and Swage-lok fittings, LEMO connectors, and cabling to the edge of the magnet. Additionally, we assume that the electronics cost is specified by the Trigger and Data Acquisition Group cost estimate.

We estimate the total projected surface area of the RPC system to be 3,821 m^2 consisting of two (somewhat redundant) concentric layers of RPCs in each super-layer for the barrel and end-cap region.

With our more accurate description of the RPC system, we find that the cost is $3M for the full RPC system (no electronics cost included). So the cost of the RPC system will be about $700 per square meter (the RPC itself is about $200/m^2). The breakdown of the cost is follows

For a 3,821 m^2 system, the total cost would be about $2.8M. The largest uncertainty is in the structural support and integration cost estimate. For completeness we will take the cost of electronics to be $11/channel (same as for other muon chamber electronics) x 111K channels = $1.22M, although this cost does not appear in the WBS worksheets. Thus a conservative estimate for the total cost with electronics is about $5M.

Standard Bakelite RPC design

	Item	Cost ($/$m^2$)	Total Cost ($K)
1.	Aluminum U-channel	4.3	16.4
2.	Resistive plastic sheet (6 per chamber)	39.4	150.4
3.	Foam (e.g. polyurethane sheet, 15 mm average thickness, 6 sheets per chamber)	49.5	189.0
4.	Aquadag	22.5	85.9
5.	Aluminized Mylar sheet	20.5	78.3
7.	Spacers , glue	0.48	1.8
	Total Materials	136.7	521.8

	Cost ($/$m^2$)	Total Cost ($K)
Total Materials (x.25 for mach'g and waste):	**170.9**	**652.3**

	Item	Cost ($/$m^2$)	Total Cost ($K)
8.	Fabrication cost estimate: $60/hr @ 1$m^2$/hr	60.0	229.3
9.	Gas fittings (edge x 2 for gas manifold)	6.4	24.5
10.	Steel tubing (1/4" diameter, 20 km long)	22.1	84.4
11.	RG-174 coaxial cabling (160 km)	12.3	46.8
12.	Connectors (3 x 111K channels)	77.3	295.3
13.	Gas (Recirculator)	65.4	250.0
Total	**Miscellaneous**	**243.5**	**930.4**

Subtotal:	Cost ($/$m^2$)	Total Cost ($K)
Materials, Fab., Gas system, Electrical system	**414.4**	**1582.7**

Thus the total cost is $1.6 M for a 3,821 m^2 three layer RPC barrel plus end-cap system. We will conservatively estimate the cost of any RPC specific structural support to be $300/$m^2$ which is probably a gross overestimate and so zero contingency is assumed for this. Contingency for materials is set to be 5% and contingency for labor is assumed to be 100%.

	Cost ($/m^2)	Total Cost ($K)
RPC Materials, Fab., Gas system	414.4	1582.7
Structural supports and integration with drift tubes	300.0	1146.3
Materials contingency (5%)	15.85	60.6
Labor contingency (100%)	60.00	229.3

	Cost ($/m^2)	Total Cost ($K)
TOTAL	**790.3**	**3018.9**

The two Cost Estimate Worksheets: WBS # 3.2.1.2.4.1.3 and WBS # 3.2.1.2.4.1.5 have been revised to reflect these new costs. Percentages are broken down differently than was done in the previous worksheets to reflect what we think is a more realistic percentage for Materials, Machining and Fab/Ass'y. The total Materials cost is now about $171/m^2. Taking 25% of this number for machining and waste gives $43/m^2 and we still use $60/m^2 for Fab/Ass'y. This gives the percentages: 54%, 13%, and 33%, respectively, which are used for the basis of estimates in WBS # 3.2.1.2.4.1.3 and WBS # 3.2.1.2.4.1.5.

MUON SYSTEM
COST ESTIMATION WORKSHEET

WBS Element Title: Barrel and End-cap Region Sector Assembly; RPCs; Off-Site; Assembly
WBS Element No: 3.2.1.2.4.1.3 **Date:** 08 Jan 93 **Rev:** 4 **Estimator:** T. Hamilton, C. Wuest

---

Scope: This element covers the labor and labor cost for the assembly of the RPC chambers, and the purchase and labor cost for assembly equipment.

Engineering/Design **PY:** **Comp. Rate($K/PY):** **PoP:**
N/A

M&S: Engineering/Design and Inspection/Administration ($K): 14

Misc. office supplies for Administration:	$6K
PC/Mac/workstation charges:	$8K

Inspection/Administration **PY:** 2.25 **Comp. Rate($K/PY):** 133 **PoP:** 7/94-6/96
Assumes Eng (nat'l avg) oversight of assy equipment purchase activity: 1 eng, full-time for 3 mos = .25 PY from Weinstein/Osborne estimate: ('cost of production')
- reduced to 76% (for central region only), actually time-scaled reduced from 36 to 24 mos (67%)
- Eng (nat'l avg) oversight of assembly activity: 1 eng, full-time for 2 years = 2.00 PY

Procurement/Fabrication Material **($K):** 300
LSDT/Weinstein/Osborne estimate was $365K + $50K misc

- assumed misc assy equip:	$250K
- assumed misc nuts/bolts, pins, etc.:	$50K

Installation/Assembly **PY:** 7.6 **Comp. Rate($K/PY):** 112 **PoP:** 7/94-6/96
LSDT/Weinstein/Osborne estimate was 1 PY Eng, 1 PY Sr. Tech for machine set-up
- assumed same for RPC estimate
from Wuest/Pless estimate:
- $60/m^2 x 3821 m^2 = $229.3K/$107K/PY(sr. tech, nat'l avg) 2.1 PY
-for assembly: Wuest/Pless estimate of $300/m^2 was prorated against materials, machining, and assembly based on percentages established on Page 3 of Wuest/Pless "Second Order" estimate: $300/m^2 x 3821 m^2 x 33% = $378.3K/107K/PY 3.5 PY

Material: Installation/Assembly **($K):** 6

Misc. office supplies for Install/Assembly:	$6K

Contingency **Total:** 38

Technical:	0	Basis:	none
Cost:	30	Basis:	engineering judgment, labor rate & material concern
Schedule:	8	Basis:	delays completion of critical path item

Comments

Because all costs were given in $/m^2, all labor rates/categories were assumed to be national average. This assumption is reflected in the PY labor loading. If lower rates were assumed by Wuest/Pless, the labor loading would be higher.

MUON SYSTEM
COST ESTIMATION WORKSHEET

WBS Element Title: Barrel and End-cap Region Sector Assembly; Plastic RPCs; Off-Site; Machining/Inspection
WBS Element No: 3.2.1.2.4.1.5 **Date:** 08 Jan 93 **Rev:** 6 **Estimator:** T. Hamilton, C. Wuest

---

Scope: This element covers the labor and labor costs for the machining and inspection of the Plastic RPC and assembly fixturing. Also, costs for oversight and purchasing of stock and material for machining.

Engineering/Design **PY:** **Comp. Rate($K/PY):** **PoP:**
N/A

M&S: Engineering/Design and Inspection/Administration ($K): 45

Misc. office supplies for Inspection/Administration:	$15K
PC/Mac/workstation charges:	$22K
Travel: 1 person, 4 trips to machine shop, inspection shop @$2K/trip	$8K

Inspection/Administration **PY:** 6.19 **Comp. Rate($K/PY):** 72 **PoP:** 1/94-3/96
Assumes Engineering (nat'l avg) oversight of stock/material purchase activity: 1/4-time for 24 mos=.50 PY
Assumes Engineering (nat'l avg) oversight of mach'g & inspect activity: 1/2-time for 2.25 yrs = 1.13 PY
Assumes Sr. Tech (job shop) performing inspection activity: 1 tech, full-time for 2 yrs = 2.00 PY
Assumes Jr. Tech (job shop) performing inspection activity: 1 tech, full-time for 2 yrs = 2.00 PY
- no inspection cost estimate provided from Wuest/Pless
- estimate of $100K (approx. 2 PY) for inspection from Weinstein/Osborne estimate approx doubled

---

Procurement/Fabrication Material **($K):** 1,141
from Wuest/Pless "Second Order" estimate: Wuest/Pless cost estimate multiplied by 3821 m^2 for barrel plus e cap regions

Aluminum U-channel:	$16.4K
Resistive plastic sheet (six sheets, 0.020 inch):	$150.4K
Foam sheet (six sheets 15 mm on average):	$189.0K
Aquadag:	$85.9K
Aluminized mylar (0.005"):	$78.3K
spacers, glue, etc:	$1.8K
material for structural support:	$619K

- for structural support material: Wuest/Pless "Second Order" estimate of $300/$m^2$ was prorated against materials, machining, and assembly based on percentages established on Page 3 of Wuest/Pless "Second Order" estimate : $300/$m^2$ x 3821 m^2 x 54% = $619K

- general M&S (nuts, screws, gas fittings, elect. connectors):	$260K
- fixtures stock (ss tubing, coax cable):	$119.6K

Installation/Assembly **PY:** 12.5 **Comp. Rate($K/PY):** 75 **PoP:** 1/94-12/95
from Wuest/Pless "Second Order" estimate:

RPCs Machining
1.) $43/m^2 x 3821 m^2 = $164.3K/$74.5K/PY = 2.2 PY
2.) for structural support machining: Wuest/Pless estimate of $300/m^2 was prorated against materials, machining, and assembly based on percentages established on Page 3 of Wuest/Pless "Second Order" estimate $300/m^2 x 3821 m^2 x 54% = $619K/$74.5K/PY = 8.3 PY
Assumed assembly fixtures: 2 machinists, full-time for 1 year: 2 PY = 12.5 PY total

Material: Installation/Assembly **($K):** 18
Misc. office supplies for Installation/Assembly: $18K

Contingency **Total:** 38

Technical:	0	Basis:	none
Cost:	30	Basis:	engineering judgment, labor rate & material concern
Schedule:	8	Basis:	delays completion of critical path item

Comments

4. Development, engineering, procurement/fabrication, installation/assembly

Research and development will likely continue to refine the RPC with emphasis on reduction of materials (for increased muon resolution and decreased structural cost). In addition, new materials that show promise for high rate applications in the expected neutron background are being studied at the present time. These materials are typically low resistivity plastics that are commercially available with similar costs to Bakelite, however the manufacturers have greater flexibility to provide these materials in odd sizes and non-standard thicknesses with little impact on cost.

Engineering is being carried out at LLNL to determine the structural requirements of the RPCs and will likely continue in coordination with engineering efforts at Draper Labs and SSC Laboratory.

Procurement will be carried out by coordinators at LLNL and SSCL and fabrication of RPCs can take place overseas if cost of labor is an issue. Installation/assembly, of course, takes place at SSCL and requires similar conditions for installation/assembly of drift tube technologies, although the individual chamber weights are not as demanding on personnel and facilities. Estimates of manpower for these items are given in the Cost Estimation Worksheets in the previous section.

5. Cost Uncertainties

The major cost uncertainty at this time is the structure cost, because the RPC may be incorporated into the drift tube structure and utilize its interface to the super-structure. In addition, the cost of machining and fabrication is somewhat uncertain. Also, electronics costs are not included in this review and estimates vary from about $11/channel to about $35/channel depending on the source of the electronics and whether the fabrication is in the US or overseas. Cost of materials is more certain, given the standard nature of the materials involved. Cost estimates for materials have been based on manufacturer's quotes or LLNL stock book prices for fittings, connectors, plastics, glues, etc. Details of costs have been presented in a number of reviews over the past year and can be found in various Cost Review proceedings.

In summary, it appears that a complete RPC system can be built for a less than $5M. This cost can perhaps be further reduced by a simplification of the structural requirements if the RPCs are incorporated in the drift tube support system.

G. Strength of Supporting Group

The RPC collaboration consists of a number of physicists, engineers and technicians from 6 institutions and is listed at the beginning of this report. We have demonstrated a strong multi-disciplinary R&D effort in FY 1992 in fields of RPC theory, design, fabrication, and characterization, materials science, structural engineering, and costing. We draw on our experience from a number of different programs in high energy physics, nuclear physics, applied physics, chemistry and materials science, mechanical engineering, and electronics engineering. MIT and LLNL both maintain laboratories exclusively dedicated to RPC research and development. In addition, a number of special purpose facilities are

available. For example, MIT has facilities for measurement of RPC behavior in magnetic fields. LLNL maintains a number of electron linear accelerators for beam testing of RPCs. LLNL also has an extremely strong mechanical engineering support group already in place for the GEM Muon system with expertise in designing very large systems, CAD/CAM, structural engineering, systems integration, costing, and mass production techniques. Both LLNL and MIT have very strong shop support for prototyping large chambers. We have fostered contacts with overseas institutions such as ITEP in Moscow and Tsing Hua University, and the Institute for High Energy Physics (IHEP) in Beijing, as well as contacts at the highest levels of the Chinese Academy of Sciences which could be useful for mass production of chambers with a substantial cost savings in labor.

H. Summary

We summarize this report by reiterating a number of important facts about RPCs:

A. They are the only Muon System technology currently made by industry. The standard sized RPC is one meter by two meters. In principle sizes much larger than this can be built.

B. They have the following pulse characteristics:

1. Pulse height about 0.5 volts without amplification into 50 ohms.
2. Pulse rise time less than 5 nanoseconds.
3. Pulse width about 10 nanoseconds.
4. Measured rise time jitter less than 1.4 nanoseconds (no other Muon System technology has this speed).

C. Lifetime is greater than 16.4×10^7 pulses per square centimeter with no loss of efficiency within the 3% measuring error. This is equivalent to 8.2 standard SSC years (at luminosity 10^{33} and 2×10^7 seconds per year – the expected neutron flux is 2 Hz per square centimeter.)

D. Commercial RPCs have demonstrated essentially 100% efficiency at about 100 Hz per square centimeter using standard Bakelite resistive plates.

E. RPC prototypes built with new lower resistivity materials have demonstrated counting rates of about 20,000 Hz per square centimeter for short periods of time – in agreement with theoretical models based on bulk resistitivity alone – prior to an observed increase in bulk resistivity that reduces the counting rate capability with a time constant on the order of hours. This indicates that with the proper choice of materials, i.e., with materials that exhibit stable resistive properties, we can expect RPCs with rate capabilities a factor of 1- 100 higher, with an added increase in rate capability achievable by utilizing thinner materials.

F. A number of candidate plastics have been identified and are under study, some with bulk resistivities of about 10^9 ohm-cm, which is about a factor of 100 lower than the ABS plastics currently used.

G. Refinement of the RPC design has led to an extremely low mass system with minimal muon scattering cross section of about 0.6% X_0/layer.

H. A series of cost reviews carried out over the past year indicate that the cost of the complete RPC system for GEM is about $5M including the cost of the electronics.

As part of our planned R&D program in the next year, we will measure RPC lifetimes out to 10^9 pulses per square centimeter. This corresponds to approximately 5 standard SSC years at a luminosity of 10^{34} assuming that the neutron flux can be reduced by a factor of 20-30 through the use of shielding. We plan to build larger prototype RPCs up to 3 meters by 4 meters. The demonstrated improvement in fully efficient rate capability of a large RPC from 100 Hz/cm^2 to over 1000 Hz/cm^2, albeit for short periods of time prior to stabilization of the plastic to higher resistivity values, is a significant result. R&D results indicate that, with the proper combination of low resistivity materials, thicknesses, and materials stability, a factor of 10 or more increase in rate corresponding to a fully efficient RPC rate capability of 10^4 - 10^5 Hz/cm^2 is achievable.

Based on the R&D we have performed, along with a detailed analysis of the cost of constructing a full RPC trigger system for GEM, we feel that the combination of pressurized drift tubes (PDTs) for precision tracking coupled to RPCs for fast Level 1 triggering has the least risk, the highest muon resolution, the best beam crossing timing accuracy, and the lowest cost of all competing technologies.

I. General References

1. G. Battistoni, et al., "Plastic Spark Counters with PVC Electrodes," Nucl. Inst. Meth. **A270**, p. 190, 1988.

2. R. Cardarelli, et al., "Progress in Resistive Plate Counters," Nucl. Inst. Meth. **A263**, p. 20, 1988.

3. M. Della Negra, et al, "Study of Muon Triggers and Momentum Reconstruction in a Strong Magnetic Field for a Muon Detector at LHC," CERN/DRDC/90-36 DRDC/P7, August 30, 1990.

4. M. Anelli, et al., "Glass Electrode Spark Counters," Nucl. Inst. Meth. **A300**, p. 572, 1991.

5. "An Expression of Interest to Construct a Major SSC Detector," B. Barish, W. Willis, Co-spokespersons, pps. 3-38 - 3-40, July, 1991, unpublished.

6. C. Bacci, et al., "Muon Tracking and Hadron Punchthrough Measurements using Resistive Plate Chambers," Preprint ROM2F/91/18, July 22, 1991.

7. A. Bohrer, et al., "Status Report of the RD5 Experiment," CERN/DRDC/91-53, January 13, 1992.

8. M. Widgoff, et al., "Resistive Plate Chamber Technology Review" GEM-TN-92-206, October 6, 1992.

J. Figure Captions

1. Sketch of Italian (single layer design) Resistive Plate Chamber.

2. Equivalent circuit of the RPC used in SPICE to predict the operating characteristics of the RPC. The RPC is modeled as a capacitor and a resistor for each plate coupled via a capacitor, corresponding to the gas gap. The calculated RPC characteristics include recovery time, which is directly correlated to the saturated counting rate capability of the RPC.

3. SPICE calculation results for different RPC recovery times. In this figure we compare a number of different materials: Bakelite, glass, and plastics.

4. Comparison of SPICE calculated RPC rate capability with measured rates for a number of different RPCs. The RPCs plotted are, in order of increasing rate, the MIT glass, the LLNL glass, the Italian Bakelite, the Abstat-M310, and the MiTech-411. The linear fit to the points is also indicated. The rate capability is defined as the inverse of the half-height time of the curves in Figure 3.

5. Measurements of bulk resistivity as function of time for different RPC plastic materials. On this time scale ABS resistivity rises rapidly and stabilizes, while other plastics exhibit slower resistivity changes.

6. Measured saturated count rate capability of ABS and PVC based plastic sheets in RPCs of identical construction as a function of time. The ABS plastics starts with a high saturated count rate and stabilizes at a reduce value. The PVC plastic also stabilizes to a reduced value, much higher than ABS, with about 10KHz/cm^2 saturated rate. This rate capability is suitable for RPC operation in the GEM Detector.

7. Schematic layout of materials in the proposed two layer RPC for the GEM Muon System. See Table 1in the text for the corresponding radiation length fractions.

8. Experimental measurement of counting rate versus high voltage for an RPC fabricated with MiTech-411 plastic. Note that the vertical scale is in counts/second/2 cm^2. Thus this RPC has a peak counting rate of about 1.5 x 10^4 Hz/cm^2.

9. Efficiency plateau curves of an RPC for diffferent isobutane concentrations versus voltage. Note that there is no freon in this gas. As the isobutane concentration is increased, the plateau is increased in voltage and the peak efficiency is increased.

10. Efficiency versus threshold for different isobutane concentrations. Again, there is no freon in the gas in this plot. Above an isobutane concentration of about 40% there is no increase in pulse height, indicating that the RPC is operating in limited streamer mode.

11. Efficiency plateau curve for a 40% isobutane mixture, now with 2.5 % Freon 13B1 included. Note that the plateau is increased in efficiency to near 100% and the width of the plateau is increased.

12. Efficiency versus threshold for a 40% isobutane mixture with 2.5% Freon 13B1. The pulse height is seen to be decreased with the addition of Freon (compared to the curves shown in Figure10).

13. Comparison of pulses taken from a 0.5 m x 0.5 m ABS plastic RPC with flammable and non-flammable gas mixtures. The mixtures were 66% argon/30 % isobutane/ 4% Freon (flammable) and 55% argon/31% CO_2/10% isobutane/4% Freon (non-flammable).

14. Plateau efficiency curves for different discriminator thresholds versus RPC high voltage. The data is for an RPC with the non-flammable gas mixture.

15. Comparison of plastic RPC time jitter measurements made with flammable and non-flammable gas mixtures.measured for 4 strips on the RPC with the flammable and non-flammable gas mixures. The time jitter is slightly worse – 6 ns versus 5 ns – for the non-flammable gas mixture, compared to the flammable gas mixture. The tails in the distribution are due to pulses on adjacent strips inducing signals on the strip in the cosmic ray telescope area and would be eliminated by fully instrumenting all the strips on the RPC with TDCs and tagging all cosmic rays.

16. Results of lifetime measurements performed on the Italian RPC. The data is consistent with no degradation in performance for an equivalent of 8.2 SSC years of operation, assuming a 2 Hz/cm^2 rate at a luminosity of 10^{33}. This rate corresponds to a flux of 10^4 neutrons/cm^2/second multiplied by an RPC efficiency for detecting neutrons of 0.5% and assumes a factor of 25 neutron shielding due to the placement of borated polyethylene in various parts of the GEM detector to shield the muon system.

17. This plst shows a distribution of RDT stop times with respect to the RPC trigger for cosmic ray triggers in the TTR. The distribution shows an uncorrected sigma of 6.9 ns. The data is uncorrected for difference in transit time from the RPC to the RDT caused by the different entry angles of the cosmic ray muons.

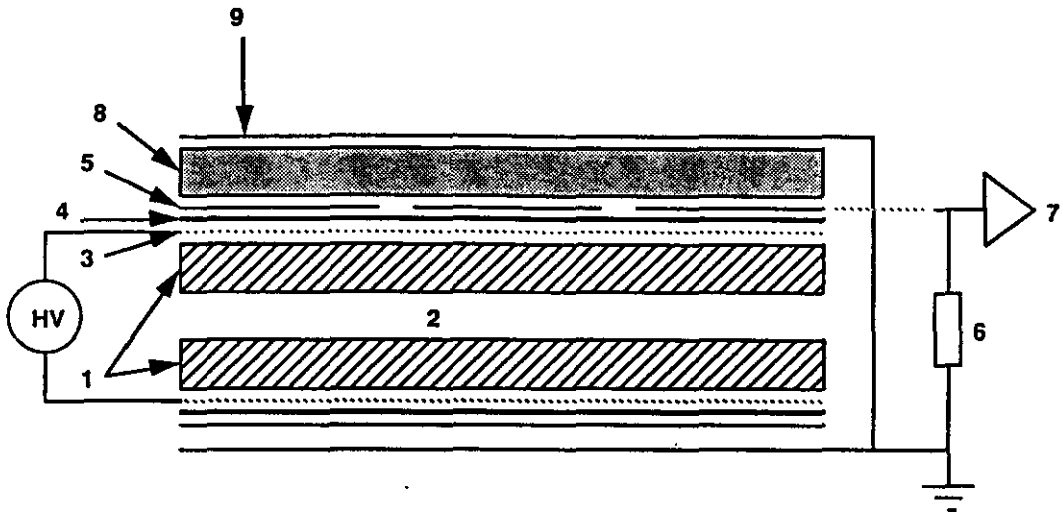

1 Bakelite plate
2 gas
3 graphite coating
4 insulating foil
5 aluminum strips
6 line termination
7 discriminator
8 foam
9 aluminum ground plane

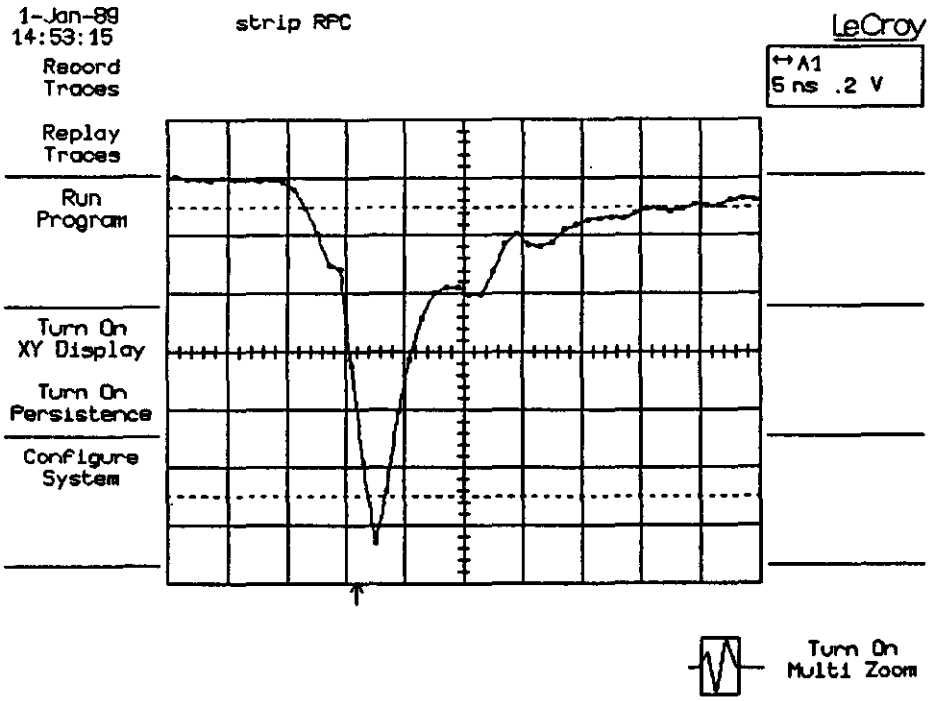

Figure 1

Spice RPC Model

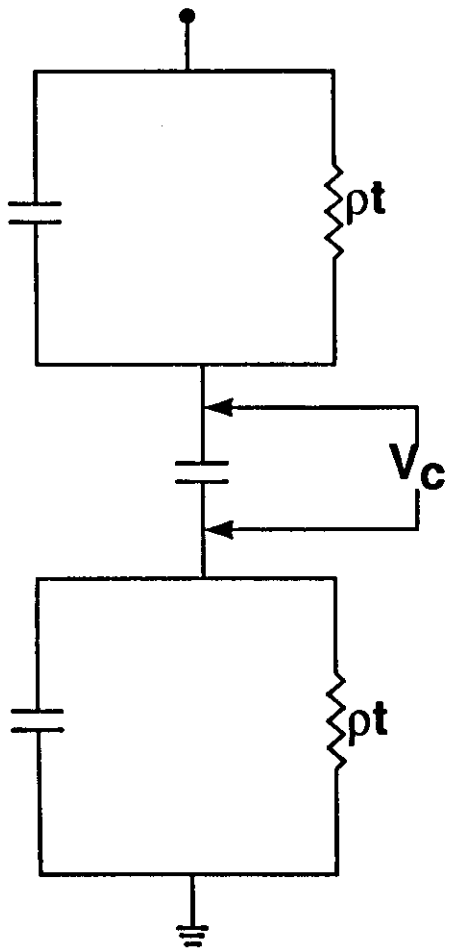

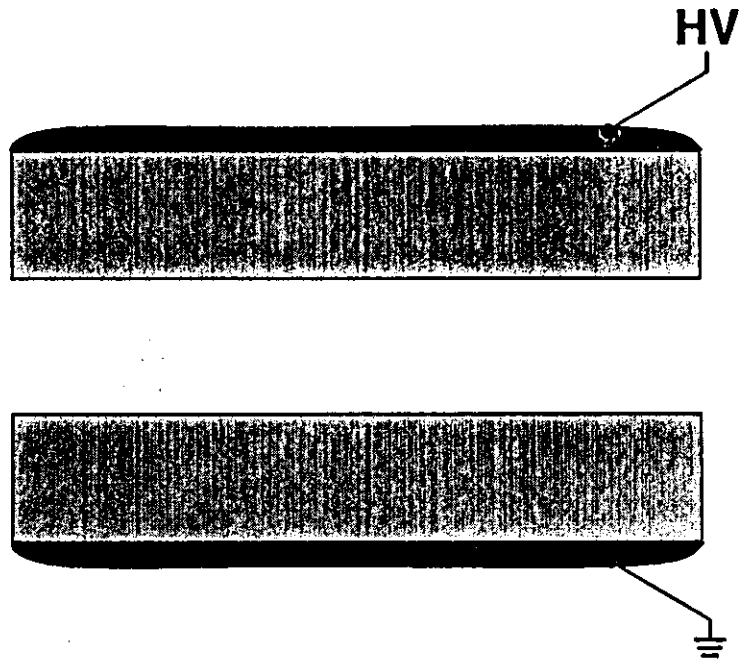

Figure 2

BAK.KA-01/RMB

Spice Calculations of Recharge

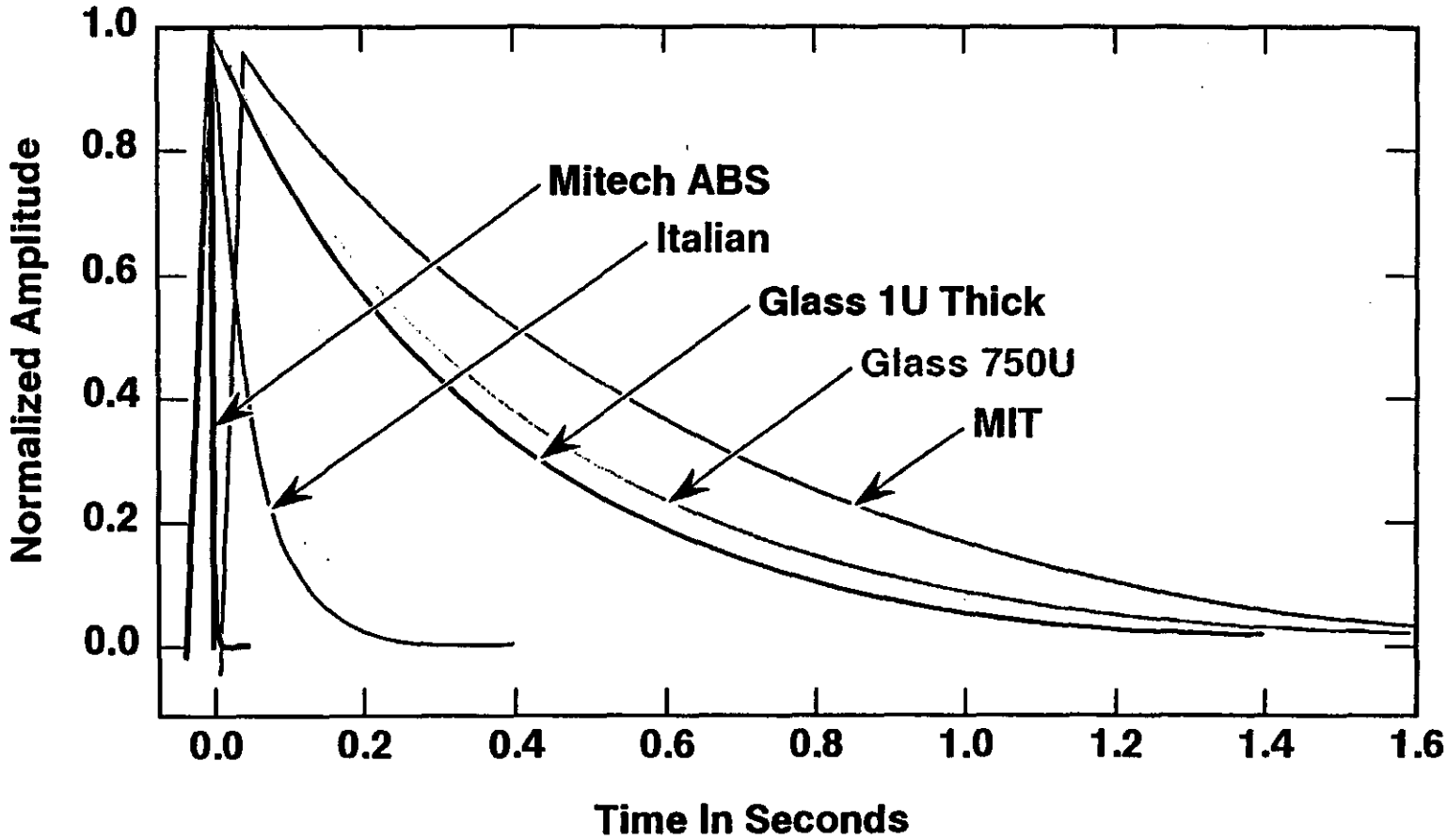

Figure 3

BAK.KA-16/RMB

Saturated Singles Rate vs SPICE 1/tau

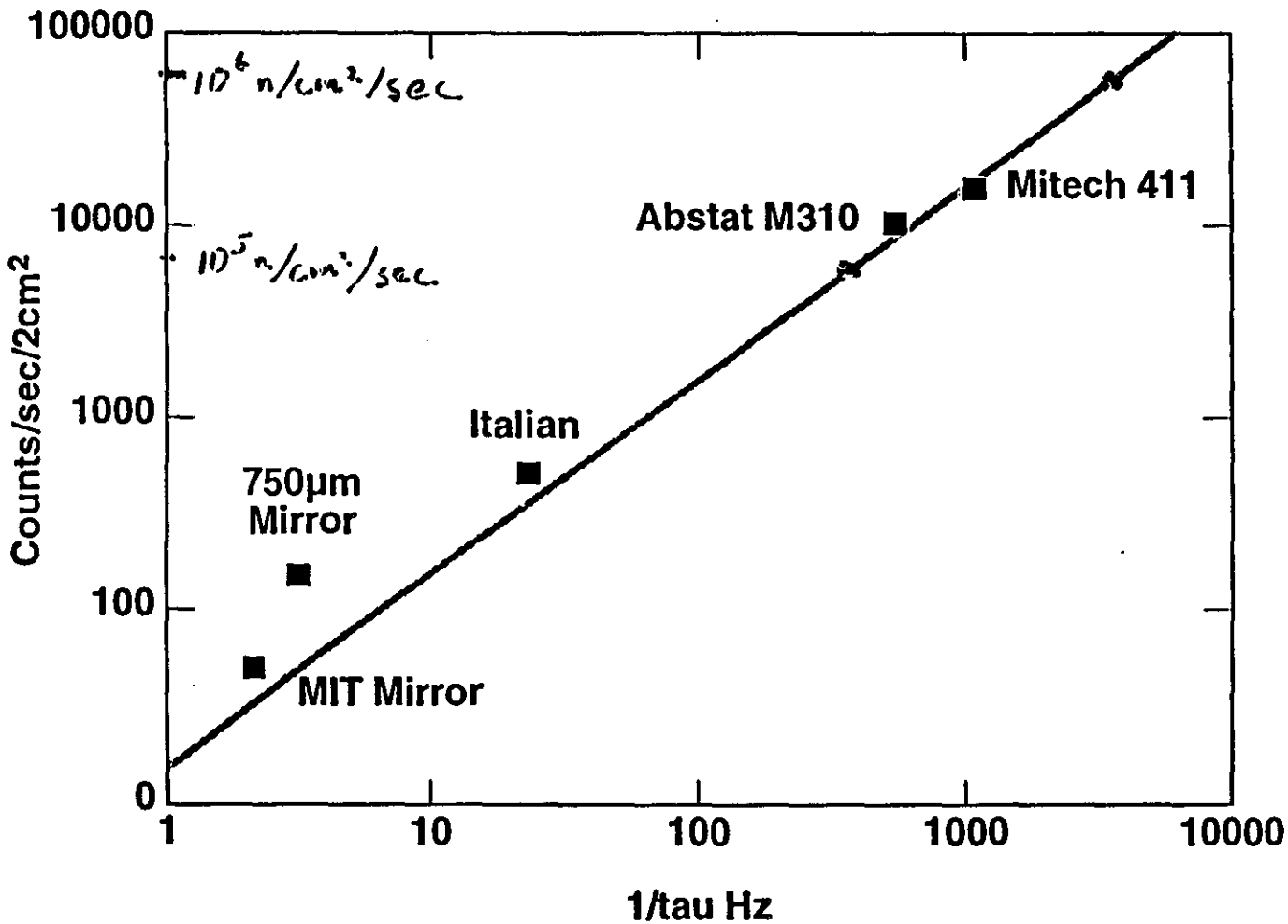

Figure 4

BAK.KA-17/RMB

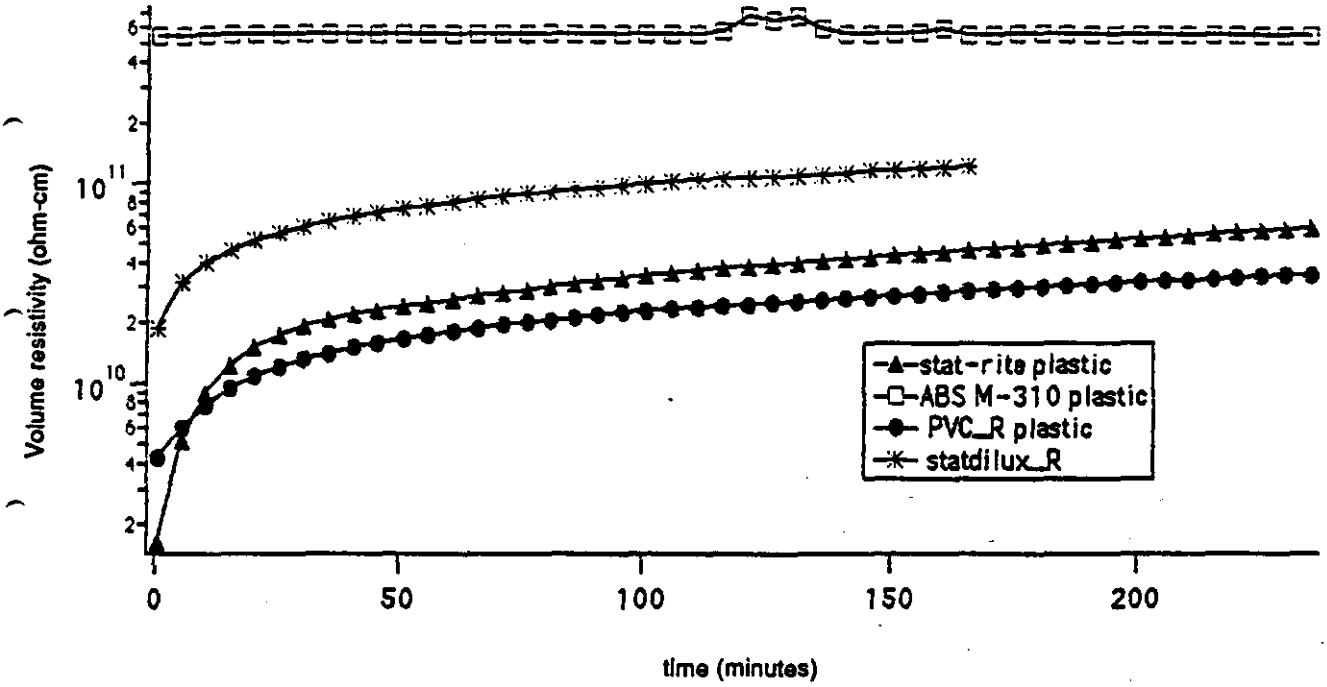
Volume resistivity (ohm-cm)
time (minutes)
0
50
100
150
200
10^{11}
10^{10}
stat-rite plastic
ABS M-310 plastic
PVC_R plastic
statdilux_R

Figure 5

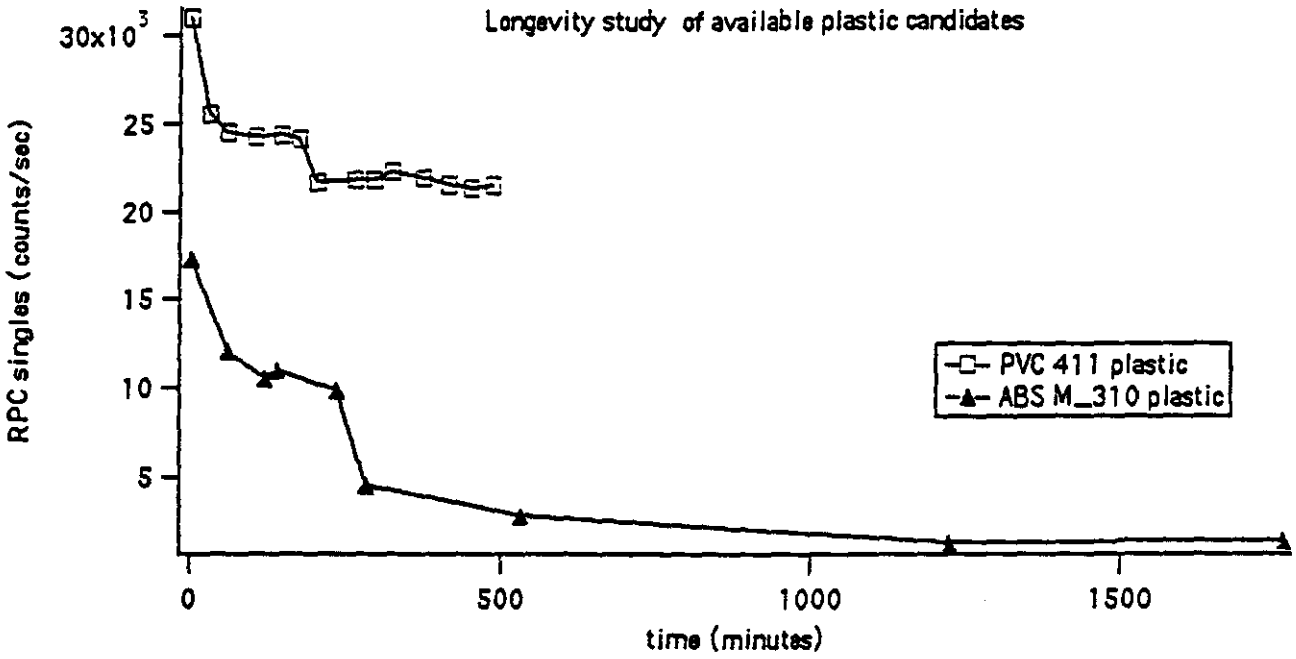
Longevity study of available plastic candidates
30x10^3
25
20
15
10
5
RPC singles (counts/sec)
0
500
1000
1500
time (minutes)
PVC 411 plastic
ABS M_310 plastic

Figure 6

Figure 7

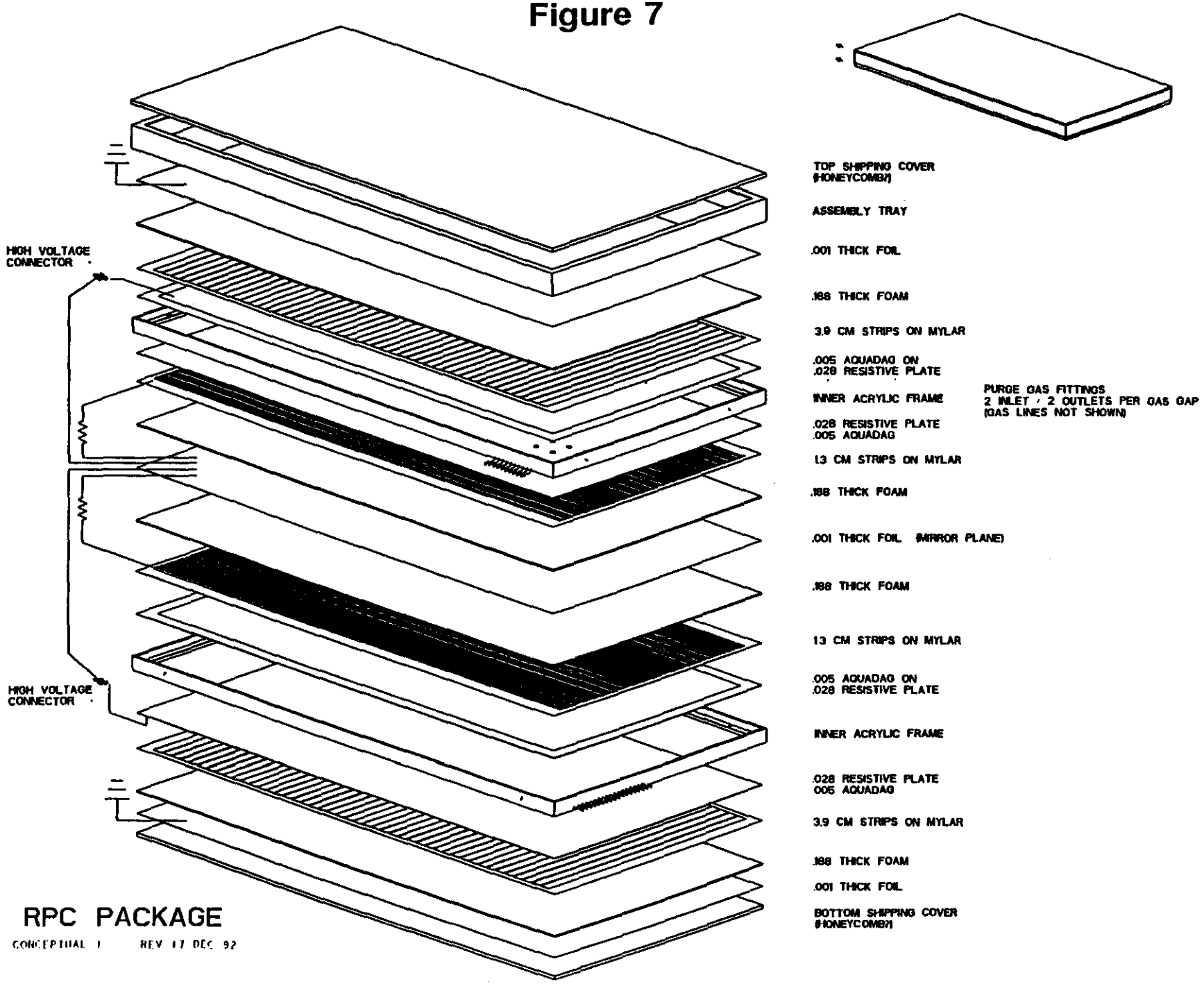
HIGH VOLTAGE CONNECTOR
HIGH VOLTAGE CONNECTOR
TOP SHIPPING COVER (HONEYCOMB?)
ASSEMBLY TRAY
.001 THICK FOIL
.188 THICK FOAM
3.9 CM STRIPS ON MYLAR
.005 AQUADAG ON .028 RESISTIVE PLATE
INNER ACRYLIC FRAME
.028 RESISTIVE PLATE .005 AQUADAG
1.3 CM STRIPS ON MYLAR
.188 THICK FOAM
.001 THICK FOIL (MIRROR PLANE)
.188 THICK FOAM
1.3 CM STRIPS ON MYLAR
.005 AQUADAG ON .028 RESISTIVE PLATE
INNER ACRYLIC FRAME
.028 RESISTIVE PLATE .005 AQUADAG
3.9 CM STRIPS ON MYLAR
.188 THICK FOAM
.001 THICK FOIL
BOTTOM SHIPPING COVER (HONEYCOMB?)
PURGE GAS FITTINGS 2 INLET / 2 OUTLETS PER GAS GAP (GAS LINES NOT SHOWN)
RPC PACKAGE
CONCEPTUAL I REV 17 DEC 92

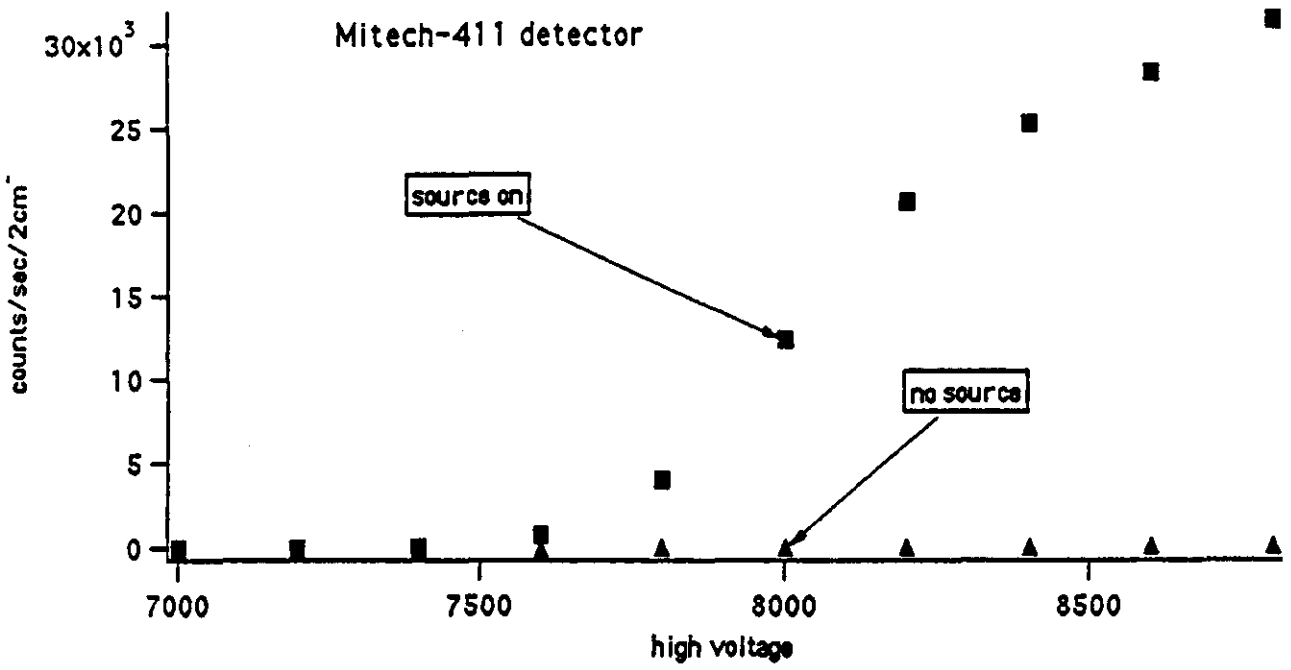
Mitech-411 detector
30x10^3
25
20
15
10
5
0
counts/sec/2cm^-
source on
no source
7000
7500
8000
8500
high voltage

Figure 8

EFFICIENCY PLATEAU FOR DIFFERENT ISOBUTANE CONCENTRATIONS

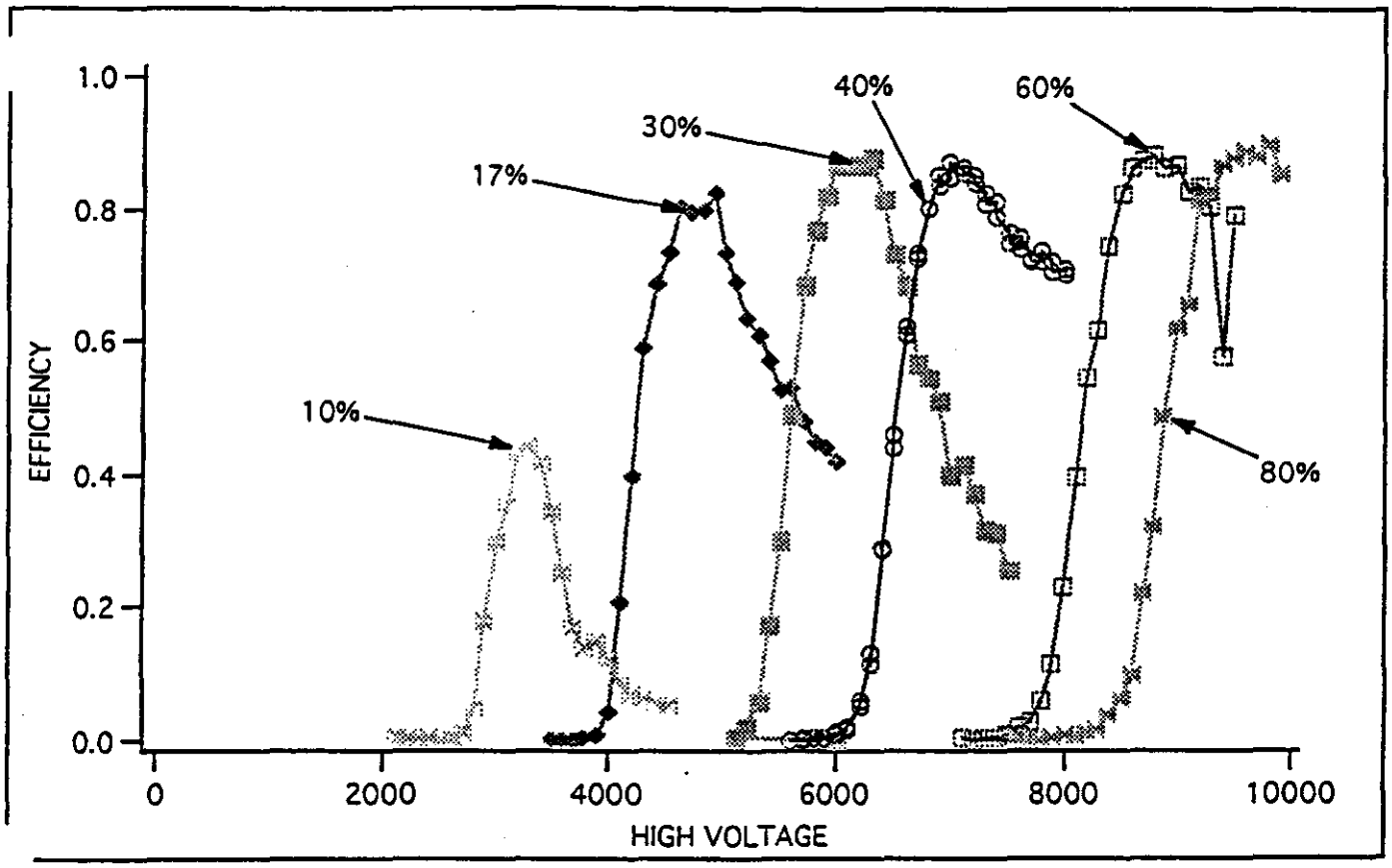

Figure 9

Efficiency vs threshold voltage for various isobutane concentrations

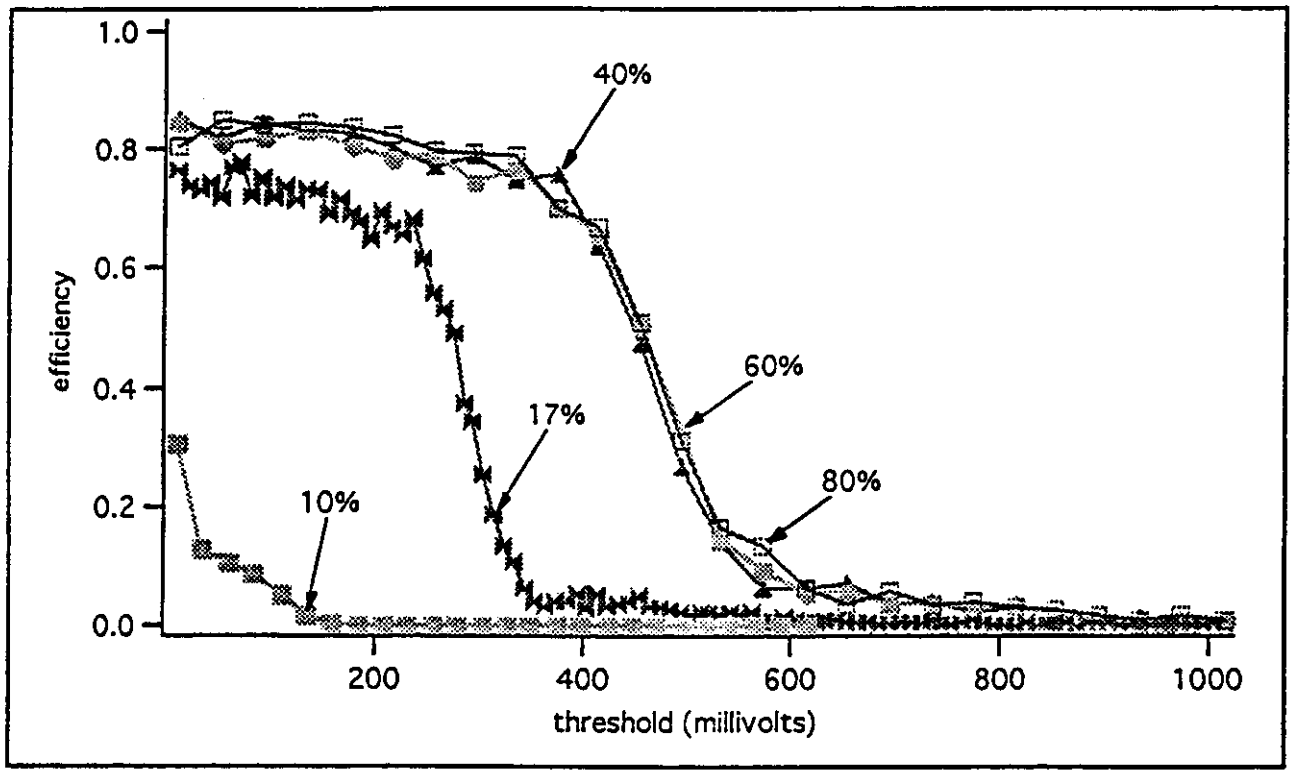

Figure 10

Efficiency curve for 40% isobutane, 2.5% freon 13B1

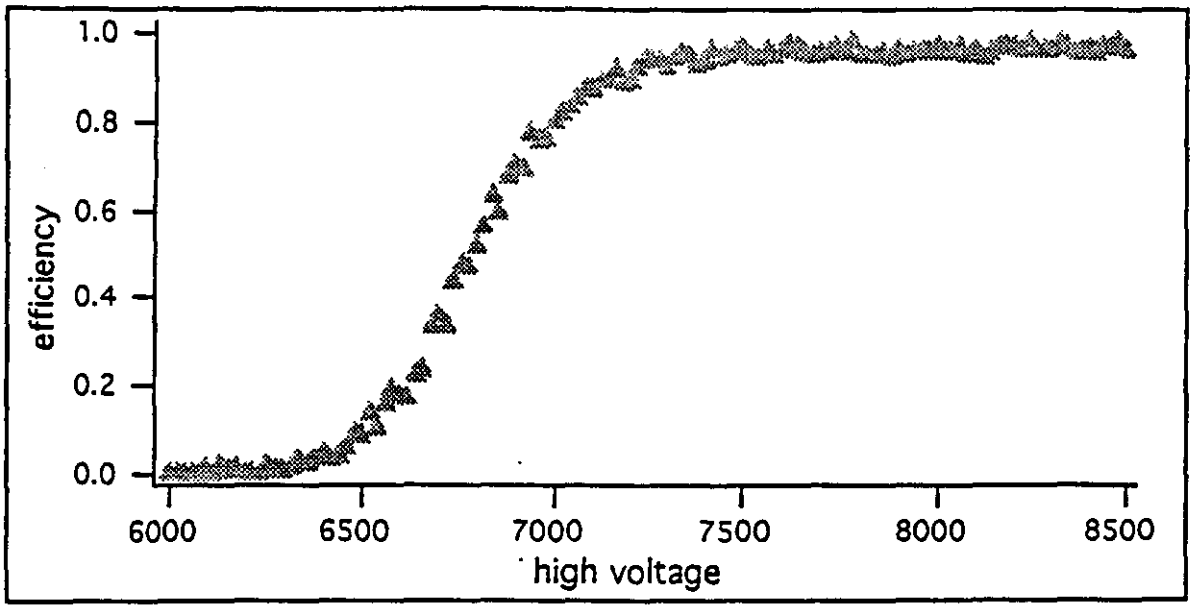

Figure 11

Efficiency vs threshold for 40% Isobutane, 2.5% freon 13B1

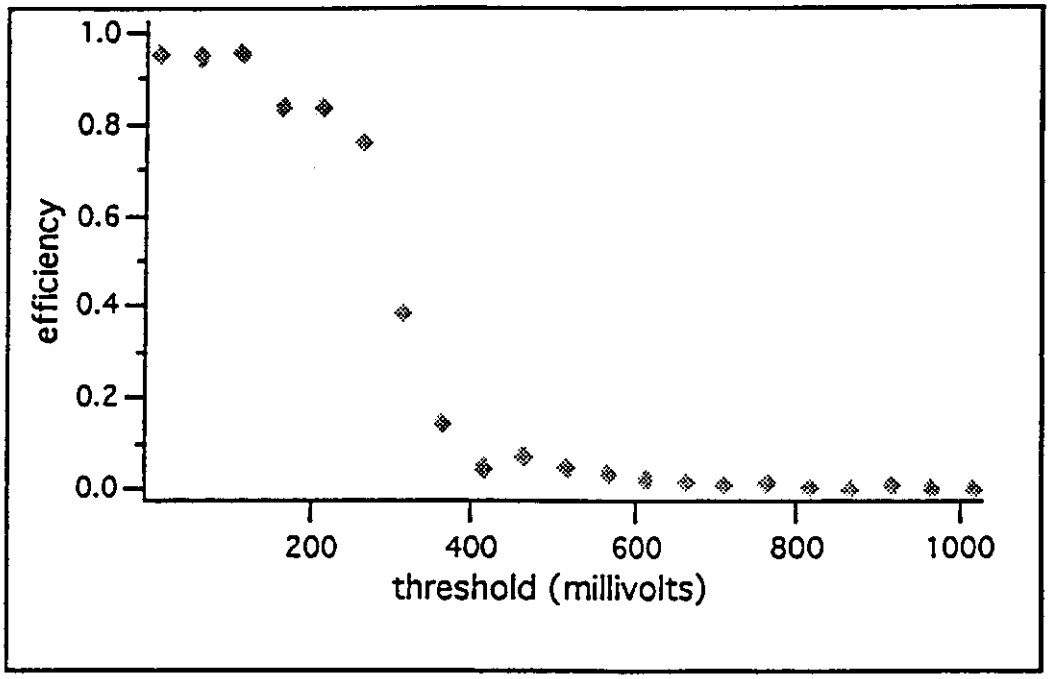

Figure 12

22-Dec-92
17:32:17

66% argon/30% isobutane/4% Freon 13B1 (flammable)

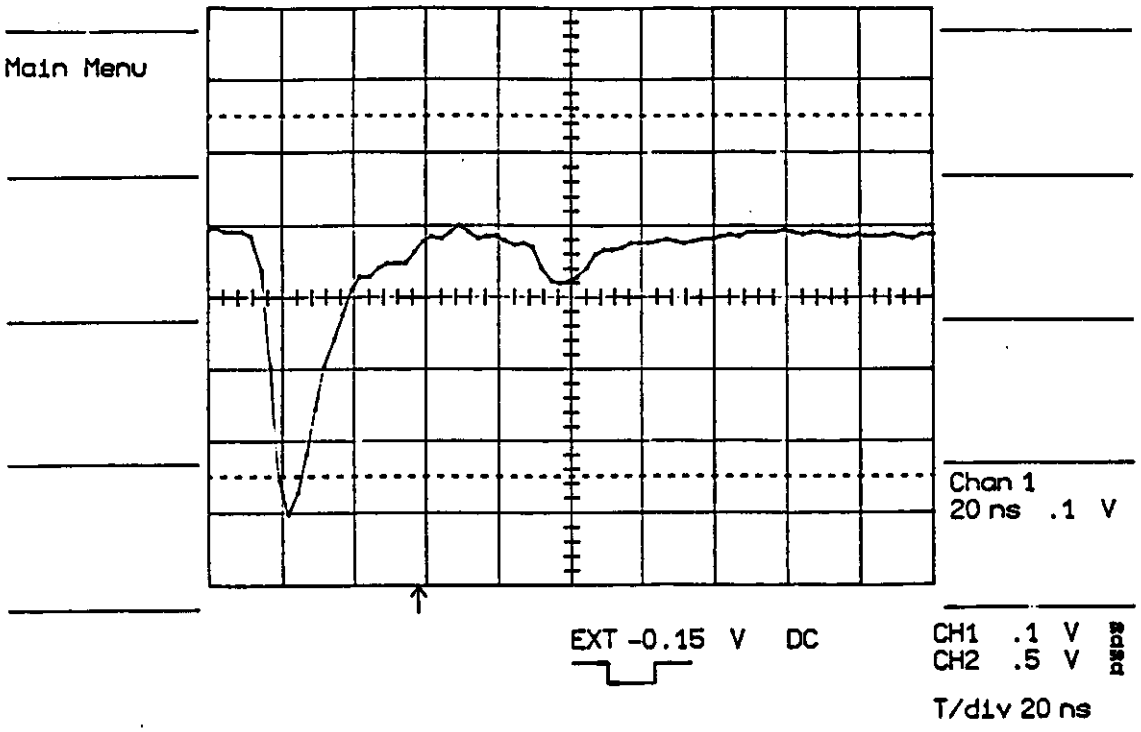

22-Dec-92
19:03:12

55% argon/31% CO_2/10% isobutane/4% Freon 13B1 (non-flammable)

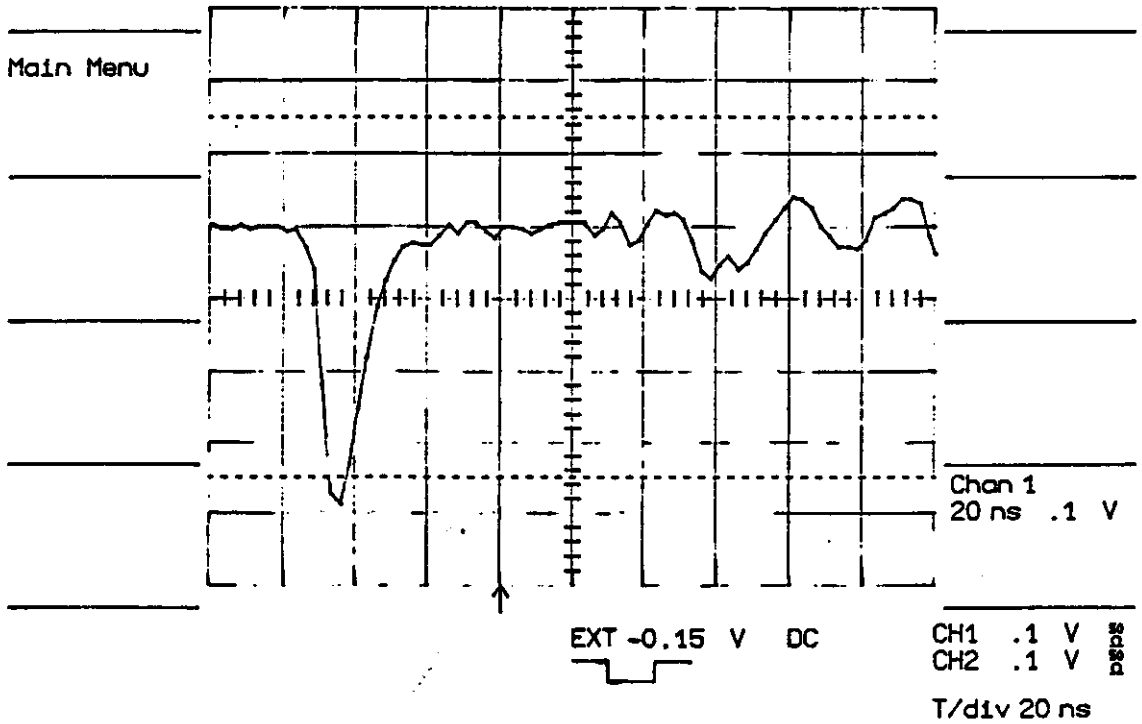

Figure 13

55%argon/31%CO_2/10%isobutane/4%Freon 13B1 (non-flammable)

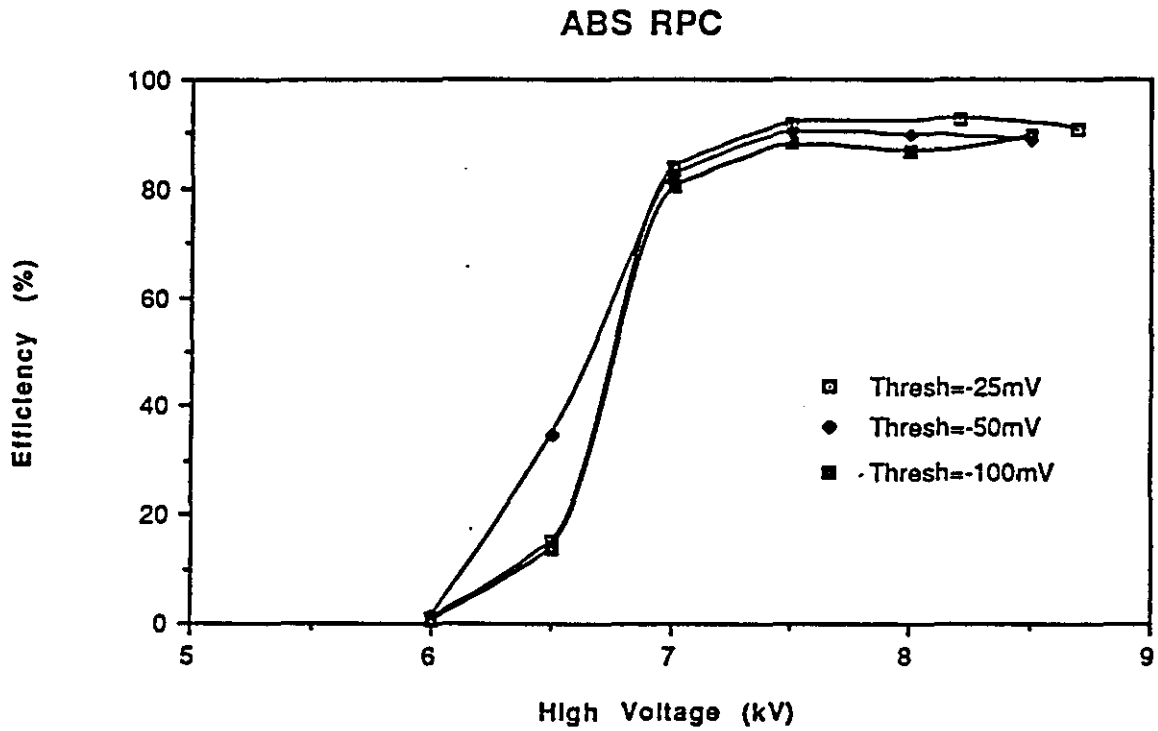

Figure 14

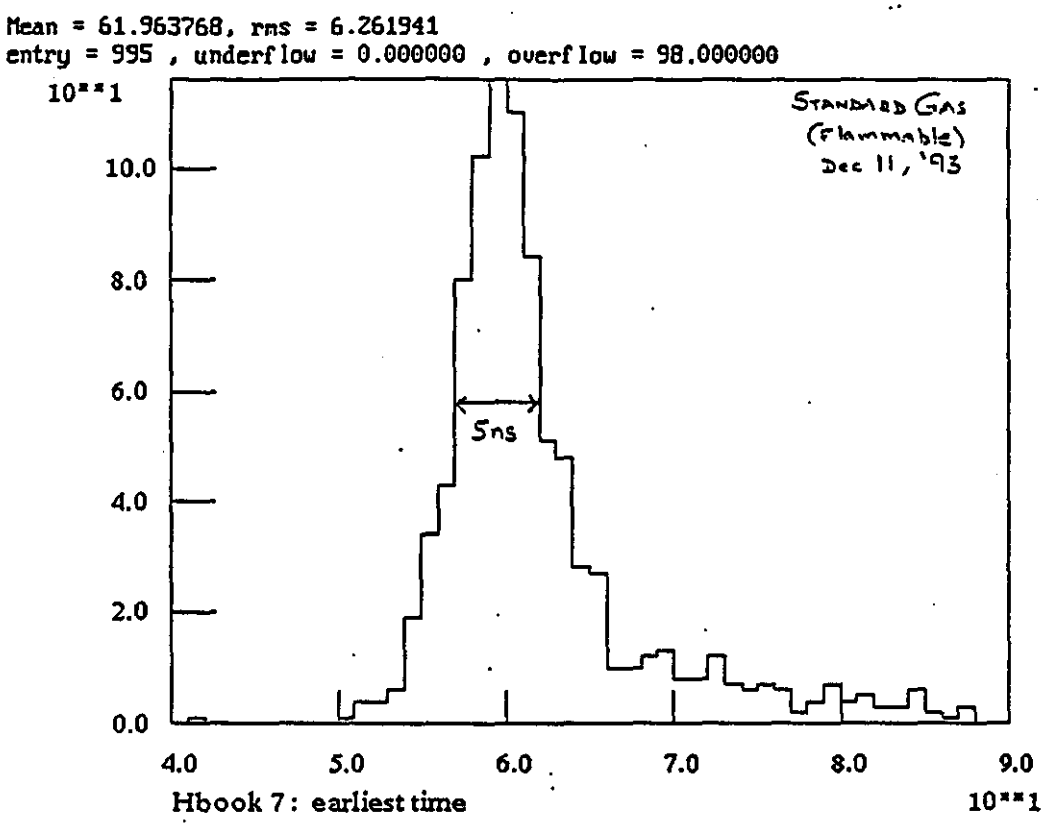
Mean = 61.963768, rms = 6.261941
entry = 995 , underflow = 0.000000 , overflow = 98.000000
10**1
10.0
8.0
6.0
4.0
2.0
0.0
4.0
5.0
6.0
7.0
8.0
9.0
Hbook 7: earliest time
10**1
Standard Gas
(Flammable)
Dec 11, '93
5ns

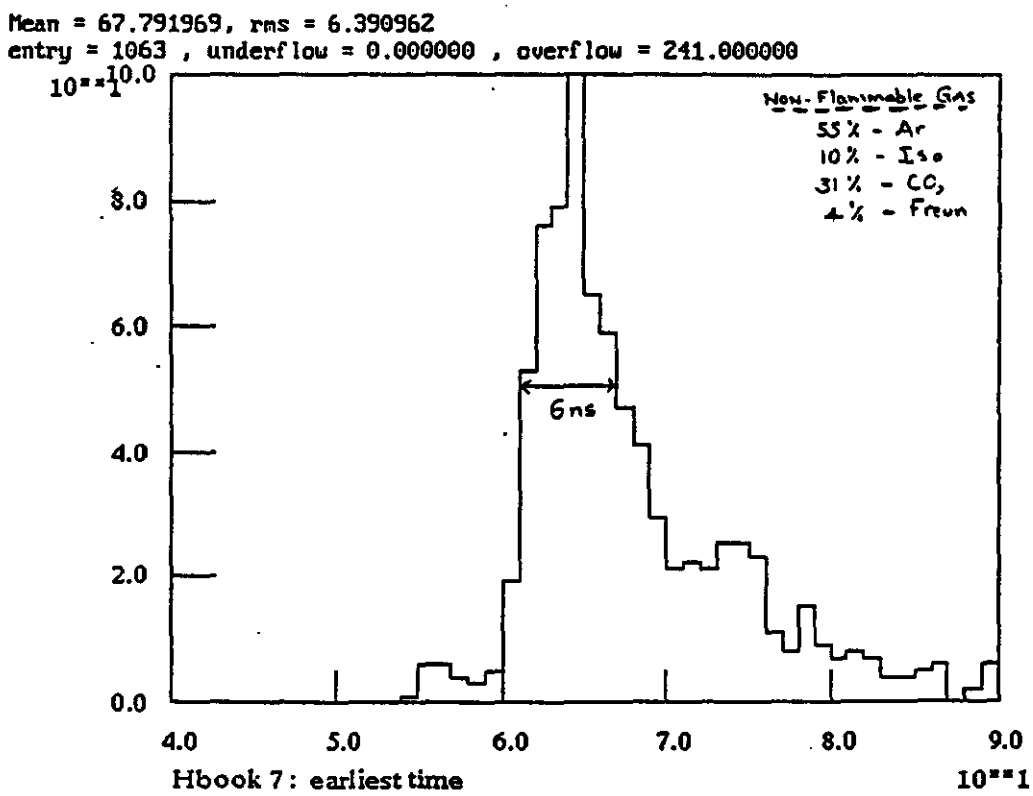
Mean = 67.791969, rms = 6.390962
entry = 1063 , underflow = 0.000000 , overflow = 241.000000
10**1
10.0
8.0
6.0
4.0
2.0
0.0
4.0
5.0
6.0
7.0
8.0
9.0
Hbook 7: earliest time
10**1
Non-Flammable Gas
55% - Ar
10% - Iso
31% - CO2
4% - Freon
6ns

Figure 15

K+E 10 X 10 TO THE CENTIMETER KEUFFEL & ESSER CO. U.S.A.

Figure 16

46 1510

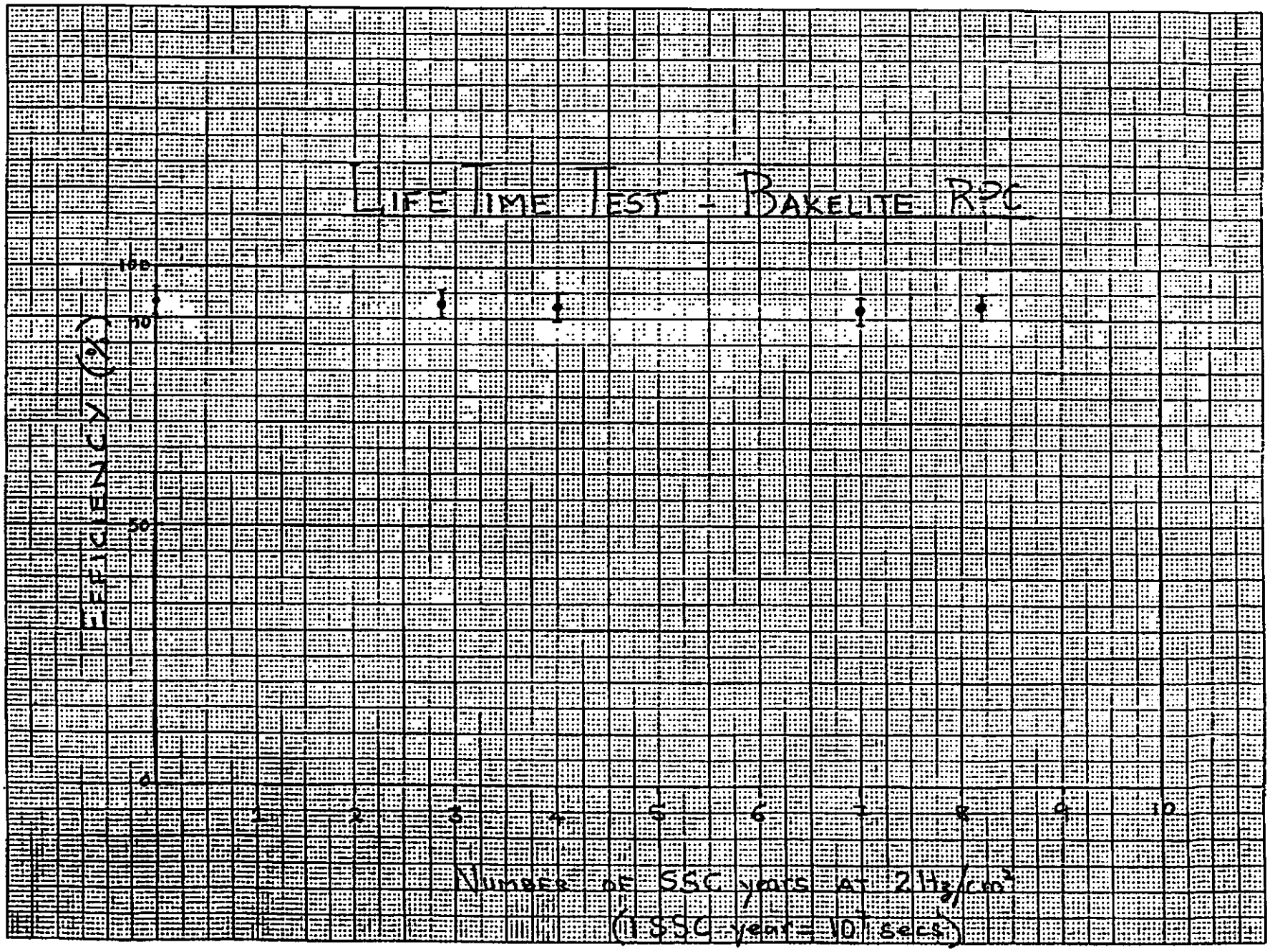

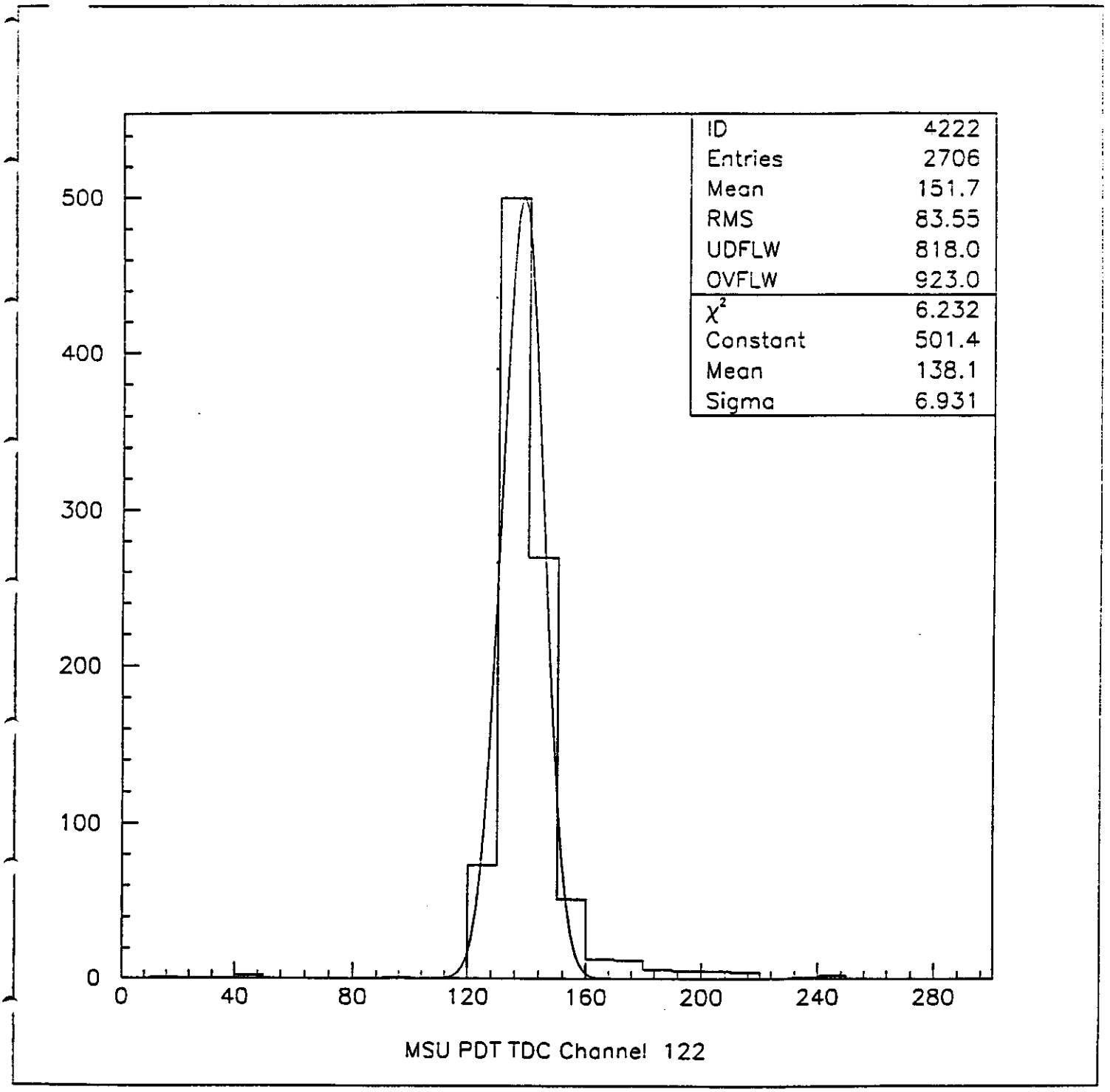
ID 4222
Entries 2706
Mean 151.7
RMS 83.55
UDFLW 818.0
OVFLW 923.0
χ² 6.232
Constant 501.4
Mean 138.1
Sigma 6.931
500
400
300
200
100
0
0
40
80
120
160
200
240
280
MSU PDT TDC Channel 122

Figure 17

APPENDIX B

Considerations of strip timing, accidental rates and system dead time.

A. Barrel Trigger

I. *Timing*

The basic barrel trigger depends on the non-barrel plane timing. We will label each of the 166 non-bend strips with an index k (k = 0 - 155) where strip D is the strip closest to the interaction point. The non-bend plane strips form a projective tower with the interaction point. Every three corresponding strips (i.e. the three strips with the same index) can be brought into time coincidence at the input to the shift register logic. This is done by having a fixed cable length difference for each strip of SL2 and SL1 with respect to SL3. The fixed cable lengths [measured in nanoseconds] for SL2 and SL1 is listed in Table A.1. Following the cable delay which is common for all strips on a superlayer there is a timing gate delay, the width of which is determined by the bend strip index. Following the gate delays there is generated a signal gate whose length is determined by the superlayer. These timings are also listed in Table A.1.

The bend plane strips also have the same cable differences as the non-bend plane strips as indicated in Table A.1. The bend plane strips do not have any timing gate delays following the cable but rather generate just a signal gate whose width is superlayer dependent. This is also listed in Table A.1.

If the numbers listed in Table A.1 are used in a straight forward, but tedious, hand calculation one finds that all the signals from any track with a transverse momentum greater than 10 GeV which passes through SL1, SL2 and SL3 will arrive in coincidence at the shift register logic with an overlap in time greater than 2 nanoseconds.

It should be noted that this system requires ± 5% logic throughout. This has been included in the above calculations.

A. Accidental Rates

Uncorrelated Background

We assume then the neutron flux is 10^5 Hertz per square centimeter per second everywhere in GEM. Hence our RPC rate is 500 Hertz per square centimeter per second.

We calculate the accidental trigger rate for all tracks with transverse momentum greater than 50 GeV/c. In order to handle this high rate, we place the three RPC

counters in all super layers in a two out of three coincidence. This yields a 95% efficient RPC system which can handle the 10^5 neutrons per square centimeter.

The non-bend plane accidental trigger rate = NBA is given by the following formula:

$$NBA = [2]\,[R_1\ R_2\ R_3\,(t_1 + t_2)\,(t_1 + t_3)]\,[166]\,[32]$$

R_1 = Rate in superlayer 1
R_2 = Rate in superlayer 2
R_3 = Rate in superlayer 3
t_1 = Signal gate width in superlayer 1 = 16 nanoseconds
t_2 = Signal gate width in superlayer 2 = 16 nanoseconds
t_3 = Signal gate width in superlayer 3 = 16 nanoseconds

$$R_1 = 3(R \times W_1\ L_1)^2 \times 2t_1 \times [2]$$

$R = 500$
$W_1 = 3.9$
$L_1 = 148.5$
$t_1 = 4 \times 10^{-9}$

The factor [2] is because $2R_1$ strips are involved in the trigger. The factor 3 is due to the combinatorics of the two out of three coincidence.

$R_1 = 2 \times 10^4$ Hertz

$$R_2 = 3(R \times W_2\ L_2)^2 \times 2t_2$$

$R = 500$
$W_2 = 6.5$
$L_2 = 239$
$t_2 = 12 \times 10^{-9}$
$t_3 = 16 \times 10^{-9}$

$R_2 = 4.3 \times 10^5$ Hertz

$$R_3 = 3(R \times W_3 \times L_3)^2 \times 2t_3$$

$$R_3 = 3(500 \times 8.9 \times 329.6)^2 \times 2 \times 16 \times 10^{-9} = 2.1 \times 10^6$$

$NBA = 2 \times 10^4 \times 4.3 \times 10^4 \times 21 \times 10^6 \times 1.6 \times 10^{-8} \times 2.0 \times 10^{-8} \times 166 \times 32 = 3.2 \times 10^4$ Hertz

The non-bend trigger must be placed in coincidence with the bend trigger. Since for every non-bend hit there is a <u>random</u> hit in coincidence in the bend plane, we

have to multiply NBA by the combinatorial factor = C to calculate the GEM false trigger rate = F.

$$F = NBA \times C$$
$$C = N3 \times N2 \times N3$$

The factor:

N3 = 1 as one strip in SL3 is hit in coincidence with NBA.

N2 = 3/184 as there are only 3 strips determined by the strip hit in SL3 which can form a bend plane trigger of either charge that has a transverse momentum of 50 GeV/c.

N1 = 6/115 as there are only six strips in super layer one that can form a trigger for the hit in SL1.

$$C = 8.5 \times 10^{-4}$$
$$F = 3.2 \times 10^{4} \times 8.5 \times 10^{-4} = 27 \text{ Hertz}$$

B. Correlated Background caused by Muons with less than 50 GeV/c Transverse Momentum

The trigger rate, in the barrel, for muons with momentum greater than 10 GeV/c is about 1,000 Hertz. Although there is no real calculation, I will assume the number of muons in the barrel less than 10 GeV/c is
6×10^{6} Hertz (one low energy muon per 10 crossings), which is of course, essentially the same for muons less than 50 GeV/c. These muons do <u>not</u> make a trigger in the bend plane. The hit they make in SL1 and SL2 in the bend plane is wrong for the hit they make in the bend plane SL3. Hence for this case we must calculate the accidental rate per sector for a 50 GeV/c bend plane trigger. The accidental rate turns out to be so high that we have to segment the SL1 into three sections along the Z coordinate. Hence each SL1 super layer has a length of 210.6 centimeters.

$$BPA = R1\ R2\ R3\ (t_1 + t_2)\ (t_1 + t_3)\ (254)\ (32)$$

We note here that like the non-bend plane counter strips for SL1, SL2 and SL3 are in coincidence.

$$R_1 = (3)\ (2)\ [(210.6)\ (1.3)\ (500)]^2\ (6)\ (16)\ (10^{-9}) = 1.1 \times 10$$
$$R2 = (3)\ (2)\ [(1{,}042.6)\ (1.3)\ (500)]^2\ (3)\ (32) \times 10^{-9} = 26.4 \times 10^{4}$$
$$R3 = (3)\ (2)\ [(1.475)\ (1.3)\ (500)]^2\ (48)\ (10^{-9} = 26.5 \times 10^{4}$$

$t_1 = 16 \times 10^{-9}$

$t_2 = 32 \times 10^{-9}$

$t_3 = 48 \times 10^{-9}$

$BPA = (1.1)\ (10^4)\ (26.4)\ (10^4)\ (26.5)\ (10^4)\ (48)\ (10^{-9})\ (64)\ (10^{-9})\ (254) = 6.0 \times 10^2$

This must be put in coincidence with the rate in the non-bend plane per small sector = NBPA.

$NBPA = 6 \times 10^6 / 32 \times 3 = 6.3 \times 10^4$

Accidentals per small sector = ASS

$$ASS = (NBPA)\ (BPA)\ (t_1 + t_2)$$
$$= (6.3)\ (10^4)\ (6\ (10^2)\ (16 + 16)\ (10^{-9}) = 1.2$$

The accidental for the full sector = AFS is given by:

$AFS = (3ASS) = 3.6$

Total accidental for GEM = (3.6) (32) = 115 Hertz. To this we add 27 Hertz which gives the GEM accidental rate of 142 Hertz.

Dead Time

To calculate the dead time we must consider what is the probability that a track will generate a signal in all three RPC super layers. In each super layer a track goes through three pairs of bend and non-bend strips. Since we use 2 out of 3 logic we must calculate the probability that at least two pairs of bend and non-bend strips are "alive." Let this probability for any bend plane super layer $B_j = (LTP)_{Bj}$, j = 1, 2, 3.

$$(LTP)_j = [3\ D_{Bj}\ (1 - D_{Bj})^2 + (1 - D_{Bj})^3]$$

D_{Bj} = Dead time probability for bend plane strip Bj.

Total bend live time = $(LTP)_{B1}\ (LTP)_{B2}\ (LTP)_{B3} = L_B$

Total bend dead time = $1 - (LTP)_1\ (LTP)_2\ (LTP)_3 = D_B$

We will assume that after each hit on any strip the strip is "dead" for 100×10^{-9} seconds. From the previous information we calculate:

$$D_{B1} = (631.9)\ (1.3)\ (500)\ (100)\ (10^{-9}) = .041$$

$$D_{B2} = (1{,}042.6)\ (1.3)\ (500)\ (100)\ (10^{-9}) = .068$$

$$D_{B3} = (1{,}475)\ (1.3)\ (500)\ (100)\ (10^{-9}) = .096$$

$$D_{NB1} = (148.5)\ (3.9)\ (500)\ (100)\ (10^{-9}) = .028$$

$$D_{NB2} = (239)\ (6.5)\ (500)\ (100)\ (10^{-9}) = .077$$

$$D_{NB3} = (329)\ (8.9)\ (500)\ (100)\ (10^{-9}) = .147$$

D_{NBj} $j = 1, 2, 3$ is the dead time probability for non-bend plane strip B_j

$$(LTP)_{B1} = (3)\ (.04)\ (.96)^2 + (.96)^3 = .995$$

$$(LTP)_{B2} = (3)\ (.068).(.932)^2 + (.932)^3 = .987$$

$$(LTP)_{B3} = (3)\ (.096)\ (.904)^2 + (.904)^3 = .974$$

Total bend live time = LB = (.995) (.987) (.974) = .957

Total bend dead time = 1 - LB = 1 - .957 = .043

Let $(LTP)_{NBj}$ = Live time probability of the non-bend plane j.

$$(LTP)_{NB1} = (3)\ (.028)\ (.972)^2 + (.972)^3 = .998$$

$$(LTP)_{NB2} = (3)\ (.077)\ (.923)^2 + (.923)^3 = .983$$

$$(LTP)_{NB3} = (3)\ (.147)\ (.853)^2 + (.853)^3 = .942$$

Let LNB = total non-bend live time.

$$LNB = (LTP)_{NB1}\ (LTP)_{NB2}\ (LTP)_{NB3}$$

Total non-bend dead time = 1 - LNB

$$LNB = (.998)\ (.983)\ (.942) = .924$$

Total non-bend dead time = 1 - .924 = .076

Let total GEM live time = LT

$$LT = (LB)\ (LNB) = (.957)\ (.924) = .88 = 88\%$$

GEM dead time = 12%

If we assume our pulse dead time is 50 nanoseconds instead of 100 the dead time is reduced to about 6%. Both numbers are acceptable. If we assume, because of the high rates, the efficiency of the RPC degrades then there will be a different calculation for the GEM live time and dead time. Assume that the efficiency of an RPC plane is E.

$$\text{GEM live time} = [(3)\ (1 - E)\ (E)^2 + E^3]^6$$

E	GEM Live Time	GEM Dead Time
95%	96%	4%
90%	84%	16%
85%	69%	31%
80%	52%	48%

Obviously the dead time is sensitive to the efficiency of the individual RPC plane. A proper, by definition, high rate RPC will have an efficiency greater then 95%. It should be noted that at efficiencies greater than 95%, the previous calculation is the relevant calculation.

End Cap

The problems of the end cap are much simpler than the barrel due to the much greater segmentation. Without presenting the details, all accidentals and dead times are reduced by about two orders of magnitude. The timings are essentially as in the barrel, but all delays are reduced by about a factor two.

TABLE B.1

Cable length difference for all strips (both bend plane and non-bend plane):

SL3 and SL2	= 30.65 (nanoseconds)
SL3 and SL1	= 59.82 (nanoseconds)

(Note about half this (difference) is used just to get the signals to the input to the shift registers). This cable delay should be accurate to ± 0.5 nanoseconds or about ± 10 centimeters of cable.

The delay gate width DT_k for non-bend strip k superlayer SL3:

$DT_k = (k/165)\ (31)$ nanoseconds (k = 0 to 165)

Superlayer SL2:
$DT_k = (k/165)\ (13)$ nanoseconds (k = 0 to 165)

Superlayer SL1:
$DT_k = 0$

The error on any delay gate width can be as large as ± 5%.
The signal gate width DT_s for non-bend strips:

Superlayer SL3:
$DT_s = 11.5$ nanoseconds

Superlayer SL2:
$DT_s = 10$ nanoseconds

Superlayer SL1:
$DT_s = 4$ nanoseconds

The signal gate width DT_s for bend strips superlayer SL3:

$DT_s = 42.5$ nanoseconds

Superlayer SL2:
$DT_s = 23$ nanoseconds
Superlayer SL1:
$DT_s = 4$ nanoseconds

The error on any signal gate width can be as large as ± 5%.

The accidental rate turns out to be so high that we have to segment the SL1 into three sections along the Z coordinate. Hence each SL1 super layer has a length of 210.6 centimeters.

$$R_1 = (3)\ (2)\ [(210.6)\ (1.3)\ (500)]^2\ (6)\ (16)\ (10^{-9}) = 1.1 \times 10^4$$

$$BPA = (1.1)\ (10^4)\ (26.4)\ (10^4)\ (26.5)\ (10^4)\ (48)\ (10^{-9})\ (64)\ (10^{-9})\ (254) = 6.0 \times 10^2$$

This must be put in coincidence with the rate in the non-bend plane per small sector = NBPA.

$$NBPA = 6 \times 10^6 / 32 \times 3 = 6.3 \times 10^4$$

Accidentals per small sector = ASS

$$ASS = (NBPA)\ (BPA)\ (t_1 + t_2) = (6.3)\ (10^4)\ (6\ (10^2)\ (16 + 16)\ (10^{-9}) = 1.2$$

The accidental for the full sector = AFS is given by:

$$AFS = (3ASS) = 3.6$$

Total accidental for GEM = (3.6) (32) = 115 Hertz. To this we add 27 Hertz which gives the GEM accidental rate of 142 Hertz.

Appendix C

Cost of Baseline - RDT/RPC System

RDT: 8-10-8 configuration in both the barrel and endcaps (348,000 drift channels)
RPC: 3-3-3 configuration

Item	Barrel	Endcaps	Total
Sector assembly	4835	3905	8741
RDT Chambers	21191	13596	34787
RPC Chambers	6595	4579	11174
Support Structure	3216	2415	5630
Gas Systems	3501	3355	6856
Cooling Systems	143	150	292
Alignment	2192	809	3001
Installation	2890	1475	4364
Mechanical Subtotal	37968	25704	74845
RDT Electronics Subtotal	5607	9818	15425
RPC Electronics Subtotal	1300	1300	2600
Subtotal	6907	11118	18025
R&D	2423	2246	4669
Conceptual design			1692
Project Management			3731
Subtotal			10092
Total (w/o contingency)			102962
Contingency (28%)			28829
Grand total			131791

Notes:

(a) The RDT electronics were computed at Costs = $2.1M + $38.29 x channels (Dan Marlow).
(b) The RPC electronics costs were doubled to include frontend electonics and boards mounted on chambers.

Source of information: Rick Sawicki and Dick Gustavson 1/17/93.

Cost of Baseline - RDT/PWC System

RDT: 8-10-8 configuration in both the barrel and endcaps (348,000 drift channels)
PWC: 4-3-3 configuration - scaled from CSC barrel chamber costs (see below).

Item	Barrel	Endcaps	Total
Sector assembly	4835	3905	8741
RDT Chambers	21191	13596	34787
PWC Chambers	6000	2000	8000
Support Structure	3216	2415	5630
Gas Systems	3501	3355	6856
Cooling Systems	143	150	292
Alignment	2192	809	3001
Installation	2890	1475	4364
Mechanical Subtotal			71671
RDT Electronics Subtotal	5607	9818	15425
PWC Electronics Subtotal	1300	1300	2600
Subtotal	6907	11118	18025
R&D	2423	2246	4669
Conceptual design			1692
Project Management			3731
Subtotal			10092
Total (w/o contingency)			99788
Contingency (28%)			27941
Grand total			127729

Notes:

(a) The RDT electronics were computed at Costs = $2.1M + $38.29 x channels.
(b) The PWC electronics costs taken to be same as RPC costs above.
(c) The PWC costs were determined from the CSC barrel chamber costs by the following scaling:

- reduce cost of precision strip panels by 0.10
- reduce cost of hexcell panels by 0.10
- fraction of CSC cost in above two items is 25% and 61%, respectively
- cost of 6-6-4 CSC barrel chambers $41M
- area of 4-3-3 PWC system for GEM is 11785.6 m^2
- cost of PWC system so scaled $679/$m^2$

Source of information: Rick Sawicki and Dick Gustavson 1/17/93.

Appendix D

RDT System with a PWC - T_0 Trigger

The prompt nature of a PWC signal is the main advantage of the CSC proposal while the natural compensation for E×B effects and lower costs are the RDT strong points. We combine both with a proposal to use two layers of PWC (in a wire-OR) at each superlayer and use a coincidence of the three superlayers to measure the time of the muon crossing. The time of the crossing is then combined with the momentum determined from the RDT hits to form the muon trigger. It should be noted that the time of the muon crossing is needed only for muons which are in muon triggers , i.e., for high momentum tracks. In all other triggers the time of the muon crossing can be determined off-line from the RDT data.

The PWC wires are laid on a 2.5mm pitch in a direction perpendicular to the drift tubes with projective staggering at each superlayer. They are grouped into $\Delta\eta$ = .025, $\Delta\phi$ =0.2 trigger elements (1520 total) with a maximum length of 1.6 m (± 4 ns). In superlayer-2 the segments are 15 cm wide at η = 0 decreasing to 5.0 cm wide at η = 2.0. In the high muon-flux region η = 2.0 - 2.5 the orientation of the PWC wires is changed to parallel to the drift tubes with $\Delta\eta$ = 0.25, $\Delta\phi$ = .02 trigger elements (3768 total). The t_0 pre-trigger is a coincidence of 1 hodoscope element in each of the three superlayers in a straight line pointing toward the collision point. The coincidence is strobed with the accelerator clock and the earliest time in the coincidence is the t_0 for the muon track at that h.

A neutron fluxxefficiency of 100Hz/cm^2 yields a maximum signals rate of about 0.6MHz in the largest hodoscope elements (near η = 0). Assuming a 20 ns wide signal the triple-coincidence probability is 8×10^{-6}; the coincidence rate from neutrons is then < 5Hz. The coincidence rate from tracks near η = 0 is very low due to the filtering of the calorimeter. Near η=2.5 the energy spectrum is much harder and the rate can be as high as 25 kHz in a hodoscope element and also in the three-element coincidence. Tracks in this region separated by more than 100 nsec (> 99%) will have a unique t_0 association with the drift information.

Since this proposal uses a PWC trigger, it has many similarities to the CSC proposal, however, the momentum information is obtained from the drift tubes alone while only t_0 need be obtained from the PWC planes. Consequently, only a small number of PWC channels are needed at each superlayer that yield a total channel count of 19,000 Since the PWCs have continuous cathodes that are easy to make and have easily achievable tolerance requirements, an estimate of the PWC cost is not more than 1k\$/m^2 . In the system proposed there are about 3500 m^2 of PWC and thus the cost will be 3.5M\$ with contingency added the total price tag will be around 5M\$.

RDT/PWC Trigger and Layout

Drift Tube Sections for DA and Momentum Trigger

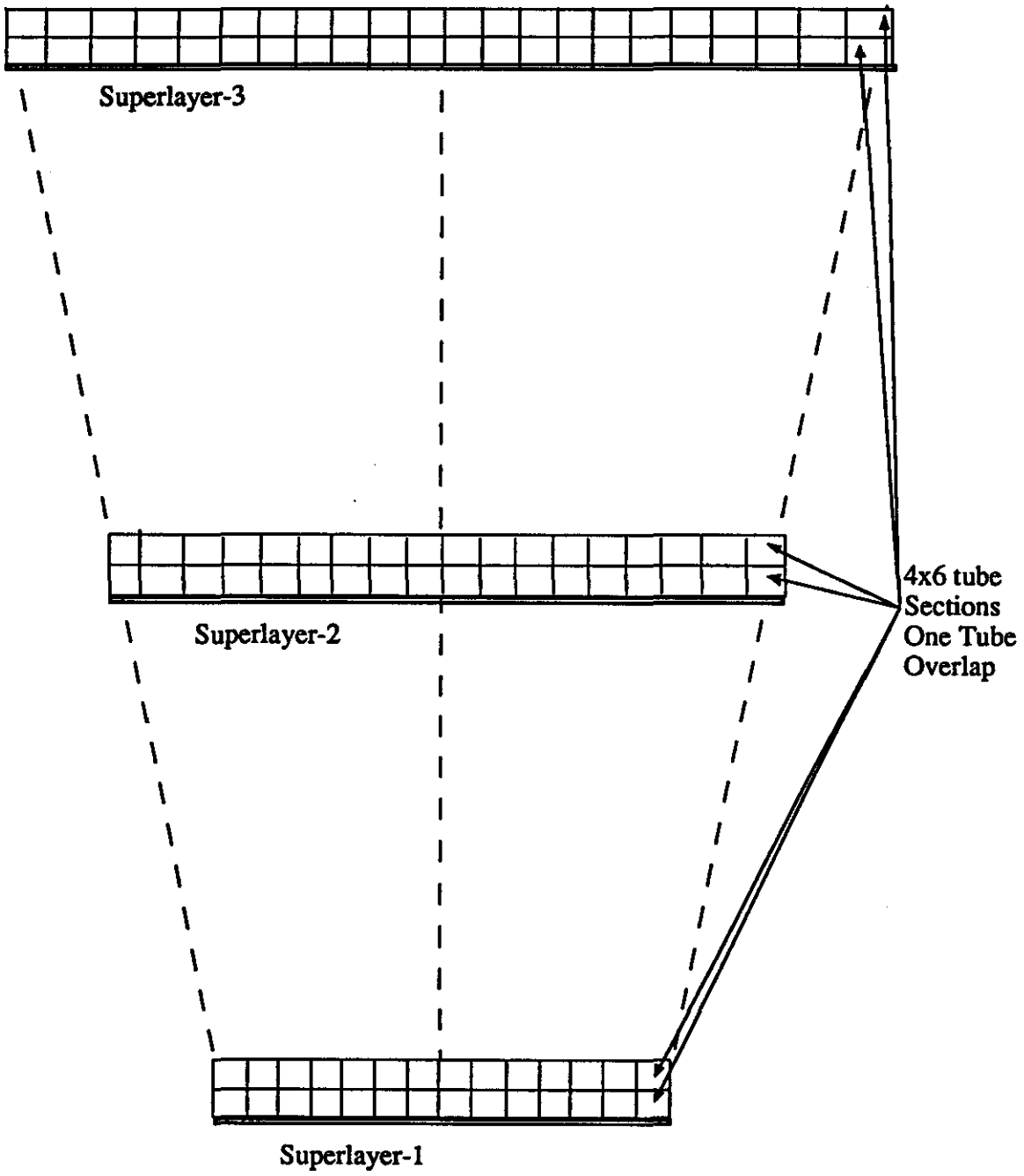

Muon Pt Trigger Components

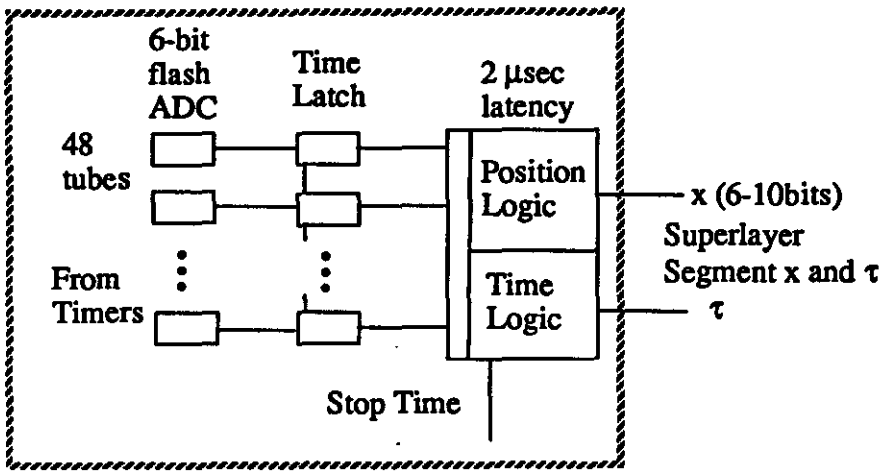

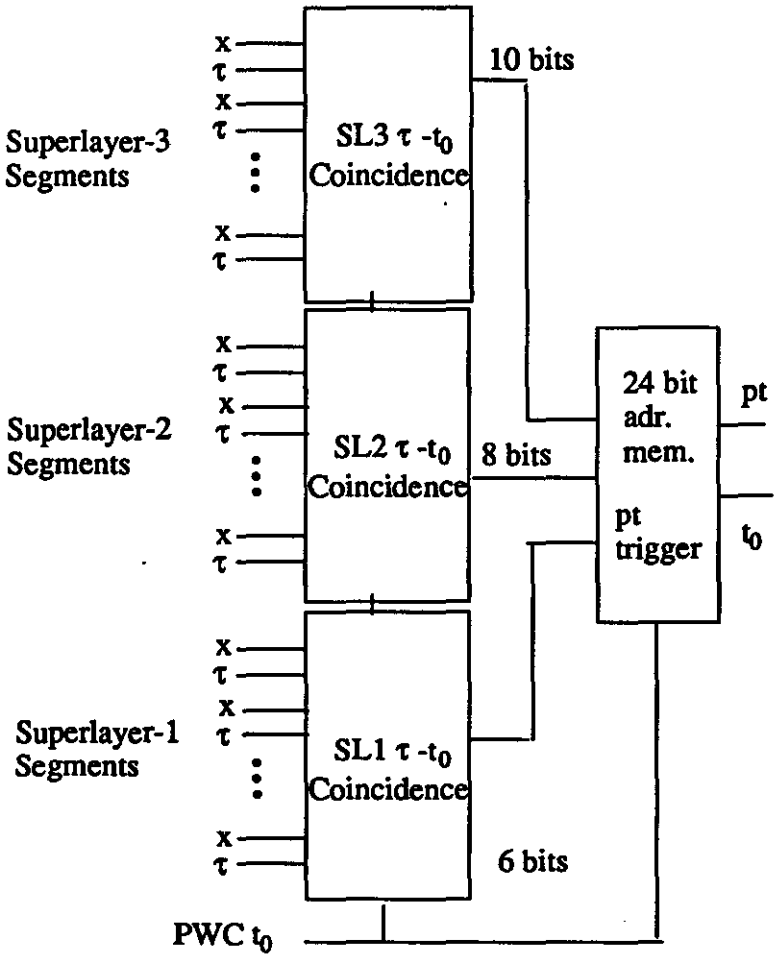

PWC segmentation in η and φ

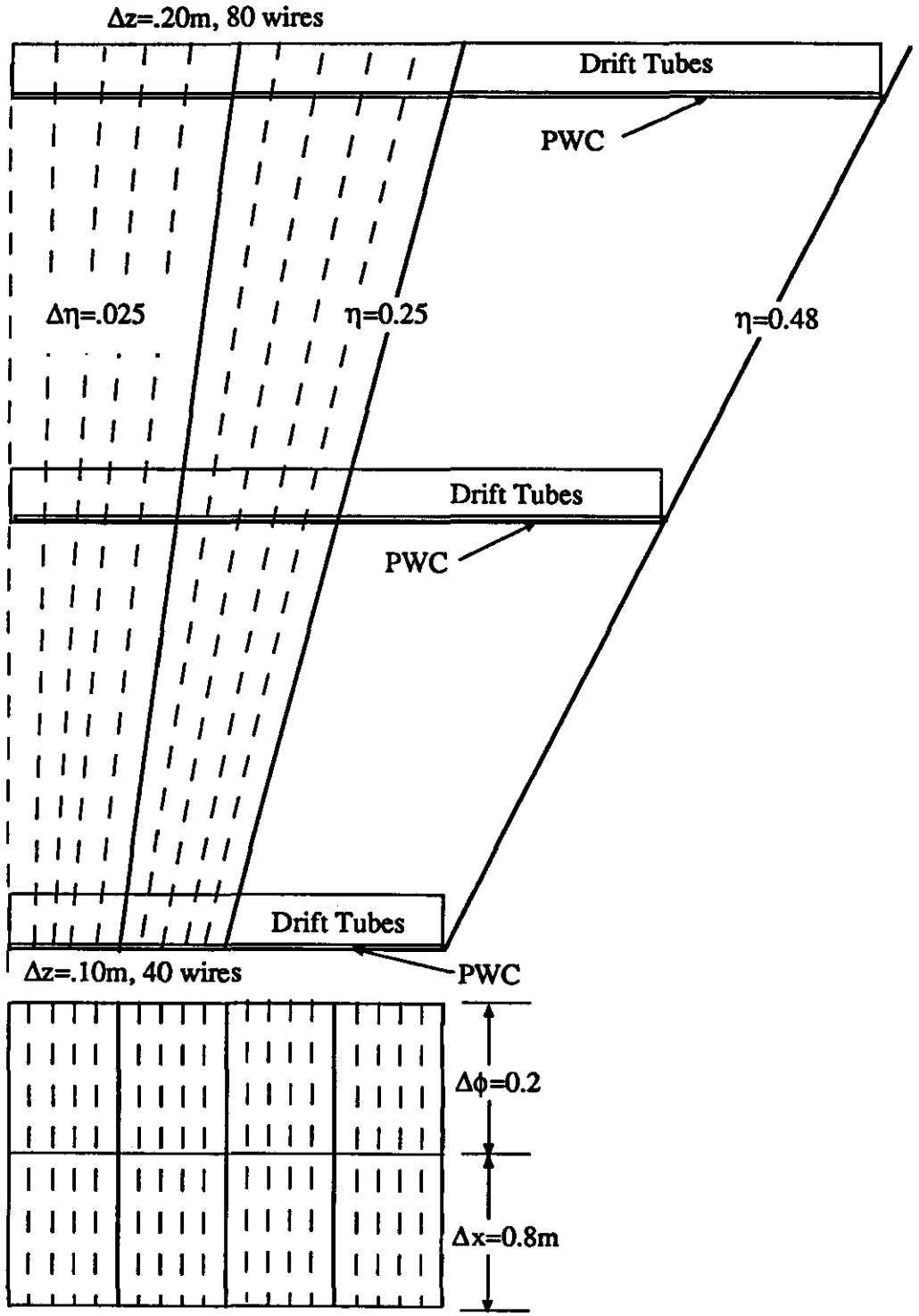

Track-Segment Pattern Logic

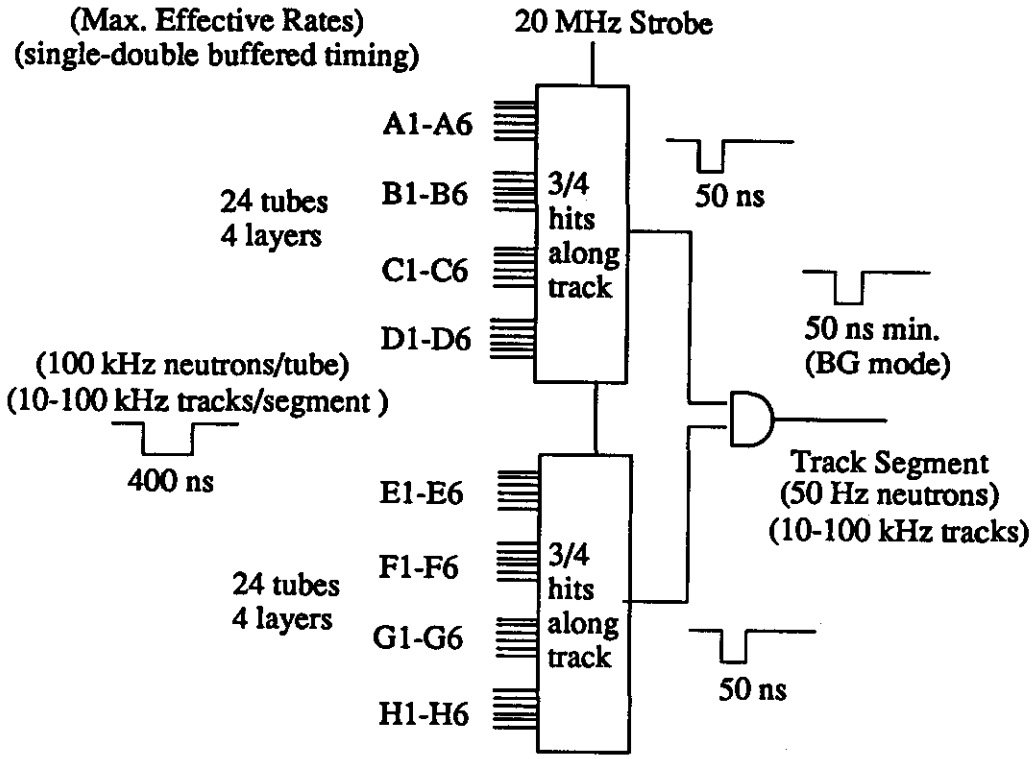

Track Segment Drift Timer

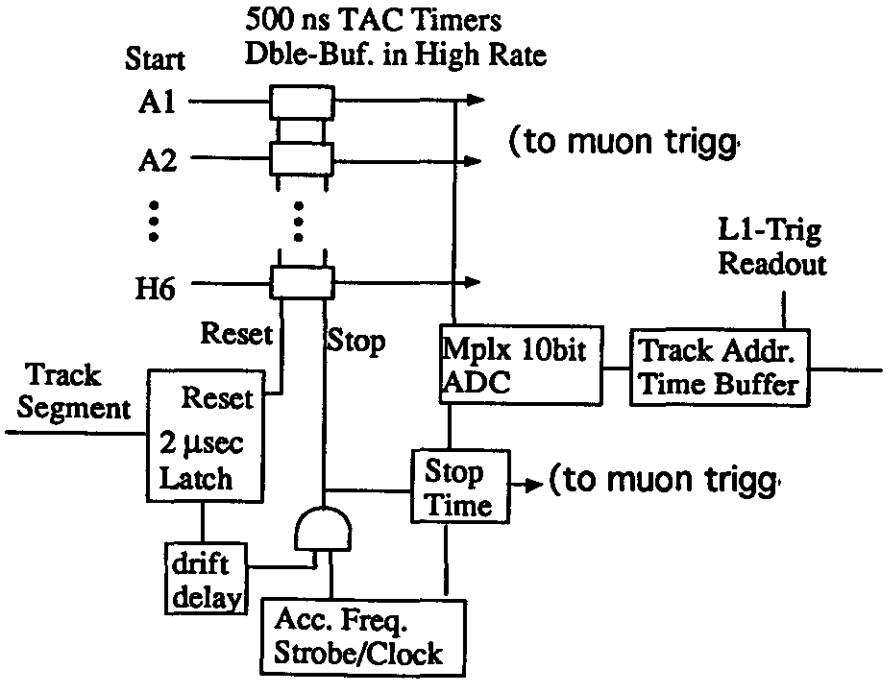

Appendix E

February 1, 1993
A.Korytov,
MIT

T_0 and P_T Stand Alone Trigger in a Muon System Based on Drift Tubes

SUMMARY.

Shown is an option of the time and momentum muon trigger based on drift tubes only. Simulation, experimental data and electronics analysis prove that the scheme is viable (reliable and well within the cost budget).

1. The Idea.

The idea of a stand alone trigger is to measure p_T of a track in the muon system and to assign this trigger to a single bunch crossing (i.e. to measure T_0 with an accuracy better than 16 ns) using drift tubes only. This information is assumed to be obtained at the level 1 trigger, i.e. faster than during 1 μs including drift time.

p_T-trigger itself is not any different from any other proposed system (RPC's or CSC's). Segmentation (1 inch tube diameter) seems to be adequate (only Yes-No information is assumed) and maximum drift time of 300 ns does not make any constrain. Calculations of the bending are trivial (fig.1) and cannot take longer than 100-200 ns. However, the very forward region (θ~9-15^0) might require a smaller tube diameter (~1cm). However, drift time of 300 ns is definitely too long for straight forward timing. It is a measurement of T_0 that is the main issue.

The concept of T_0-measurement comes from an old idea as shown in fig.2. One can see that drift times measured in a pair of staggered cells do really provide information about T_0. However, one may notice that the reality is not so simple as presented in fig.2. First, drift time vs. distance, in general, is not a linear function. Secondly, the track can have a certain inclination (can be far not perpendicular to the chamber plane -- fig.3(a)). In third, as soon as the track is not perpendicular, it can go by one side of wires, rather than between wires -- fig.3(b). And at last, δ-electrons and other time errors result in additional complications.

Does it mean that the idea of timing based on slow drift chambers hopeless? The answer is *not at all*.

First of all, it turns out that function T(x) for typical gases can be rather reasonably approximated by linear plus parabolic terms (fig.4):

$$T(x) = a \cdot x + b \cdot x^2 \qquad (1)$$

Secondly, if one would know a track angle, it would make possible a simple calculation of T_0 (fig.5) as follows:

$$T_0 = \frac{T_1 + T_2}{2} - \frac{a}{2} C_\alpha - \frac{b}{4}\left(C_\alpha{}^2 + \frac{(T_1 - T_2)^2}{(a + bC_\alpha)} \right), \qquad \text{where } C_\alpha = R + \alpha D. \qquad (2)$$

However, it is obvious that this expression gives the right answer only in a case when the track goes between wires. If it does not, the formula would give a rather arbitrary number.

These three assumptions gave an idea for stand along trigger:
1) indeed, one can see from fig.4 that formula (1) gives very good approximation (difference between fit and data does not exceed ~ 4 ns in the worst points)*;
2) inclination of a track in the chamber is a sum of angle which an infinitely high momentum track would have (this is determined by a hit position within the chamber with an accuracy ~ 1 mrad) and an additional bending angle (which can be trivially obtained from comparison of hit positions in super layer SL2 and super layer SL3; in fact this angle is a measure of p_T which has to be measured any way -- fig.1 and Appendix 1);
3) if one would calculated T_0's for each pair of tubes in a super layer, then the pairs where a track went between wires would give the right (and the same) number, whilst the other pairs would give rather random numbers which would be spread around with a very low chance of coincidence; thus, by picking up the most frequent answer one should get the right T_0 with a very high efficiency;
4) δ-electrons should also give random T_0's so that their influence on the T_0-trigger could turn out to be negligible for reasonable probabilities to get a δ-electron in a drift cell.

Another way to do the same was proposed by L.Barabash [1]. One can see that any track is fully described by three parameters: T_0, a point of track

* It should be noted that the function T(x) could be any monatomic function when look-up tables are used for the calculations instead of a direct computation as given by formula (2). Therefore, the fact that we have assumed in this note $T(x)=a*x+b*x^2$ does not hurt the generality of the approach.

entrance in a chamber and a track angle. Therefore, one need three equations to solve this. The idea was to use cell triplets to get these three equations. However, this can turn out not to be so easy. First of all, due to left-right ambiguities each triplet gives four possible answers, just one of them being right. Then, number of usable triplets (all three cells are in row) per given number of layers is smaller than the number of possible pairs. And finally, the bigger the number of planes participating in a single calculation is, the more distractible the effect of δ-electrons would be.

2. Monte Carlo.

We assumed that the middle super layer consists of eight axial layers (N=8), all layers being assumed to be in one chamber -- fig.6. (Some results simulated for the case when these eight planes are grouped by four in two independent chambers can be found elsewhere [2]. The case of 6 axial planes, one pair of u- and one pair of v-planes has also been simulated [3]. All results are quite similar.) It is reasonable to restrict ourselves to the pairs of neighboring planes (N-1) and the pairs of planes with only one layer in between (N-2). The pairs separated far apart would give bigger angle sensitivity in T_0-calculations, and, also, a constant C_α becomes angle dependent. Thus, total number of pairs to be used in calculations 2N-3=13 (one can calculate that number of triplets is N-2=6).

First, we ran MC without introducing any measurement errors and δ-electron production, to check how many pairs have a track going between wires. Fig.7 shows that in average there are about 8 good pairs (out of 13). These pairs give right answers. Also, one can see that wrong answers are spread far away around so that a probability for coincidence of two wrong answers should be very low. Table 1 shows that in case of measurements without errors each event has at least 7 right answers.

To figure out sensitivity of such kind of trigger to measurement errors, we put in MC following error sources:
1) δ-electron production (ε - probability to get a δ-electron per cell, δ-electrons had a random distribution between 0 and actual distance from a track to a wire). Typical probability is 3-5% as was measured in our Fermilab tests [4].

2) δT, drift time error (jitter) due to diffusion, misalignment, electronics and etc. (2ns error is considered to be typical what corresponds to about 100 μm space resolution).
3) ΔT, TDC bin width, the error which essentially could be included in the previous one.
3) δa, an error in estimation of a track angle in the chamber (it is easy to estimate that if one uses only Yes-No information from tubes in SL2 and SL3 the error would be .003 rad (RMS) or smaller).

We ran the MC with uniform angular spread of tracks within $-11^0<\varphi<+11^0$. A beam crossing number was assigned to each of 13 answers obtained for a track depending on a bucket (16 ns wide) the answer had dropped in.

Tracks had no spread in θ so that no time correction on signal propagation along a wire was needed. It has been shown [5] that drift tubes have a very important advantage in terms of this correction since z-coordinate is available from the same wires (by means of time difference from connected wire pairs) so that there is no need to correlate $r\varphi$-measurements with independent z-measurements. The z-information is also necessary even for a p_T trigger in the end-cups [6].

At this first stage we also did not put multiple scattering in the MC. Nevertheless, it is shown (Appendix 2) that the multiple scattering does not lead to errors exceeding the typical measurement errors mentioned above.

Applied separately, the errors result in trigger inefficiencies as presented in Fig.8(a,b,c). One can see that the typical errors (marked by arrows) are far away from dangerous boundaries where inefficiency drastically increases. Fig.9 shows inefficiency vs. muon momentum when all three errors are turned on. One can see that inefficiency remains to be very small even when all errors have been arbitrary doubled(!); also, a TDC bin width of 8 ns seems to be very well adequate (this is not surprising since this does not add much to already assumed time error of 4 ns (RMS)).

It is worthwhile to mention that neutrons with a rate estimated to be $10^4\,cm^{-2}s^{-1}$, are equivalent to δ-electrons giving a small addition of about 1% to ε. Also, should it be necessary, the neutrons can be easily sorted out on the base of z-coordinate correlation between planes in the chamber (this information is immediately available from time differences on the connected wires).

3. Experimental Data.

The results of the Monte Carlo simulation have been checked against the data obtained with the large scale LSDT prototype [7] during tests at TTR. The 4 m long prototype had 4 planes of tubes. It operated at limited streamer mode in a gas mixture Ar+Isobutane=1+3. The TTR trigger on a cosmic muon was not exactly correlated with the time at which the triggered muon went through. Thus, the drift chamber a priori did not have any T_0 information so that these tests have provided a very reliable comparison.

The analysis was done in the following way.

Some data cuts were made to insure that the chamber did really have a clean track at the level better than 1% (it is very important for inefficiency estimations).

First, a requirement of self-consistency of TTR data had been applied (a reliable track and just one). These cuts are not essential for the discussion since at this step no information from the LSDT chamber had been used.

Secondly, some soft requirements had been applied to the cleanness of the chamber data:

-) number of fired cells had been required to be smaller than 6; this suppressed the rest of multitracks events which had not been caught at the stage of TTR cuts;

-) at least one hit per plane had been required to suppress events with tracks went trough the edge of the chamber;

-) just one hit in the top plane had been required to make sure that there is information about a coordinate along a wire (only this plane had wires connected in pairs).

No other cuts which would require any self-consistency of measurements in the chamber had been applied.

After that an experimental function T(x) had been fitted by sum of linear and parabolic terms - fig.10.

Then, using an external information (from TTR) about angle of a track, all 6 T_0's were calculated (one can make 6 pairs out of 4 planes). Then, using TTR data (scintillators), actual T_0 was calculated. The difference between these zero times is shown in fig.11. One can see that the majority of answers sits in zero and the peak is quite narrow ($\sigma \sim 3$ ns is mostly determined by the angle error).

After that, each of 6 answers was assigned to a particular 16 ns wide bucket and the bucket containing the biggest number of answers was chosen

as T_0-trigger. Fig.12 shows distribution of such decisions. One can see that the bucket "Zero" ('right' answer) have been selected in 94% of cases. About 5% gave wrong answers and less than 1% of cases (most left bucket) did not give any coincidence.

Then, we ran MC for this 4 plane chamber. The following table (Table 2 in fig.13) compares the MC predictions and the data:

Four plane chamber:

	MC	DATA
Right answers	93.6%	94%
Wrong answers	6.1%	5%
No answer	0.3%	1%

The remarkable coincidence of data and simulation allows to rely on the MC results.

4. Is it necessary to know a bending angle?

When one thinks about this scheme a reasonable question emerges: how difficult is it to correlate hits in superlayer 2 and 3 to get a bending angle (which is needed for calculations)?

First of all, this has to be done anyway in any system to get a p_T trigger. Therefore, this is not a problem specific to the stand alone trigger.

The only worry one might have is a case when two actual tracks get close to each other. Let us assume that there are two tracks of relatively high momentum close to each other so that we could make several combinations between one of hits in the SL2 and two hits in the SL3. Also, let us assume that both combinations satisfy to the p_T trigger. Then, one might have a dilemma which of two possible bending angles to chose for T_0 calculations: two different angles could result in two different T_0-answers.

First, let us estimate if this problem is serious in the barrel. There are two components to be considered: accidental coincidence (when a track gets

close to another one accidentally), and a correlated case (a decay of a high momentum Z^0 would be an example).

The simplest tactics could be as follows. As soon as one gets a track segment in SL3, it is projected back in the SL2. A track segment closest to this projected point is considered to be the right segment to be used for calculations of bending and T_0. The distance between the projected point and the actual hit point in SL2 is (see fig.1(a))

$$\Delta Y = eB\frac{L_2(L_3 - L_2)}{2}\cdot\frac{1}{p_T} = \frac{3.6m}{p_T(GeV/c)} \tag{3}$$

Therefore, the probability to get an independent track within this distance (fig.14(a)) is

$$p = N\cdot(2\cdot\Delta Y\cdot L)\cdot T_{drift} \sim \frac{8.6\%}{p_T(GeV/c)} \tag{4}$$

where N - charged particle rate (~1. $cm^{-2}s^{-1}$ in SL2 @ 10^{34} luminosity [8]), T_{drift}~300 ns, L - drift tube length (~4 m). One can see that this probability is absolutely acceptable even for the lowest p_T~10 GeV/c.

Now let us consider a case of two correlated muons on an example of a Z^0 decay. If a Z^0 energy is E, then it decays into two muons with p_T~E/2 (in the barrel) and opening angle θ~2m/E~m/p_T. With this opening angle a distance between these two muons in the SL2 would be R~θ *L_2~m*L_2/p_T what is considerably bigger than ΔY. The probability to have these muons aligned so that in r_φ-projection they would be closer than ΔY (fig.14(b)) is

$$p = \frac{(2\cdot\Delta Y)/R}{\pi} \sim 0.4\% \tag{5}$$

what is again negligible (and does not depend on p_T).

Thus, these estimations convince that there is no problem with a bending angle and the T_0-trigger will, therefore, definitely work in the barrel.

Before going to the end-cup regions where the rate will be much higher, let us take a look at what happens if information about bending is ignored. That means the angle to be used in calculations is determined by a track segment coordinate in SL2 alone (this is equivalent to an infinitely

high momentum track). Fig.15 (we are still in the barrel) shows that if one would wish to have trigger for muons with p_T>30 GeV/c, this would work perfectly. However, it is definitely not enough when the goal is 10 GeV/c and higher.

Now when we go to the end-cups, the position of drift tubes is different. In the barrel the bending angle is directly connected with the angle of a track in a chamber, and in the end-cups this relationship is not so strong (fig.16) and the angle of a track in a chamber is much more predictable (due to a large axial component of a muon momentum). At $\theta \sim 30^0$ the uncertainty in the angle a muon goes through the chamber is 2 times smaller than that in the barrel. In the very forward region the rate becomes very high and does not allow to rely on unambiguous measuring of a bending angle. However, this is a region that does not need this measurement: the uncertainty does simply vanish. The efficiency of the T_0 trigger in the very forward chambers is shown in fig.17 (no information about bending angle has been used in T_0 calculations).

The conclusion is as follows:

BARREL: one needs to measure a bending angle and to use it in T_0 trigger and this does not seem to be difficult;

END-CUPS: the change of chamber orientation allows to have a full T_0 efficiency without measuring a bending angle which makes a T_0 trigger be even simpler.

6. Time Budget for the Calculations.

The following very naive model is given with the only purpose to show that even a very conservative estimation of the time needed to perform the calculations does not exceed 1 μs, including full drift time. More realistic (and simpler) electronics will be shown to do the same faster (~750 ns).

Table 3 shows that if one makes direct arithmetical calculations in three parallel streams (and assuming 50 ns per one operation), the all T_0 answers would be obtained in 400 ns. About 100 ns should be enough to select the most frequent answer out of N~13. Adding 300 ns for full drift

time, 50 ns for signal propagation along anode wires and 100 ns for bending angle estimation, one ends up with about 950 ns.

7. Electronics.

The possible realizations of the trigger electronics is attached in the Appendix 3. The general conclusion (R.Sumner [Appendix 3], D.Marlow [Appendix 4], M.Shaevitz [10], M.Atya [10]) is that this electronics does not seem to be any difficult to build. It does not require anything not available today.

Since this trigger scheme does not require any special additional detectors, the cost of electronics represents the entire cost of the trigger. The trigger electronics has been costed to be about ~$21.4/channel (R.Sumner, LeCroy).

8. Conclusions.

- **The Stand Alone Trigger proved to provide p_T and T_0 triggers.**
- **The experimental data validate the idea and the MC results.**
- **It has been shown that the decision can be easily made within the time range available at level 1 trigger (<1 μs).**
- **All information (p_T; T_0 and z (coordinate along a wire: axial in the Barrel and radial in End-Cups)) is available from the same end of a chamber, i.e. there is no problem inherent to the designs where this information has to be correlated (e.g. time and z from wires, bending from strips).**
- **Electronics required is not primitive but not a state-of-art either. Electronics cost is estimated to be around $22/channel.**

9. Acknowledgments.

The author is very thankful to all who got involved in numerous and fruitful discussions of the concept: L.Barabash, G.Mitselmakher, L.Osborne, L.Rosenson, F.Taylor and many other members of the muon group. The expertise in electronics of R.Sumner and D.Marlow have played a crucial role in justifying the viability of the scheme and can not be overestimated. A deep in-look made by the external review committee (J.Branson, K.Foley, C.Fubjan) is appreciated very much. The critical overviews made by M.Atya and M.Shaevitz were very important for better understanding of the matters concerned and validating the concept.

References:

1. L.Barabash and et al.,
in GEM internal note TN-92-133, p.145; July 3, 1992
2. A.Korytov, in GEM internal note TN-92-192; Sept 2, 1992.
3. A.Korytov, in GEM muon group meeting, Jan 18, 1993.
4. MIT group, "Tests of a LSDT chamber at .5 TeV muon beam",
to be published
5. "Drift Prototype Results at TTR",
in GEM muon group meeting, Jan 18, 1993
6. A.Korytov, GEM internal note TN-93-264.
7. Description of the LSDT prototype can be found in
GEM internal note TN-92-203
8. GEM LOI, Nov 30, 1991, p.19
9. The talks given at Brookhaven Muon Group Meeting, 5 Nov 1992,
GEM internal note TN-92-241

Figure Captions.

Fig.1(a). A muon track going through chambers of SL2 and SL3. The value ΔY is a measure of bending and, therefore, p_T.

Fig.1(b). A muon track in SL2: α_{02} is an angle which an infinitely high momentum muon would have; α_2 is an additional bending angle; $\alpha_{2TOT}=\alpha_{02}+\alpha_2$ is an angle of a track in the chamber.

Fig.2. The concept of T_0 calculations in a pair of staggered cells.

Fig.3(a). A track can be inclined.

Fig.3(b). An inclined track can go on one side from wires.

Fig.4. Fit of drift time data by a simple function $T(x)=a*x+b*x^2$:
(a) Ar+Isobutane=1+3;
(b) $CF_4+CO_2+C_4H_{10}$=70+20+10.

Fig.5. Calculation of T_0 in a pair of staggered cells when a track angle is known and the drift time function is $T(x)=a*x+b*x^2$.

Fig.6. Layout of drift tubes in SL2 used in the MC calculations.

Fig.7. Distribution of all T_0's (13 T_0's per event). No measurement errors have been assumed.

Fig.8. Inefficiency of T_0-trigger when different sources of errors have been applied separately:
(a) inefficiency vs. probability per cell of getting a δ-electron;
(b) inefficiency vs. time error (RMS);
(c) inefficiency vs. angle error (RMS).

Fig.9. Inefficiency of T_0-trigger when different sources of errors have been applied together. Three numbers in the legend mean a δ-electron probability, time error (ns), angle error (mrad) correspondingly.
The first set of numbers represent typical values one might expect. Notice that the inefficiency is still small when all errors have been arbitrary doubled (the second set of numbers) and an additional error corresponding to a wide TDC bin width has been applied.

Fig.10. Fit of data (drift time vs. distance) obtained with the large scale

LSDT prototype at TTR by a simple function $T(x)=a*x+b*x^2$.

Fig.11. The difference between T_0 as calculated in the drift chamber and T_0 as measured at TTR (scintilators). All 6 T_0's per track are in the same histogram.

Fig.12. A distribution of final T_0-decisions. A hist bin width is 16 ns.

Fig.13. A four plane LSDT prototype and table 2 where cosmic muon results compared with the MC simulation made for this chamber.

Fig.14(a). A scheme for calculation of probability that two independent tracks will get close enough to confuse the T_0 calculations.

Fig.14(b). A scheme for calculation of a probability that two correlated muons ($Z^0 \rightarrow \mu,\mu$) will get close enough (in r_φ-projection) to confuse the T_0 calculations.

Fig.15. A T_0-efficiency in the barrel when the information about a bending angle (α_2; fig.1(b)) is ignored.

Fig.16. The change of chamber orientation in the end-cups makes the track angle in a chamber be much more predictable than in case of a track with the same p_T in the barrel.

Fig.17. A T_0-efficiency vs. muon p_T in the end-cup region for different θ <u>without</u> using any information from SL3 (δ-electrons (.05) and time error (2 ns) have been included).

table 1

ONE BUNCH (+-8 ns) WIDE BUCKET:
a= 5.031063 b= 1.411695
KEY=1
eps=.000 Terror(ns)=0.0 Tbin(ns)= 0.0 Aerror(rad)=.000

P= 10.GeV:	Nyes-Nno-Nwrong-Nminus-Nplus=	100.00	0.00	0.00	0.00	0.00
P= 14.GeV:	Nyes-Nno-Nwrong-Nminus-Nplus=	100.00	0.00	0.00	0.00	0.00
P= 20.GeV:	Nyes-Nno-Nwrong-Nminus-Nplus=	100.00	0.00	0.00	0.00	0.00
P= 28.GeV:	Nyes-Nno-Nwrong-Nminus-Nplus=	100.00	0.00	0.00	0.00	0.00
P= 40.GeV:	Nyes-Nno-Nwrong-Nminus-Nplus=	100.00	0.00	0.00	0.00	0.00
P= 80.GeV:	Nyes-Nno-Nwrong-Nminus-Nplus=	100.00	0.00	0.00	0.00	0.00
P=160.GeV:	Nyes-Nno-Nwrong-Nminus-Nplus=	100.00	0.00	0.00	0.00	0.00
P=320.GeV:	Nyes-Nno-Nwrong-Nminus-Nplus=	100.00	0.00	0.00	0.00	0.00

C.L.*	p=10	=14	=20	=28	=40	=80	=160	=320 GeV/c
0	0	0	0	0	0	0	0	0
1	0	0	0	0	0	0	0	0
2	0	0	0	0	0	0	0	0
3	0	0	0	0	0	0	0	0
4	0	0	0	0	0	0	0	0
5	0	0	0	0	0	0	0	0
6	0	0	0	0	0	0	0	0
7	1859	1874	1875	1882	1902	1852	1904	1881
8	2386	2583	2724	3027	2873	2904	2975	2977
9	2219	2234	2220	2035	2193	2150	2100	2124
10	2240	2273	2276	2253	2260	2271	2186	2200
11	1101	884	725	627	585	619	605	585
12	92	65	81	84	87	76	69	60
13	103	87	99	92	100	128	161	173

* C.L. – Coincidence level (number of right answers per event)

TABLE 5

(INPUTS : $T1$, $T2$, α, a, b, $C1$, $C2$)

# 0 INPUT	$X1 = T1$	$Y1 = T2$	$Z1 = \alpha$
# 1	$X1 = X1 + Y1$ $(T1+T2)$	$Y1 = X1 - Y1$ $(T_1 - T_2)$	$Z1 = Z1 \cdot C2$ (αC_2)
# 2	$X1 = X1/2$ $\left(\frac{T_1+T_2}{2}\right)$	$Y1 = Y1 * Y1$ $(T_1 - T_2)^2$	$Z1 = Z1 + C1$ $(C_0 = C_1 + \alpha C_2)$
# 3	$X2 = a \cdot Z1$ $(a \cdot C_0)$	$Y2 = Z1 * Z1$ $(C_0)^2$	$Z1 = b \cdot Z1$ $(b \cdot C_0)$
# 4	$X2 = X2/2$ $(\frac{a}{2} C_0)$	$Y2 = b \cdot Y2$ $(b C_0^2)$	$Z1 = a + Z1$ $(a + b C_0)$
# 5	$X1 = X1 - X2$ $\left(\frac{T_1+T_2}{2} - \frac{a}{2} C_0\right)$	$Y2 = Y2/4$ $\left(\frac{b}{4} C_0^2\right)$	$Z1 = Z1 * Z1$ $(a + b C_0)^2$
# 6	$X1 = X1 - Y2$ $\left(\frac{T_1+T_2}{2} - \frac{a}{2} C_0 - \frac{b}{4} C_0^2\right)$	$Y2 = b/4$ $\left(\frac{b}{4}\right)$	$Z1 = Y1/Z1$ $\left(\Delta T^2/(a + b C_0)^2\right)$
# 7	—	—	$Z1 = Z1 * Y2$ $\frac{b}{4}\left(\Delta T^2/(a + b C_0)^2\right)$
# 8	$X1 = X1 - Z1$ (T_0)	—	—

$$T_0 = \frac{T_1 + T_2}{2} - \frac{a}{2} C_0 - \frac{b}{4}\left(C_0^2 + \frac{(T_1 - T_2)^2}{(a + b C_0)^2}\right)$$

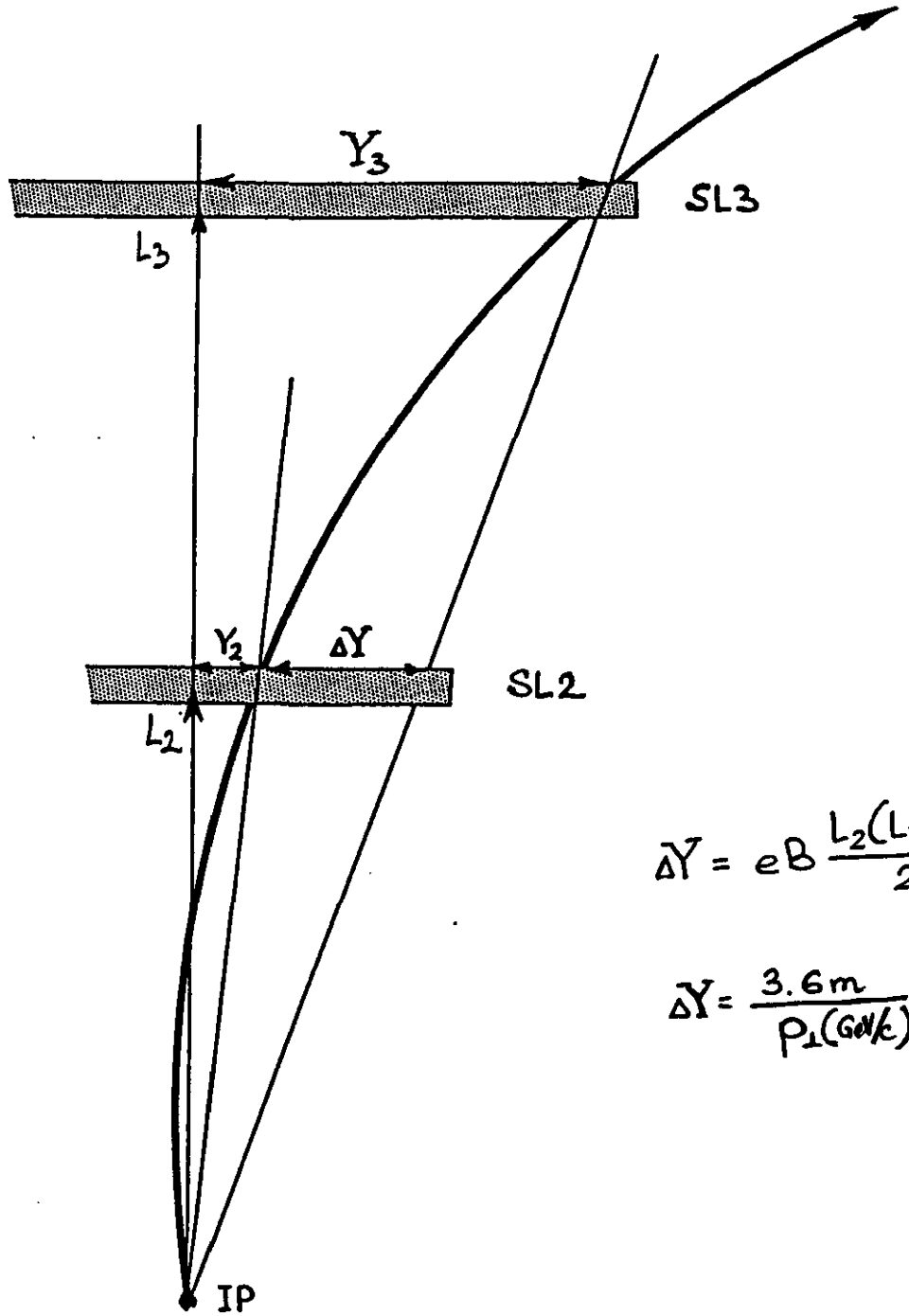

$$\Delta Y = eB\,\frac{L_2(L_3-L_2)}{2}\,\frac{1}{P_\perp}$$

$$\Delta Y = \frac{3.6\,m}{P_\perp(GeV/c)}$$

Fig. 1(a)

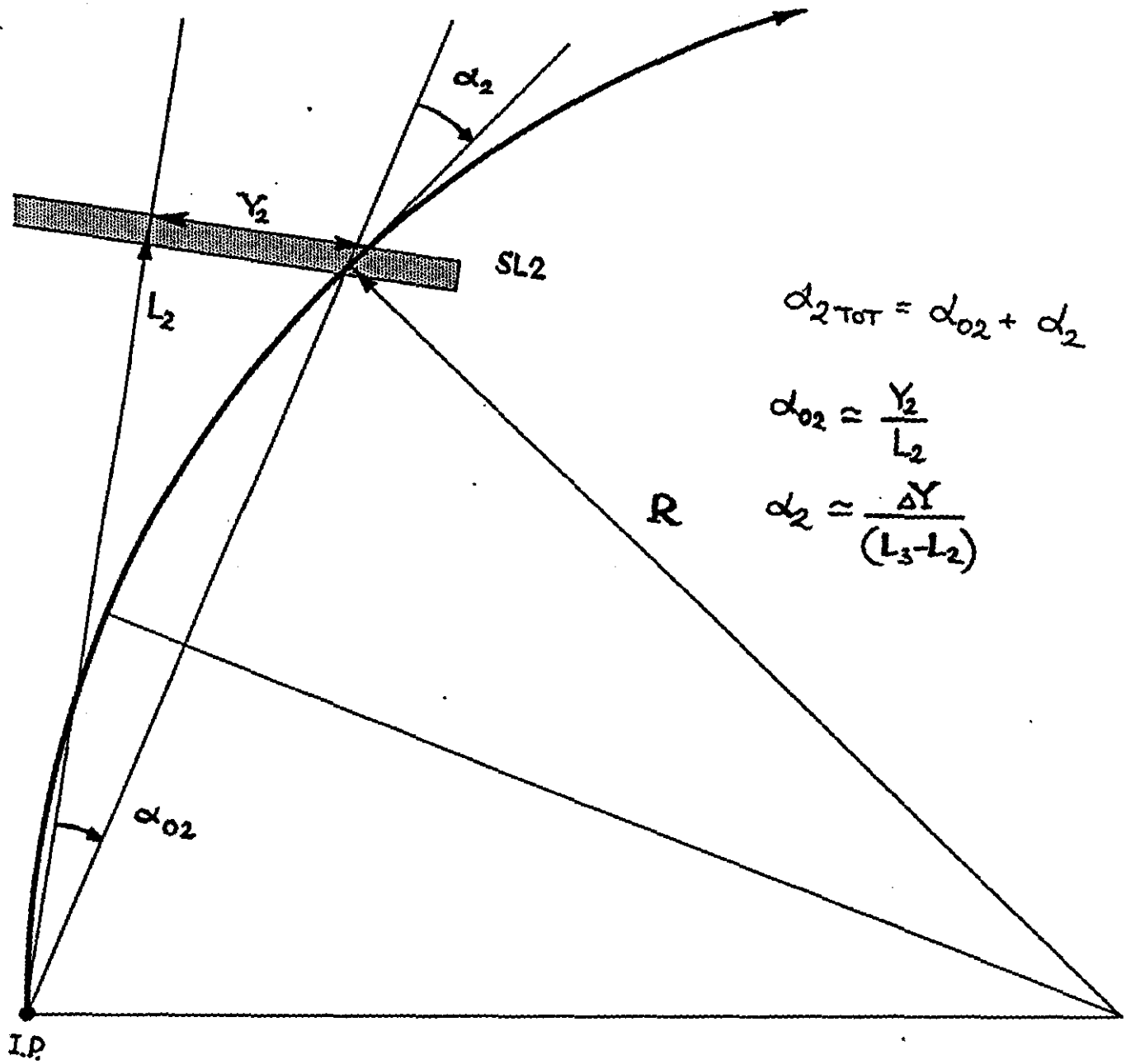
α_2
Y_2
SL2
L_2
$\alpha_{2TOT} = \alpha_{02} + \alpha_2$
$\alpha_{02} \simeq \frac{Y_2}{L_2}$
R
$\alpha_2 \simeq \frac{\Delta Y}{(L_3 - L_2)}$
α_{02}
I.P.

Fig. 1(b)

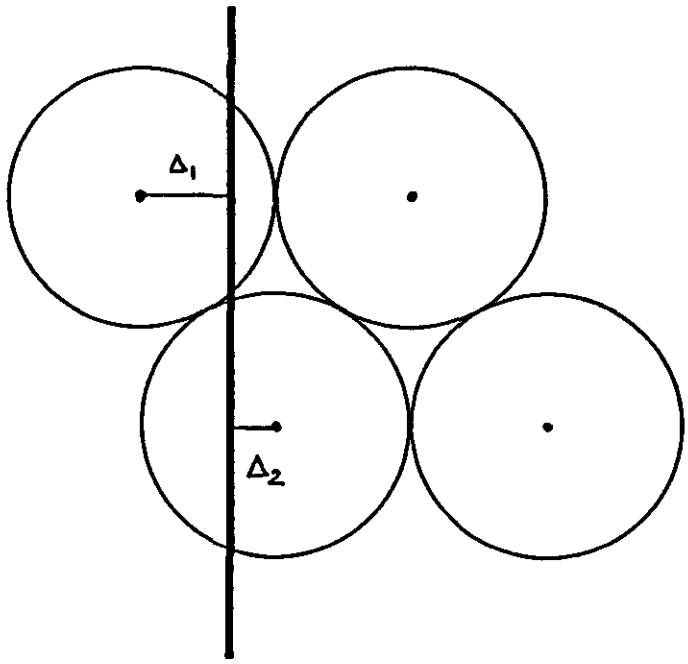

Drift Times:

$\tau_1 = \frac{\Delta_1}{V}$ $\qquad$ $\tau_1 = T_1 - T_0$

$\tau_2 = \frac{\Delta_2}{V}$ $\qquad$ $\tau_2 = T_2 - T_0$

$$\boxed{T_0 = \frac{T_1 + T_2}{2} - \frac{\Delta_1 + \Delta_2}{V}\frac{1}{2} = \frac{T_1 + T_2}{2} - \frac{T_{dr}}{2}}$$

WHAT WAS USED:

1. V_{drift} = const
2. Vertical track ($\alpha = 0$) $\Rightarrow$ $\Delta_1 + \Delta_2 = R$
3. Track went between wires
4. Measurements are good (no δ-electrons, no background)

Fig. 2

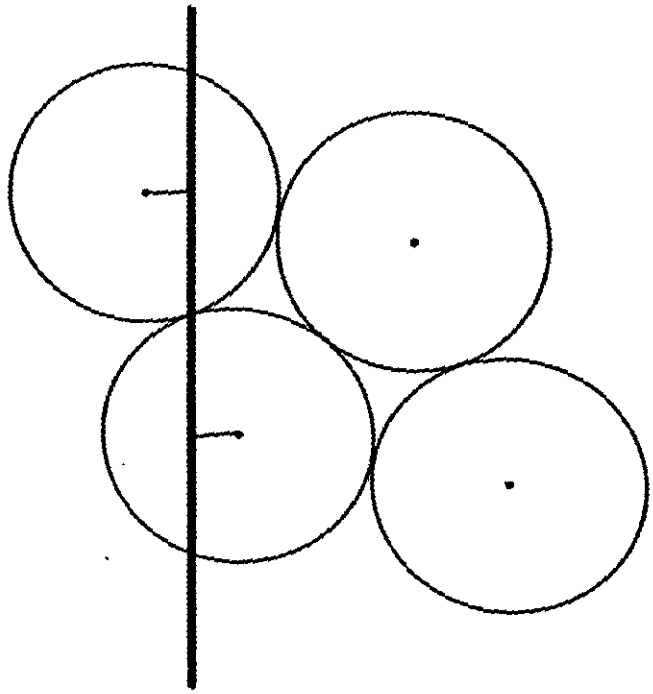

(a)

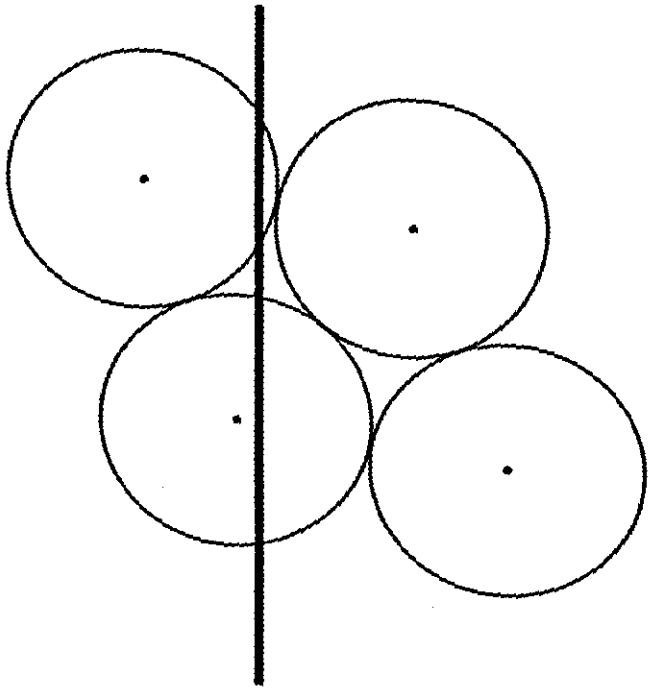

(b)

Fig 3

y = m1*M0 + m2*M0*M0		
	Value	Error
m1	17.357073062	0.094725
m2	0.28546071821	0.0104131
Chisq	13.306709135	NA
R	0.99994534341	NA

T=a*X + b*X^2
(Points are calculated
from accurate fit of LASER DATA),
Ar+IB =25+75

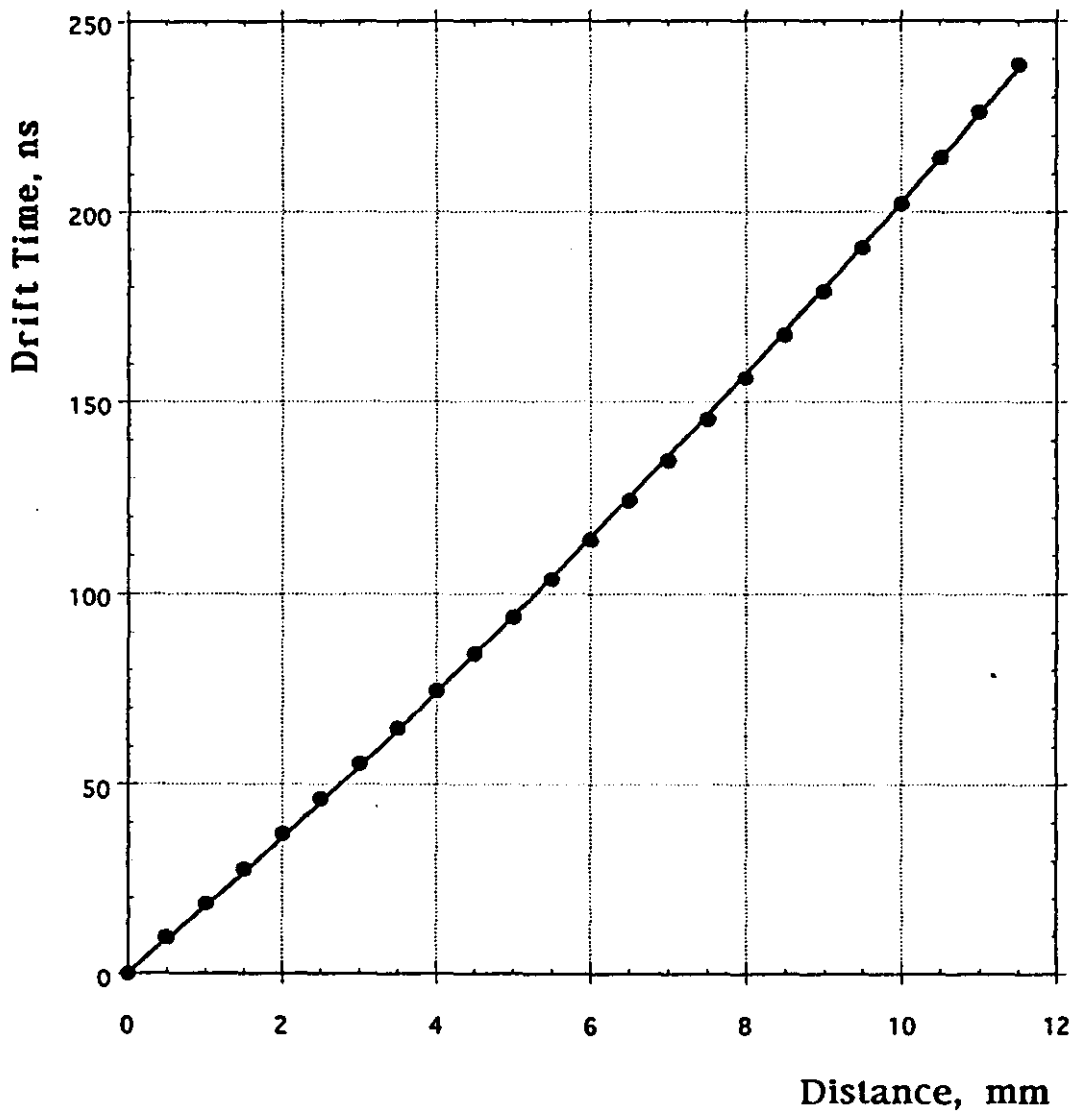

Fig. 4(a)

y = m1+m2*M0 + m3*M0*M0		
	Value	Error
m1	3.3417585497	0.484641
m2	5.031063318	0.23408
m3	1.4116950994	0.0239047
Chisq	2.9760939244	NA
R	0.99995388072	NA

$CF_4 + CO_2 + C_4H_{10} = 69 + 20 + 11$

U = 5.4 kV

Laser Data

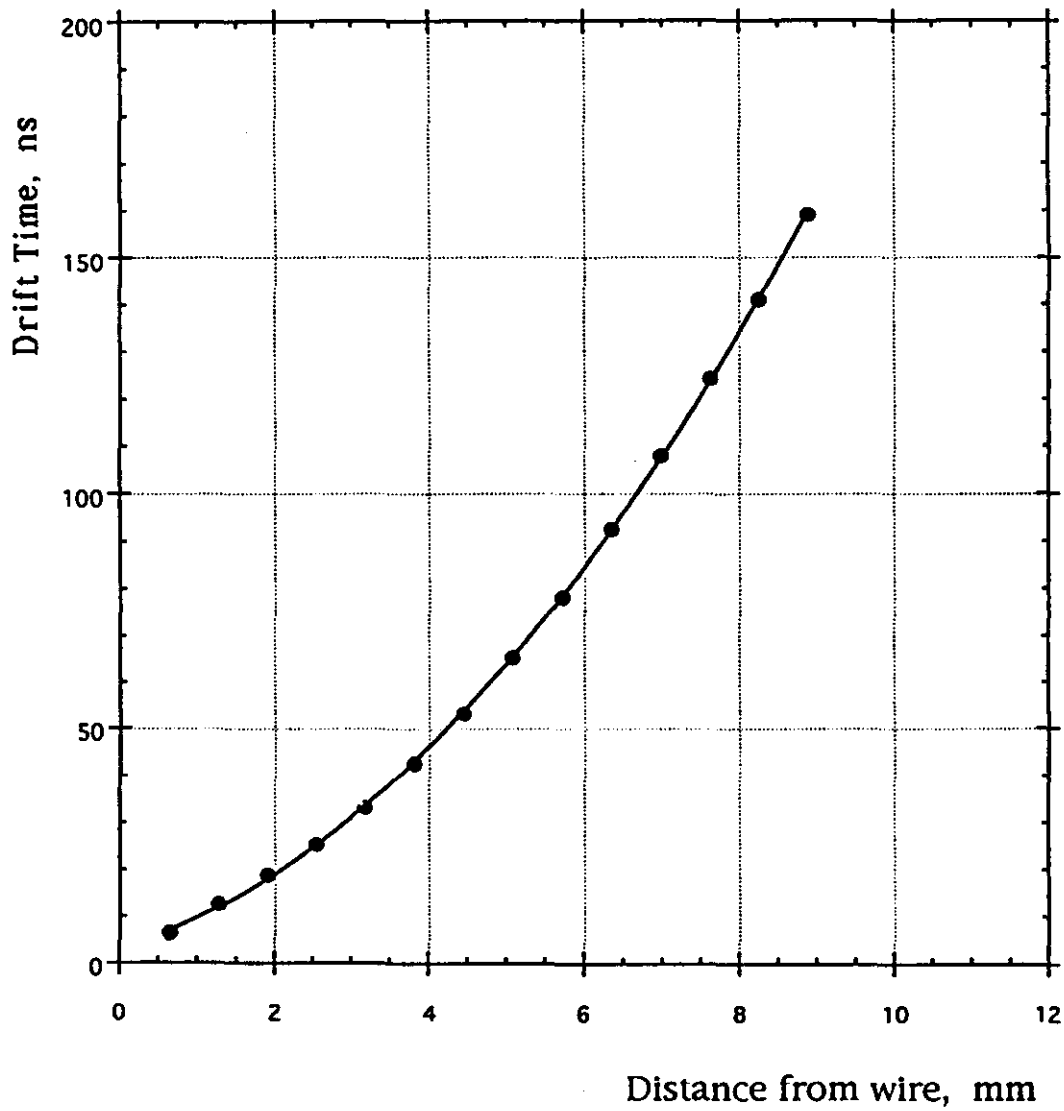

Fig.4(b)

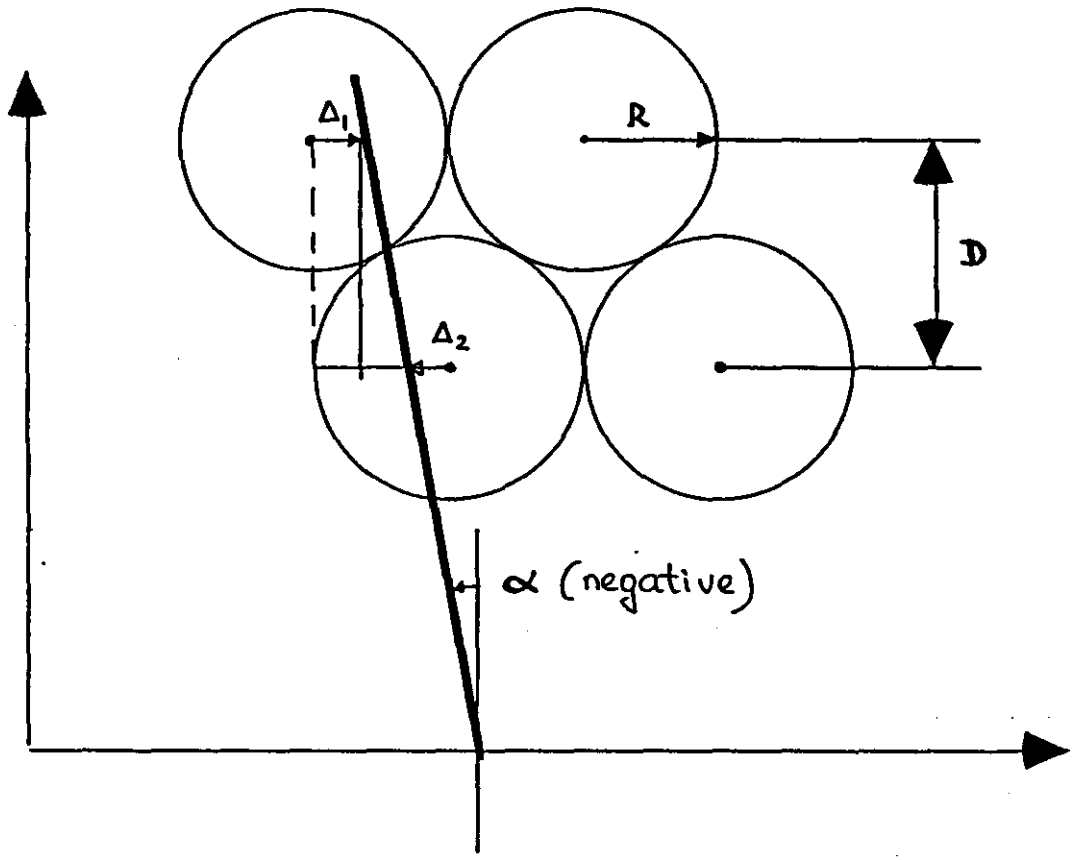

Drift Times:

$$\tau_1 = a \cdot \Delta_1 + b \cdot \Delta_1^2 \qquad \tau_1 = T_1 - T_0$$

$$\tau_2 = a \cdot \Delta_2 + b \cdot \Delta_2^2 \qquad \tau_2 = T_2 - T_0$$

$$\Delta_2 = R + \alpha D - \Delta_1 = C_0 - \Delta_1$$

$$\boxed{\begin{gathered} T_0 = \frac{T_1 + T_2}{2} - \frac{a}{2} C_0 - \frac{b}{4}\left(C_0^2 + \frac{\Delta T^2}{(a + bC_0)^2}\right) \\ C_0 = R + \alpha D \end{gathered}}$$

Fig. 5.

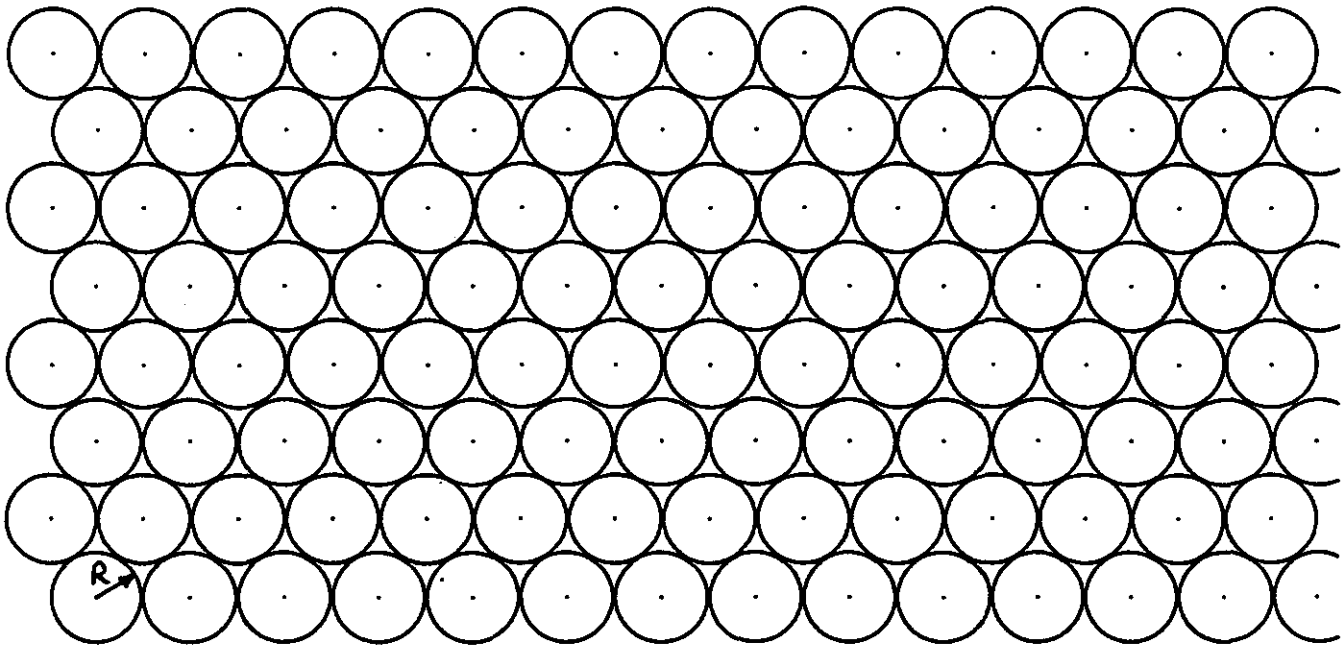

R = 12.5 mm

Fig.6

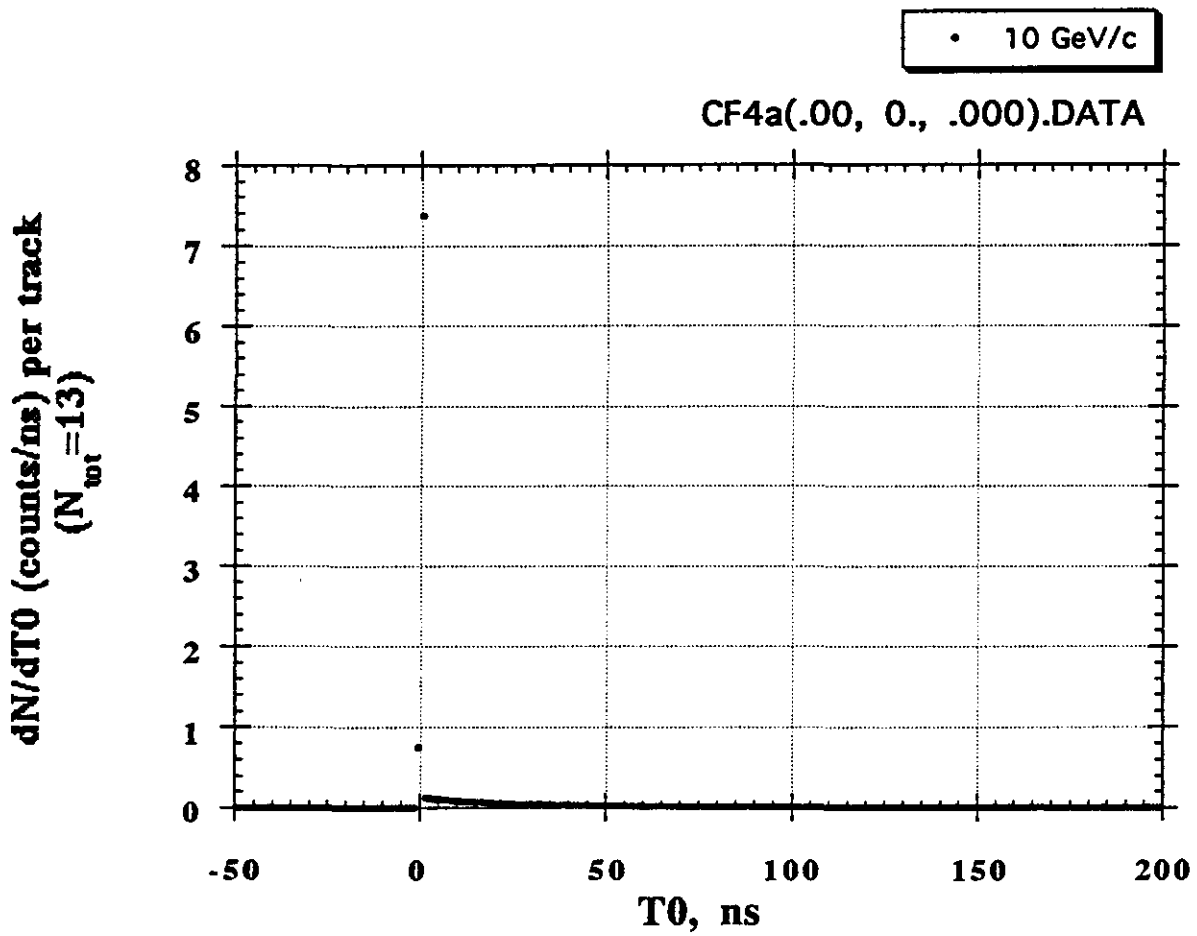
10 GeV/c
CF4a(.00, 0., .000).DATA
dN/dT0 (counts/ns) per track
(N_{wt}=13)
8
7
6
5
4
3
2
1
0
-50
0
50
100
150
200
T0, ns

Fig. 7

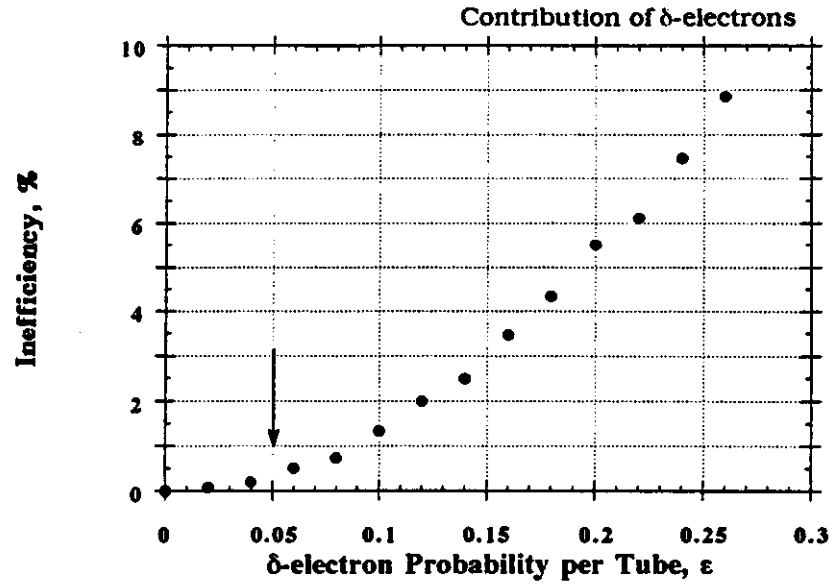
Contribution of δ-electrons
Inefficiency, %
δ-electron Probability per Tube, ε
0
0.05
0.1
0.15
0.2
0.25
0.3
0
2
4
6
8
10

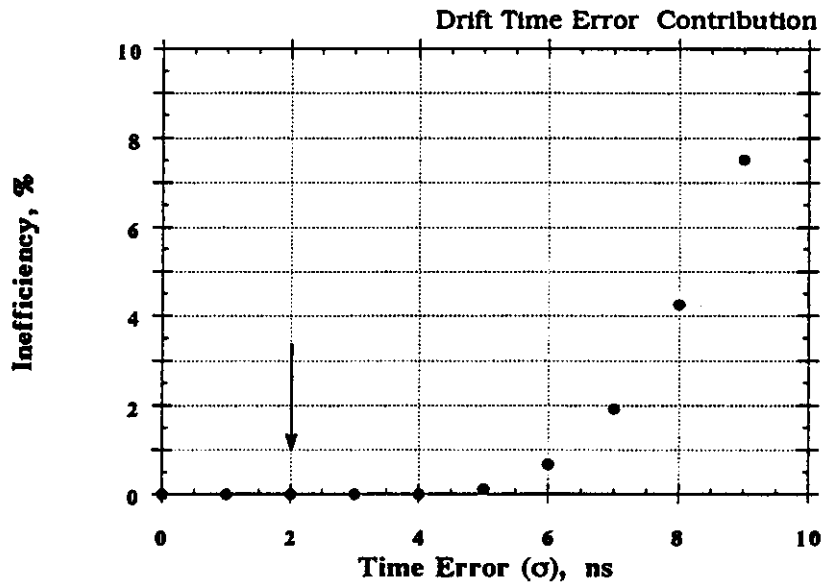
Drift Time Error Contribution
Inefficiency, %
Time Error (σ), ns
0
2
4
6
8
10

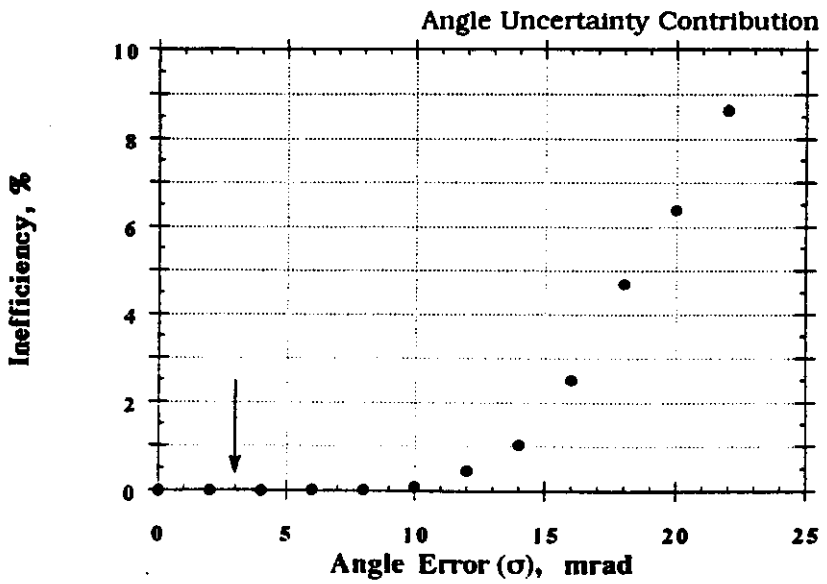
Angle Uncertainty Contribution
Inefficiency, %
Angle Error (σ), mrad
0
5
10
15
20
25
0
2
4
6
8
10

Fig. 8.

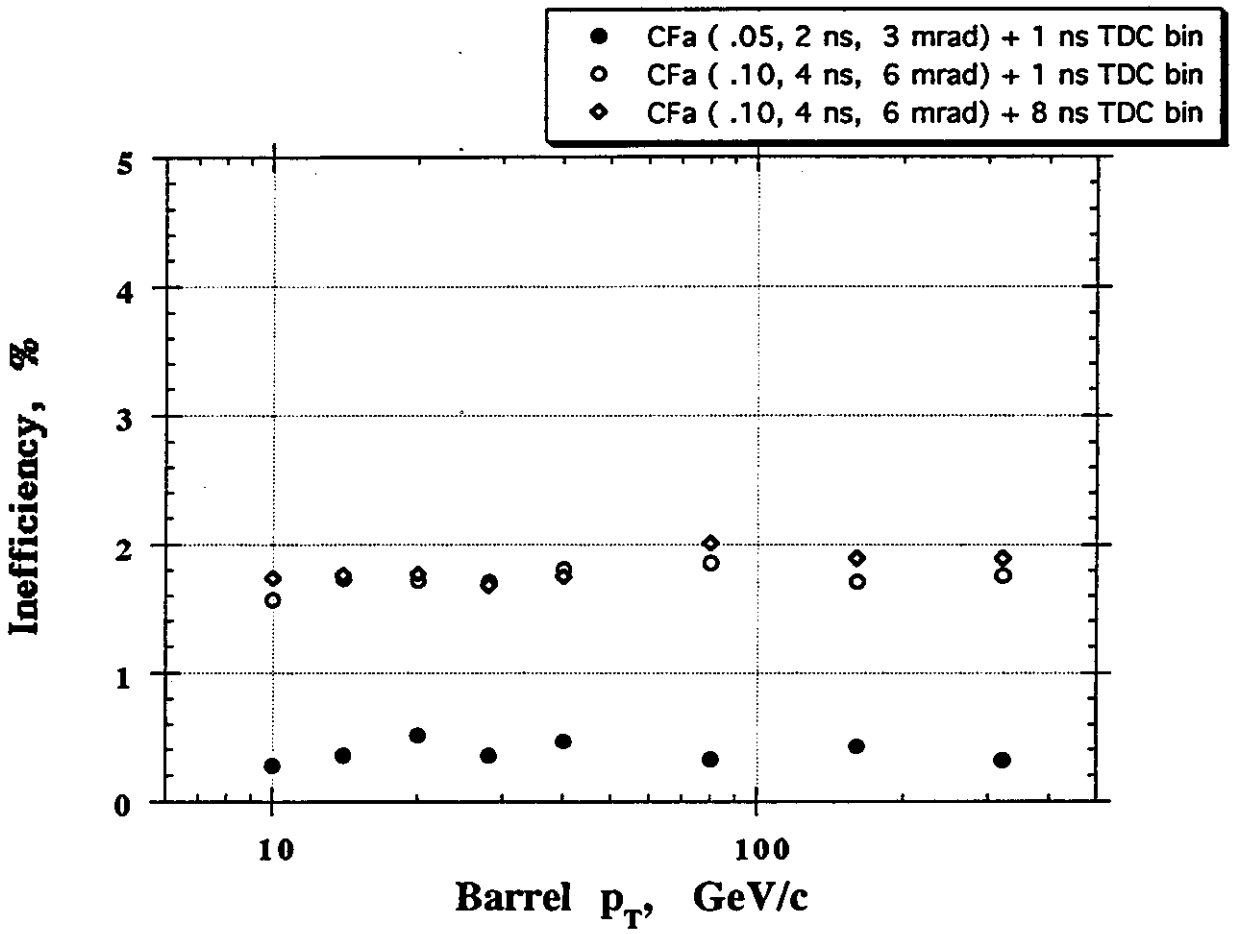
CFa (.05, 2 ns, 3 mrad) + 1 ns TDC bin
CFa (.10, 4 ns, 6 mrad) + 1 ns TDC bin
CFa (.10, 4 ns, 6 mrad) + 8 ns TDC bin
Inefficiency, %
0
1
2
3
4
5
10
100
Barrel p_T, GeV/c

Fig. 9.

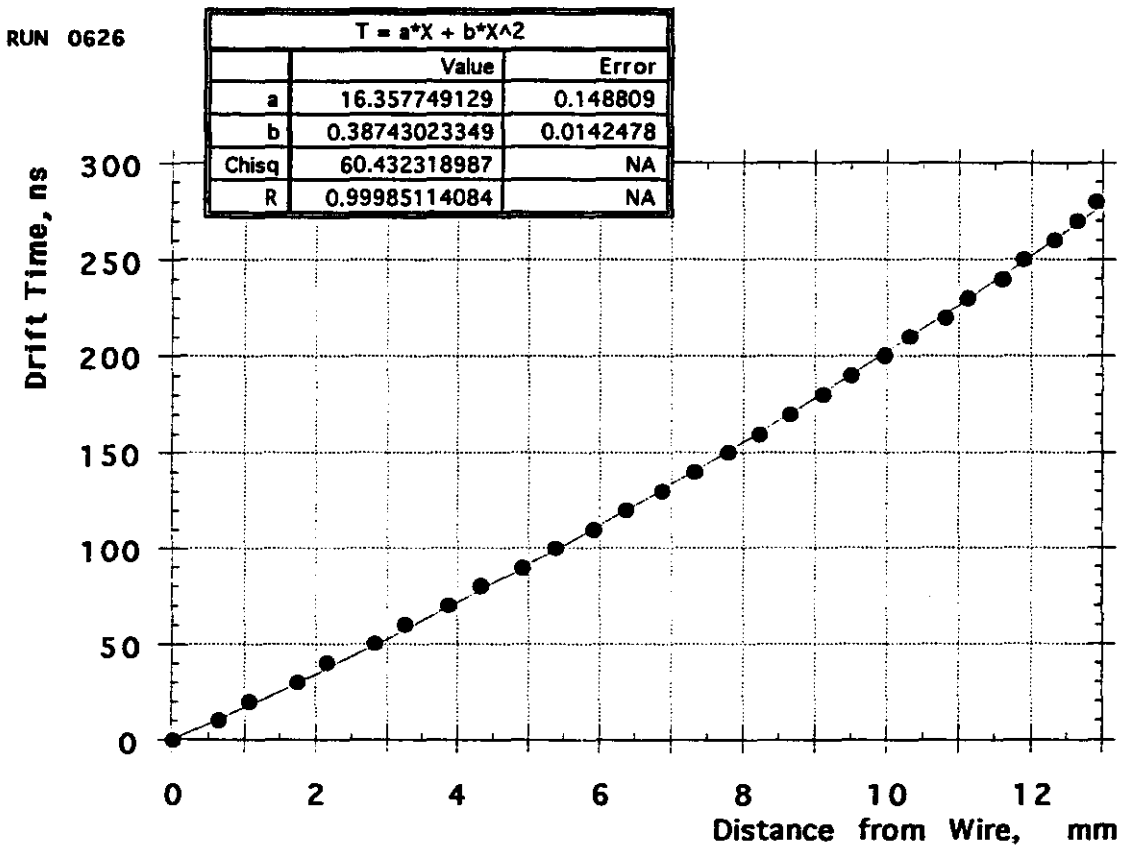
RUN 0626
T = a*X + b*X^2
Value
Error
a
16.357749129
0.148809
b
0.38743023349
0.0142478
Chisq
60.432318987
NA
R
0.99985114084
NA
Drift Time, ns
300
250
200
150
100
50
0
0
2
4
6
8
10
12
Distance from Wire, mm

Fig. 10

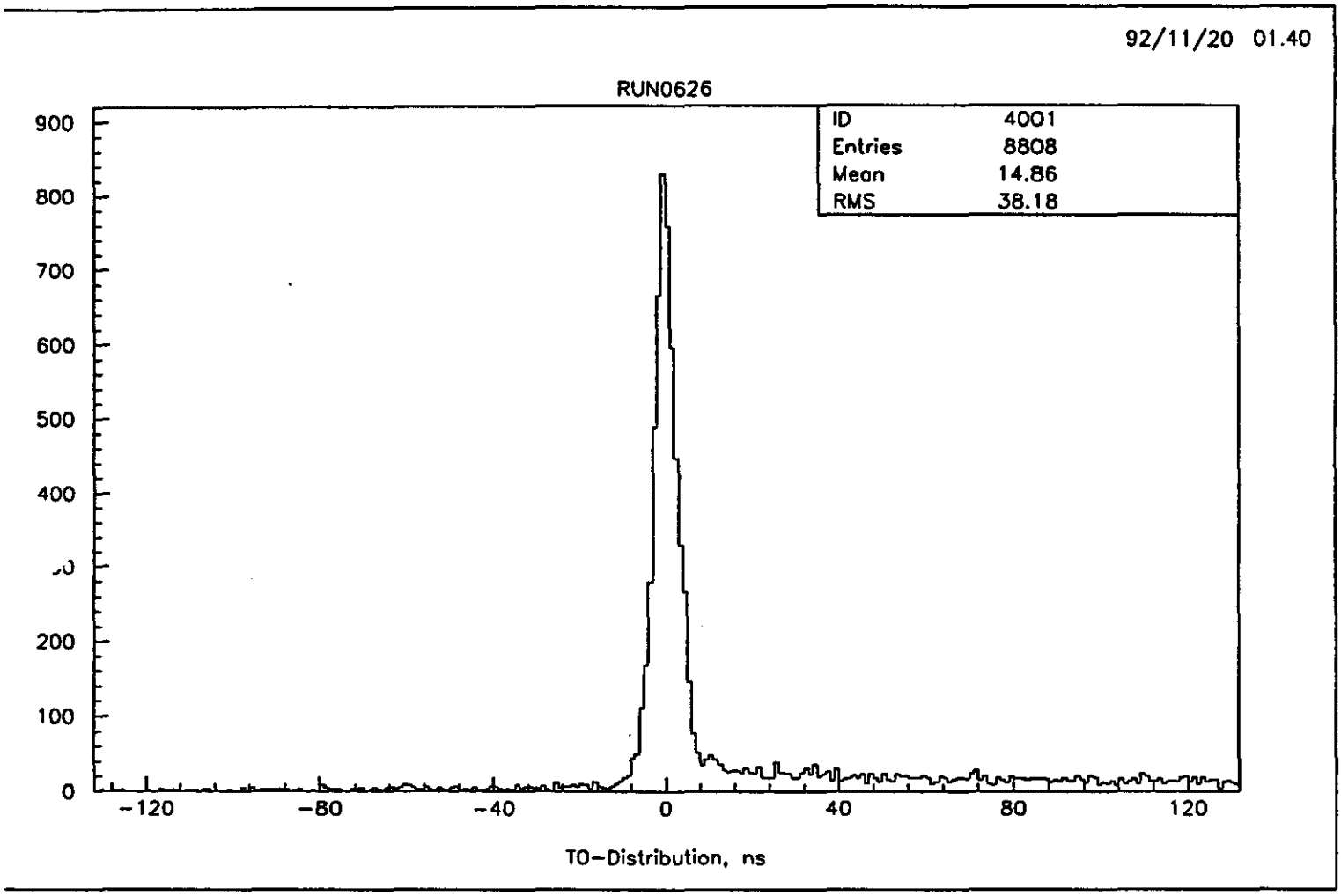
92/11/20 01.40
RUN0626
ID 4001
Entries 8808
Mean 14.86
RMS 38.18
900
800
700
600
500
400
200
100
0
-120
-80
-40
0
40
80
120
T0-Distribution, ns

Fig.11(a)

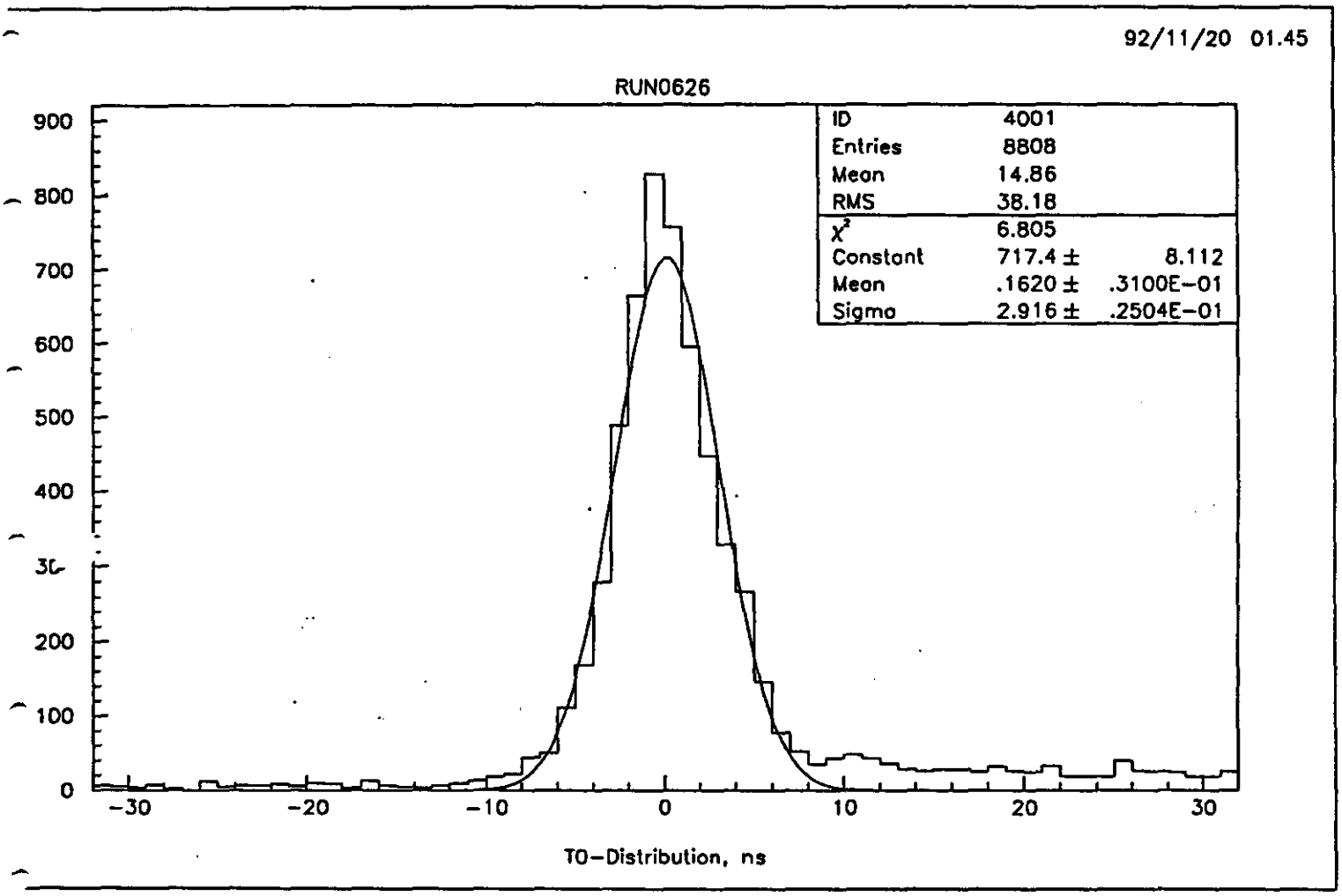
92/11/20 01.45
RUN0626
ID 4001
Entries 8808
Mean 14.86
RMS 38.18
χ² 6.805
Constant 717.4 ± 8.112
Mean .1620 ± .3100E-01
Sigma 2.916 ± .2504E-01
900
800
700
600
500
400
300
200
100
0
-30
-20
-10
0
10
20
30
T0-Distribution, ns

Fig. 11 (b)

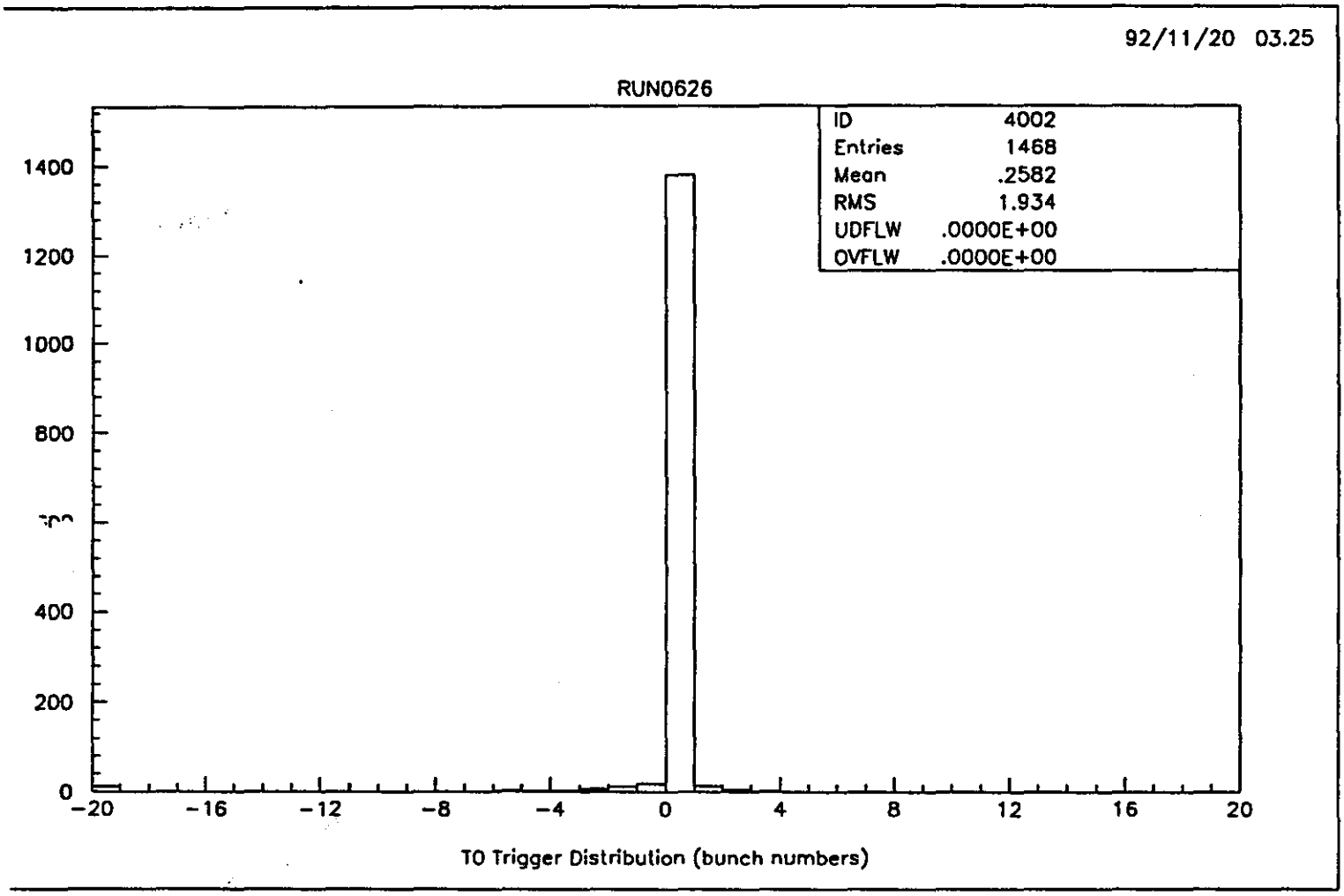
92/11/20 03.25
RUN0626
ID 4002
Entries 1468
Mean .2582
RMS 1.934
UDFLW .0000E+00
OVFLW .0000E+00
1400
1200
1000
800
400
200
0
−20
−16
−12
−8
−4
0
4
8
12
16
20
T0 Trigger Distribution (bunch numbers)

Fig. 12

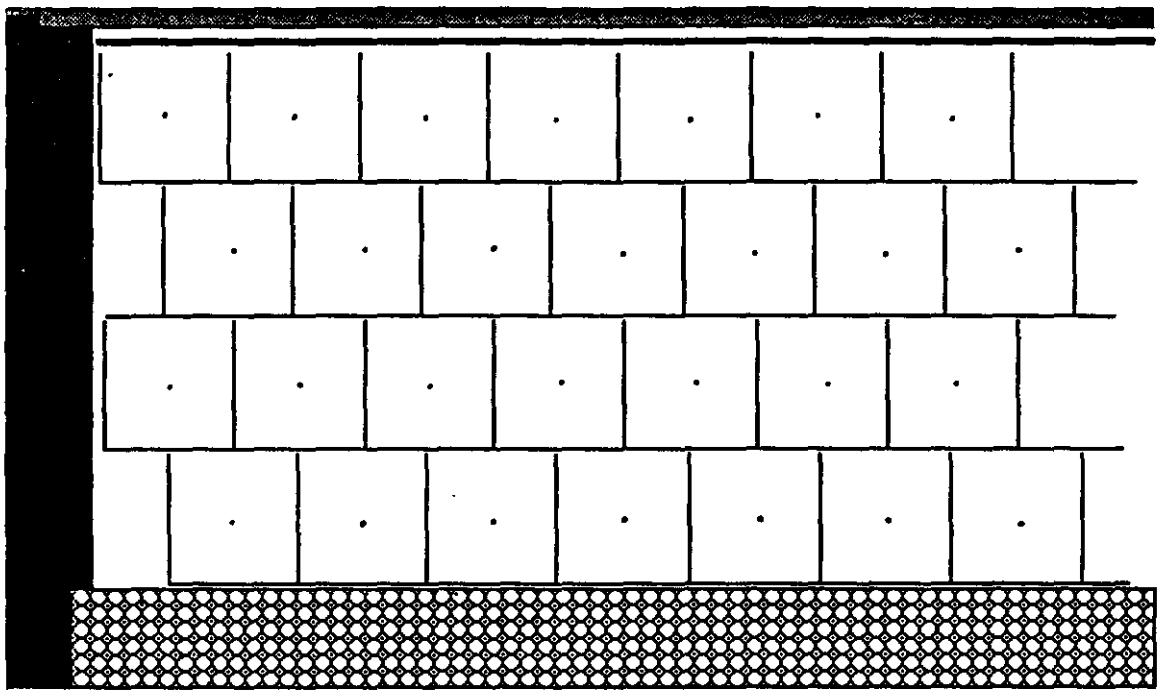

Four plane LSDT chamber

Table 2

	MC	DATA
Right answers	93.6%	94%
Wrong answers	6.1%	5%
No answer	0.3%	1%

Fig. 13

$$p \sim (2\Delta Y \cdot L) \cdot N \cdot T_{drift}$$

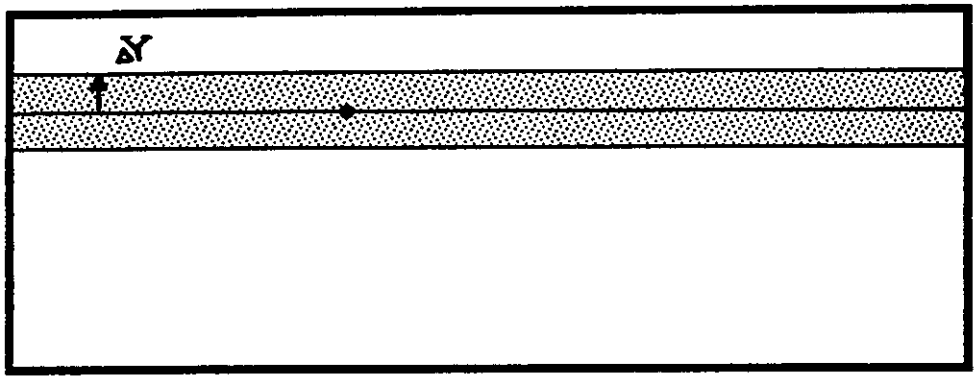

(a)

$$p \sim \left(\frac{2 \cdot 2\Delta Y}{R}\right) / 2\pi$$

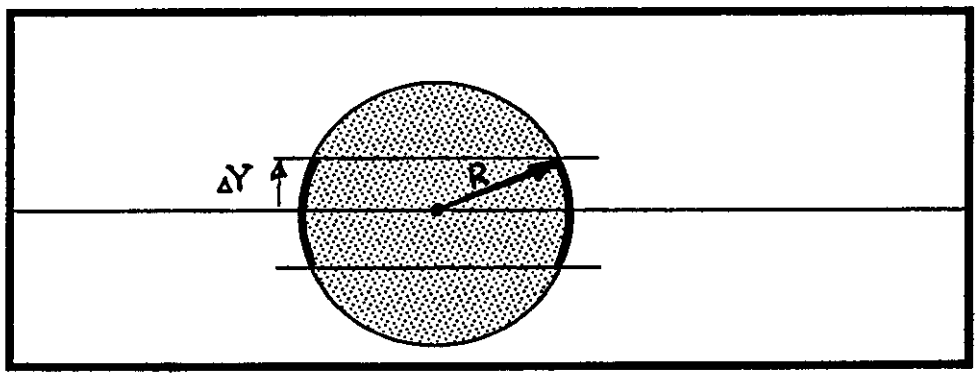

(b)

Fig. 14

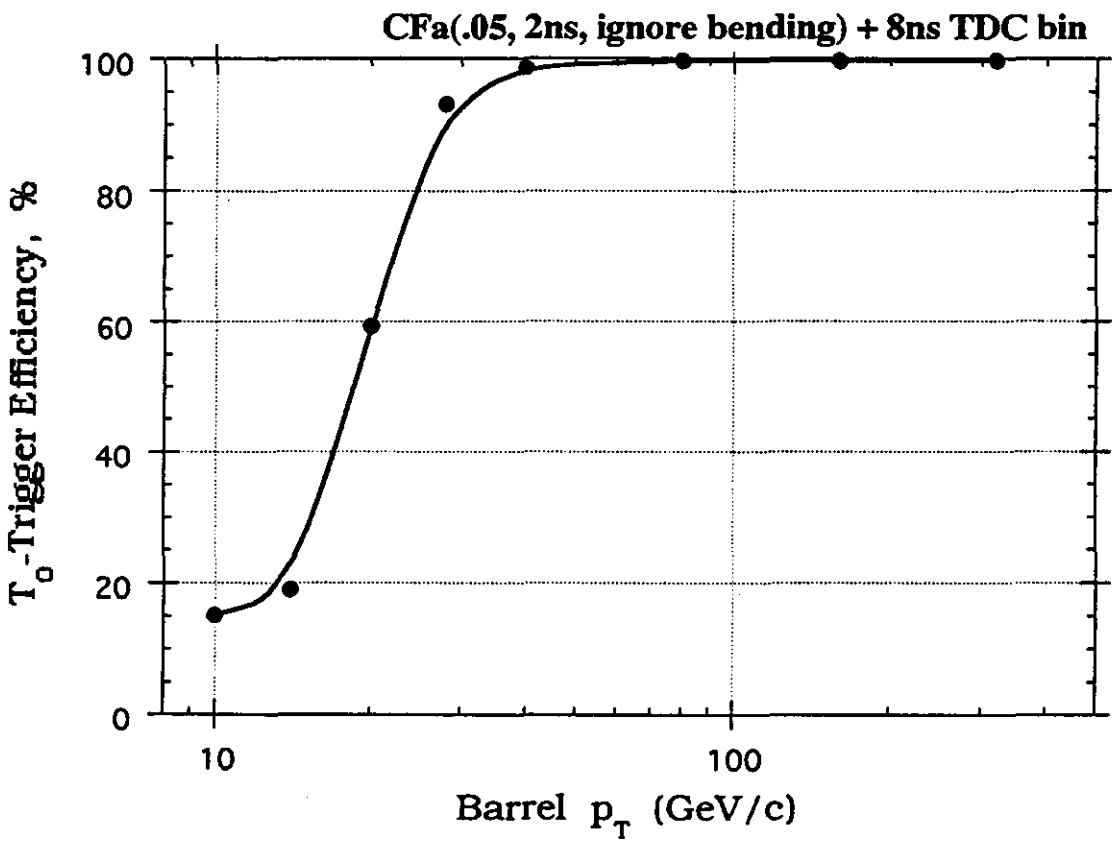
CFa(.05, 2ns, ignore bending) + 8ns TDC bin
100
80
60
40
20
0
10
100
T_0-Trigger Efficiency, %
Barrel p_T (GeV/c)

Fig. 15

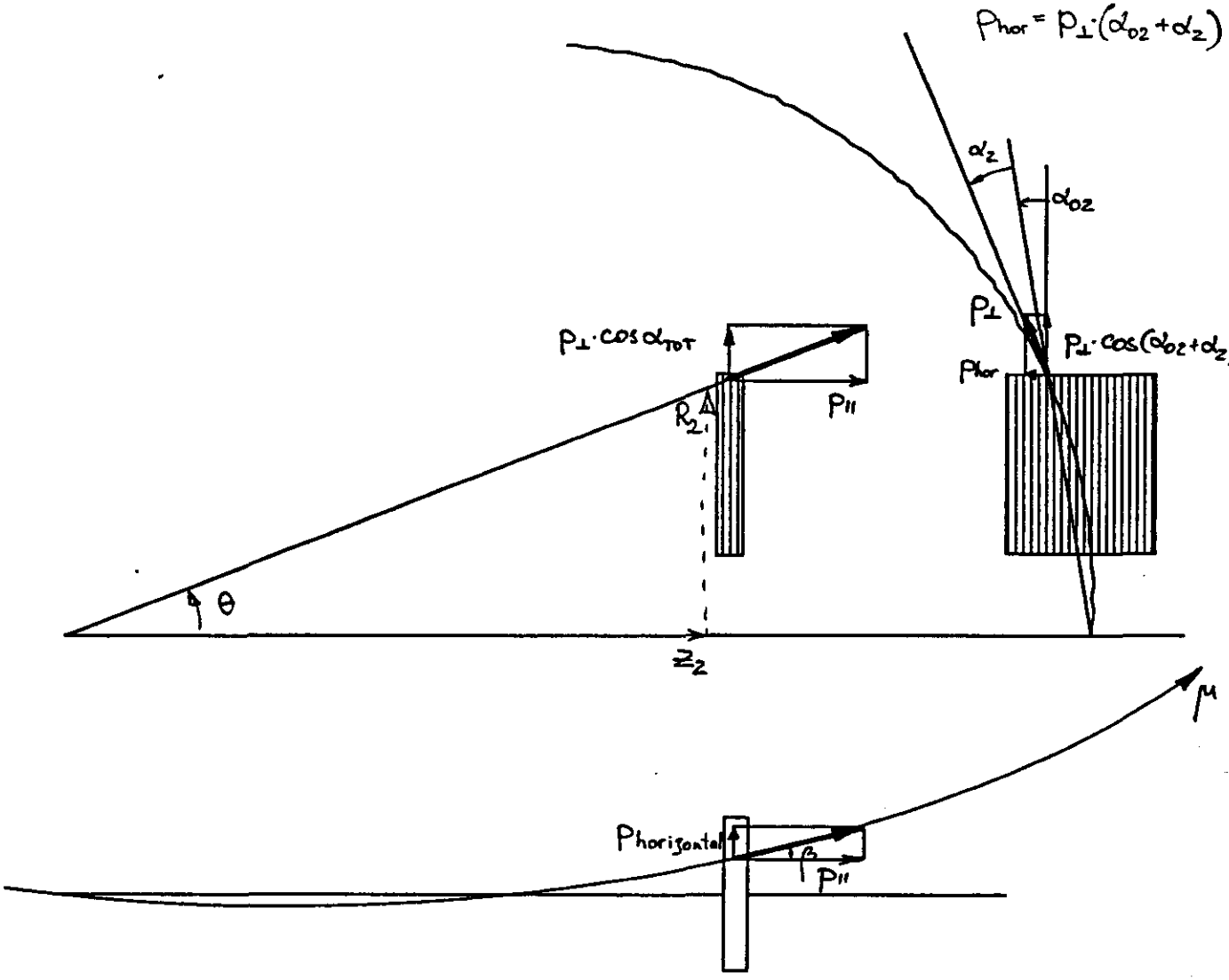

$$\beta \sim \frac{p_{hor}}{p_{\parallel}} \sim \frac{p_\perp \cdot (\alpha_{02} + \alpha_2)}{p_{\parallel}} \sim \theta \cdot (\alpha_{02} + \alpha_2) \sim \frac{\theta}{\theta_{max}} \frac{\alpha_{02} + \alpha_2}{2}$$

$$\theta_{max} \lesssim \frac{1}{2}$$

$$\beta_{END\text{-}CUP} \sim \frac{\beta_{BARREL}}{2} \cdot \frac{\theta}{\theta_{max}}$$

Fig. 16

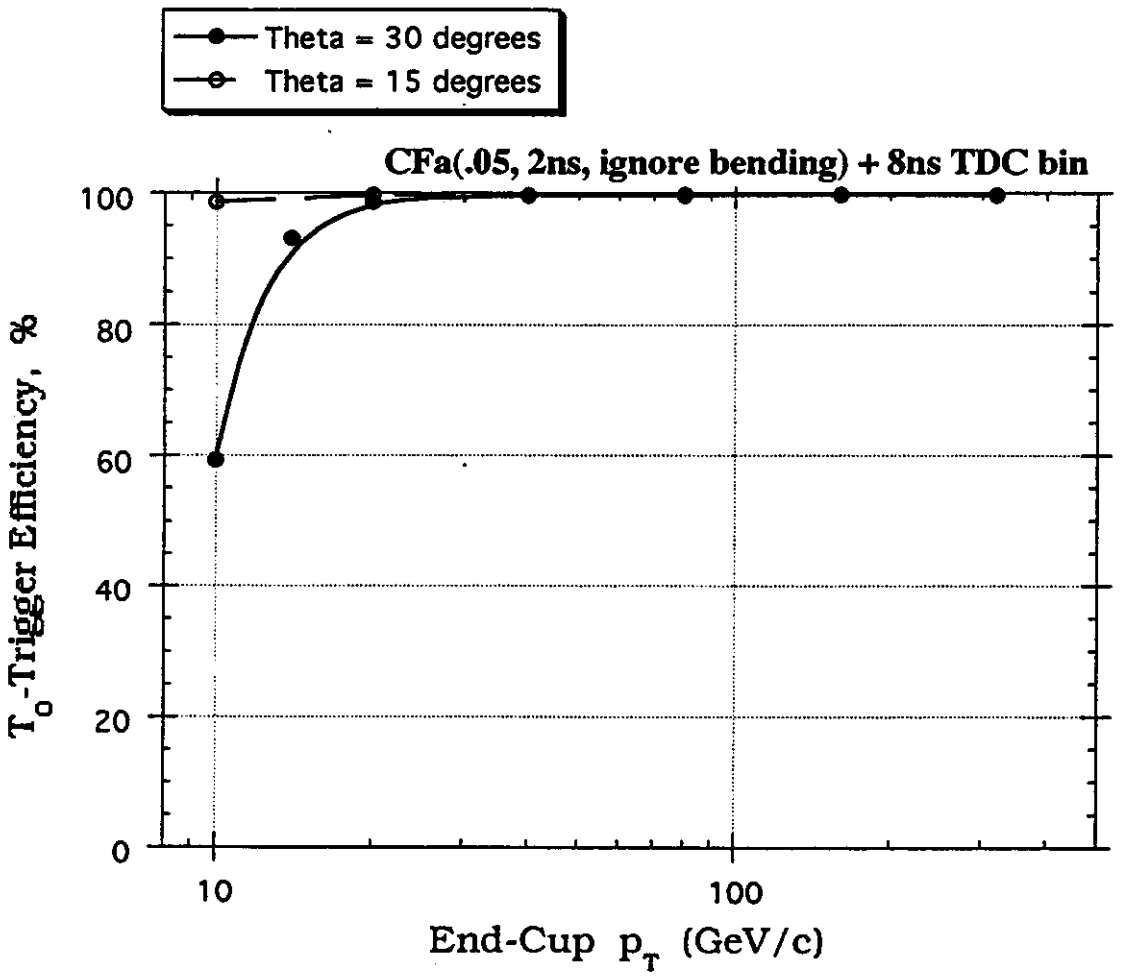
Theta = 30 degrees
Theta = 15 degrees
CFa(.05, 2ns, ignore bending) + 8ns TDC bin
100
80
60
40
20
0
10
100
T_0-Trigger Efficiency, %
End-Cup p_T (GeV/c)

Fig. 17

Appendix 1. Calculations of bending (p_T and/or α_2).

Let horisonatal axis be Y, and vertical - X (fig.1(a)).

An equation for a muon track is

$$Y = \frac{X^2}{2R} + \beta X, \quad \text{where} \quad R = \frac{p_T}{eB} = \frac{X^2}{2R} + \beta X.$$

One can easily calculate Y_3, Y_2, and, then, $\Delta Y=(L_2/L_3)Y_3-Y_2$:

$$\Delta Y = \frac{L_2(L_3 - L_2)}{2R} = \frac{L_2(L_3 - L_2)}{2p_T} eB.$$

One can see that ΔY is indeed a measure of bending:

$$p_T = \frac{L_2(L_3 - L_2)}{2\Delta Y} eB$$

$$\alpha_2 = \frac{\partial Y(L_2)}{\partial X} - \frac{Y_2}{L_2} = \frac{\Delta Y}{L_3 - L_2}$$

Appendix 2. Contribution of Multiple Scattering in the Calorimeter.

1. To calculate T_0, the scheme requires the determination of α_2^T - inclination angle of a track in the SuperLayer#2 (superscript T stands for "Total"). This angle is $\alpha_2^T = \alpha_0 + \alpha_2$, where α_2 is an angle due to track bending in the magnetic field, α_0 is a geometrical angle (angle of a straight line coming out of the vertex). Angle α_2 is momentum dependent and determined as follows (fig.4):

$$\alpha_2 = \frac{d}{\Delta L}, \text{ where } \Delta L = L_3 - L_2 .$$

2. If there is no multiple scattering, the track line is described by the following expression (fig.A2.1):

$$y = \frac{x^2}{2R}, \text{ where } R = p/(eB) \text{ is a radius of cuvature} .$$

A muon coming out of the calorimeter has a y-coordinate y_1 and an inclination angle α_1^T ($\alpha_1^T = \frac{\partial y_1}{\partial x}$). (In the following calculations we will assume that axis X is perpendicular to the chamber. We are looking for the error in determination of angle α_2 and this does not depend on a sector rotation with respect to a muon.)

3. The consequence of multiple scattering is that a muon has some displacement δy_1 and a slight change of an angle $\delta\alpha_1$ in the outcoming point. Let's call for simplicity sake $\delta y_1 = \Delta$ and $\delta\alpha_1 = \theta$. The RMS's and correlation of this parameters depend on the calorimeter thickness and are as follows:

$$\theta_0 = \frac{14.1 MeV}{p}\sqrt{\frac{X_{cal}}{X_0}}; \qquad \Delta_0 = \frac{1}{\sqrt{3}} X_{cal}\theta_0; \qquad \rho_{\theta\Delta} = \frac{\sqrt{3}}{2}$$

4. This results in a change of a trajectory; now it will be:

$$y = \frac{x^2}{2R} + bx + c$$

where $b=\theta$ and $c=\Delta-\theta L_1$ to satisfy new boundary conditions on the calorimeter surface.

5. Actual angle α_2 will be:

$$\alpha_2 = \alpha_1^{\mathrm{T}} - \alpha_0 = \frac{\partial y_2}{\partial x} - \frac{y_2}{L_2} = \frac{L_2}{2R} - \frac{c}{L_2} \ .$$

(Notice that this does not depend on the sector rotation).

6. Angle α_2 as measured ($\alpha_2 = \frac{d}{\Delta L}$):

$$\alpha_2^{meas} = \frac{\frac{L_2}{L_3} y_3 - y_2}{\Delta L} = \frac{1}{\Delta L}\left(\frac{L_2}{L_3}\left(\frac{L_3^2}{2R} + bL_3 + c\right) - \left(\frac{L_2^2}{2R} + bL_2 + c\right)\right) = \frac{L_2}{2R} - \frac{c}{L_3}$$

7. Error in Angle Measurement:

$$\delta\alpha_2 = \alpha_2^{meas} - \alpha_2 = \frac{c}{L_2} - \frac{c}{L_3} = (\Delta - \theta L_1)\frac{\Delta L}{L_3 L_2}$$

Taking into account RMS's and correlation function one gets:

$$\overline{\delta\alpha_2^2} = \theta_0^2 (L_1^2 - L_1 X_{cal} + \frac{1}{3} X_{cal}^2)\frac{\Delta L^2}{L_3{}^2 L_2{}^2} \ .$$

Using the LOI numbers (L_1=3.9m, L_2=6.3m, L_3=8.7m, X=2.5m, Cu calorimeter of effective 12λ thickness) for <u>p=10 GeV/c</u> one get **<u>the angle error of about δα~.002, what is smaller than the assumed measurement error (and, of course, it is far away from the biggest tolerable error)</u>**.

8. Momentum Error Due to Multiple Scattering.

The angle α_2 gives a measure of p_T.

Without multiple scattering:

$$\alpha_2(no\ \mathrm{m.s.}) = \frac{L_2}{2R} = \frac{eBL_2}{2p} \ .$$

Due to multiple scattering, the measured angle will have an error:

$$\delta\alpha_2 = \alpha_2^{meas} - \alpha_2(no\ \mathrm{m.s.}) = -\frac{c}{L_3},$$

what corresponds to momentum error of **<u>δp/p~.066</u>**.

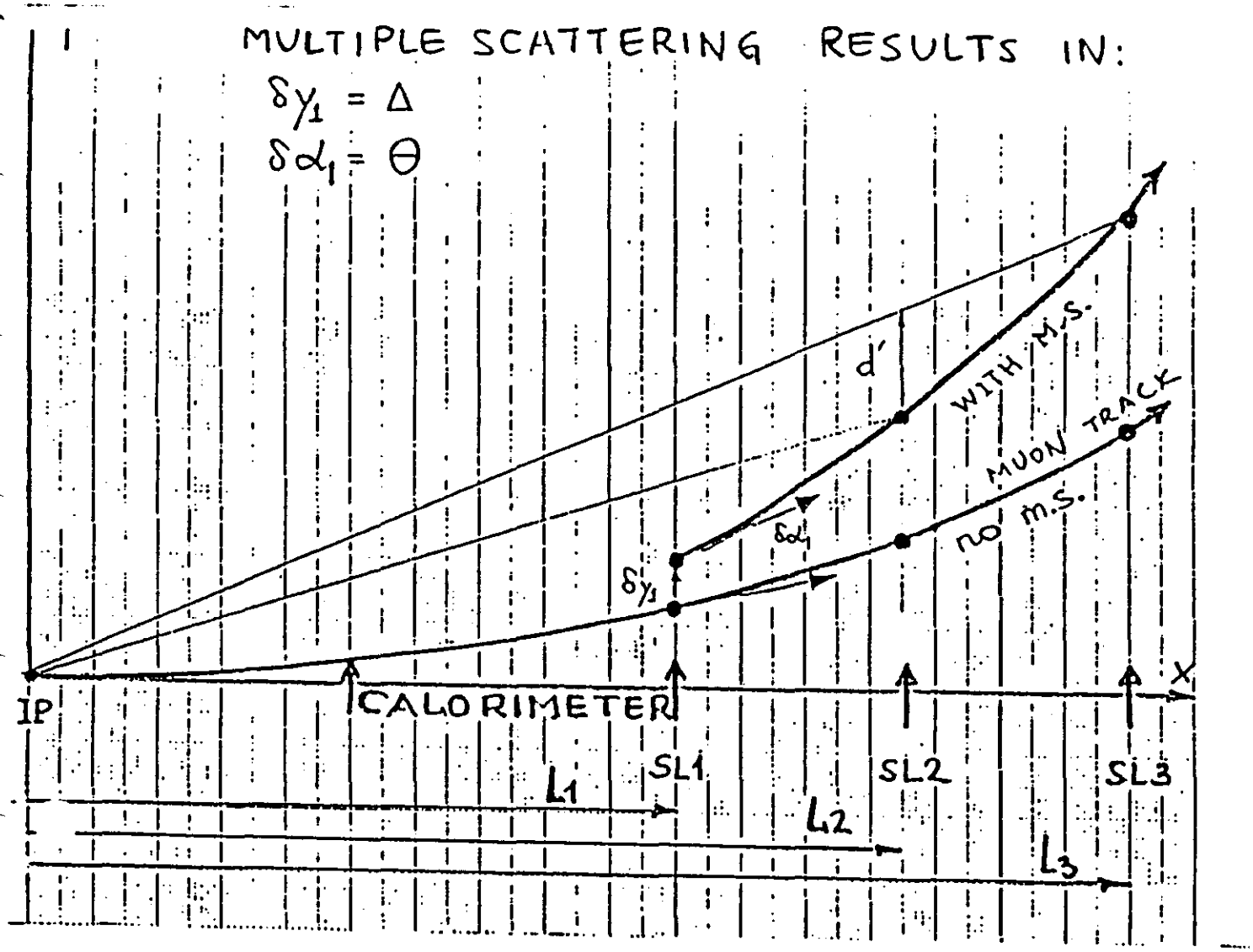
MULTIPLE SCATTERING RESULTS IN:
$\delta y_1 = \Delta$
$\delta \alpha_1 = \Theta$
d'
WITH M.S.
MUON TRACK
no M.S.
$\delta\alpha_1$
δy_1
IP
CALORIMETER
SL1
SL2
SL3
X
L_1
L_2
L_3

Fig. A2.1

R. Sumner, October 1992

Appendix 3 : Hardware Implementation of the Level 1 Trigger

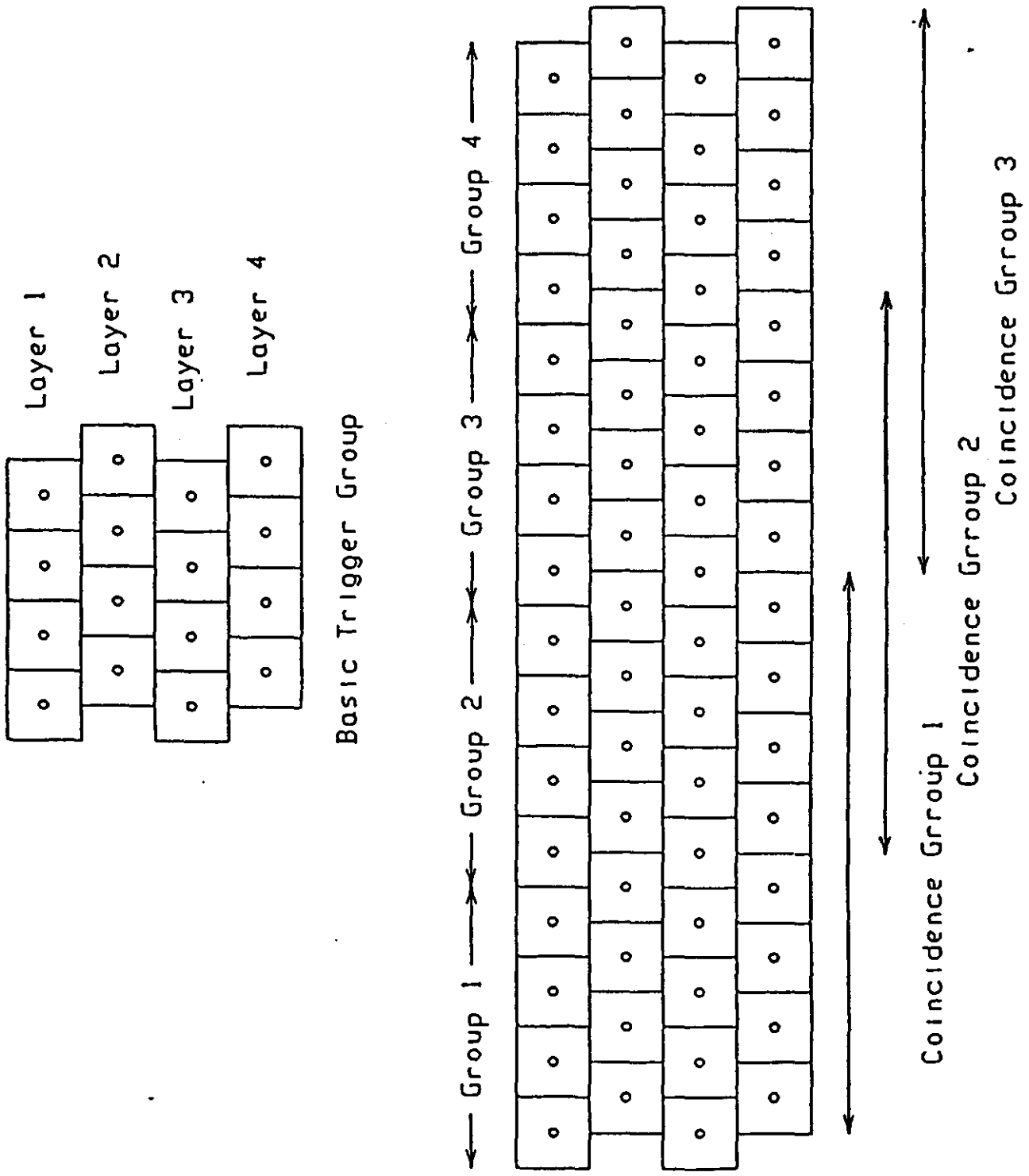

Fig.A3.1.

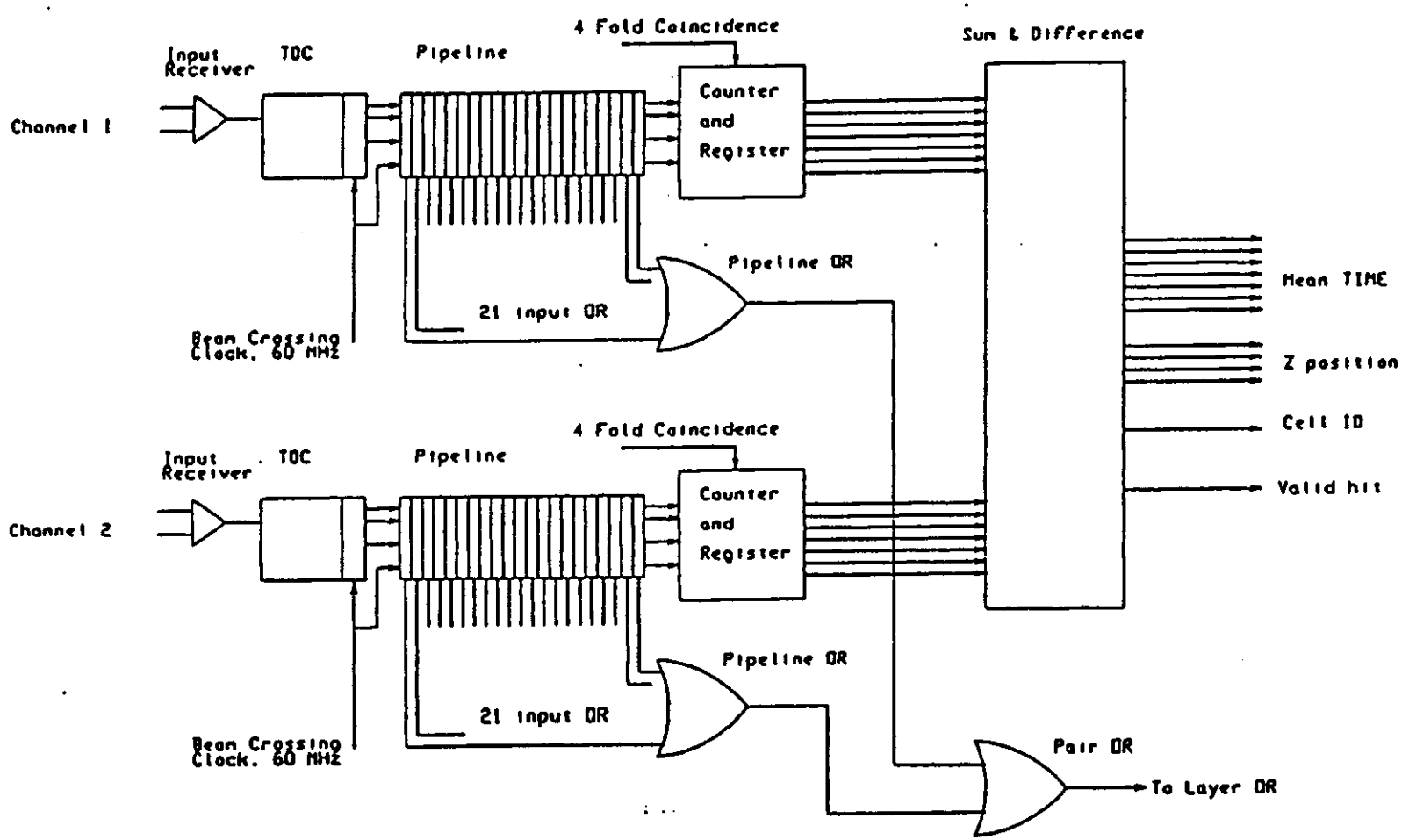

Fig.A3.2 Muon Trigger TDC

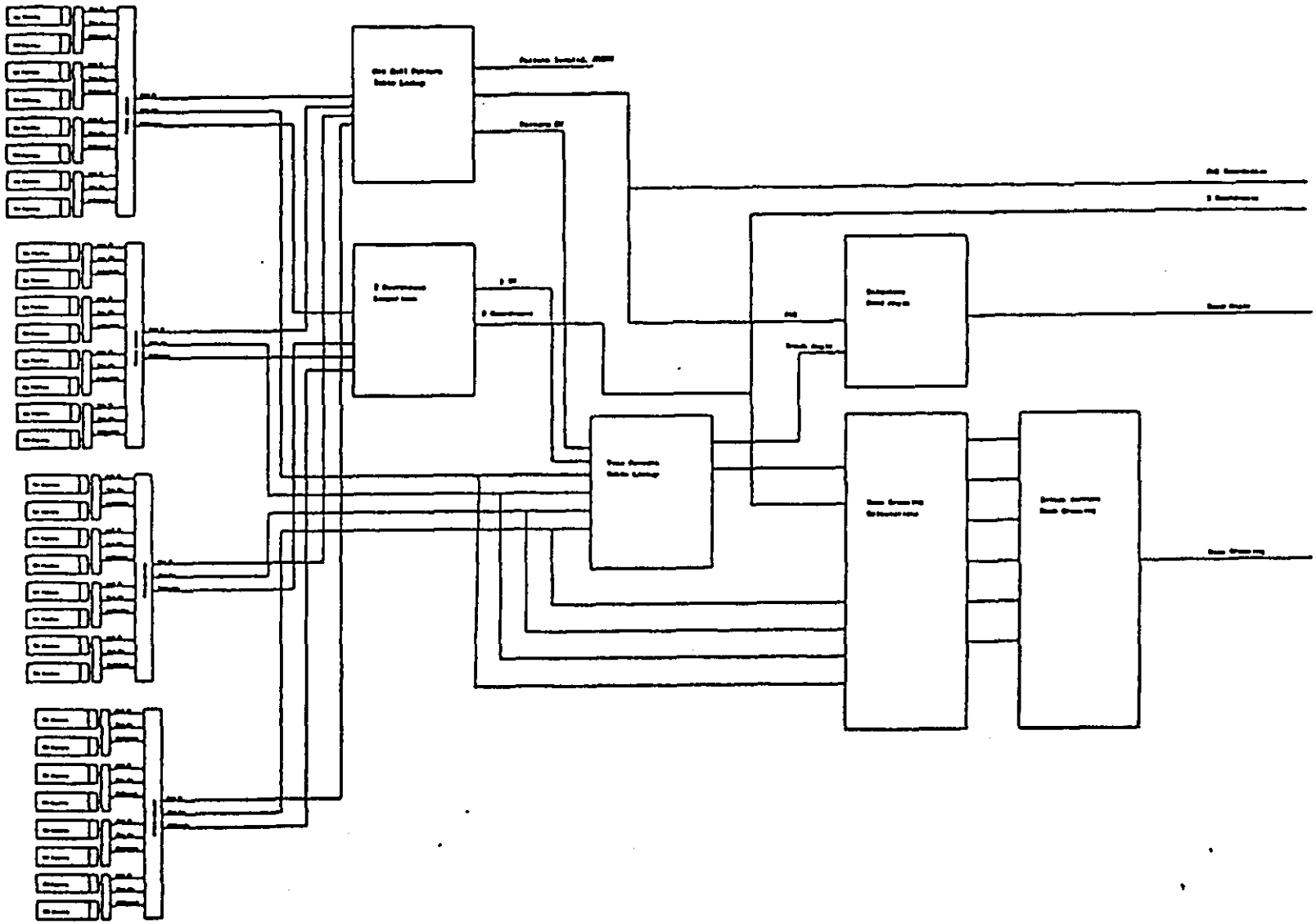

Fig.A3.3

Appendix 4.

Daniel R. Marlow
September 23, 1992

A Short-Delay-Time Implementation of the LSDT Trigger

Recently, Korytov proposed a trigger scheme for the GEM LSDT's suitable for determining the bunch crossing for the Level 1 trigger. Korytov's analysis shows that for staggered square tubes of transverse dimension D (see figure 1) having a time-distance relationship of the form

$$t_i = ad_i + bd_i^2$$

where t_i is the drift time of charge originating a distance d_i away from the wire, T_0, the absolute time of the particle's incidence, is given by

$$T_0 = \frac{(t_1 + t_2)}{2} - \frac{aC_0}{2} - \frac{b}{4}\left[C_0^2 + \frac{\Delta T^2}{(a + bC_0)^2}\right]$$

where $\Delta T = t_1 - t_2$ and

$$C_0 = \frac{D}{2} + \alpha D \qquad \text{and} \qquad \alpha = \tan\theta$$

where θ is the angle of incidence (zero for normal incidence).

The first term in the expression for T_0 is just $\bar{t} = (t_1 + t_2)/2$, the mean time of arrival of the two pulses. Note that for a linear gas ($b = 0$) and normal incidence ($\alpha = 0$) the second and third terms vanish, apart from a fixed constant. In practice these terms are not zero, but they can be viewed as corrections to the mean time, i.e.

$$T_0 \equiv \bar{t} + \Gamma(\alpha, \Delta T) + t_0$$

where t_0 is a constant offset. Figures 2a shows the additive time correction as a function of momentum, which is closely related to α; and figure 2b shows the corrections as a function of ΔT for various choices of α.

Circuits capable of performing the meantiming function in realtime can be implemented in a number of ways. A popular approach is shown in figure 3. As the figure suggests, the same circuit has been used in past high-energy physics experiments to correct for position dependence in long scintillators. In practice the delays can be implemented using logic gates, permitting very fine granularity. Although the *time* at which the first AND-gate coincidence is satisfied depends only on $\bar{t}$, the *position* of the first AND gate to fire depends on ΔT. Thus by adding small amounts of extra circuitry (a priority encoder) one can devise a circuit that simultaneously meantimes its inputs and produces a binary word proportional to ΔT.

This block can in turn be incorporated into the system shown in figure 3. The pulse emerging from the meantimer is delayed (slightly) allowing enough time for the ΔT information to be combined with a binary representation of α to form an address for the

memory lookup unit (MLU). The contents of the MLU are loaded with the required correction time—i.e. they contain the function $\Gamma(\alpha, \Delta T)$. The value of Γ is then used to dynamically adjust the delay time such that a pulse emerges at time T_0 (plus a constant). One simple implementation of the adjustable delay is a presettable down-counter, although it may prove desirable to seek designs based solely on asynchronous logic, as discussed below.

For values of α and ΔT of practical interest, Γ is always less than $\sim$ 100 ns or so. Requiring $\leq$ 4 ns of "quantization error" in Γ leads to the need for only five or six bits of accuracy. Assuming comparable accuracies for α and ΔT are required, the number of address lines to the MLU is in the range of 10 to 12 bits, a modest size by today's standards.

The outputs of the corresponding circuits from other left right wire pairs can be combined using a standard majority logic circuit that requires a specified multiplicity. This will provide immunity to noise and to the (presumably) small number of cases where the T_0 signal from a given pair comes out of time.

For normal incidence the latency time of this scheme is the drift time plus the fixed delay of the meantimer. In the implementation shown this is one half of the maximum drift time, yielding a total latency of 1.5 times the total drift time. The MLU also adds some delay, but this can be kept to a few tens of ns. Finally, some allowance must be made for non-normal incidence, which will also add to the latency, but this is probably less than 100 ns. We note that there is some room left between the latency of this circuit and the irreducible limit imposed by causality, suggesting that further improvements are possible. This would require a meantimer design with no fixed propagation delay.

Another such concern in any such scheme is the deadtime. For schemes employing sequential logic, this will likely be of the same order as the latency. If, however, a pipelined version of the adjustable delay can devised—this should be possible—the entire circuit can be fully pipelined. In this case, the effective deadtime can be reduced to the few $\times$10 ns level. An added benefit would be the elimination of the need for a high-speed clock.

One loose end in this design is the determination of α, which will require additional circuitry. This could entail some additional latency due to propagation delays since α is an inherently non-local quantity.

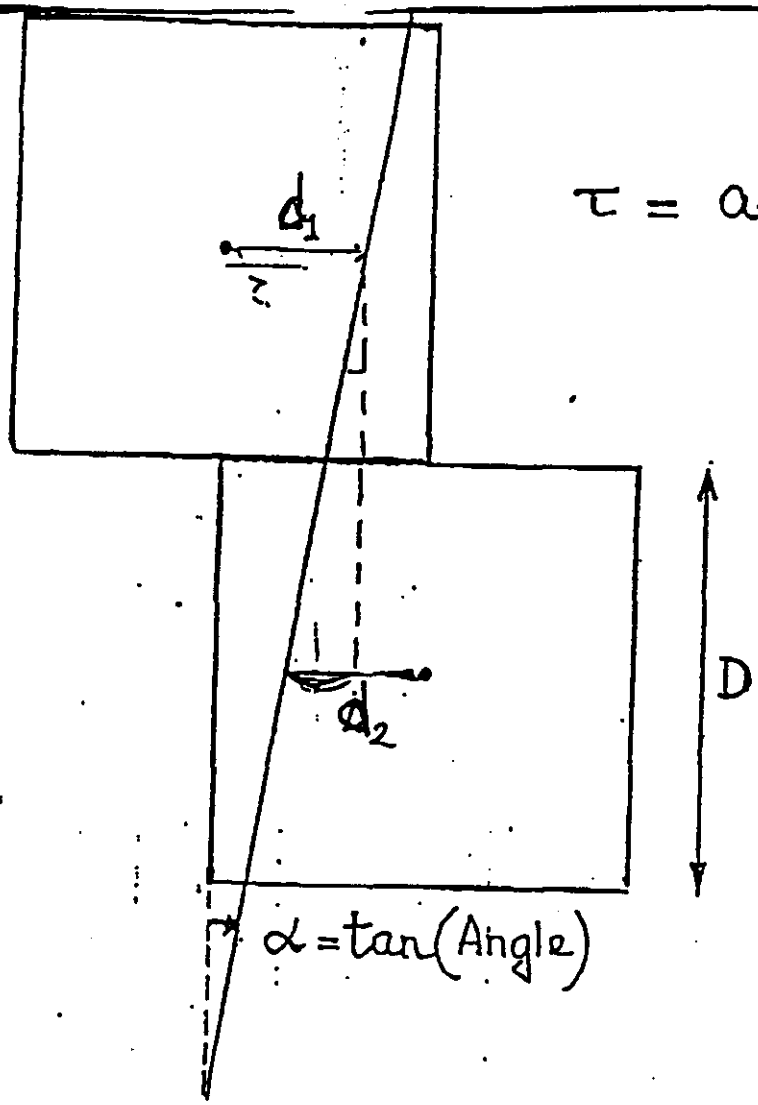

$$\tau = a \cdot \Delta + b \cdot \Delta^2$$

$$T_0 = \frac{t_1 + t_2}{2} - \frac{a \cdot C_0}{2} - \frac{b}{4}\left(C_0^2 + \frac{(\Delta T)^2}{(a + bC_0)^2}\right)$$

$$C_0 = \frac{D}{2} + \alpha \cdot D$$

Figure 1 (App.4)

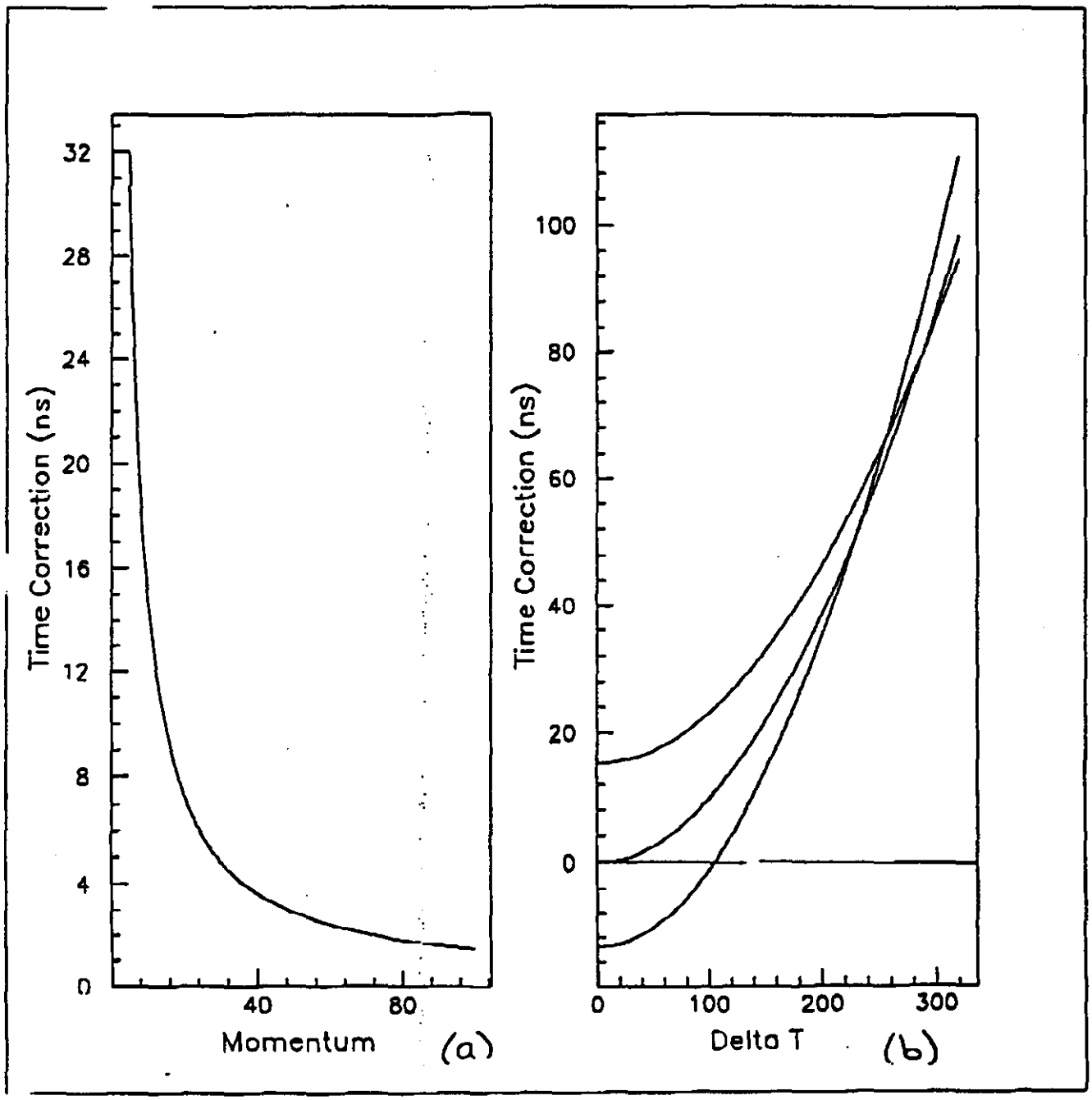

Figure 2 (App. 4)

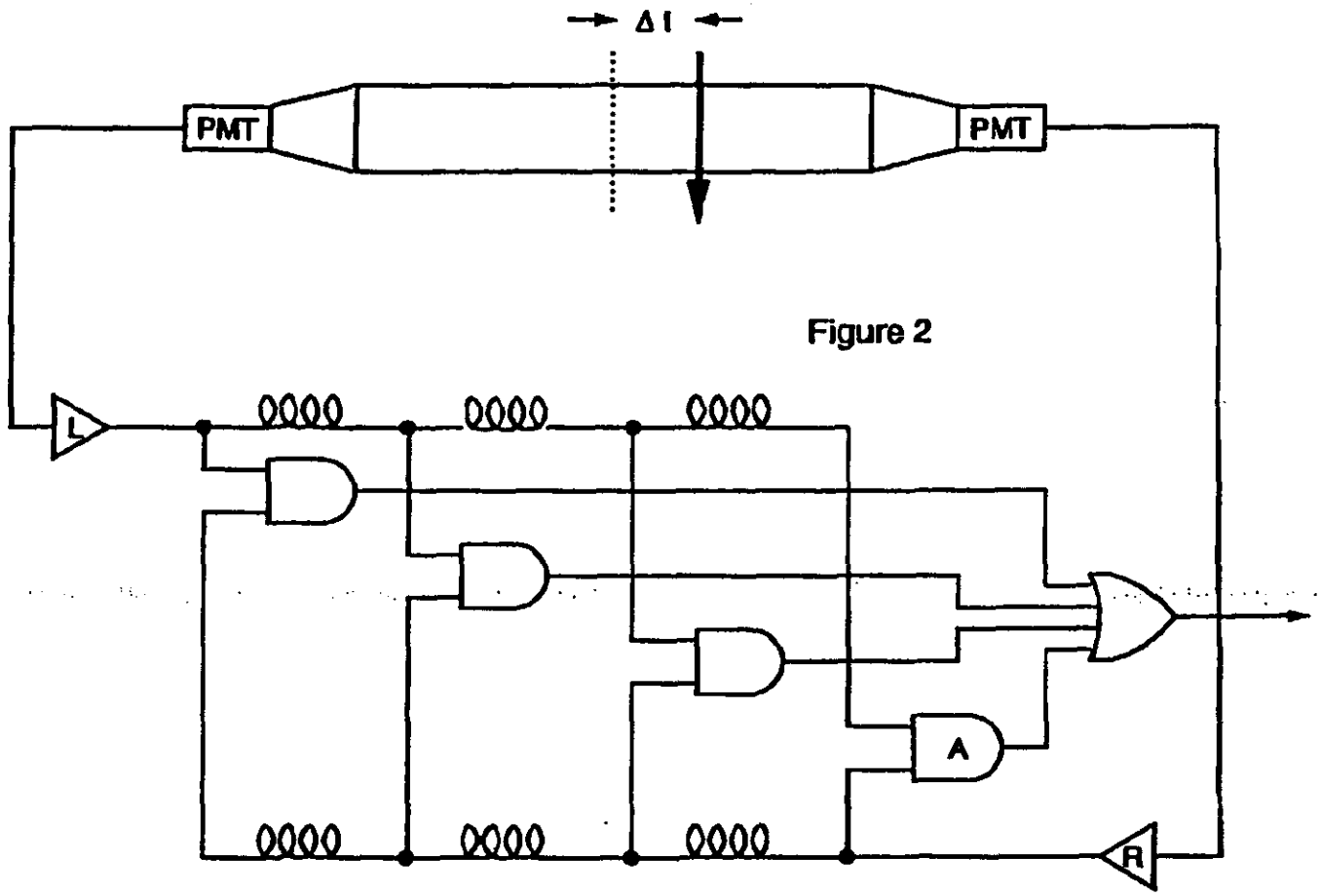

Figure 2

Figure 3 (App. 4)

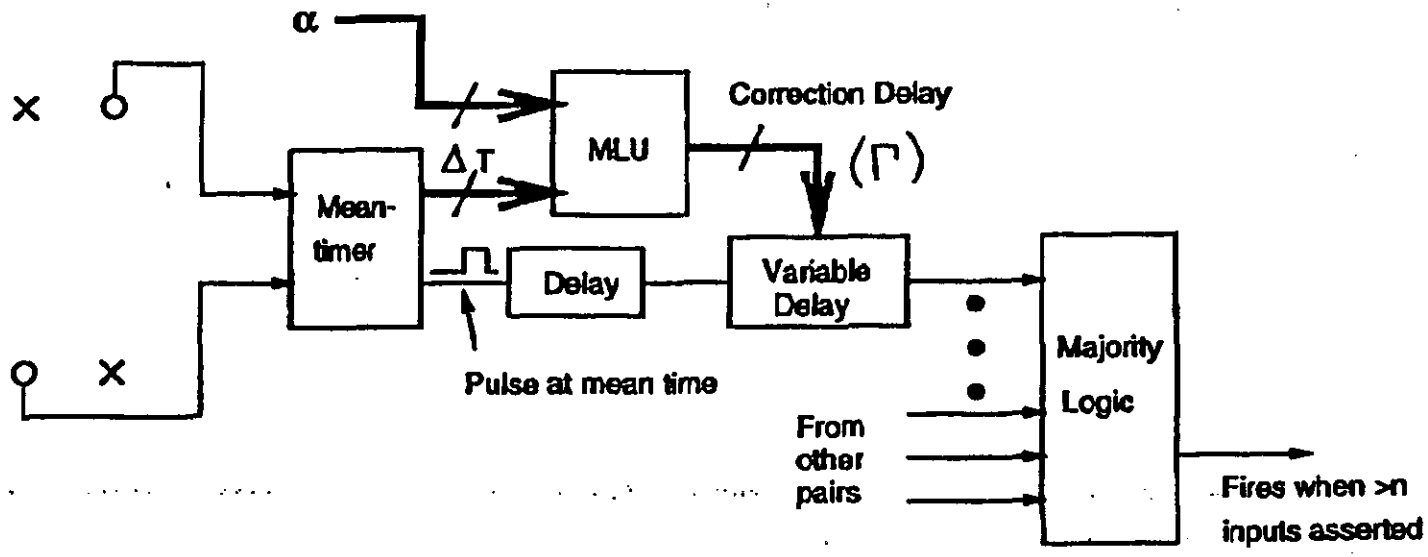

Figure 4 (App. 4)